Convection géostrophique turbulente engendrée par chauffage radiatif

Vincent Bouillaut

To cite this version:

Vincent Bouillaut. Convection géostrophique turbulente engendrée par chauffage radiatif. Fluid Dynamics [physics.flu-dyn]. Université Paris-Saclay, 2022. English. NNT : 2022UPASP008 . tel-03677597

HAL Id: tel-03677597
https://theses.hal.science/tel-03677597

Submitted on 24 May 2022

université
PARIS-SACLAY

Radiative heating achieves the geostrophic turbulence regime of convection

Convection géostrophique turbulente engendrée par chauffage radiatif

Thèse de doctorat de l'université Paris-Saclay

École doctorale n° 564, Physique en Île-de-France (PIF)
Spécialité de doctorat: Physique
Graduate School : Physique. Référent : Faculté des sciences d'Orsay

Thèse préparée dans l'unité de recherche SPEC (université Paris-Saclay, CEA, CNRS) sous la direction de Sébastien AUMAÎTRE et le co-encadrement de Basile GALLET, chercheurs au CEA Paris-Saclay.

Thèse présentée et soutenue à Paris-Saclay, le 14 Janvier 2022, par

Vincent Bouillaut

Composition du jury:

Francesca CHILLÀ Professeur des universités, École Normale Supérieure de Lyon	Présidente
Fabien GODEFERD Directeur de recherches, CNRS, École Centrale de Lyon	Rapporteur & Examinateur
Nicolas MORDANT Professeur des universités, Université Grenoble-Alpes	Rapporteur & Examinateur
Christophe GISSINGER Maître de conférences, École Normale Supérieure de Paris	Examinateur
Sébastien AUMAÎTRE Chercheur CEA Paris-Saclay	Directeur de thèse

Thèse de doctorat

NNT: 2022UPASP008

Titre: Convection géostrophique turbulente engendrée par chauffage radiatif

Mots clés: Convection thermique, Turbulence, Géostrophique, Rotation, Dynamique des fluides astrophysiques.

Résumé: Nous nous intéressons au phénomène de convection en rotation rapide forcée par une source radiative de chaleur. La convection par forçage radiatif s'avère pertinente pour décrire les intérieurs stellaires et planétaires, où le principal défi est de quantifier le transport turbulent. Une question fondamentale est l'impact de la rotation globale sur ce transport turbulent. Du point de vue théorique, ces systèmes peuvent a priori opérer dans différents régimes, depuis une convection faiblement affectée par la rotation jusqu'au régime de « turbulence géostrophique » de convection en rotation rapide. Ce dernier a été prédit en 1979 mais attend toujours une confirmation expérimentale. Les expériences existantes sont toutes basées sur une injection de chaleur par conduction entre la paroi et le fluide, un transfert qui s'avère peu efficace. L'idée ici est d'utiliser un forçage radiatif, i.e., une source de chaleur partiellement volumique, afin d'injecter en partie la chaleur directement dans l'écoulement turbulent. Ce type de forçage a déjà démontré sa capacité à atteindre des régimes de convection pleinement turbulente. Nous avons donc modifié l'expérience existante et son système de mesure afin d'ajouter une rotation d'ensemble. Après avoir vérifié que le seuil de la convection en rotation est peu modifié par l'utilisation d'une source de chaleur partiellement volumique, nous étudions expérimentalement l'effet de la rotation sur l'efficacité de la convection thermique turbulente, en termes de flux de chaleur adimensionné. Nous observons que, pour une vitesse de rotation suffisamment grande, l'efficacité de la convection thermique diminue comparée au cas sans rotation. Nous montrons que cette diminution suit la loi de puissance du régime de « turbulence géostrophique » prédite en 1979. L'utilisation d'une source radiative de chaleur nous permet donc de réaliser la première observation expérimentale de ce régime extrême de convection.

Title: Radiative heating achieves the geostrophic turbulence regime of convection

Keywords: Thermal convection, Turbulence, Geostrophic, Rotation, Astrophysical fluid dynamics

Abstract: We study rapidly rotating convection forced by a radiative heat source. Radiative heating is relevant to stellar and planetary interiors, where the main challenge is to quantify the transport of heat and tracers by turbulent convection, including the crucial impact of global rotation. Rotating convection can operate in various regimes ranging from weakly rotating convection to the "geostrophic turbulence" regime of rapidly rotating convection. The latter was predicted in 1979, and has been awaiting laboratory confirmation ever since, despite the development of ever-taller rotating convection experiments worldwide. The common point of these experiments is heat injection through conduction between the wall and the fluid, a rather inefficient transfer mechanism. The idea here is to use radiative forcing, i.e., a partially volumic heat source, to inject heat directly into the turbulent flow. This type of forcing has already proven able to achieve fully turbulent convection. We modified the existing experiment to subject the flow to uniform global rotation. After verifying, through the development of a finite difference code, that the threshold of rotating convection is hardly modified by the partially volumic heat source, we experimentally study the effect of rotation on the turbulent convective flow (in terms of dimensionless heat flux). We observe that, for sufficiently fast rotation, the efficiency of thermal convection decreases as compared to the case without rotation. Finally, we show that this decrease follows the scaling prediction of the "geostrophic turbulence" regime. Radiative heating thus allows us to provide the first clear experimental observation of this extreme regime.

Contents

List of figures

List of Tables

Remerciements

Après trois années passées pour réaliser ce manuscrit de thèse il me faudrait l'équivalent en termes de pages pour remercier de manière exhaustive tous ceux qui ont eu un impact dans son déroulement. Je suis arrivé au Sphynx pour mon stage de fin d'étude et j'y ai trouvé une équipe extrêmement dynamique et agréable. Je garderai un très bon souvenir de ces trois années et je le dois à chacun des membres du laboratoire et les stagiaires qui y sont passés.

Je tiens à remercier en premier mes directeurs de thèse... enfin mon directeur de thèse Sébastien Aumaître et mon co-encadrant Basile Gallet. Leur bonne humeur a été extrêmement communicative et leur passion pour la physique ont rendu chaque conversation des (trop ?) nombreuses pauses cafés particulièrement enrichissantes. Leur impressionnante culture générale scientifique m'a permis d'en apprendre énormément sur bien d'autres aspects de la physique que seulement ce qui touche à mon sujet de thèse. Et si cette dernière a fourni autant de résultats et produit autant de publications c'est bien grâce à leur encadrement exemplaire qui laisse largement place au débat et à la prise d'initiatives individuelles. Merci de m'avoir fait confiance pour mener à bien ce projet.

Je remercie les membres du jury pour avoir accepter d'évaluer mon travail de thèse et pour leurs remarques et questions pertinentes lors de la soutenance ainsi que dans les rapports des deux rapporteurs Nicolas Mordant et Fabien Godeferd.

Pendant ces trois ans j'ai eu l'immense honneur de partager mon bureau avec Benjamin Miquel, amateur de jazz et de jeux de mots gênants, qui arrive en plus de son travail de chercheur et son rôle de père à faire de la guitare simplifiée (aussi appelée basse), du piano, du vélo, de l'escalade et autres activités d'extérieur tout aussi peu recommandables. Je n'ai jamais su comment il arrivait à augmenter le nombre d'heures dans une journée mais ça a été un vrai plaisir de travailler avec lui.

Que serait un doctorant sans le soutien des autres thésards ? Et bien pas grand chose.

Depuis mon arrivée au Sphynx en 2018 en tant que stagiaire j'ai eu la chance de côtoyer la fine fleur des étudiants en physique. Merci à Alyzée qui mettait un point d'honneur à ce que les **heures** de pause "contractuelles" soient scrupuleusement respectées. Merci aussi à Paul, Damien et Hugues pour m'avoir laissé venir discuter dans leur bureau aussi souvent. Merci à Kanna, postdoc à l'époque, d'avoir toujours eu des madeleines dans son tiroir et surtout l'envie de les partager. Et merci à tous les autres d'avoir animé les pauses post-prendiales.

Cette thèse n'aurait pas non plus pu se passer aussi bien sans l'aide de Vincent et Cécile, dont le savoir-faire a largement contribué à ce que l'expérience soit opérationnelle aussi vite. Je mesure ma chance d'avoir pu compter sur des personnes aussi compétentes qui m'ont permis d'apprendre autant sur la mécanique (et l'importance du silicone pour l'étanchéité) et l'informatique dans un cadre expérimental. Je garderai un très bon souvenir des discussions musicales avec Vincent et celles sur la meilleure manière de faire pousser une rose bleue avec Cécile. La fin de rédaction n'a pas été des plus faciles et je tiens donc à remercier mon comité de suivi de thèse composé de Frédéric Moisy et François Ladieu dont les remarques pertinentes, et l'écoute dont ils ont su faire preuve, ont permis à cette thèse de se passer dans les meilleures conditions. Et enfin merci à Caroline, garant technique de ma soutenance, sans qui la préparation de cette exercice hybride entre visio et présentiel aurait été beaucoup moins fluide.

J'ai eu l'occasion de travailler cette dernière année avec Enzo et Gabriel, nouveaux doctorants de Sébastien et Basile. De toute évidence leur expérience en stage a été tout aussi agréable que la mienne puisqu'ils ont décidé de poursuivre avec une thèse. Bon courage à vous deux et profitez bien, ça passe vite trois ans... Et merci à Benoît, stagiaire dans le groupe dont la compagnie et les talents de saxophoniste ont agréablement accompagné le début de ma troisième année de thèse.

Pour finir j'aimerais remercier tous ceux qui m'ont soutenu sans comprendre et qui ont amorti mes sautes d'humeur (en particulier pendant les derniers mois). Je pense bien sûr en premier à Manon qui a dû faire preuve de beaucoup de patience au quotidien et que je ne remercierai jamais assez (oui on va pouvoir partir en voyage maintenant), mais aussi à Thibault, Nico et Laetitia (mention spéciale pour elle qui a même corrigé mon manuscript). Et enfin merci à ma famille bien évidemment qui m'a permis de faire d'aussi longues études, et dont le sacrifice est même allé jusqu'à monter sur Paris pour la soutenance et endurer 45 minutes de présentation scientifique sans s'endormir (ou presque mais je ne t'en veux pas Papa tu as quand même pris des notes pendant toute la première moitié).

Pour les francophones qui liront les chapitres qui suivent, j'espère que vous aurez autant de plaisir à découvrir cette thèse que j'en ai eu à l'écrire.

Chapter 1

Introduction to radiatively driven rotating convection

There are three primary ways of transferring heat: radiation, conduction, and convection. The latter is the transport that results from the motion of a fluid, usually forced externally. For example, the heat transfer between human skin and air is realized through conduction. However, the heat is then advected away by the wind, which results in enhanced heat transfer between the skin and the air. One then "feels" a lower temperature than in the absence of wind, the notion of "felt temperature" being related to the body heat loss. In physics we commonly study "natural" convection, which refers to motions in a fluid induced by density variations in a gravitational field. The density of a fluid decreases with temperature, a cold fluid being thus heavier than a hot one. Therefore, the presence of temperature gradients inside a system will lead to density variations. If those density variations are unstable, i.e. if heavier (colder) fluid is on top of lighter (hotter) fluid, a buoyancy force arises, that acts to reorganize the fluid.

Convection phenomena are ubiquitous both in nature and technology, representing a way of enhancing heat transport. In daily life, the motions inside a heated pot, or the efficiency of underfloor heating systems are due to convective instabilities. In technological devices, convection is used as a way to enhance the evacuation of heat. The design of the latest gaming devices is based on optimizing convection, a feature put forward in their marketing campaign. In the atmosphere, convection is responsible for the wind, the high streams in altitude, and cloud formation. Inside stars, one of the main motivations for the present thesis, convection is one of the main ways of transporting heat from the core to the outer regions.

Due to the large variety of applications, convection has been actively studied since the beginning of the 20^{th} century. The present thesis aims at determining the transport of heat in a turbulent convective fluid subjected to rapid rotation. This question is of prime interest in astrophysics, where the turbulent closures implemented in stellar models have never been validated in a laboratory experiment. With the goal of closing this gap between astrophysical models and real-world data, we will focus on a particular way of forcing convection: radiatively driven rotating convection. However, as a preamble, we will first introduce the canonical Rayleigh-Bénard set-up, before moving on to radiatively driven convection through a quick recap of the results obtained by (and sometimes with) Simon Lepot in the non-rotating configuration. We will then review the literature on the impact of rotation on the canonical Rayleigh-Bénard set-up, thus precisely setting the frame for the combination of radiative heating and rapid rotation.

1.1 Rayleigh-Bénard convection

The experimental study of convection dates back to the very last year of the 19th century. In 1900, Henri Bénard (Bénard (1900)) performed the first quantitative experiment, by studying the stability of a thin fluid layer with a top free surface, submitted to a vertical temperature gradient. More than a decade later, Lord Rayleigh (F.R.S. (1916)) developed a complete linear stability analysis of Bénard's experiment with a simplified two-dimensional model, consisting of a layer of fluid between impermeable horizontal stress-free boundaries. Those are separated vertically by a distance H, and held at a fixed top and bottom temperatures T_0 and $T_0 + \Delta T$, respectively. A schematic of the system is shown in figure 1.1. Rayleigh showed that, for sufficiently large ΔT, steady coherent convection rolls set in and enhance the heat flux. Through the impulse of experimental physics, this model was adapted to rigid plates, with no-slip boundary conditions. The fluid is heated by the bottom plate and becomes lighter. It rises until it reaches the upper plate, where it is cooled and thus becomes heavier. It sinks to be finally heated again by the bottom plate, etc, leading to what is known as a convection roll. This set-up has come to be called the "Rayleigh-Bénard convection" (RBC) configuration and represents the most commonly studied convection system in the literature.

This system obeys a particular set of equations under the Boussinesq approximation, described in section 1, while section 2 is focused on the two regimes of convection that will be of interest in this thesis.

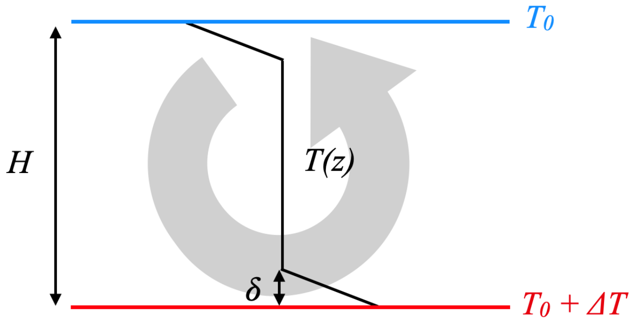

Figure 1.1: Sketch of the Rayleigh-Bénard convection set-up.

1.1.1 Equations

The equations used when studying convection are the Navier-Stokes equations coupled to the heat equation in the Boussinesq approximation. As is customary in fluid mechanics, we will use dimensionless equations that will allow us to define dimensionless numbers.

In a convection experiment, a temperature difference arises in the system, imposed or emerging. This temperature difference drives fluid motions and modifies the fluid properties such as viscosity ν, density ρ, or the thermal diffusivity κ. The Boussinesq approximation assumes that those variations due to the temperature difference are negligible. The fluid parameters are thus considered constant, except in the buoyancy term (i.e., the term involving the temperature in the Navier-Stokes equations) where the density varies linearly with temperature:

$$\rho(T) = \rho_0 \left(1 - \alpha(T - T_0)\right) \tag{1.1}$$

Hence, we have the momentum, heat, and mass conservation equations:

$$\partial_t \mathbf{u} + (\mathbf{u} \cdot \nabla)\, \mathbf{u} = -\frac{1}{\rho_0} \nabla p + \nu \nabla^2 \mathbf{u} + \frac{\rho(T)}{\rho_0} \mathbf{g} \tag{1.2}$$

$$\partial_t T + \mathbf{u} \cdot \nabla T = \kappa \nabla^2 T \tag{1.3}$$

$$\nabla \cdot \mathbf{u} = 0 \tag{1.4}$$

with $\mathbf{u} = (u, v, w)$ the velocity field, p the pressure field, and T the temperature field.

In the standard Rayleigh-Bénard configuration, the plates are kept at constant temperature, leading to the following boundary conditions:

$$T(z=0) = T_h \quad ; \quad T(z=H) = T_c \tag{1.5}$$

with z the vertical coordinate whose origin is located on the bottom boundary, $T_c < T_h$, and we define $\Delta T = T_h - T_c$, the temperature difference between the two plates.

In order to study convection we need to subtract the static temperature profile obtained for $\mathbf{u_s} = \mathbf{0}$. The subscript "s" corresponds to the static variables. The momentum conservation equation becomes:

$$\frac{1}{\rho}\nabla p_s = \frac{\rho(T_s)}{\rho_0}\mathbf{g} \tag{1.6}$$

The heat equation becomes:

$$\kappa\boldsymbol{\Delta} T_s = 0. \tag{1.7}$$

Solving this equation gives $T_s(z) = T_h - \Delta T\frac{z}{H}$.

We can decompose the variables between a diffusive solution and fluctuations. Hence we have $T = T_s + \theta$, with θ the temperature fluctuations and $p = p_s + p'$ with p' the pressure fluctuations. The previous set of equations then becomes:

$$\partial_t\mathbf{u} + (\mathbf{u}\cdot\nabla)\,\mathbf{u} = -\frac{1}{\rho_0}\nabla p' + \nu\nabla^2\mathbf{u} + \rho\theta\mathbf{g} \tag{1.8}$$

$$\partial_t\theta + \mathbf{u}\cdot\nabla\theta = \kappa\nabla^2\theta + w\frac{\Delta T}{H} \tag{1.9}$$

Dimensionless equations

The same problem in fluid mechanics can be seen at very different scales. Convection can arise in a cup of tea as well as in stars. To compare such systems, it is customary to non-dimensionalize the system's variables by multiplying them with a suitable combination of some reference parameters. The purpose here is to determine the heat transport enhanced by convective motions. It means that we are interested in the link between the heat flux P induced by the applied temperature difference ΔT. As a result, the system can be fully described by eight dimensional parameters: the induced flux P, the temperature difference ΔT, the viscosity ν, the thermal diffusivity κ, the thermal expansion coefficient α, the density ρ_0, the acceleration of gravity g and the height H. As they always be used as a pair, we define the dimensional group αg, instead of the two separately, leading thus to 7 dimensional parameters. Then, the variables of the problem are non-dimensionalized as follows:

$$\widetilde{\mathbf{x}} = \frac{\mathbf{x}}{H} \quad ; \quad \widetilde{t} = t\frac{\kappa}{H^2} \quad ; \quad \widetilde{\mathbf{u}} = \mathbf{u}\frac{H}{\kappa} \quad ; \quad \widetilde{\theta} = \frac{\theta}{\Delta T} \quad ; \quad \widetilde{p'} = p'\frac{H^2}{\rho\kappa^2} \quad ; \quad \widetilde{\nabla} = H\nabla \tag{1.10}$$

We have seven dimensional parameters and four primary dimensions (length, mass, time and temperature) involved. The Vaschy-Buckingham Π theorem (Buckingham

(1914)) states that the number of dimensionless groups necessary to study a system is equal to the number of dimensional parameters minus the number of primary units. Here, we can describe ou system with $7-4=3$ dimensionless groups.

The Rayleigh number $\mathrm{Ra} = \frac{\alpha g \Delta T H^3}{\kappa\nu}$. It is the ratio between the buoyancy characterized by ΔT and the thermal and viscous dissipations that will damp the motion.

The Prandtl number $\mathrm{Pr} = \frac{\nu}{\kappa}$. It compares the effect of the viscosity to the thermal diffusivity. At 20°C, the Prandtl number of water is $\simeq 7$.

The Nusselt number $\mathrm{Nu} = \frac{PH}{\lambda\Delta T}$. It represents the ratio between the heat flux P enhanced by convection and the typical diffusive one $\lambda\Delta T/H$ inside the fluid in the absence of motion, where $\lambda = \rho C\kappa$, C being the heat capacity. It is an expression of the mixing efficiency.

Injecting (1.10) into the convection equations leads to the appearance of the hereabove dimensionless numbers. The dimensionless set of equations is:

$$\partial_{\widetilde{t}}\widetilde{\mathbf{u}} + \left(\widetilde{\mathbf{u}}\cdot\widetilde{\nabla}\right)\widetilde{\mathbf{u}} = -\widetilde{\nabla}\widetilde{p'} + RaPr\left(\widetilde{\nabla}^2\widetilde{\mathbf{u}} + \widetilde{\theta}\mathbf{z}\right) \tag{1.11}$$

$$\widetilde{\nabla}\cdot\widetilde{\mathbf{u}} = 0 \tag{1.12}$$

$$\partial_{\widetilde{t}}\widetilde{\theta} + \widetilde{\mathbf{u}}\cdot\widetilde{\nabla}\widetilde{\theta} = \widetilde{\nabla}^2\widetilde{\theta} + \widetilde{w} \tag{1.13}$$

In the following, the "$\sim$" and "$'$" will be dropped for clarity. The objective of most convection studies is to quantify the relation between the imposed temperature difference and the resulting heat flux, which often takes the form of a power law:

$$\mathrm{Nu} \sim \mathrm{Ra}^{\beta}\mathrm{Pr}^{\gamma} \tag{1.14}$$

Thus, studying the efficiency of thermal convection often boils down to studying the value of the exponent β. Different regimes of convection have been described depending on the value of β. Here, we are interested in the asymptotic behavior of this relation, i.e., when Ra becomes extremely large. In this region of the parameter space, two regimes have been proposed: the "classical" regime of convection and the "ultimate" regime, characterized by a value of β equal to 1/3 and 1/2, and γ equal to 0 and 1/2, respectively.

1.1.2 The classical and the ultimate regimes of convection

In the literature, the most commonly observed regime is the **classical regime of convection**. It corresponds to a regime controlled by the boundary layers. Those layers are created near a boundary demanding a null velocity, such as the two rigid plates of RBC, where the velocity has to go from a finite value in the bulk to zero on the rigid plate. In the boundary layers, the slow velocities prevent any efficient extraction of heat from the plate, leaving only diffusion as a way to transport heat. Having only this very inefficient path to the bulk, the system's behavior is constrained by the boundary layers where a strong temperature gradient is needed to transfer heat. In this situation, the classical theory asserts $\mathrm{Nu} \sim \mathrm{Ra}^{1/3}$. This scaling law has been simultaneously, and independently, predicted by Priestley and Malkus (Priestley (1954); Malkus (1954)) with two different argumentations. Priestley said that, in a system highly constrained by the boundary layers, the relation between the heat flux P and ΔT must be independent of the total height H. By contrast, Malkus developed a maximal heat transport theory to derive the exponent β. Later, Howard (Howard (1966)) used only dimensional arguments to explain the scaling law of the classical regime. He considered that the boundary layers are marginally stable, meaning that the Rayleigh number built on the layers' height δ will always be equal to the threshold value at which convection occurs (denoted as $\mathrm{Ra_c}$). We have:

$$\mathrm{Ra}_\delta = \frac{\alpha g \Delta T \delta^3}{\kappa \nu} = \mathrm{Ra_c} = O(1) \tag{1.15}$$

Then we can derive a relation for δ as a function of Ra:

$$\frac{\delta}{H} \sim \mathrm{Ra}^{-1/3} \tag{1.16}$$

The flux of heat P has to be transferred diffusively through the boundary layer of height δ leading to:

$$P = \lambda \frac{\Delta T}{\delta} \tag{1.17}$$

By injecting the relation (1.16) in (1.17) we obtain the following relation:

$$\mathrm{Nu} \sim \mathrm{Ra}^{1/3} \tag{1.18}$$

This relation implies two conclusions: first, this regime is independent of the height of fluid H, which is in agreement with the dominance of the boundary layers over the bulk; secondly, even if the bulk is turbulently mixed, it could be argued that this regime is not fully turbulent because the relation between the heat flux and the temperature difference still involves the molecular diffusivity coefficients ν and κ.

The ultimate regime of convection is the way around the second conclusion of the previous paragraph. Spiegel (1963) proposed another scaling law for highly turbulent convection:

$$\mathrm{Nu} \sim (\mathrm{RaPr})^{1/2} \tag{1.19}$$

This scaling comes from the assumption that, in astrophysical objects such as stars, there must exist a "fully turbulent" regime of convection where the diffusivity coefficients do not play any part. It implies that convective heat flux is not longer limited by the boundaries, but rather by transport across the bulk of the fluid layer. Kraichnan (Kraichnan (1962)) modified this scaling by adding a factor $log\,(\mathrm{Ra})^{-3/2}$. In the literature, the observation of this regime in standard RBC remains debated (Chillà & Schumacher (2012); Chavanne *et al.* (1997, 2001); Niemela *et al.* (2000); Roche *et al.* (2010); He *et al.* (2012); Iyer *et al.* (2020); Doering *et al.* (2019); Doering (2020)). Basile Gallet, Sébastien Aumaître and Simon Lepot thus designed an experiment built to bypass the boundary layers. Their idea is that the boundary layers, throttling the efficiency of convection by forcing the heat to be transferred through diffusion, must be circumvented. They decided to use a combination of internal heating and cooling to do so. The solution chosen in the thesis of Simon Lepot was to radiatively force convection to achieve the ultimate regime of convection.

1.2 Why consider radiatively driven convection ?

The goal of the present thesis is to study turbulent regimes of rotating convection. Hence, it is important to use an experimental set-up that has already proven able to achieve this kind of extreme regimes. This section will focus on radiatively driven convection and the motivations behind the use of such a particular type of forcing. After an explanation of what radiatively driven convection means, natural flows where this forcing arises will be presented. This forcing has been previously used by Simon Lepot during his thesis in the non rotating case. He showed that an experimental realization of this forcing leads to the "ultimate" regime of convection. The following parts of this section will be dedicated to the presentation of the laboratory experiment, and the results that motivated us to use the same forcing to study fully turbulent regimes of rapidly rotating convection.

A schematic of radiatively driven convection is provided in figure 1.2. It consists in using as heat source a flux of light P directed toward the transparent bottom of a tank filled with an opaque fluid. The light is absorbed over a length ℓ by the fluid and converted into heat. Heating the lower part of the system creates an unstable density stratification that will lead, if the forcing is powerful enough, to a convective flow. The radiative source injects the heat in a volume of fluid of depth ℓ, directly into the bulk of the flow. The point of this technique is to be able to inject heat beyond the boundary layers to achieve the ultimate regime of convection.

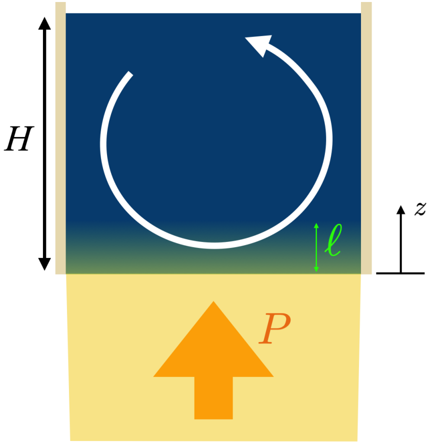

Figure 1.2: Schematic of the radiatively driven convection system.

1.2.1 Radiatively forced natural flows

We can ask ourselves whether the standard RBC configuration is relevant to all natural flows. In nature, many flows are driven by a flux of light or radiation, instead of heating and cooling plates. In this section we introduce examples of natural flows where RBC is not relevant.

The first example is convection inside stars. In those astrophysical objects, the heat is produced within the core by nuclear reactions. In stars can be found two different regions visible in figure 1.3: a convective zone and a radiative zone. The former is an unstable region where heat is transported by convective motions. The latter is a stably stratified region where heat is transported through radiative transfer (Garaud (2021*b*)). Depending on the stellar mass, the location of those regions vary, as shown in figure 1.3. Convective zones overlap with the core for stars with a

mass superior to 1.5 times the solar mass, or stars with a mass inferior to half that of the sun (Christensen-Dalsgaard *et al.* (1996); Featherstone & Hindman (2016); Garaud (2002); Shaviv & Salpeter (1973); Spiegel (1971); Spiegel & Zahn (1992)). In this situation, the heat is produced directly inside the convective zone, which is an example of internal heating.The boundary conditions of RBC would be irrelevant, and the system is closer to a situation where convection is forced internally in some fraction of the fluid volume. To describe the transport of heat and tracers in the convective zone, the "mixing length theory" is used, where a length l is defined as the distance traveled by a rising plume before disappearing, giving its heat to the background (Vitense (1953)). If we define the Nusselt and Rayleigh numbers using a temperature drop over this height l, and if we assume that the velocity behaves as a free-fall velocity over the height l, we can derive the following power-law $\mathrm{Nu}_l \sim (\mathrm{Ra}_l \mathrm{Pr})^{1/2}$. To recover (1.19) we need to connect l with the characteristic height H of the system. For example, it can be done by choosing l as a fraction of the pressure scale height (Garaud (2021*a*)), or by defining l as a fraction of the correlation length of the temperature fluctuations (Gibert *et al.* (2006)). As observations in stars are mostly restrained to surface measurements obtained through the study of emission spectra, the field would greatly benefit from experiments able to achieve the convection regime involved in the transport of heat in stars.
The second example is frozen lakes where a convective flow is forced by the absorption of light emitted by the sun. The sunlight is absorbed at the upper surface, under an ice layer, over a depth ℓ. Between 0°C and 4°C the density of water increases with temperature, i.e. the higher the temperature, the heavier the fluid. Hence, an internal heat source located near the upper surface of a frozen lake creates an unstable density stratification leading to convective motions (Farmer (1975); Bengtsson (1996); Jonas *et al.* (2003)). This is a situation where convection is forced internally by a flux of light, in a similar fashion to the radiatively driven convection experiment.

There are other examples of radiatively driven convection in nature, such as convection in the Earth's mantle which is partly driven by radioactive decay (Davaille *et al.* (2002); Limare *et al.* (2015)) or the powering of supernova explosions by neutrino absorption in the collapsing stellar core (Herant *et al.* (1992); Janka & Müller (1996); Radice *et al.* (2016)). Radiatively driven convection is thus relevant to many natural flows. Convection in stars is of particular interest because the convective zones are impacted by global rotation as will be discussed in section 1.3. Radiative forcing is interesting for its geophysical and astrophysical applications but also at the fundamental level, because it has proven able to achieve the "ultimate" regime of convection (Lepot *et al.* (2018); Bouillaut *et al.* (2019); Miquel *et al.* (2020)). To do so, Basile Gallet, Sébastien Aumaître and Simon Lepot designed a radiatively driven convection experiment that we now describe.

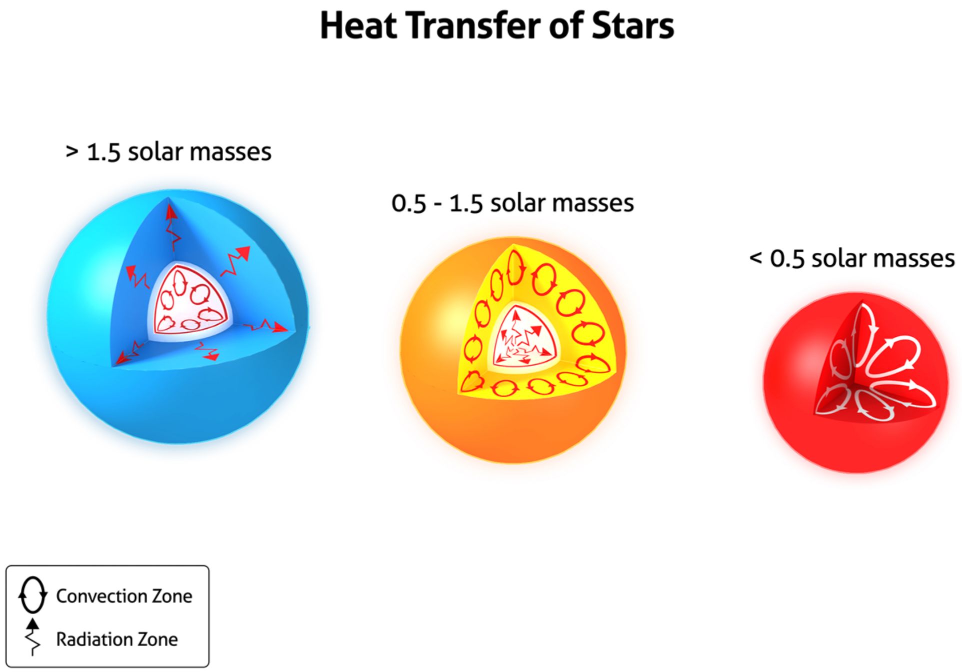

Figure 1.3: Schematics of the distribution between convective and radiative zone within a star depending on its mass. This image was taken from http://www.sun.org/encyclopedia/stars.

1.2.2 A laboratory experiment to achieve the "ultimate" regime of convection

In this section, we introduce the experimental set-up used in Lepot *et al.* (2018) and Bouillaut *et al.* (2019). For the study of rapidly rotating convection, this set-up has been adapted, but its main characteristics remain unchanged. The modifications made to the original set-up are presented in the third chapter of the present thesis.

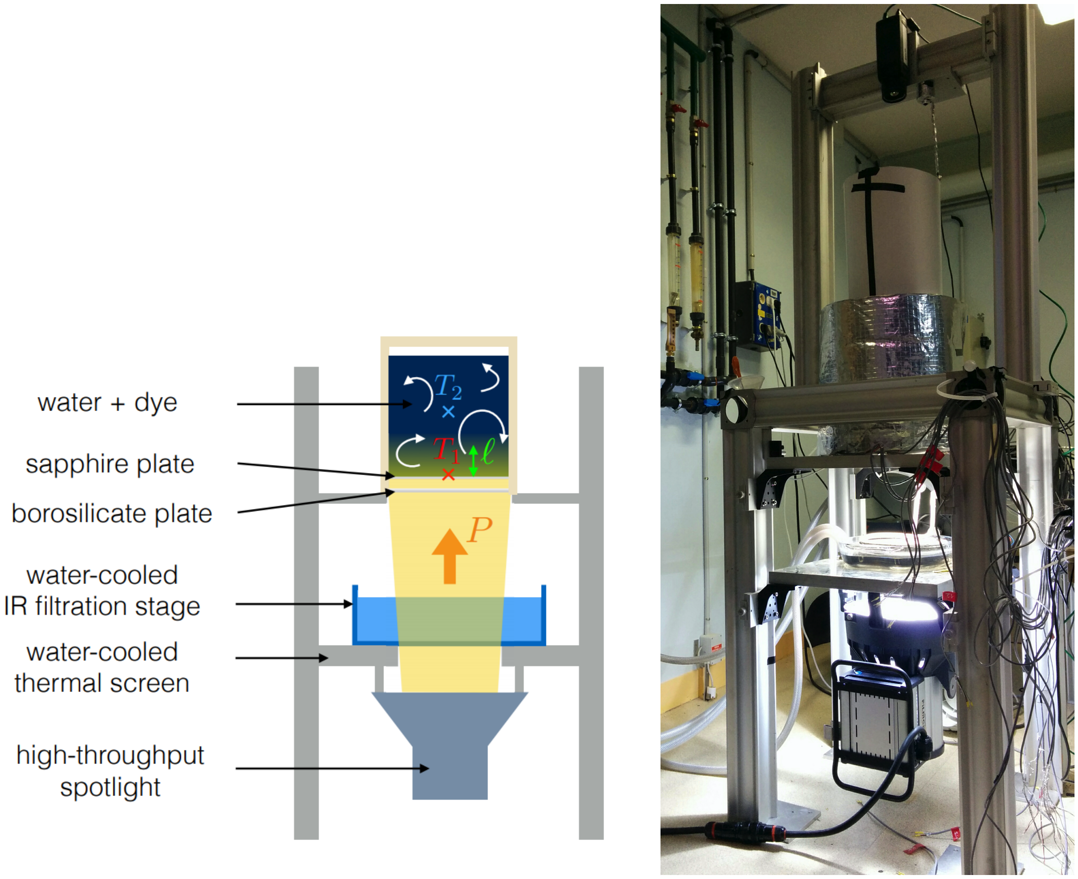

Figure 1.4: Left: Sketch of the radiatively driven convection experiment. Right: Photograph of the radiatively driven convection experiment.

Experimental apparatus

The experimental set-up is sketched in figure 1.4. It consists of a high throughput projector shining at a cylindrical tank which has a transparent bottom plate. The cell contains a mixture of water and dye which absorbs the light. The magnitude of the resulting heat source decreases exponentially with height over an e-folding scale ℓ, as stated by the Beer-Lambert law:

$$Q(z) = \frac{P}{\ell} e^{(-z/\ell)} \tag{1.20}$$

with z the vertical coordinate, P the flux of light emitted by the lamp in $W.m^{-2}$, and $\ell = \frac{1}{\epsilon c}$ the absorption length inversely proportional to ϵ the absorption coefficient of the fluid in $m^2.mol^{-1}$, and c the concentration of dye inside the fluid in $mol.m^{-3}$. This length has the interesting property to be inversely proportional to the concentration of dye. It allows us to choose between two situations presented in figure 1.5: for $\ell \to 0$, the heat source is similar to the one of RBC; for ℓ much larger than the boundary layer height δ, the fluid is heated beyond the boundary layer, the resulting internal heating leading to the ultimate regime of convection. The difficulty is to find a dye with little variation in absorbance over the visible spectrum. This is important because this criterion leads to a clean exponential shape in (1.20). Otherwise, different wavelengths would lead to exponentials with very different length scales. Simon Lepot found that carbon black dye turns out to be ideal as it leads to a clean exponential decay of light intensity inside the cell.

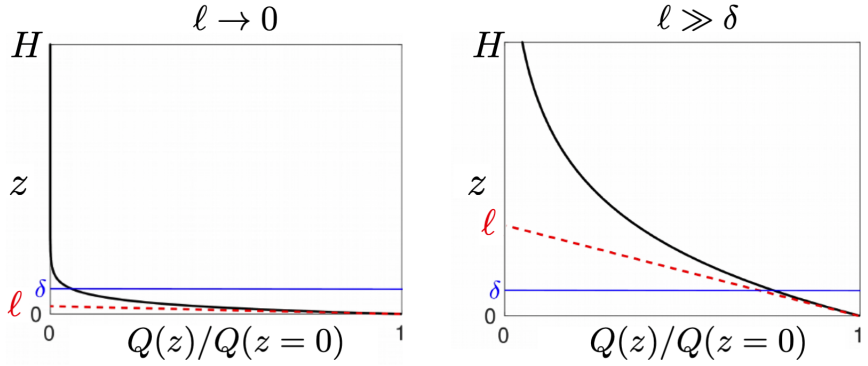

Figure 1.5: Two different heating situations depending on the length ℓ. On the left, ℓ tends to zero. As a result, the heat is injected inside the boundary layer of height δ, a situation similar to the RBC configuration. On the right, ℓ is larger than δ. The heat is injected directly inside the bulk turbulent flow.

The key concept of this experiment is to heat a fluid using only a flux of light. To be certain that this assertion is verified we need to put measures in place to avoid parasitic heat sources.

The first potential parasitic heat source comes from the lamp. The light is produced by a 2500W metal halide lamp "Filmgear Daylight" with approximately 250W converted into light. That makes a lot of power dissipated into heat. To ensure that the cell is not heated by the heat losses from the lamp a thermal screen is installed. This thermal screen is visible in figure 1.4. The first stage is a thermally cooled aluminum frame, kept at constant temperature through a circulation of cold water. The second parasitic heat source is the infrared (IR) radiation emitted by the spotlight. By contrast with visible light, IR are absorbed over the first micrometer of the cell. Such heating would lead to a RB-like situation where the heat source can be assimilated to a rigid plate. To avoid this situation, on the first stage the light passes through a 20-cm-diameter aperture covered with a water tank height of 5 cm, kept at 20°C thanks to an external water circulation. The IR radiation is thus filtered out.

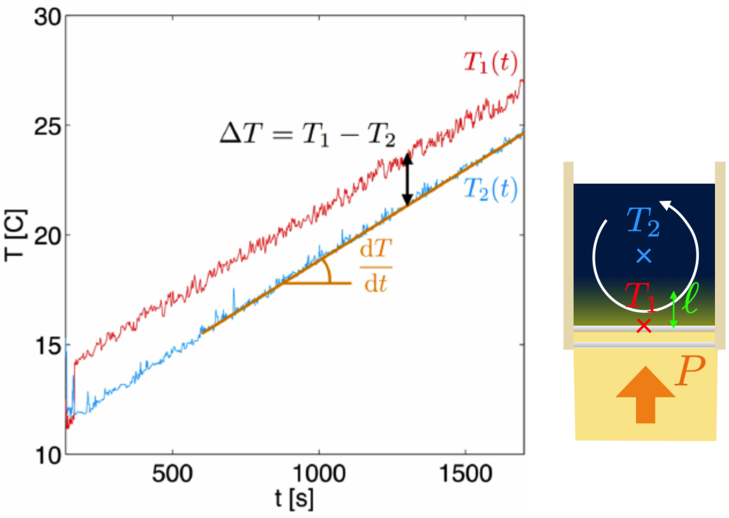

Figure 1.6: Timeseries of temperature during an experimental run. The schematic on the right shows the location of the temperature probes.

Secular heating as a heat sink. Another particularity of this experiment is its cooling mechanism; or absence thereof. The question of the cooling procedure is rather complicated, as a cooling system is usually composed of a rigid plate put in contact with the upper surface of the fluid. But adding a rigid cold boundary would create the boundary layers mentioned earlier, which would greatly constrain the system's behavior. The boundary layers created between the cooling plate and the bulk would prevent the observation of the ultimate regime of convection, as in a standard RBC experiment. To avoid boundary layers at the cooling side the solution found during Simon Lepot's thesis was to not cool down the fluid. Hence, this convection experiment has a heat source but no heat sinks. As a result, the mean temperature inside the tank drifts linearly in time, as shown in figure 1.6 presenting a timeseries of temperature during an experimental run. This paragraph will show how this drifting situation is mathematically equivalent to the fluid being uniformly cooled at a rate equal and opposite to the heating power.

Let us write the heat equation for the radiatively heated fluid:

$$\partial_t (\rho CT) + \mathbf{u} \cdot \nabla (\rho CT) = \lambda \nabla^2 T + Q(z) \tag{1.21}$$

with C the specific heat and λ the thermal conductivity, z the vertical coordinate measured upward from the bottom of the tank, and the radiative source term (1.20).

The boundaries are thermally insulating, meaning that $\nabla T \cdot \mathbf{n} = \mathbf{0}$ at all boundaries, with $\mathbf{n}$ the unit vector normal to the boundary. We define $\overline{T}(t)$ as the spatial average of the temperature field inside the fluid domain V:

$$\overline{T}(t) = \frac{1}{\pi R^2 H} \int_V T(\mathbf{x}, t) d\mathbf{x}, \tag{1.22}$$

with R the radius of the cylindrical tank. Integrating (1.21) over V, using the boundary conditions, the incompressibility constraint and the fact that $e^{(-H/\ell)} \ll 1$ (which is satisfied in the experiment), we obtain:

$$d_t \overline{T} = \frac{P}{\rho c_p H} \tag{1.23}$$

The mean temperature increases linearly with time. In a quasi-stationary state, the temperature everywhere inside the cell drifts at a constant mean rate. Therefore the timeseries of temperature give a direct access to the incoming flux through the rate of the drift.

Now, we decompose the temperature into $T(\mathbf{x}, t) = \overline{T}(t) + \theta(\mathbf{x}, t)$ with $\theta(\mathbf{x}, t)$ the fluctuations of temperature around the spatial mean. By subtracting (1.23)$/H$ from (1.21), before dividing by ρC we form the equation for θ:

$$\partial_t \theta + \mathbf{u} \cdot \nabla \theta = \kappa \nabla^2 \theta + S(z) \tag{1.24}$$

Where $\kappa = \lambda / \rho C$ the thermal diffusivity, and:

$$S(z) = \frac{1}{\rho C} \left[Q(z) - \frac{P}{H} \right]. \tag{1.25}$$

The second term inside the square brackets is an effective cooling term balancing, on average over the entire cell, the heating term. As a result, our system is heated over a length ℓ but cooled uniformly inside the fluid volume. In the Earth mantle, a similar, but opposite, phenomenon takes place and is known as secular cooling

(Gubbins *et al.* (2003); Aubert *et al.* (2009); Landeau & Aubert (2011)). As a result we call this distribution of the effective heat sink of the present experiment is referred to as "secular heating". In convection models the heat equation is coupled to the momentum equation:

$$\partial_t \mathbf{u} + (\mathbf{u} \cdot \nabla)\, \mathbf{u} = -\frac{1}{\rho_0} \nabla p + \nu \nabla^2 \mathbf{u} + \alpha \theta \mathbf{g} \tag{1.26}$$

where the pressure term absorbs the contribution from the mean temperature $\overline{T}(t)$. We see that we end up with the standard equations of convection, with internal heating decreasing exponentially with height and uniform cooling at an equal and opposite rate.

Past results and observation of the ultimate regime of convection

The main goal of Simon Lepot's thesis was to study the relation between the Nusselt number, the Rayleigh number and the Prandtl number $\mathrm{Nu} \sim \mathrm{Ra}^{\beta}\,\mathrm{Pr}^{\gamma}$ in a radiatively driven convection experiment. The main result is the observation of the "ultimate" regime of convection (1.19). Figure 1.7 shows Nu as a function of Ra. Both the Rayleigh number and the Nusselt number are based on the temperature difference between two probes located at $z = 0$ and $z = H/2$ and denoted as T_1 and T_2 in figures 1.4 and 1.6:

$$\mathrm{Ra} = \frac{\alpha g \left(T_1 - T_2\right) H^3}{\kappa \nu} \quad ; \quad \mathrm{Nu} = \frac{PH}{\lambda \left(T_1 - T_2\right)} \tag{1.27}$$

For $\ell/H < 10^{-4}$, the absorption length is so small that the heat source can be assimilated to an imposed heat flux at the rigid bottom plate. The heat is injected into the boundary layer, a situation similar to the RB configuration. The exponents β and γ behave accordingly and the scaling law that was observed is $\mathrm{Nu} \sim \mathrm{Ra}^{1/3}$: the classical regime of convection where the boundary layers dominate over the bulk. When we increase ℓ, we change the heat source to partial internal heating. For $\ell/H = 0.05$ we see in figure 1.7 that we obtain a scaling law independent of the molecular diffusivity coefficients:

$$\mathrm{Nu} \sim \mathrm{Ra}^{1/2} \tag{1.28}$$

This experimental observation was also confirmed by numerical simulation at $\mathrm{Pr} = 7$, and $\mathrm{Pr} = 1$ and, it constitutes a clear experimental observation of the ultimate regime of convection.

As an intern, I participated in the study of non rotating convection by determining the dependence of the Nusselt number with the absorption length ℓ/H (Bouillaut *et al.* (2019)). I gathered more experimental points for various values of ℓ/H, see figure 1.8. Those points showed that the parameter ℓ/H has an influence on Nu and Ra. Indeed, increasing ℓ/H increases the value of Nu and decreases the value of Ra: the higher ℓ, the more efficient the convection. The new dimensionless parameter ℓ/H needs to be taken into account in the scaling law:

$$\mathrm{Nu} \sim \left(\frac{\ell}{\mathrm{H}}\right)^{\alpha} \mathrm{Ra}^{\beta}\mathrm{Pr}^{\gamma} \tag{1.29}$$

We proposed a model that captures the impact of the new parameter ℓ/H correctly. It is described in figure 1.9 and consists in following a fluid particle during its travel inside the absorption zone. It enters the heating zone by the left at the bulk temperature. Then, the particle goes through the heating region where it is heated up. It has a temperature $T_{bulk} + \Delta T$ when reaching the other side of the tank. If, during its journey in the heating region, the particle remains near the bottom plate ($z \ll \ell \ll H$), we have:

$$\frac{D\theta}{Dt} \simeq \frac{P}{\rho c_p \ell} \tag{1.30}$$

with $D\cdot/Dt$ the total derivative. The time spent by the particle to go from the bottom-left corner to the bottom-right corner of the tank is $\Delta t \sim H/U$ with U the characteristic velocity of the system. Then, the gain of temperature ΔT during the time Δt is:

$$\Delta T \sim \frac{P}{\rho c_p \ell}\Delta t \sim \frac{PH}{\rho c_p \ell U} \tag{1.31}$$

If we suppose that the characteristic velocity is the free fall velocity, $U \sim \sqrt{\alpha g \Delta T H}$, then:

$$\Delta T \sim \frac{PH}{\rho c_p \ell \sqrt{\alpha g \Delta T H}} \tag{1.32}$$

which gives in term of dimensionless numbers:

$$\mathrm{Nu} \sim \frac{\ell}{\mathrm{H}}\sqrt{\mathrm{RaPr}} \tag{1.33}$$

To validate this model (and the exponent associated with it), we try to find a way to make all the data points collapse onto the same master curve. To this end, we use the relation (1.33) to derive the transition value between the classical regime and the ultimate regime. We note with the subscript "tr" the transition values. At the transition between the two regimes, we have:

$$\mathrm{Nu_{tr}} \sim \mathrm{Ra_{tr}^{1/3}} \sim \frac{\ell}{\mathrm{H}} \left(\mathrm{Ra_{tr}Pr}\right)^{1/2} \tag{1.34}$$

which leads to the following transition values:

$$\mathrm{Ra_{tr}} \sim \mathrm{Pr}^{-3} \left(\frac{\ell}{\mathrm{H}}\right)^{-6} \quad ; \quad \mathrm{Nu_{tr}} \sim \mathrm{Pr}^{-1} \left(\frac{\ell}{\mathrm{H}}\right)^{-2} \tag{1.35}$$

Now we can plot Nu as a function of Ra, but this time they will be compensated by their respective transition values. This plot is shown in figure 1.10. As expected, all the experimental data points collapse onto a single master curve, assessing the model's validity. We conclude that the experiment can successfully achieve an extreme regime of convection relevant to geophysical and astrophysical systems, and that it transitions continuously from the classical regime to the ultimate one. At the end of my internship, one question came up repeatedly: can this experiment go further in modeling natural flows?

1.3 Rotating convection

The study of rotating convection is a logical next step after the thesis of Simon Lepot, the motivation being to go further in the modeling of geophysical and astrophysical flows. In this section, we will first focus on the reasons behind the study of rotating radiatively driven convection. Then, we will consider the modifications of the equations of convection due to the rotation term. Finally, we will review the regimes of interest of rapidly rotating convection.

1.3.1 Motivations

As presented in the previous section, convection enhances the transport of heat and tracers, while inducing other instabilities. Indeed, buoyancy gradients inside astrophysical objects are responsible for important motions inside the fluid, which in turn can trigger instabilities, such as the generation of magnetic field through the dynamo effect. In the convective zones of stars, convection is responsible for the turbulent transport of heat and tracers. However, stellar convection is hindered by

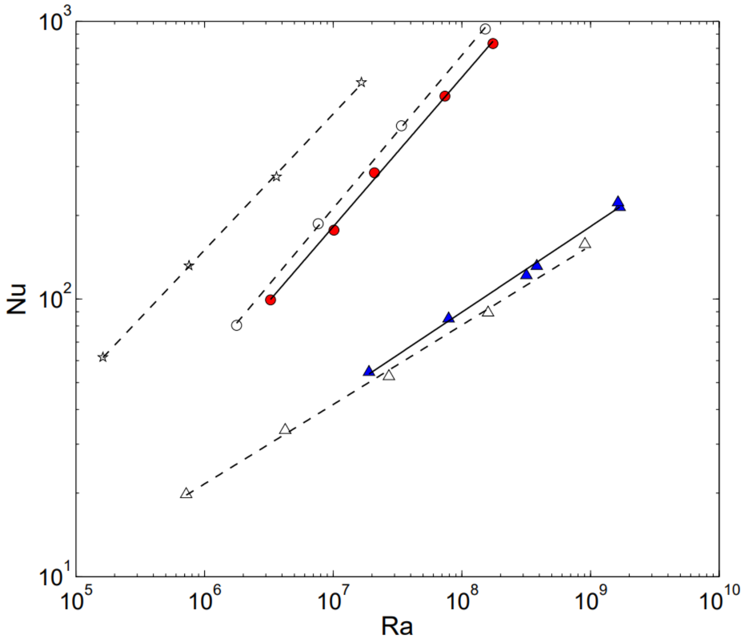

Figure 1.7: Nussel as a function of the Rayleigh number from: experimental data (filled symbol) done at $\ell/H = 0.05$ (circles) and $\ell < 10^{-4}$ (triangles), which corresponds to the RB limit; and numerical data (empty symbols), the stars correspond to $\mathrm{Pr} = 1$.

the rotation of the star. Any study aimed at quantifying the efficiency of stellar convection should thus include the crucial role of global rotation.

Rotation is a common ingredient to most geophysical and astrophysical flows. But its impact on fluid dynamics depends on the scale of the structures. Indeed, the larger the scale, the stronger the effect of rotation (Stix (2012)). It has been shown in the literature that rotation impacts the largest structures of the Sun. More precisely, we need large scales or rapid rotation for rotation to impact the fluid's behavior. Hanasoge *et al.* (2012) showed that the Sun might be a faster rotator than expected, suggesting that rotation may have a more significant impact than previously thought and may be responsible for discrepancies between the efficiency of heat transport predicted by the non-rotating model. A more detailed picture of convection in Sun-like stars has been published recently by Hanasoge *et al.* (2020), where they establish that rotation has an impact on the distribution of convective structures between the poles and the equator. Those two articles show that rotation has an impor-

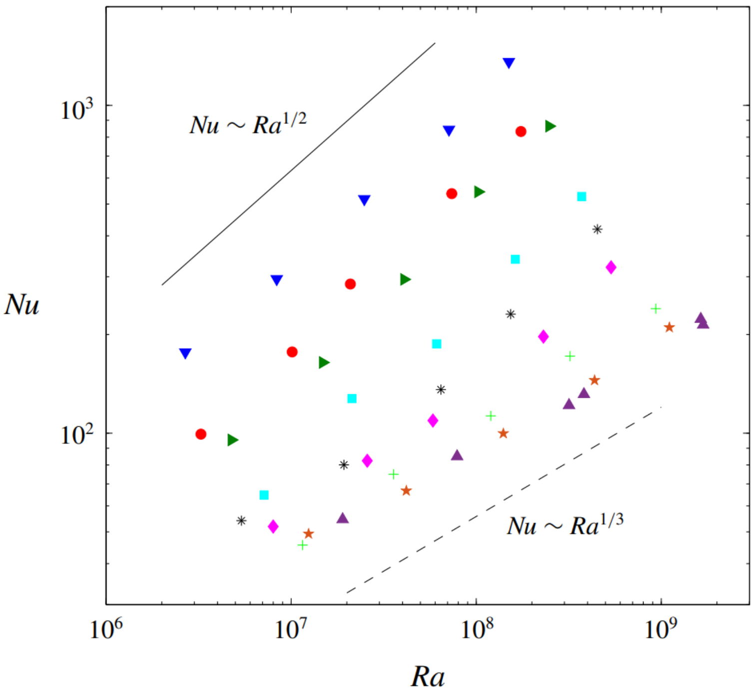

Figure 1.8: Nusselt number as a function of the Rayleigh number for various values of the absorption length ℓ. At fixed Ra, the Nusselt number increases with ℓ/H. Symbols are Δ:$\ell = 5.10^{-6}$ m; $\star$: $\ell/H = 0.0015$; $+$: $\ell/H = 0.0030$; $\diamond$: $\ell/H = 0.0060$; $*$: $\ell/H = 0.012$; $\Box$: $\ell/H = 0.024$; $\triangleright$: $\ell/H = 0.048$; $\circ$: $\ell/H = 0.05$; ∇: $\ell/H = 0.096$. The solid and dashed lines are eyeguides.

tant influence on the dynamics of convective regions, creating discrepancies between the prediction of the non-rotating mixing length theory and observations (Garaud (2021*b*)). Convection in stellar interiors is an important player in the transport of heat and tracers. As observations are rare, the parametrization of convection would greatly benefit from experimental data that include global rotation.

The experimental apparatus developed by Simon Lepot, Sébastien Aumaître, and Basile Gallet has proven successful in observing the asymptotic regime of non-rotating convection, thus validating the mixing length approach used in the context of stellar convection. The idea of the present thesis is to assess if the asymptotic regime of rapidly rotating convection can be observed using radiatively driven convection.

Before getting into the detailed aspects of radiatively driven rotating convection

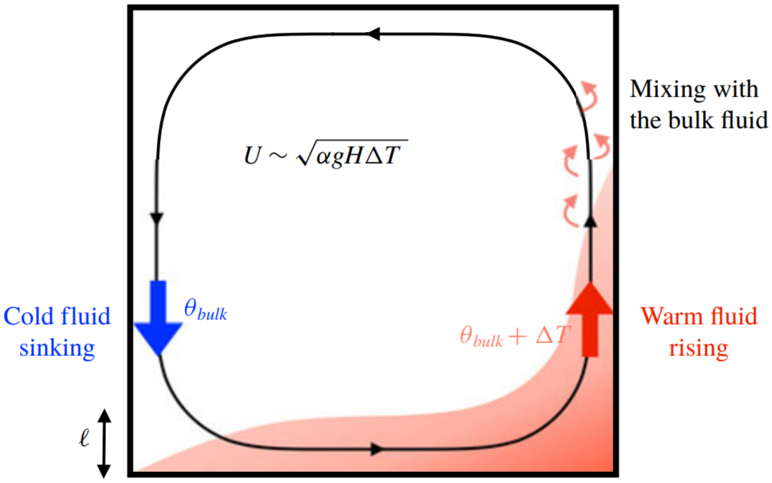

Figure 1.9: Model of radiatively heated convection roll: The black line is a streamline of the mean flow. Near the bottom left corner, a cold fluid element at the bulk temperature enters the heating region. It gets heated as it travels along the bottom boundary, gaining an overall temperature increment of the order of ΔT during a time of flight H/U. The fluid element has maximum temperature as it passes near the bottom-right corner. It then starts rising and follows the mean cellular motion while mixing with the bulk fluid.

(RDRC), we first review the literature on rotating Rayleigh-Bénard convection.

1.3.2 Rotating Rayleigh-Bénard convection (RRBC)

To derive the rotating convection equations, we first need to see what changes in the Navier-Stokes equations when adding rotation. Once this feature is added to the equations, we will derive the dimensionless equations and the new dimensionless number. Finally, we will describe two asymptotic regimes of rotating convection.

Rotating Navier-Stokes equations

In a framework rotating at a uniform rate we must add two additional inertial forces: the centrifugal force, and the Coriolis force. The convective set of equation becomes:

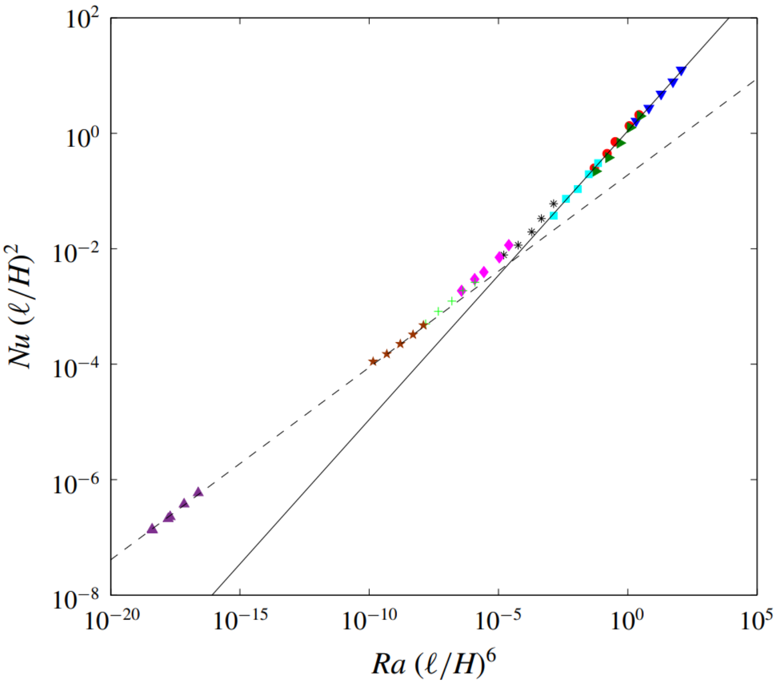

Figure 1.10: Rescaled Nusselt number as a function of the rescaled Rayleigh number, for various values of the absorption length ℓ (same symbols as figure 1.8). The data indicate a clear transition from an exponent $\gamma = 1/3$ (dashed-line) to an exponent $\gamma = 1/2$ (solid line).

$$\partial_t \mathbf{u} + (\mathbf{u}\cdot\nabla)\,\mathbf{u} + 2\boldsymbol{\Omega}\wedge\mathbf{u} = -\frac{1}{\rho_0}\nabla p + \nu\nabla^2\mathbf{u} + \frac{\rho(T)}{\rho_0}\mathbf{g} + \frac{1}{2}\nabla\left(\boldsymbol{\Omega}\wedge\mathbf{r}\right)^2\frac{\rho(T)}{\rho_0}, \quad (1.36)$$

$$\partial_t T + \mathbf{u}\cdot\nabla T = \kappa\nabla^2 T, \quad (1.37)$$

$$\nabla\cdot\mathbf{u} = 0, \quad (1.38)$$

with $\mathbf{r}$ the position vector and $\boldsymbol{\Omega} = \Omega\mathbf{z}$, with Ω the rotation rate. The term $2\boldsymbol{\Omega}\wedge\mathbf{u}$ is the Coriolis force and will be central in our study of rotating convection. The term $(1/2)\,\nabla\left(\boldsymbol{\Omega}\wedge\mathbf{r}\right)^2(\rho(T)/\rho_0)$ is the centrifugal force. It is negligible for low rotation rates, the centrifugal acceleration being much smaller than gravity. Precise criteria for the subdominance of the centrifugal term are discussed in chapter 3. Now that we have our new set of equations, we can apply the same previous steps to obtain the dimensionless equations.

Dimensionless convection equations

The new term in the equations is the Coriolis force. Hence, the equations of convection have a new parameter Ω, the rotation rate. According to the Π theorem mentioned in section 1.1, this new parameter implies the existence of an additional dimensionless number.

The Ekman number $\mathrm{E} = \frac{\nu}{2\Omega H^2}$. It describes the ratio of viscous dissipation to Coriolis force. It gives the importance of rotational effects on the dynamics of the system. Small Ekman number means high global rotation rate. When the rotation axis is aligned with gravity, rotation has a stabilizing effect on convection (Chandrasekhar (1961)). Small values of E result in smaller vertical velocities, a key aspect of the convective instability. But rotation is also involved in the creation of new characteristic length scales, such as the Ekman layer that appears near solid horizontal boundaries. With the inclusion of rotation around the vertical axis, the dimensionless equations (1.11) and (1.13) become

$$\partial_t \mathbf{u} + \frac{\mathrm{Pr}}{\mathrm{E}} \mathbf{z} \wedge \mathbf{u} = -\nabla p + \mathrm{Ra}\mathrm{Pr}\theta \mathbf{z} + \mathrm{Pr}\nabla^2 \mathbf{u} \tag{1.39}$$

$$\partial_t \theta + (\mathbf{u} \cdot \nabla)\,\theta = \nabla^2 \theta + w \tag{1.40}$$

$$\nabla \cdot \mathbf{u} = 0 \tag{1.41}$$

The Ekman number greatly impacts the transport properties of the flow, and thus the relation between the Nusselt number and the Rayleigh number. A general power-law ansatz thus yields:

$$\mathrm{Nu} \sim \mathrm{Ra}^{\beta} \mathrm{E}^{\gamma} \mathrm{Pr}^{\chi}. \tag{1.42}$$

In the following, we review the theoretical prediction for the scaling exponents β, γ and χ.

1.3.3 The various regimes of RRBC

As for non-rotating convection, two regimes will be of interest: one controlled by the boundaries and a second one controlled by the bulk. The derivation of those regimes appeals to the results of the linear stability analysis of rotating convection. After recalling those results, we will derive the corresponding scaling laws. The first one will be derived using an argument of marginally stable boundary layers, as for the classical regime of non-rotating convection. The second one is the fully turbulent regime of rotating convection independent of the diffusivities.

Impact of rotation on the threshold of convection

In the standard RBC configuration, convection is triggered by an imposed temperature difference, strong enough for buoyancy to overcome gravity. Hence, we have a critical value for the Rayleigh number ($\mathrm{Ra_c}$) that will trigger convection. In non-rotating convection, $\mathrm{Ra_c}$ is a constant which depends on the boundary conditions (Goluskin (2015)).

Chandrasekhar showed that, for rotating convection, the threshold is strongly dependent on the rotation rate. For fixed temperature and stress-free boundary conditions, this result can be computed analytically. For rapid rotation, the threshold behaves as follows:

$$\mathrm{Ra_c} \sim \mathrm{E}^{-4/3} \tag{1.43}$$

This result means that rotation indeed stabilizes convection.

The "classical" regime of RRBC

In the non-rotating case, the classical regime of turbulent convection is derived using the assumption that the boundary layer is marginally stable (King *et al.* (2012)). The same argument will lead to the classical regime of RRBC.

Assuming that the Rayleigh number based on the height δ of a marginally stable boundary layer is equal to its critical value yields:

$$\mathrm{Ra}_\delta = \frac{\alpha \mathrm{g} \Delta \mathrm{T} \delta^3}{\kappa \nu} \sim \mathrm{E}_\delta^{-4/3} = \left(\frac{\nu}{2\Omega\delta^2}\right)^{-4/3} \tag{1.44}$$

$$\frac{\delta}{H} \sim \mathrm{Ra}^{-3}\mathrm{E}^{-4} \tag{1.45}$$

Then, the heat flux is transferred diffusively over the height δ, as in (1.17). Assuming that the bulk transfers heat more efficiently than those boundary layers, the resulting scaling law for the classical regime of RRBC is:

$$\mathrm{Nu} \sim \mathrm{Ra}^3\mathrm{E}^4 \tag{1.46}$$

In the literature, the exponent β is slightly larger than the value 3 associated with 1.46. Plumley *et al.* (2016); Julien *et al.* (2016) showed that Ekman pumping may be responsible for this slight discrepancy. The Ekman pumping is a suction phenomenon that happens in the presence of Ekman boundary layers, created in a rotating flow near solid boundaries. The height of the Ekman boundary layers scales as $\sim \mathrm{E}^{1/2}\mathrm{H}$. This phenomenon becomes negligible when $\mathrm{E} \rightarrow 0$ as the rotation rate tends to infinity.

The geostrophic turbulence regime of rotating convection

The rapidly rotating regime of fully turbulent convection, also known as the geostrophic turbulence regime of rotating convection, is based on two main assumptions in the literature.

The first assumption is similar to the ultimate regime of convection. In this asymptotic regime, the relation between the heat flux and the temperature gradient should be independent of the molecular diffusivity coefficients. This argument is used in the non-rotating situation to describe the ultimate regime. For astrophysical objects, this argument is known as the mixing length theory, as mentioned earlier. As it has been done for the non-rotating case, this dimensional argument aims at finding a relation $\mathrm{Nu} = \mathrm{f}(\mathrm{Ra}, \mathrm{Pr}, \mathrm{E})$ that cancels the effects of ν and κ. At this point, there is a major difference between the non-rotating and the rotating cases: there are several possible combinations.

The second assumption is that the efficiency of convection in the rapidly rotating limit depends only on the supercriticality of the system. It means that the relation between the heat flux and the gradient of temperature must be a function of the ratio of the Rayleigh number over the critical Rayleigh number $\mathrm{Ra_c}$. The function we seek is no longer $\mathrm{Nu} = \mathrm{f}(\mathrm{Ra}, \mathrm{Pr}, \mathrm{E})$ but $\mathrm{Nu} = \mathrm{f}(\mathrm{Ra}\mathrm{E}^{-4/3}, \mathrm{Pr})$, (Julien & Knobloch (1998); Sprague *et al.* (2006); Julien *et al.* (2012); Aurnou *et al.* (2020)). This argument can be related to the ability of rotation to stabilize convection. The critical Rayleigh number being proportional to $\sim \Omega^{4/3}$, the higher the rotation rate, the more difficult it will be for convection to be triggered. The distance from onset thus becomes a crucial parameter.

The combination of both assumptions leads to the following scaling law, predicted by Stevenson (1979):

$$\mathrm{Nu} = \mathcal{C} \times \mathrm{Ra}^{3/2}\mathrm{E}^{2}\mathrm{Pr}^{-1/2} \tag{1.47}$$

where $\mathcal{C}$ is a dimensionless prefactor.

The geostrophic turbulence regime associated with (1.47) is a topic of intense ongoing research, without any clear experimental observation so far.

1.3.4 The quest to the geostrophic turbulence regime.

This section's purpose is not to present an extensive description of the literature in the domain but to focus on some representative pieces.

Several experiments in the Rayleigh-Bénard geometry have been developed with the goal of achieving the geostrophic turbulence regime of rotating convection (see Kunnen (2021) for a recent review). An overview is shown in figure 1.11. The system needs to overcome the throttling effect of the boundary layers to achieve a bulk-dominated regime of convection. Much effort has been put into this goal worldwide through various approaches. The TROCONVEX experiment in Eindhoven (Cheng *et al.* (2020)) and NoMag in UCLA (Cheng *et al.* (2015); King & Aurnou (2013)) use water as a working fluid. In contrast, U-Boot in Göttingen (Zhang *et al.* (2020); Wedi *et al.* (2021)) and Trieste at ICTP (Niemela *et al.* (2000); Ecke & Niemela (2014)) use sulfur hexafluoride and helium, respectively. The common goal is to produce a rotationally constrained, strongly turbulent flow. This is not an easy task, as it demands to have large velocities despite the fast rotation: one aims for low Ekman numbers with negligible centrifugal effects. However, these apparatus only achieve transitional regimes where the value of β increases sharply. When DNS are used to extend the experimental data, the observed regime satisfies the scaling law (1.46), indicating that the boundary layers' influence remains dominant, putting the molecular diffusivity coefficients ν and κ back into play(King *et al.* (2009)).

Another approach to study the geostrophic turbulence regime is Direct Numerical Simulation (DNS) of idealized situations (Stellmach *et al.* (2014); **?**); Currie *et al.* (2020)), which comes with its own challenges. One issue is the plurality of small scales that codes aiming at simulating the geostrophic turbulence regime have to resolve on a sufficiently long time for the flow to be stationary. One way of decreasing the computational cost is to simplify the equations (Julien & Knobloch (1998); Sprague *et al.* (2006); Julien *et al.* (2012)). They build a system of reduced equations by defining new time and space variables and expanding the velocity, temperature, and pressure in terms of a small parameter $\epsilon = E^{1/3}$ and eliminate the orders superior to $E^{1/3}$. The difficulties in simulating rotating convection are due to fast inertial waves and thin boundary layers. By limiting their reduced system of equations to the order $O(1)$ and $O(E^{1/3})$, these costly features of the flow are filtered. This method has proven successful in observing the geostrophic turbulence regime of rotating convection, as shown in figure 1.12. However, this reduced system of equations is only valid in the limit of strong rotational constraint (Julien *et al.* (2012)). For the reduced equations to be valid, the Rayleigh number must be comprised a priori between $\sim E^{-4/3}$ and $\sim E^{-5/3}$. Another particularly interesting numerical attempt has been made to achieve the geostrophic turbulence regime of convection. Barker *et al.* (2014) simulate a system where the domain is divided into three parts: a lower part with internal heating, an upper part with internal cooling, and the middle part where convection occurs. The schematic of their domain is presented in figure 1.13. This set-up is close to the radiatively driven convection configuration, except for the cooling mechanism, which is volumic and uniform over the entire cell in the experiment. In this configuration, Barker et al. observed the geostrophic turbulence regime of rotating convection. This configuration, although successful at eliminating the effect of the boundary layers, is somewhat unrealistic.

From the literature, we learn that, as for the non-rotating case, constraining boundary layers prevent the observation of the geostrophic turbulence regime in RBC experiments. This makes the numerical studies the only ones able to achieve this regime albeit using reduced equations or unrealistic set-ups and/or boundary conditions. Both examples presented here-above aim at getting rid of the boundary layers to make the bulk dominant. This thesis aims at adapting the apparatus of radiatively driven convection experiment, which we know can bypass the boundary layers, to achieve the geostrophic turbulence regime of rotating convection. We saw in this section that supercriticality is important in observing the geostrophic turbulence regime. The first chapter of the present thesis will be dedicated to the computation of the threshold of rotating radiatively driven convection. A linear stability analysis will be performed, and the results will be compared to the known value of the onset of RRBC. Once this value is known, we will see in the second chapter how we transform the existing set-up to study radiatively driven convection in a laboratory experiment. The fourth chapter will consist in a computation of the upper bound of radiatively driven non-rotating convection supported by experimental and numerical data. The final chapter of the present thesis will sum up the achievements of this study and present perspectives for future work.

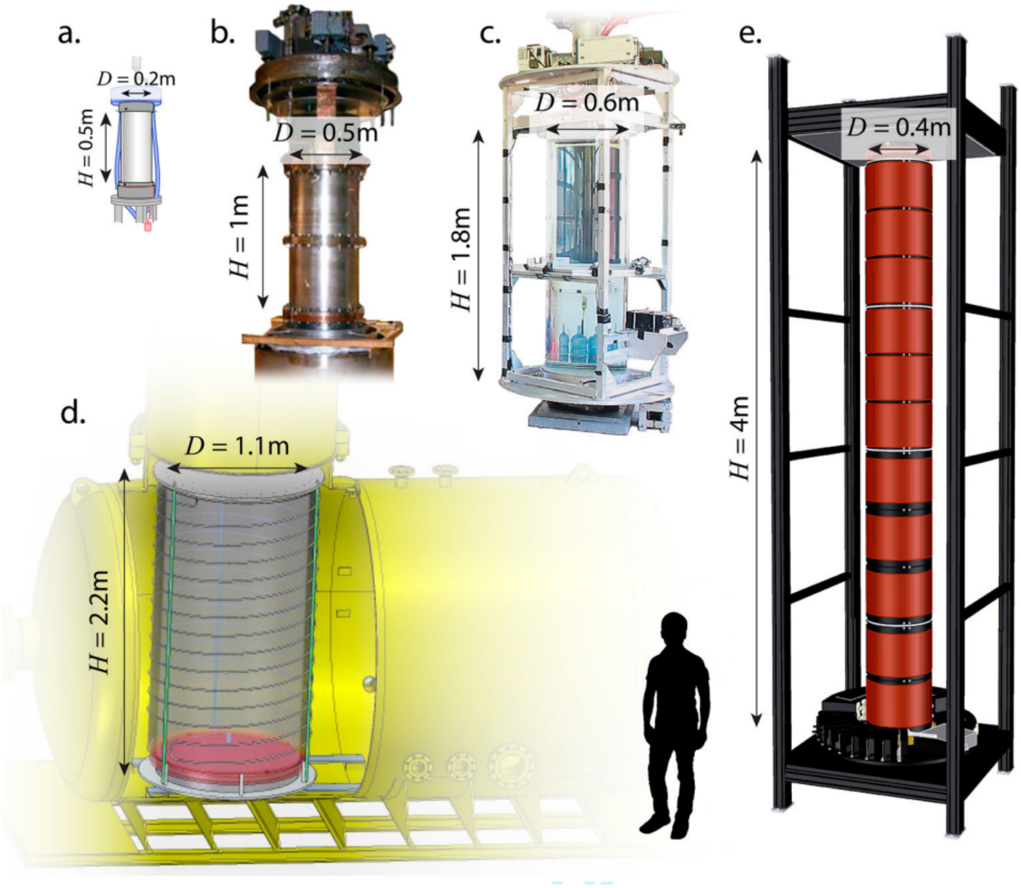

Figure 1.11: This figure is taken from Cheng *et al.* (2018). Images of several extreme rotating RBC setups. a) 'RoMag' at UCLA (liquid gallium, Pr $\simeq$ 0.025). b) Trieste experiment at ICTP (cryogenic liquid He, Pr $\simeq$ 0.7). c) 'NoMag' at UCLA (water, Pr $\simeq$ 4–7). d) 'U-Boot' at the Max Planck Institute for Dynamics and Self-Organization (SF6, N2, He gas,Pr $\simeq$ 0.8). e) 'TROCONVEX' at Eindhoven University of Technology (water,Pr $\simeq$ 2–7).

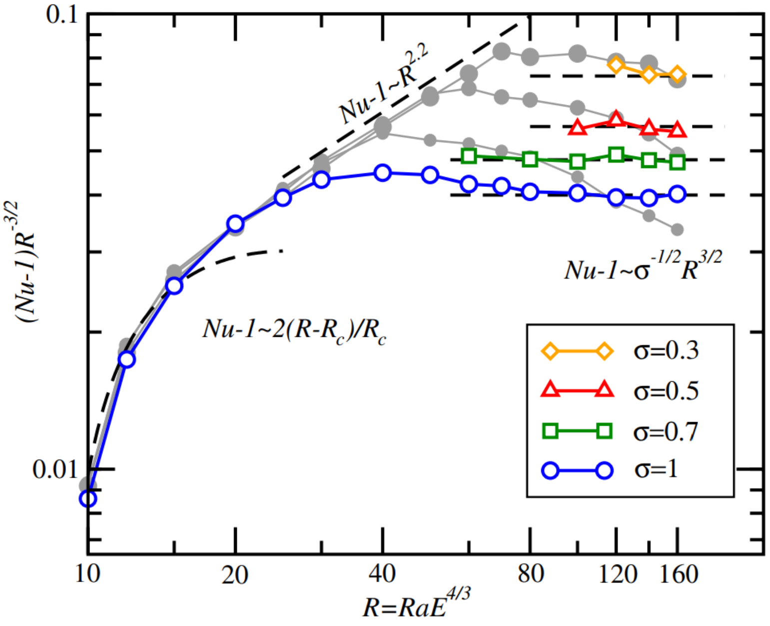

Figure 1.12: Figure from Julien *et al.* (2012). $Nu - 1$ as a function of $R = RaE^{4/3}$, compensated with the geostrophic turbulence scaling prediction $R^{3/2}$. The curves for $\sigma \leq 1$ exhibit the predicted scaling for geostrophic turbulence, $Nu - 1 \propto C_1 \sigma^{-1/2} R^{3/2}$ to within 6%. The $\sigma = 3$, 7 and 15 states, shown as small, medium, and large gray circles, respectively, have yet to reach the turbulent scaling regime.

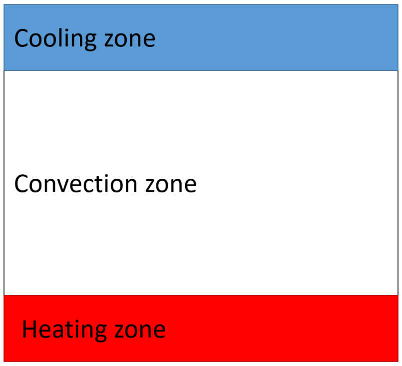

Figure 1.13: Schematic of the system used in Barker *et al.* (2014).

Bibliography

Aubert, Julien, Labrosse, Stéphane & Poitou, Charles 2009 Modelling the palaeo-evolution of the geodynamo. *Geophysical Journal International* **179** (3), 1414–1428, arXiv: https://academic.oup.com/gji/article-pdf/179/3/1414/6006621/179-3-1414.pdf.

Aurnou, Jonathan M., Horn, Susanne & Julien, Keith 2020 Connections between nonrotating, slowly rotating, and rapidly rotating turbulent convection transport scalings. *Phys. Rev. Research* **2**, 043115.

Barker, A. J., Dempsey, A. M. & Lithwick, Y. 2014 Theory and simulations of rotating convection. *Astrophys. J.* **791** (1), 13.

Bénard, Henri 1900 étude expérimentale des courants de convection dans une nappe liquide. régime permanent : tourbillons cellulaires. *J. Phys. Theor. Appl.* **9** (1), 513–524.

Bengtsson, Lars 1996 Mixing in ice-covered lakes. *Hydrobiologia* **322**, 91–97.

Bouillaut, V., Lepot, S., Aumaître, S. & Gallet, B. 2019 Transition to the ultimate regime in a radiatively driven convection experiment. *J. Fluid Mech.* **861**, R5.

Buckingham, E. 1914 On physically similar systems; illustrations of the use of dimensional equations. *Phys. Rev.* **4**, 345–376.

Chandrasekhar, S. 1961 *Hydrodynamic and Hydromagnetic Stability*. Dover Publications.

Chavanne, X., Chillà, F., Castaing, B., Hébral, B., Chabaud, B. & Chaussy, J. 1997 Observation of the ultimate regime in Rayleigh–Bénard convection. *Phys. Rev. Lett.* **79**, 3648–3651.

Chavanne, X., Chillà, F., Chabaud, B., Castaing, B. & Hébral, B. 2001 Turbulent rayleigh–bénard convection in gaseous and liquid he. *Physics of Fluids* **13** (5), 1300–1320.

Cheng, Jonathan S., Aurnou, Jonathan M., Julien, Keith & Kunnen, Rudie P. J. 2018 A heuristic framework for next-generation models of geostrophic convective turbulence. *Geophysical & Astrophysical Fluid Dynamics* **112** (4), 277–300, arXiv: https://doi.org/10.1080/03091929.2018.1506024.

Cheng, Jonathan S., Madonia, Matteo, Aguirre Guzmán, Andrés J. & Kunnen, Rudie P. J. 2020 Laboratory exploration of heat transfer regimes in rapidly rotating turbulent convection. *Phys. Rev. Fluids* **5**, 113501.

Cheng, J. S., Stellmach, S., Ribeiro, A., Grannan, A., King, E. M. & Aurnou, J. M. 2015 Laboratory-numerical models of rapidly rotating convection in planetary cores. *Geophysical Journal International* **201** (1), 1–17, arXiv: https://academic.oup.com/gji/article-pdf/201/1/1/2149282/ggu480.pdf.

Chillà, F. & Schumacher, J. 2012 New perspectives in turbulent Rayleigh–Bénard convection. *Eur. Phys. J. E* **35** (7), 58.

Christensen-Dalsgaard, J., Dappen, Werner, Ayukov, S., Anderson, Edwin, Antia, H., Basu, S, Baturin, Vladimir, Berthomieu, G, Chaboyer, B, Chitre, S., Cox, A., Demarque, P, Donatowicz, Jadzia, Dziembowski, W., Gabriel, Milstain, Gough, Douglas, Guenther, D., Guzik, J., Harvey, J. & Ulrich, Roger 1996 The current state of solar modeling. *Science (New York, N.Y.)* **272**, 1286–92.

Currie, Laura K, Barker, Adrian J, Lithwick, Yoram & Browning, Matthew K 2020 Convection with misaligned gravity and rotation: simulations and rotating mixing length theory. *Monthly Notices of the Royal Astronomical Society* **493** (4), 5233–5256, arXiv: https://academic.oup.com/mnras/article-pdf/493/4/5233/32968673/staa372.pdf.

Davaille, Anne, Girard, Fabien & Le Bars, Michael 2002 How to anchor hotspots in a convecting mantle? *Earth and Planetary Science Letters* **203** (2), 621–634.

Doering, Charles R 2020 Absence of evidence for the ultimate state of turbulent rayleigh-bénard convection. *Physical review letters* **124** (22), 229401.

Doering, Charles R, Toppaladoddi, Srikanth & Wettlaufer, John S 2019 Absence of evidence for the ultimate regime in two-dimensional rayleigh-bénard convection. *Physical review letters* **123** (25), 259401.

Ecke, Robert E. & Niemela, Joseph J. 2014 Heat transport in the geostrophic regime of rotating rayleigh-bénard convection. *Phys. Rev. Lett.* **113**, 114301.

Farmer, David M. 1975 Penetrative convection in the absence of mean shear. *Quarterly Journal of the Royal Meteorological Society* **101** (430), 869–891, arXiv: https://rmets.onlinelibrary.wiley.com/doi/pdf/10.1002/qj.49710143011.

Featherstone, Nicholas A. & Hindman, Bradley W. 2016 The spectral amplitude of stellar convection and its scaling in the high-rayleigh-number regime. *The Astrophysical Journal* **818** (1), 32.

F.R.S., Lord Rayleigh O.M. 1916 Lix. on convection currents in a horizontal layer of fluid, when the higher temperature is on the under side. *The London, Edinburgh, and Dublin Philosophical Magazine and Journal of Science* **32** (192), 529–546, arXiv: https://doi.org/10.1080/14786441608635602.

Garaud, P. 2002 Dynamics of the solar tachocline — I. An incompressible study. *Monthly Notices of the Royal Astronomical Society* **329** (1), 1–17, arXiv: https://academic.oup.com/mnras/article-pdf/329/1/1/3871990/329-1-1.pdf.

Garaud, Pascale 2021*a* Double-diffusive processes in stellar astrophysics, arXiv: 2103.08072.

Garaud, Pascale 2021*b* Journey to the center of stars: the realm of low prandtl number fluid dynamics, arXiv: 2103.14214.

Gibert, M., Pabiou, H., Chillà, F. & Castaing, B. 2006 High-rayleigh-number convection in a vertical channel. *Phys. Rev. Lett.* **96**, 084501.

Goluskin, David 2015 Internally heated convection and rayleigh-bénard convection. *arXiv* .

Gubbins, D., Alfé, D., Masters, G., Price, G. D. & Gillan, M. 2003 Can the earth's dynamo run on heat alone? *Geophysical Journal International* **155**, 609–622.

Hanasoge, Shravan M., Duvall, Thomas L. & Sreenivasan, Katepalli R. 2012 Anomalously weak solar convection **109** (30), 11928–11932.

Hanasoge, Shravan M., Hotta, Hideyuki & Sreenivasan, Katepalli R. 2020 Turbulence in the sun is suppressed on large scales and confined to equatorial regions **6** (30).

He, X., Funfschilling, D., Nobach, H., Bodenschatz, E. & Ahlers, G. 2012 Transition to the ultimate state of turbulent rayleigh-bénard convection. *Phys. Rev. Lett.* **108**, 024502.

Herant, Marc, Benz, Willy & Colgate, Stirling 1992 Postcollapse hydrodynamics of sn 1987a: Two-dimensional simulations of the early evolution. ApJ **395**, 642.

Howard, L. N. 1966 Convection at high rayleigh number. In *Applied Mechanics* (ed. Henry Görtler), pp. 1109–1115. Berlin, Heidelberg: Springer Berlin Heidelberg.

Iyer, Kartik P, Scheel, Janet D, Schumacher, Jörg & Sreenivasan, Katepalli R 2020 Classical 1/3 scaling of convection holds up to ra= 1015. *Proceedings of the National Academy of Sciences* **117** (14), 7594–7598.

Janka, H-T & Müller, Ewald 1996 Neutrino heating, convection, and the mechanism of type-ii supernova explosions. *Astronomy and Astrophysics* **306**, 167.

Jonas, Tobias, Terzhevik, Arkady Y., Mironov, Dmitrii V. & Wüest, Alfred 2003 Radiatively driven convection in an ice-covered lake investigated by using temperature microstructure technique. *Journal of Geophysical Research: Oceans* **108** (C6), arXiv: https://agupubs.onlinelibrary.wiley.com/doi/pdf/10.1029/2002JC001316.

Julien, Keith, Aurnou, Jonathan M., Calkins, Michael A., Knobloch, Edgar, Marti, Philippe, Stellmach, Stephan & Vasil, Geoffrey M. 2016 A nonlinear model for rotationally constrained convection with ekman pumping. *Journal of Fluid Mechanics* **798**, 50–87.

Julien, K. & Knobloch, E. 1998 A new class of equations for rotationally constrained flows. *Theoretical and Computational Fluid Dynamics* **11**, 251–261.

Julien, Keith, Knobloch, Edgar, Rubio, Antonio M. & Vasil, Geoffrey M. 2012 Heat transport in low-rossby-number rayleigh-bénard convection. *Phys. Rev. Lett.* **109**, 254503.

King, Eric M. & Aurnou, Jonathan M. 2013 Turbulent convection in liquid metal with and without rotation. *Proceedings of* *the National Academy of Sciences* **110** (17), 6688–6693, arXiv: https://www.pnas.org/content/110/17/6688.full.pdf.

King, E. M., Stellmach, S. & Aurnou, J. M. 2012 Heat transfer by rapidly rotating rayleigh-bénard convection. *Journal of Fluid Mechanics* **691**, 568–582.

King, Eric M., Stellmach, Stephan, Noir, Jerome, Hansen, Ulrich & Aurnou, Jonathan M. 2009 Boundary layer control of rotating convection systems. *Nature* **457**, 301–304.

Kraichnan, Robert H 1962 Turbulent thermal convection at arbitrary prandtl number. *Phys. Fluids* **5** (11), 1374–1389.

Kunnen, Rudie P. J. 2021 The geostrophic regime of rapidly rotating turbulent convection. *Journal of Turbulence* **22** (4-5), 267–296.

Landeau, Maylis & Aubert, Julien 2011 Equatorially asymmetric convection inducing a hemispherical magnetic field in rotating spheres and implications for the past martian dynamo. *Physics of the Earth and Planetary Interiors* **185**, 61–73.

Lepot, S., Aumaître, S. & Gallet, B. 2018 Radiative heating achieves the ultimate regime of thermal convection. *Proc. Natl. Acad. Sci.* **115** (36), 8937–8941.

Limare, A., Vilella, K., Di Giuseppe, E., Farnetani, C. G., Kaminski, E., Surducan, E., Surducan, V., Neamtu, C., Fourel, L., Jaupart, C. & et al. 2015 Microwave-heating laboratory experiments for planetary mantle convection. *Journal of Fluid Mechanics* **777**, 50–67.

Malkus, W.V.R. 1954 The heat transport and spectrum of thermal turbulence. *Proc. R. Soc. Lond. A* **225**, 196–212.

Miquel, Benjamin, Bouillaut, Vincent, Aumaître, Sébastien & Gallet, Basile 2020 On the role of the prandtl number in convection driven by heat sources and sinks. *Journal of Fluid Mechanics* **900**, R1.

Niemela, J.J., Skrbek, L., Sreenivasan, K.R. & Donnelly, R.J. 2000 Turbulent convection at very high rayleigh numbers. *Nature* **404** (6780), 837.

Plumley, Meredith, Julien, Keith, Marti, Philippe & Stellmach, Stephan 2016 The effects of ekman pumping on quasi-geostrophic rayleigh-bénard convection. *Journal of Fluid Mechanics* **803**, 51–71.

Priestley, C. H. B. 1954 Convection from a Large Horizontal Surface. *Australian Journal of Physics* **7**, 176.

Radice, David, Ott, Christian D, Abdikamalov, Ernazar, Couch, Sean M, Haas, Roland & Schnetter, Erik 2016 Neutrino-driven convection in core-collapse supernovae: high-resolution simulations. *The Astrophysical Journal* **820** (1), 76.

Roche, P.-E., Gauthier, F., Kaiser, R. & Salort, J. 2010 On the triggering of the ultimate regime of convection. *New J. Phys.* **12** (8), 085014.

Shaviv, Giora & Salpeter, Edwin E. 1973 Convective Overshooting in Stellar Interior Models. *The Astrophysical Journal* **184**, 191–200.

Spiegel, EA & Zahn, J-P 1992 The solar tachocline. *Astronomy and Astrophysics* **265**, 106–114.

Spiegel, Edward A 1963 A generalization of the mixing-length theory of turbulent convection. *Ap. J.* **138**, 216.

Spiegel, Edward A 1971 Convection in stars i. basic boussinesq convection. *Annu. Rev. Astro. Astrophys.* **9** (1), 323–352.

Sprague, M., Julien, K., Knobloch, E. & Werne, J. 2006 Numerical simulation of an asymptotically reduced system for rotationally constrained convection. *Journal of Fluid Mechanics* **551**, 141–174.

Stellmach, S., Lischper, M., Julien, K., Vasil, G., Cheng, J. S., Ribeiro, A., King, E. M. & Aurnou, J. M. 2014 Approaching the asymptotic regime of rapidly rotating convection: Boundary layers versus interior dynamics. *Phys. Rev. Lett.* **113**, 254501.

Stevenson, D.J. 1979 Turbulent thermal convection in the presence of rotation and a magnetic field: A heuristic theory. *Geophysical and Astrophysical Fluid Dynamics* **12** (1), 139–169.

Stix, M. 2012 *The Sun: An Introduction*. Springer Berlin Heidelberg.

Vitense, E. 1953 Die wasserstoffkonvecktionszone der sonne. *Z. Astrophysik* **32**, 135–164.

Wedi, M., van Gils, D.P.M., Bodenschatz, E. & Weiss, S. 2021 Rotating turbulent thermal convection at very large rayleigh numbers. *Journal of Fluid Mechanics* **912**.

Zhang, Xuan, van Gils, Dennis P. M., Horn, Susanne, Wedi, Marcel, Zwirner, Lukas, Ahlers, Guenter, Ecke, Robert E., Weiss, Stephan, Bodenschatz, Eberhard & Shishkina, Olga 2020 Boundary zonal flow in rotating turbulent rayleigh-bénard convection. *Phys. Rev. Lett.* **124**, 084505.

Chapter 2

Rotating Convection: Linear Stability Analysis

2.1 Introduction

This chapter presents a linear stability analysis of a radiatively driven rotating convection system. Stability analysis aims to assess the forcing necessary to reach the onset of a given instability. Since 1916 and the study of the stability of RBC, legion of variations have been made to this problem. In 1961, Chandrasekhar studied the onset of convection for a rotating RBC. Chandrasekhar (1961) showed that rotation increases the threshold for convection, the critical temperature drop increasing as a power-law of the rotation rate. More recently, Julien & Knobloch (1998); Sprague *et al.* (2006); Julien *et al.* (2012); Aurnou *et al.* (2020) predicted important consequences of this rotation-delayed threshold on the statistics of the resulting equilibrated convective flow. The system studied here is a variation of the radiatively forced convection experiment (see Lepot *et al.* (2018); Bouillaut *et al.* (2019); Miquel *et al.* (2020)), where the fluid is not heated through a rigid plate but through the absorption of light. Indeed, as presented in Bouillaut *et al.* (2021) our experimental apparatus consists in a cylinder tank filled with dyed water, heated through the absorption of a light flux P over a depth ℓ, and connected to a drive shaft rotating at a rate Ω as sketched in Figure 2.1. The present thesis seeking to investigate the heat transport efficiency of rotating convection, the natural first step is to derive the scaling law governing the onset of radiatively forced rotating convection.

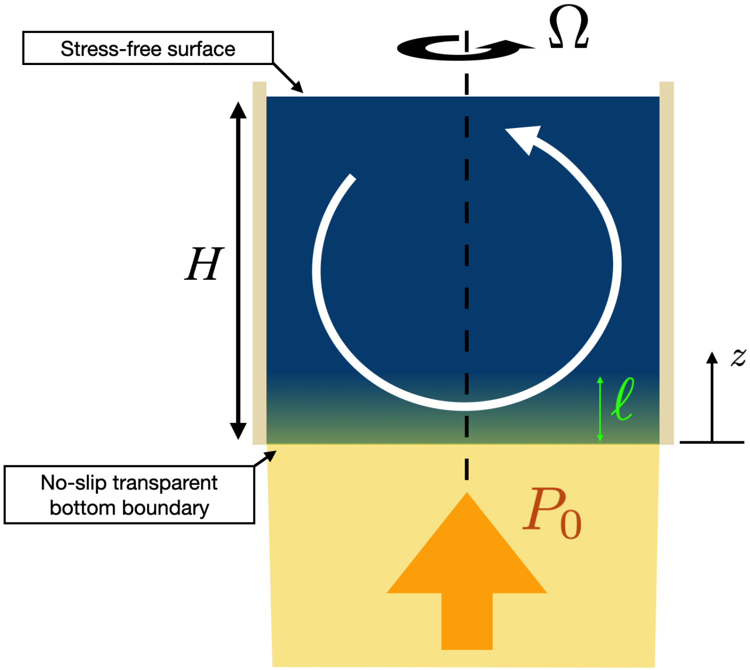

Figure 2.1: Sketch of the radiatively driven rotating convection system.

In a first section, we introduce the equations of the problem. This set of equations will be seen as an eigenvalue problem in order to compute the critical Rayleigh number which will be compared to values found in the literature, when available, or to 2D DNS of radiative convection.

2.2 From experimental apparatus to equations

In this section we adapt the standard Boussinesq equations to the system described above. As is customary in fluid mechanics we will make the equations dimensionless after having introduced the Boussinesq approximation and the boundary conditions. Linear stability analysis consists first, in computing the base state, then adding some perturbations to see how they respond. As the subsections will go, we will transform the system of equations into an eigenvalue problem that we solve numerically.

2.2.1 Boussinesq approximation and boundary conditions

The system is described by the 3D rotating Navier-Stokes equations (2.3) in the Boussinesq approximation, i.e. the kinematic viscosity ν, the thermal diffusivity κ, the specific heat c_p and the density ρ are independent of the temperature except in the buoyancy term where density is modified as follows:

$$\rho(T) = \rho_0 \left(1 - \alpha(T - T_0)\right) \tag{2.1}$$

The heat equation (2.4) then describes advection of heat in the flow. We recall the reader that this convection experiment has a heat source but no cooling mechanism. As a result, the mean temperature inside the tank drifts linearly in time. We showed in the previous chapter that this drifting situation is mathematically equivalent to the fluid being uniformly cooled at a rate equal and opposite to the heating power. It leads to the following radiative source term in the heat equation:

$$P(z) = P_0 \left(\frac{H}{\ell} e^{-z/\ell} + e^{-H/\ell} - 1\right) \tag{2.2}$$

This forcing stems from an application of the Beer-Lambert law, and the parameter ℓ is the absorption length of light in the dyed water, while z is the vertical coordinate measured upwards from the bottom plate.

$$\partial_t \mathbf{u} + (\mathbf{u} \cdot \nabla)\, \mathbf{u} + 2\Omega \wedge \mathbf{u} = -\frac{1}{\rho_0} \nabla p + \nu \nabla^2 \mathbf{u} - \alpha T \mathbf{g} \tag{2.3}$$

$$\partial_t T + \mathbf{u} \cdot \nabla T = \kappa \nabla^2 T + \frac{P(z)}{\rho_0 c_p H} \tag{2.4}$$

$$\nabla \cdot \mathbf{u} = 0 \tag{2.5}$$

We seek 2D solutions functions of x and z, meaning $\partial_y = 0$ and $\nabla = \begin{pmatrix} \partial_x \\ 0 \\ \partial_z \end{pmatrix}$. Rotation implies that the velocity vector has three non-zero components, hence $\mathbf{u} = \begin{pmatrix} u(x,z,t) \\ v(x,z,t) \\ w(x,z,t) \end{pmatrix}$.

In terms of boundary conditions we have a mix between no-slip (NS) surface on the bottom, and a stress-free (SF) condition on the upper free surface, both being impenetrable :

$$w|_{z=0} = 0 \quad ; \partial_z w|_{z=0} = 0 \quad ; \quad u|_{z=0} = v|_{z=0} = 0 \tag{2.6}$$

$$w|_{z=H} = 0 \quad ; \quad \partial_z u|_{z=H} = \partial_z v|_{z=H} = 0 \quad ; \quad \partial_{zz} w|_{z=H} = 0. \tag{2.7}$$

We neglect the slight curvature of the free surface associated with the centrifugal acceleration. Regarding temperature, both boundaries are insulated leading to:

$$\partial_z T|_{z=0} = 0 \quad ; \quad \partial_z T|_{z=H} = 0 \tag{2.8}$$

To facilitate comparison between various systems, we now non-dimensionalize the equations.

2.2.2 Dimensionless equations

The distances, temperature, velocities, pressure and time are non-dimensionalized by H, $\frac{\kappa\nu}{\alpha g H^3}$, $\frac{\kappa}{H}$, $\frac{\rho\kappa^2}{H^2}$ and $\frac{H^2}{\kappa}$ respectively.

$$\partial_{\widetilde{t}}\widetilde{\mathbf{u}} + \left(\widetilde{\mathbf{u}}\cdot\widetilde{\nabla}\right)\widetilde{\mathbf{u}} + \frac{\mathrm{Pr}}{\mathrm{E}}\mathbf{z}\wedge\widetilde{\mathbf{u}} = -\widetilde{\nabla}\widetilde{p} + \mathrm{Pr}\left(\widetilde{\nabla}^2\widetilde{\mathbf{u}} + \widetilde{T}\mathbf{z}\right) \tag{2.9}$$

$$\partial_{\widetilde{t}}\widetilde{T} + \widetilde{\mathbf{u}}\cdot\widetilde{\nabla}\widetilde{T} = \widetilde{\nabla}^2\widetilde{T} + \mathrm{Ra_P}\left(\frac{1}{\widetilde{\ell}}e^{\left(-\frac{\widetilde{z}}{\widetilde{\ell}}\right)} + e^{-\frac{1}{\widetilde{\ell}}} - 1\right) \tag{2.10}$$

The tildes indicating dimensionless variables. For comfort, the tildes will be dropped there-after.

We now build the dimensionless control parameters of the problem:

$$\mathrm{Ra_P} = \frac{\alpha g P_0 H^4}{\rho c_p \kappa^2 \nu} \quad ; \quad \mathrm{Pr} = \frac{\nu}{\kappa} \quad ; \quad \mathrm{E} = \frac{\nu}{2\Omega H^2} \quad ; \quad \widetilde{\ell} = \frac{\ell}{H} \tag{2.11}$$

Traditionally the dimensionless number used to describe convection is the Rayleigh number $\mathrm{Ra} = \frac{\alpha g \Delta T H^3}{\kappa\nu}$. But when the convection is radiatively driven, the input quantity is not ΔT, as in RB configurations, but the light (and heat) flux P_0. The control parameter becomes $\mathrm{Ra_P}$ instead of Ra.

2.2.3 Steady base state

Now that the equations are derived, we need to compute the temperature profile when $\mathbf{u} = 0$. The equations (2.9) and (2.10) can then be simplified by removing all terms involving $\mathbf{u}$.

The subscript "s" corresponds to the static state. Equation (2.12) shows that the gradient of static pressure will absorb the variation of density caused by the static temperature, i.e. the static variables in the Navier-Stokes equations balance each other. Integrating twice the heat equation, (2.13), allows to derive the static temperature profile shown in Figure 2.2.

$$\frac{1}{\rho_0}\partial_z p_s = -\frac{\rho(T_s)}{\rho_0} g \tag{2.12}$$

$$0 = \nabla^2 T_s + \mathrm{Ra_P}\left(\frac{1}{\ell} e^{-z/\ell} + e^{-H/\ell} - 1\right) \tag{2.13}$$

$$T_s = -\mathrm{Ra_P}\left(\ell e^{-\frac{z}{\ell}} + \frac{e^{-\frac{1}{\ell}} - 1}{2} z^2 + z\right) \tag{2.14}$$

We perturb the static state by adding fluctuating terms : $T(z) = T_s(z) + \theta(x, z, t)$, $p(z) = p_s(z) + p'(x, z, t)$ and $\mathbf{u} = \mathbf{u_s} + \mathbf{u'(x, z, t)}$.

$$\partial_t \mathbf{u}' + \left(\mathbf{u}' \cdot \nabla\right) \mathbf{u}' + \frac{\mathrm{Pr}}{\mathrm{E}} \mathbf{z} \wedge \mathbf{u}' = -\nabla p' + \mathrm{Pr}\left(\nabla^2 \mathbf{u}' + \theta \mathbf{z}\right) \tag{2.15}$$

$$\partial_t \theta + \mathbf{u}' \cdot \nabla\theta + w \partial_z T_s = \nabla^2 \theta \tag{2.16}$$

The perturbed system can still be simplified by narrowing the physics of interest at the onset of convection.

2.2.4 Linear equations and eigenvalue problem

The point of a stability analysis is to assess the forcing amplitude at which some perturbation grows exponentially. Those perturbations are infinitesimal, so we can assume that the system remains linear. It means that we consider negligible the

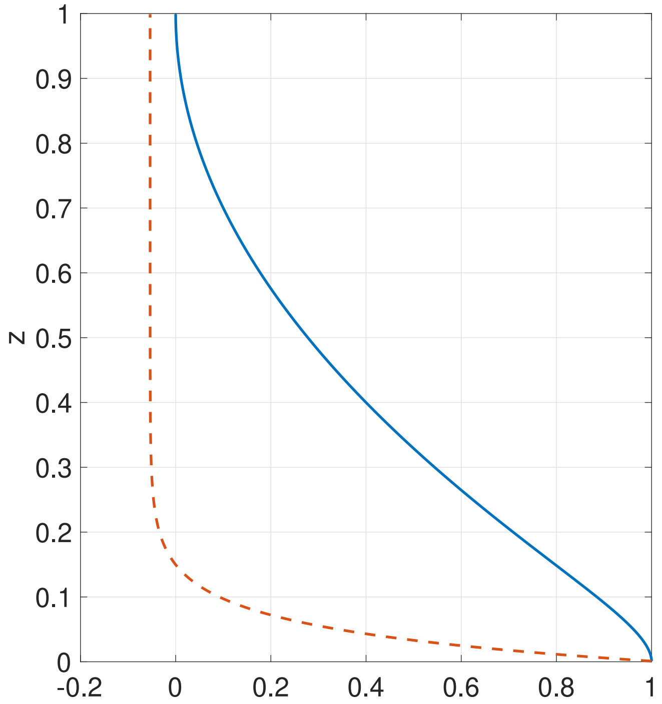

Figure 2.2: Profiles of radiative forcing (dashed line) and the static temperature (straight line). The profiles have been compensated with their maximum value. The origin of the static temperature profile has been chosen arbitrarily.

contributions from $\mathbf{u}' \cdot \nabla \mathbf{u}'$ and $\mathbf{u}' \cdot \nabla \theta$ to the dynamics of the system.
We restrict attention to the threshold for a stationary instability. This implies $\partial_t = 0$. With these assumptions the final set of equations reads:

$$\frac{\mathrm{Pr}}{\mathrm{E}} \mathbf{z} \wedge \mathbf{u}' = -\nabla p' + \mathrm{Pr} \left(\nabla^2 \mathbf{u}' + \theta \mathbf{z} \right) \tag{2.17}$$

$$w \partial_z T_s = \nabla^2 \theta \tag{2.18}$$

$$\nabla \cdot \mathbf{u}' = 0 \tag{2.19}$$

By taking the curl of the first equation we get rid of the pressure term. Equation (2.17) becomes:

$$\frac{1}{\mathrm{E}} \begin{pmatrix} -\partial_z u' \\ -\partial_z v' \\ \partial_x u' \end{pmatrix} = \begin{pmatrix} -\partial_z \nabla^2 v' \\ -\partial_x \nabla^2 w' + \partial_z \nabla^2 u' \\ \partial_x \nabla^2 v' \end{pmatrix} + \begin{pmatrix} 0 \\ -\partial_x \theta \\ 0 \end{pmatrix} \tag{2.20}$$

In order to end up with a general eingenvalue problem we want a system of the form:

$$\mathbf{A} \overline{X} = \mathrm{Ra}_{\mathrm{P}c} \mathbf{B} \overline{X}, \tag{2.21}$$

where the generalized eigenvalue $\mathrm{Ra}_{\mathrm{P}c}$ is the threshold flux-based Rayleigh number.

The problem being invariant to translations along x, the Fourier modes in that direction are decoupled in the linear equations.

$$\mathbf{u}' = \mathbf{U}(z) e^{ikx} \quad \text{and} \quad \theta = \Theta(z) e^{ikx} \tag{2.22}$$

In the following: $\partial_x = ik$ and $\partial_z = D$ or $D_\perp$ if applied respectively to w or u, v. The subscript "θ" means that the derivative is applied to θ.

$$\nabla^2 = D^2 - k^2 \quad ; \quad \nabla^2_\theta = D^2_\theta - k^2 \quad ; \quad \nabla^2_\perp = D^2_\perp - k^2 \tag{2.23}$$

In the following we will drop the superscript for clarity. We have five equations for four variables, one equation being redundant. We choose to use (2.20)$\cdot\mathbf{y}$ and (2.20)$\cdot\mathbf{z}$

in addition to the heat equation and the incompressibility equation. Differentiating u three times would demand more boundary conditions than we have. To bypass this issue we use the continuity equation to transform our third order differentiate on u in a fourth order differentiation on w. It gives the following system:

$$\begin{pmatrix} -D_\perp k^2 & \frac{D_\perp}{E} & -\left(ik\nabla^2 + \frac{1}{ik}D^4\right) & -ik \\ -\frac{ik}{E} & ik\nabla_\perp^2 & 0 & 0 \\ 0 & 0 & 0 & \nabla_\theta^2 \\ ik & 0 & D & 0 \end{pmatrix} \begin{pmatrix} u \\ v \\ w \\ \theta \end{pmatrix} = \mathrm{Ra}_{\mathrm{P}c} \begin{pmatrix} 0 & 0 & 0 & 0 \\ 0 & 0 & 0 & 0 \\ 0 & 0 & \partial_z T_s & 0 \\ 0 & 0 & 0 & 0 \end{pmatrix} \begin{pmatrix} u \\ v \\ w \\ \theta \end{pmatrix} \tag{2.24}$$

To find the solutions of this eigenvalue problem, I designed a simple numerical solver.

2.3 A finite difference code to resolve the eigenvalue problem

This method aims at discretizing the 1D fields over N points. Each variable is evaluated on points, separated by a distance $h = 1/N$:

$$u = (u_1, u_2, ..., u_{N-1}) \tag{2.25}$$

$$v = (v_1, v_2, ..., v_{N-1}) \tag{2.26}$$

$$w = (w_1, w_2, ..., w_{N-1}) \tag{2.27}$$

$$\theta = (\theta_1, \theta_2, ..., \theta_{N-1}) \tag{2.28}$$

with $u_n = u(0+nh)$. The eigenvalue problem is then reduced to a difference equation where the derivatives are approximated through Taylor expansions:

$$f(z+h) = f(z) + h\partial_z f(z) + \frac{h^2}{2}\partial_{zz} f(z) + O(h^3) \tag{2.29}$$

$$f(z-h) = f(z) - h\partial_z f(z) + \frac{h^2}{2}\partial_{zz} f(z) + O(h^3) \tag{2.30}$$

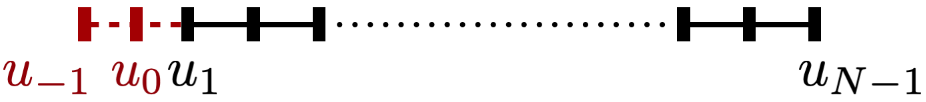

Figure 2.3: Schematic of the numerical discretization with examples of ghost points in red.

$$f(z+2h) = f(z) + 2h\partial_z f(z) + \frac{h^2}{2}\partial_{zz} f(z) + O(h^3) \tag{2.31}$$

$$f(z-2h) = f(z) - 2h\partial_z f(z) + \frac{h^2}{2}\partial_{zz} f(z) + O(h^3) \tag{2.32}$$

By combining these equations we can compute the derivation matrices constrained by the boundary conditions (derivatives of higher degree demand the use of higher order expansions). To apply those we use ghost points, i.e. points beyond the limits of the system whose only purpose is to enforce the boundary conditions as shown in 2.3. For instance:

$$\partial_z w_0 = \frac{w_1 - w_{-1}}{2h} \tag{2.33}$$

(2.6) imposes $\partial_z w|_{H=0} = 0$. Hence, $\partial_z w_0 = 0$ giving $w_1 = w_{-1}$. This ghost point w_{-1} is then used to enforce the boundary condition on the second derivative of w.

It leads to the following derivation matrices for NS-SF boundary conditions, here represented for $N = 6$:

$$D_\perp = \frac{1}{2h}\begin{pmatrix} 0 & 1 & 0 & 0 & 0 \\ -1 & 0 & 1 & 0 & 0 \\ 0 & -1 & 0 & 1 & 0 \\ 0 & 0 & -1 & 0 & 1 \\ 0 & 0 & -1/2 & 0 & 1/2 \end{pmatrix} \tag{2.34}$$

$$D_\perp^2 = \frac{1}{h^2}\begin{pmatrix} -2 & 1 & 0 & 0 & 0 \\ 1 & -2 & 1 & 0 & 0 \\ 0 & 1 & -2 & 1 & 0 \\ 0 & 0 & 1 & -2 & 1 \\ 0 & 0 & 1/4 & 0 & -1/4 \end{pmatrix} \tag{2.35}$$

$$D^2 = \frac{1}{h^2}\begin{pmatrix} -2 & 1 & 0 & 0 & 0 \\ 1 & -2 & 1 & 0 & 0 \\ 0 & 1 & -2 & 1 & 0 \\ 0 & 0 & 1 & -2 & 1 \\ 0 & 0 & 0 & 1 & -2 \end{pmatrix} \tag{2.36}$$

$$D^4 = \frac{1}{h^4}\begin{pmatrix} 7 & -4 & 1 & 0 & 0 \\ -4 & 6 & -4 & 1 & 0 \\ 1 & -4 & 6 & -4 & 1 \\ 0 & 1 & -4 & 6 & -4 \\ 0 & 0 & 1 & -4 & 5 \end{pmatrix} \tag{2.37}$$

$$D^2_\theta = \frac{1}{h^2}\begin{pmatrix} -1/4 & 0 & 1/4 & 0 & 0 \\ 1 & -2 & 1 & 0 & 0 \\ 0 & 1 & -2 & 1 & 0 \\ 0 & 0 & 1 & -2 & 1 \\ 0 & 0 & 1/4 & 0 & -1/4 \end{pmatrix} \tag{2.38}$$

with $\perp$ meaning that the matrix will be applied to u and v and the subscript θ meaning that it will be applied to the variable θ. The equations can now be written as a linear combination of these matrices applied to the variables of the system in the form of (2.21) that can be solved using MatLab.

2.4 Results

The stability of a system heated from below and cooled from above has been studied tirelessly since the beginning of the last century. Here, we focus on two fragments of this dense literature. If we choose ΔT as the temperature difference between the bottom plate and the center of the cell (see Lepot *et al.* (2018)),before defining the temperature-based Rayleigh number as

$$\mathrm{Ra} = \frac{\alpha g \Delta T H^3}{\kappa \nu}, \tag{2.39}$$

the relation between the critical flux-based Rayleigh number and the traditional Rayleigh number becomes $\mathrm{Ra}_{\mathrm{P}_c} = 2.3 \times \mathrm{Ra}_c$.
The first reference used here is a paper written by Goluskin (2015), where onsets are computed for several types of heating: RBC, i.e. with heating and cooling imposed

on rigid plates on the bottom and at the top of the cell, or for different kinds of internal heating. Our situation, when $\ell/H \to 0$, and $\partial_z\theta = 0$ at both boundaries, is similar to the second type of internal heating in Goluskin (2015), except that our imposed flux is not at the top boundary but at the bottom one. These two situations are equivalent up to a Boussinesq symmetry. We thus compare our results to his "stress-free bottom" boundary condition. The critical Ra number (noted Ra_c hereafter), for SF-NS boundary conditions, of interest for our situation are listed in Table 2.1.

Forcing	$\mathrm{Ra}_c = \mathrm{Ra_P}_c$
RBC	320
Internal Heating	720

Table 2.1: Ra_c found in Goluskin (2015)

The second piece of literature is a book written by Chandrasekhar in 1961 containing stability analysis for a large number of instabilities. Among them is the study of rotating RBC. For SF boundary conditions, the threshold reported by Chandrasekhar is :

$$\mathrm{Ra}_c = 3\left(\frac{\pi}{\sqrt{2}}\right)^{4/3} \mathrm{E}^{-4/3} = 8.695\mathrm{E}^{-4/3} \tag{2.40}$$

It has been shown by Niiler & Bisshopp (1965) that, in the rapidly rotating limit, the threshold of convection is independent of the surfaces which bound the fluid. Hence, the onset found for stress-free boundary conditions is also valid for our set of boundary conditions.

We compute $\mathrm{Ra_P}_c$ for various $\mathrm{E} \in [10^{-6}; 100]$ for both rotating RBC and radiatively driven convection. The results are presented in Figure 2.4. The first step is to assess the validity of the code. To that end, we apply RB-like heating and compute the critical values for no-slip and stress-free boundary conditions for the bottom and top plate, respectively. The result is visible on the right plot of figure 2.4. For high E we recover the non-rotating Ra_c (see table 2.1). When E decreases, Ra_c increases following the scaling law (2.40), as expected. The code developed here is thus able to compute the threshold values of rotating convection. On this basis, we can study the stability of rotating radiatively driven convection, which has not been done before. We compute Ra_{Pc} for $\ell/H = 0.05$, the resulting plot is shown in figure 2.4. For high E, the critical flux-based Rayleigh number tends to a constant, which is the one computed in Goluskin (2015) for the non-rotating case. In the low E limit, $\mathrm{Ra_P}_c$

increases following the scaling law:

$$\mathrm{Ra}_{\mathrm{P}_c} = 14.775\mathrm{E}^{-4/3} \tag{2.41}$$

Hence, we can assert that the radiative forcing does not modify the exponent of (2.40). However, the conclusion is different regarding the prefactor. Indeed, radiative heating seems to increase the value of this prefactor (when looking at the scaling law for Ra_P). The value of $\mathrm{Ra}_{\mathrm{P}_c}$ for rotating radiatively driven convection has been validated by 2D-DNS performed with the spectral code Dedalus (Burns *et al.* (2020)). We compare fields from the DNS with 2D fields built from the profiles of the first unstable mode (figure 2.5). As shown in figure 2.6, the fields computed from the eigenvalue problem and through DNS look extremely similar. DNS also confirm the value of $\mathrm{Ra}_{\mathrm{P}_c}$.

In conclusion, this stability analysis led to the derivation of the scaling law governing the stability threshold of a rapidly rotating radiatively driven convection experiment for $\ell/H = 0.05$. This result will be later used to study the nonlinear regime of rapidly rotating convection.

The threshold has also been validated using another pseudo-spectral code, CoRaL, presented in Miquel (2021). 3D DNS have been performed and they confirm the value of $\mathrm{Ra}_{\mathrm{P}_c}$. This validation also confirms that convection arises through a stationary instability (oscillatory modes having been discarded at the outset of the linear stability analysis). On a side note, oscillatory modes have been found for rotating convection at low Pr by Horn & Schmid (2017).

2.5 Conclusion

This chapter showed the impact of radiative forcing on the threshold of convection. It assessed that the rotation rate impacts rotation in a similar way for radiatively forced convection and RBC, except for the numerical prefactor. Now that we know the exponent of the threshold of convection remains the same in radiatively forced convection, we can move on to the study of the turbulent state arising in the strongly non-linear regime. Hence, the next step will focus on the laboratory experiment that aims at providing a first laboratory observation of the geostrophic turbulence regime of rotating convection.

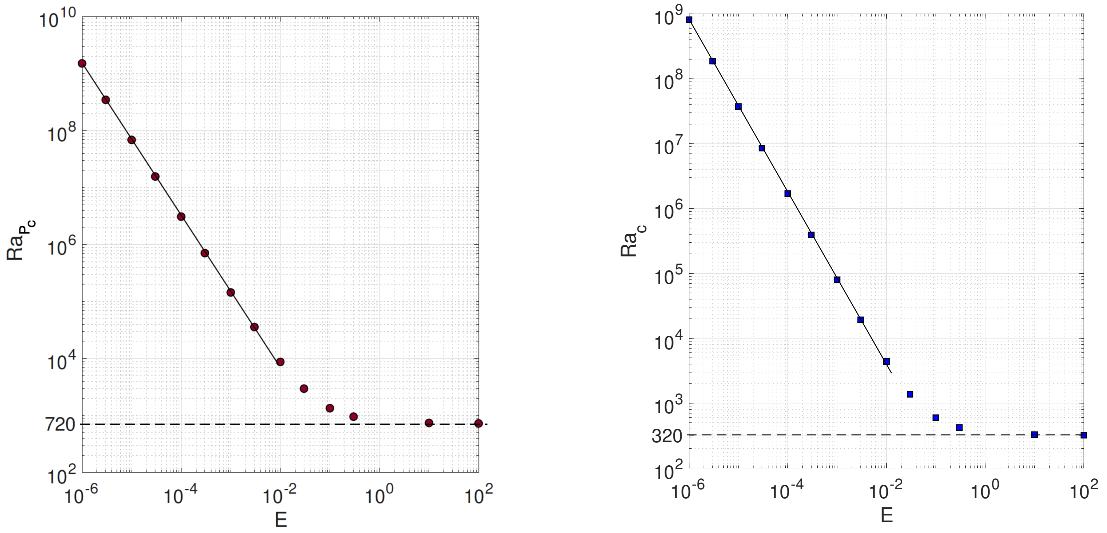

Figure 2.4: Left: Stability of rotating radiative convection for NS-SF boundary conditions and $\ell/H = 0.05$. The dashed line corresponds to the $\mathrm{Ra}_{\mathrm{P}_c}$ computed by Goluskin without rotation. The solid line corresponds to $\mathrm{Ra}_{\mathrm{P}_c} = 14.775\mathrm{E}^{-4/3}$. Right: stability of RB convection for NS-SF boundary conditions. The solid line is the scaling law (2.40) derived in Chandrasekhar (1961) for rotating RBC. The dashed line corresponds to the $\mathrm{Ra}_{\mathrm{P}_c}$ computed by Goluskin without rotation.

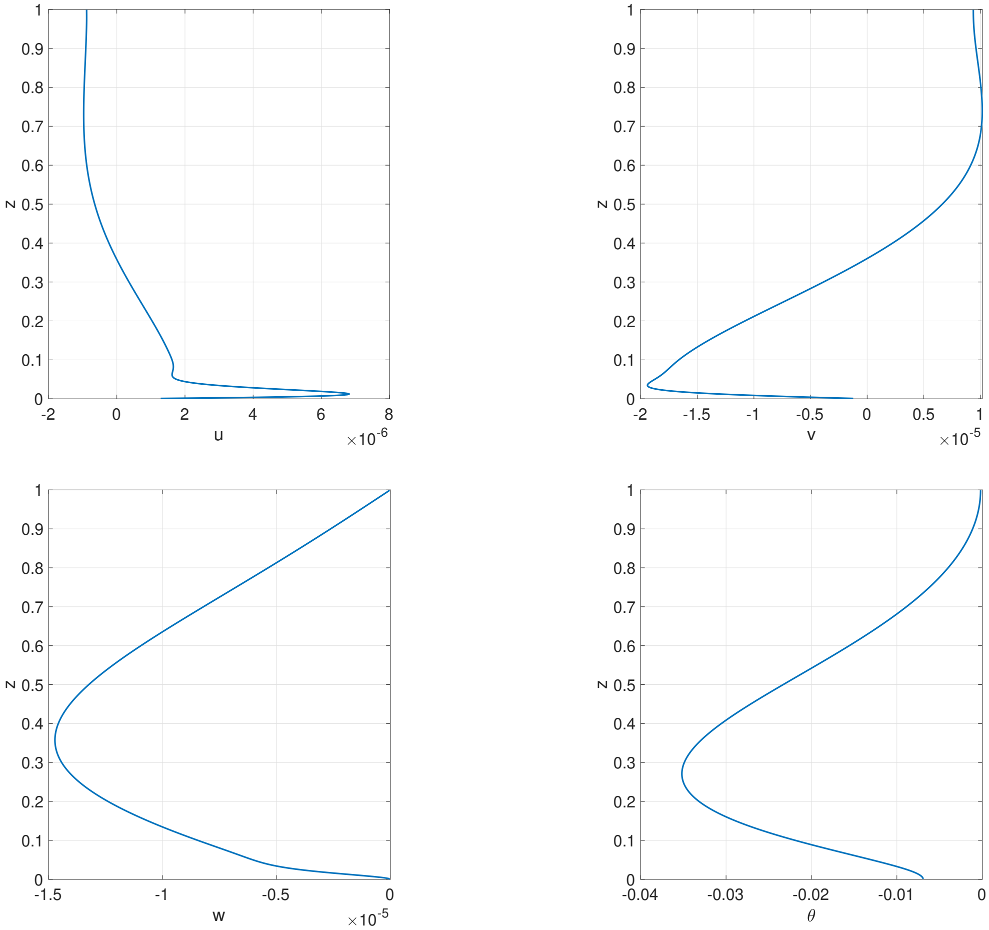

Figure 2.5: Velocity $\mathbf{u} = (u, v, w)$ and temperature θ profiles for the first unstable mode of rotating radiative convection for $\ell/H = 0.05$, $\mathrm{E} = 10^{-4}$.

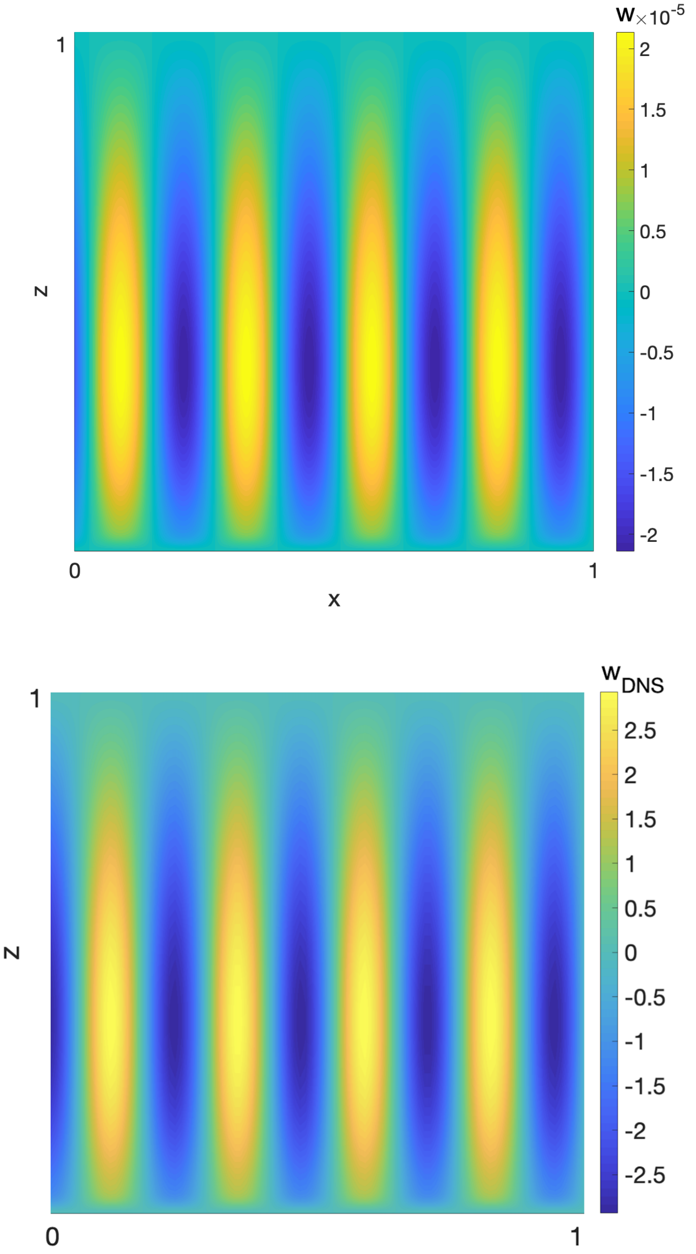

Figure 2.6: Top:Vertical velocity from the first unstable eigenmode for E $= 10^{-4}$,$\ell/H = 0.05$. Bottom: Velocity field from 2D DNS for E $= 10^{-4}$,$\ell/H = 0.05$ near the onset of convection.

Bibliography

AURNOU, JONATHAN M., HORN, SUSANNE & JULIEN, KEITH 2020 Connections between nonrotating, slowly rotating, and rapidly rotating turbulent convection transport scalings. *Phys. Rev. Research* **2**, 043115.

BOUILLAUT, V., LEPOT, S., AUMAÎTRE, S. & GALLET, B. 2019 Transition to the ultimate regime in a radiatively driven convection experiment. *J. Fluid Mech.* **861**, R5.

BOUILLAUT, VINCENT, MIQUEL, BENJAMIN, JULIEN, KEITH, AUMAÎTRE, SÉBASTIEN & GALLET, BASILE 2021 Experimental observation of the geostrophic turbulence regime of rapidly rotating convection. *Proceedings of the National Academy of Sciences* **118** (44), arXiv: https://www.pnas.org/content/118/44/e2105015118.full.pdf.

BURNS, KEATON J., VASIL, GEOFFREY M., OISHI, JEFFREY S., LECOANET, DANIEL & BROWN, BENJAMIN P. 2020 Dedalus: A flexible framework for numerical simulations with spectral methods. *Phys. Rev. Research* **2**, 023068.

CHANDRASEKHAR, S. 1961 *Hydrodynamic and Hydromagnetic Stability*. Dover Publications.

GOLUSKIN, DAVID 2015 Internally heated convection and rayleigh-bénard convection. *arXiv* .

HORN, SUSANNE & SCHMID, PETER J. 2017 Prograde, retrograde, and oscillatory modes in rotating rayleigh–bénard convection. *Journal of Fluid Mechanics* **831**, 182–211.

JULIEN, K. & KNOBLOCH, E. 1998 A new class of equations for rotationally constrained flows. *Theoretical and Computational Fluid Dynamics* **11**, 251–261.

Julien, Keith, Knobloch, Edgar, Rubio, Antonio M. & Vasil, Geoffrey M. 2012 Heat transport in low-rossby-number rayleigh-bénard convection. *Phys. Rev. Lett.* **109**, 254503.

Lepot, S., Aumaître, S. & Gallet, B. 2018 Radiative heating achieves the ultimate regime of thermal convection. *Proc. Natl. Acad. Sci.* **115** (36), 8937–8941.

Miquel, Benjamin 2021 Coral: a parallel spectral solver for fluid dynamics and partial differential equations. *submitted to JOSS* .

Miquel, Benjamin, Bouillaut, Vincent, Aumaître, Sébastien & Gallet, Basile 2020 On the role of the prandtl number in convection driven by heat sources and sinks. *Journal of Fluid Mechanics* **900**, R1.

Niiler, Pearn Peter & Bisshopp, Frederic E 1965 On the influence of coriolis force on onset of thermal convection. *Journal of Fluid Mechanics* **22** (4), 753–761.

Sprague, M., Julien, K., Knobloch, E. & Werne, J. 2006 Numerical simulation of an asymptotically reduced system for rotationally constrained convection. *Journal of Fluid Mechanics* **551**, 141–174.

Chapter 3

Rotating Convection in the Laboratory

The introductory chapter of the present thesis presented the different attempts to observe the geostrophic turbulence regime of turbulent convection in the literature. As far as our knowledge goes, only numerical studies have proven able to achieve such extreme solutions to the Boussinesq equations, albeit with stress-free boundary conditions. In this chapter will be described the experiment used to radiatively force rotating convection. The idea is the same than in the thesis written by Simon Lepot (also see Lepot *et al.* (2018)), but the new spinning feature led to some changes, mostly in the temperature measurements described in the following. The experimental protocol will be detailed along with the method for processing the data. Finally, the results will be discussed, providing clear evidence that the present experiment achieves the geostrophic turbulence regime of rapidly rotating convection.

3.1 Modification of the experimental apparatus and measurement system

The experimental set-up is an adaptation of the one developed by Basile Gallet, Sébastien Aumaître and Simon Lepot, to achieve the ultimate regime in the non rotating convection configuration. The apparatus is described in the first chapter, and we briefly recall its main characteristics. A cylindrical cell of radius $R = 10$ cm is filled with a homogeneous mixture of water and carbon black dye, up to a height H.

A powerful spotlight shines at the tank from below, the latter having a transparent bottom boundary. Absorption of light by the fluid leads to an internal source of heat, the magnitude of which decreases exponentially with height over an e-folding scale ℓ (Beer-Lambert law). The absorption length ℓ can be tuned through the concentration of dye: for large dye concentrations, ℓ is much smaller than the thermal boundary layer thickness and we recover a standard RB-like boundary-heated configuration. By contrast, for low dye concentrations, ℓ is larger than the boundary layer thickness. The internal heating then bypasses the boundary layers and, in the absence of global rotation, leads to the mixing-length or "ultimate" scaling regime of turbulent heat transport (Lepot *et al.* (2018); Bouillaut *et al.* (2019)). As one cannot cool down the fluid using a cold plate without inducing a heat-transport-restricting upper boundary layer, we resort to "secular cooling" instead: in the absence of cooling and with insulating boundaries, the volume-averaged temperature grows linearly in time. However, the temperature difference between any two points inside the tank is governed by the equations of Boussinesq convection driven by the radiative heat source and effectively cooled at an equal and opposite rate by a uniform internal heat sink (see the introductory chapter for details). The schematic of the modified set-up can be seen in figure 3.1. The apparatus is mostly the same as in Lepot *et al.* (2018), except that the tank is now bound to a DC motor that drives rotation around the vertical axis of the cylindrical tank. This modification forbids using a standard measurement system consisting in two probes connected to a computer (unless using a rotating table). To avoid the use of such constraining equipment, we resort to remote, autonomous and wireless temperature probes described in the following.

3.1.1 Measurement system

The measurement system is composed of two groups of devices: two thermocouples measuring the temperature connected to an Arduino board that sends the data through WiFi to a second Arduino which saves them on an SD card (the two green boxes in figure 3.1).

Probing the fluid with thermocouples.

The temperature is measured using thermocouples. Those are temperature probes based on the thermoelectric properties of two metals welded together. The variation of temperature around the junction will create variations of the electric potential. This is known as the Seebeck effect and is widely documented in the literature. A

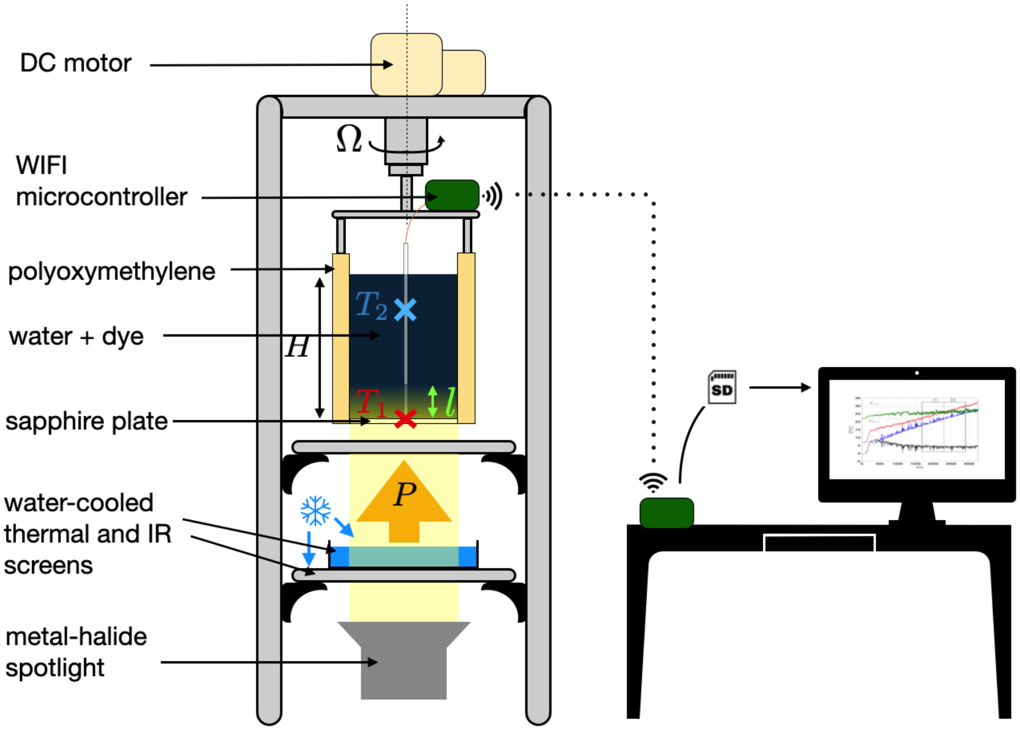

Figure 3.1: Schematics of the radiatively driven convection experiment.

thermocouple is composed of two junctions. The hot junction lies at the measurement location, while the cold junction is kept at a reference (or closely monitored) temperature, see figure 3.2. The temperature difference between the hot and cold junctions induces an electric potential difference ΔV through Seebeck effect. Different types of thermocouples can be found, identified by different letters, depending on the metals used to realize the junctions. They differ in range, solidity and cost. Here, we use type K thermocouples, the most common ones, which work well under 300°C. They are made of one wire of alumel, an alloy of nickel and aluminum, and a second wire of chromel, an alloy of chrome and nickel. It is worth noting that the hot junction is fragile and need to be handled with care to avoid rupture.

The Arduino micro-controller measures the potential difference and, simultaneously, the temperature at the cold junction with a PT100 probe (a resistive temperature probe made of platinum). The value of ΔV is related to the temperature difference $\Delta T_j = T_{hj} - T_{cj}$ by a linear function. The temperature of the hot junction, T_{hj}, is then the difference between ΔT_j and T_{cj}, with T_{cj} the temperature of the cold

Figure 3.2: Functional diagram of thermocouples.

junction measured by the PT100.
Depending on various factors, two thermocouples can give slightly different measurements. In convection though, we deal with temperature differences. As a result, we mostly need the thermocouples to give the same temperature in the same conditions. The calibration consists in placing the thermocouples close to each other in a tank containing 8 L of water at room temperature. We can thus estimate and correct for the slight offsets between the various probes. We checked that these offsets do not depend on temperature.

As visible in figure 3.3, two probes are used in the present experiment. One is located on the bottom plate ($z = 0$). The second probe is located at $z = 3H/4$, not too far away from the surface to measure the majority of the temperature drop, but not too close to the surface to avoid being polluted by any parasitic thermal leak. This choice will later be proven able to grasp the dynamics of extreme rotating convection regimes. To stabilize the location of the probes we use a thin ceramic pipe, in which we insert the probe that will be in contact with the bottom plate. The other probe is rolled around the ceramic, and fixed at the desired height.

As mentioned above, when dealing with a rotating experiment the first issue that arises is the impossibility to link any device to a fixed computer. Here we choose to use Arduino boards to design Wi-Fi temperature probes. Those are microcontrollers known for their modularity as one main board can support a superposition of multiple modules.

Arduino boards as acquisition devices.

We simultaneously use two Arduino boards, see figure 3.4: an Arduino MEGA and

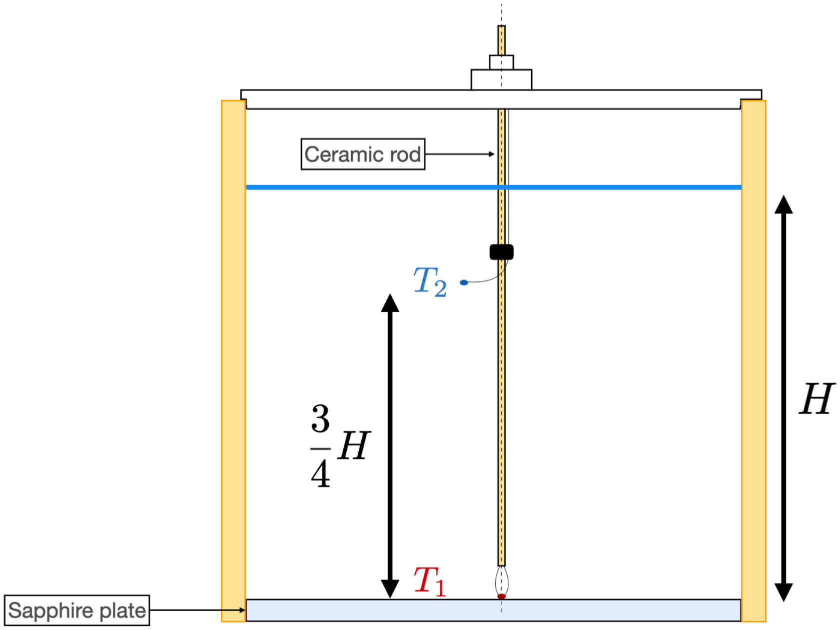

Figure 3.3: Schematic of the measurement system inside the tank

an Arduino UNO. Both are attached to a Wi-Fi module and a storage module.

The Arduino MEGA is the base for the temperature probes. Upon it, the thermocouple module is installed. This module is composed of 4 inputs into which can be plugged thermocouples of any kind. As it is rotating, its power supply has to be embedded. At first, we used 9V rechargeable batteries but it was difficult to know exactly when they were close to empty, and demanded a long time to be fully recharged. It was soon decided to switch for a more comfortable solution. The powerbanks used to charge cellphones are compatible with Arduino boards, and have the advantage of being easily and rapidly charged. The measurements are then sent to the other Arduino board through Wi-Fi.
The Arduino UNO receives the data and saves them to a text file, written on an SD card by a storage module. This board is also linked to an LCD screen which allows for live monitoring of the temperature inside the tank.

The Arduino boards are programmed using a proprietary eponymous software, based on a simplified version of C language. The main program runs in a never-ending loop. Within each loop, the Arduino emitter measures the voltages, uses the adequate function to determine the T_{hj}, and sends the measurements to the receiver. The receiver is programmed to wait until it receives a notification from the Wi-Fi module that data are arriving. Then, the program pauses until all the data are transmitted, before saving them on the SD card and displaying them on the LCD screen. The advantages of using Arduino boards are their limited cost, the profusion of tutorials that can be found on the internet, and their versatility.

To assess the accuracy of the measurement system, we present in figure 3.5 timeseries of temperature taken during the calibration of the thermocouples. The timeseries shows that, for a duration of 30 seconds with an acquisition frequency of 2Hz, the thermocouple is accurate within ±0.01°C. Indeed, the value given by the probes is mostly constant with some random incursions in a range of ±0.01°C, a signature of the finite numerical sampling. Now that the various components of the experiment have been introduced, we can see how they will be used and assembled in a protocol that gives robust experimental results.

3.2 Protocol

In this section, we recall the various dimensionless parameters. A distinction is made between the control parameters, specified at the outset of experimental runs, and the diagnostics, i.e., the dimensionless parameters based on measured data. We will then describe a typical experimental run, focussing on how the various parameters are extracted from the temperature measurements.

3.2.1 Defining and exploring the parameter space

The dimensionless numbers that characterize radiative convection have been described in chapters 1 and 2. We recall hereafter their definitions.

The dimensionless absorption length ℓ/H. This is the ratio between the absorption length ℓ of light in the fluid, and the height H of fluid inside the tank. For small values of ℓ, we heat up the fluid in the immediate vicinity of the bottom plate, in a similar fashion to the RB set-up. For larger values, we heat up the bulk turbulent flow directly, bypassing the boundary layers.
The Nusselt number $\mathrm{Nu} = \frac{PH}{\lambda \Delta T}$. It represents the ratio between the imposed radiative flux and the typical diffusive one associated with the temperature difference ΔT inside the fluid. It quantifies the efficiency of heat transport. As we impose the flux, a high value of Nu implies that a much smaller ΔT is sufficient to transfer the

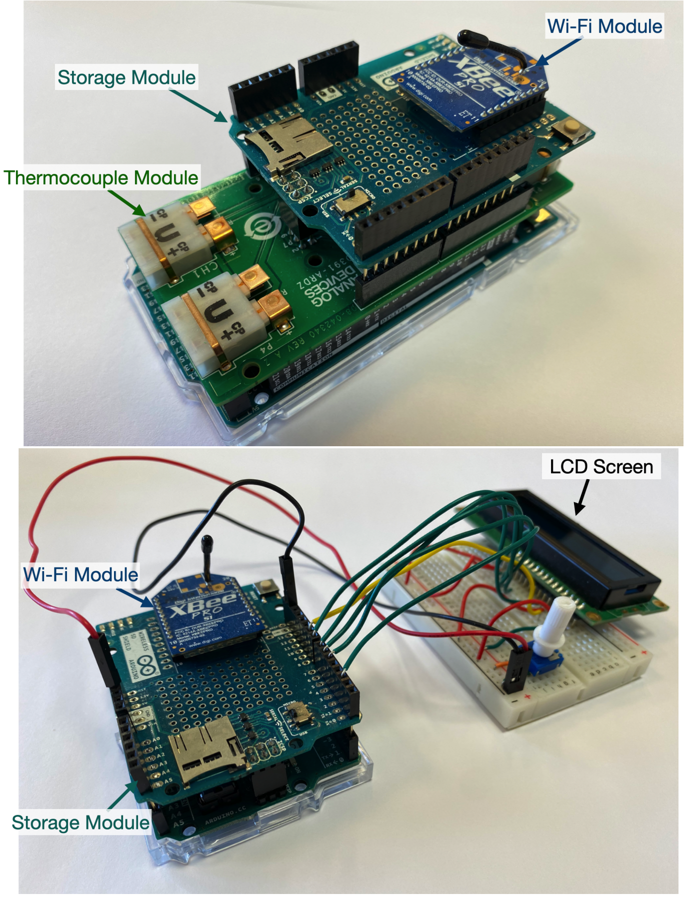

Figure 3.4: Photograph of the Arduino boards and their modules used to build remote temperature probes. On the top is the Arduino MEGA with attached modules and on the bottom is the Arduino UNO and its modules.

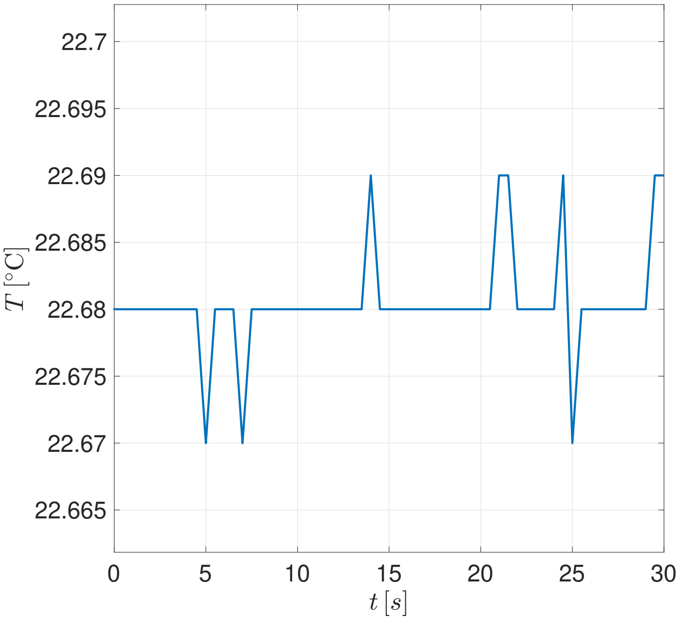

Figure 3.5: Timeseries of temperature measured by the combination of one type K thermocouple placed in a bucket of water at room temperature, and an Arduino.

flux than without convection.

The Prandtl number $\mathrm{Pr} = \frac{\nu}{\kappa}$. It compares the effect of viscous diffusion to thermal diffusion. At 20°C, the Prandtl number of water is equal to 7.

The Ekman number $\mathrm{E} = \frac{\nu}{2\Omega H^2}$. It describes the ratio of viscous forces to Coriolis forces, thus quantifying the importance of rotational effects on the dynamics of the system. The regime of rapid rotation corresponds to small Ekman number. Rotation has a stabilizing effect on thermal convection (Chandrasekhar (1961)), small values of E being characterized by reduced vertical motion and thus weaker convective transport. Rotation, through E, is also involved in the creation of new flow features: smaller flow structures in the horizontal directions and an Ekman boundary layer near the bottom solid boundary.

The Rayleigh number $\mathrm{Ra} = \frac{\alpha g \Delta T H^3}{\kappa \nu}$. It is the ratio between the buoyancy force characterized by ΔT, and the thermal and viscous dissipation that damp the fluid motion. While it is a control parameter widely used in standard RBC, it is an emergent (or diagnostic) parameter in the present experiment.

The flux-based Rayleigh number $\mathrm{Ra_P} = \mathrm{NuRa} = \frac{\alpha g P H^4}{\rho c_p \kappa^2 \nu}$. This parameter is not independent of Nu and Ra. In our experiment, the fluid is forced via the absorption of a light flux. We thus impose the total heat flux P, which makes Ra_P a control parameter.

In our experiment three dimensional parameters can be easily modified: the height H of fluid, the rotation rate Ω and the absorption length ℓ. The value of the input flux P depends on the power of the lamp. It cannot be easily modified by a large amount. In the following we always run the spotlight at maximum power to minimize the impact of parasitic thermal leaks (as compared to the input flux).
As seen in Bouillaut *et al.* (2019) for non rotating convection, the value of ℓ/H allows to transition continuously from the classical regime to the fully turbulent (or ultimate) regime of non-rotating convection. Here, we focus on $\ell/H = 0.024$ and $\ell/H = 0.048$ because, according to Bouillaut *et al.* (2019), both values lead to the fully turbulent regime of non-rotating convection.

With ℓ/H fixed and an approximately constant value of Pr, the parameter space to explore is defined by Ra_P and E. The main actor in the variation of those two dimensionless numbers is H, which appears at the power four in the definition of Ra_P and at the power -2 in the definition of E. Hence, H has been varied from 10 cm to 25 cm while Ω ranges from 2 rpm to 85 rpm. It leads to E varying from $\mathrm{E} = 2 \times 10^{-4}$ to $\mathrm{E} = 6.2 \times 10^{-7}$ and Ra_P from $\mathrm{Ra}_\mathrm{P} \simeq 2.5 \times 10^{10}$ to $\mathrm{Ra}_\mathrm{P} \simeq 9 \times 10^{11}$. The aim is to compute Nu by measuring the ΔT throughout the $(\mathrm{E}, \mathrm{Ra}_\mathrm{P})$ parameter space. As it is traditionally the main dimensionless number in RBC studies, we will also use the measured ΔT to build a temperature-based Rayleigh number.

3.2.2 Typical experimental run

An experimental run consists of the following steps: the water is taken from a thermal bath keeping it at 4°C. We fill the tank with the cold water, and mix it with carbon-black dye to obtain the aforementioned values of l. After stirring, the water is around 7°C and the tank is set into uniform rotation at a rate Ω. After an initial spin-up period, for the fluid to achieve solid body rotation, the 2500W metal-halide spotlight is turned on. At start-up, the projector goes through a transitory phase where it blinks. To ensure that only constant light flux is considered as thermal initial condition we put an opaque screen between the lamp and the tank. It is a plate covered with aluminum sheet to avoid any absorption of light. After 2 minutes the light flux is constant and the plate is removed. At the same time we turned on the spotlight, we switch on the Arduino micro-controller measuring the temperature signal of two thermocouples horizontally centered inside the tank, hence giving access to the temperature at heights $z = 0$ and $z = 3H/4$, with z the vertical coordinate. The temperature signals are transmitted through Wi-Fi to a second Arduino microcontroller, which allows for live monitoring of the signals.

3.2.3 Processing the data

Figure 3.6 shows a timeseries of the temperature for an experimental run with $H = 25\,\mathrm{cm}$ and $\Omega = 30\,\mathrm{rpm}$. This timeseries shows different features of the flow. First, for $t < 1500\,\mathrm{s}$ the system is in a transient phase. The duration of this phase increases with the rotation rate. After the transient, for $t > 1500\,\mathrm{s}$, the system settles in a quasi-stationary state characterized by a linear drift of the two timeseries at an equal rate. This is a particularity of the present experimental set-up. As explained in the first chapter, we do not cool down the fluid. Hence, the temperature inside the tank increases linearly with time. This linear drift of temperature can be seen in figure 3.6. Analytically, this drift, defined as the temporal evolution of the spatially-averaged temperature $\overline{T}(t)$, can be related to the flux P by integrating the heat equation over space, using the insulating boundary conditions. It leads to the following relation:

$$d_t\overline{T} = \frac{P}{\rho c_p H}, \tag{3.1}$$

where $d_t\overline{T}$ is obtained experimentally as the slope of the timeseries of temperature. Hence, the fact that both timeseries are parallel is an indication that the heat losses are negligible in this time interval, as they experience the same temperature drift although being located at different heights. Hence, the dimensionless parameters are computed over this window, where both timeseries are parallel.

The measurement window is delimited by the black rectangle in figure 3.6, within which both timeseries of temperature are parallel. To compute the dimensionless parameters we need the temperature difference ΔT and the heat flux P.
The former is straightforward to obtain. We first subtract the signals received by the two probes leading to $T_1(t) - T_2(t)$, the black curve in figure 3.6. Then, we take as our characteristic temperature drop $\Delta T = \langle T_1(t) - T_2(t)\rangle_t$, with $\langle\,\cdot\,\rangle_t$ the time-average of the temperature difference.
The latter is computed using (3.1). We compute P using $T_1(t)$ and $T_2(t)$ by taking the mean value of the slope of both timeseries. The value of P suffers slight variations between experimental runs as it is impacted by external factors, such as the

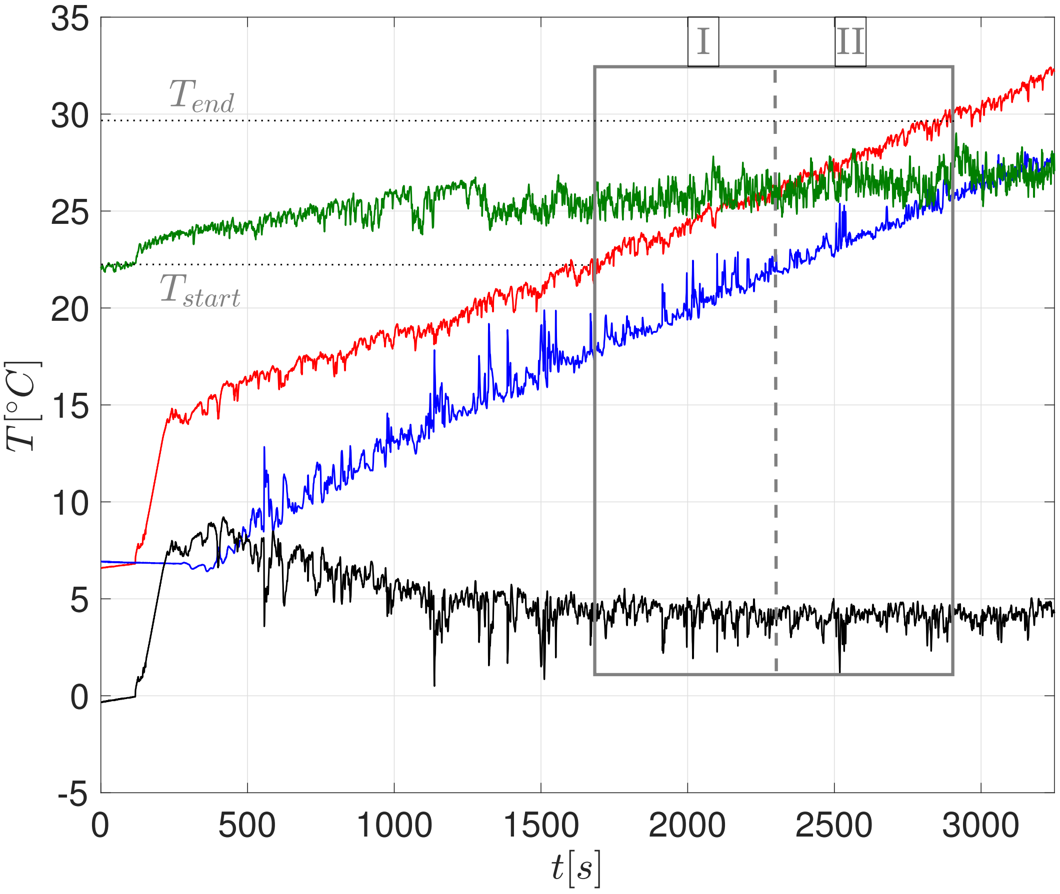

Figure 3.6: Timeseries of both temperature probes T_1 and T_2 in red and blue, respectively, and of room temperature in green. The signal in black $T_1 - T_2$. Timeseries for the experimental run with $H = 25\,\mathrm{cm}$, $\Omega = 30\,\mathrm{rpm}$ and $l/H = 0.048$.

transparency of the windows and IR filtering tank between the light source and the fluid, or the age of the light bulb.

Now that we have ΔT and P, we are almost ready to compute the dimensionless numbers. Indeed, all the parameters of the fluid, such as ν or κ, vary slightly with temperature. Those parameters are typically reported for a temperature of 20° C. Here, the measurement window spans temperature intervals that can be as large as ±5° C. For that reason we compute the various fluid properties using the mean value of T_1 over the boxed time interval as a reference. This way, the variation of the fluid parameters with temperature is taken into account. We are finally able to compute the dimensionless numbers. To quantify the error associated with the slow drift in the values of the fluid properties, we also compute the previous parameters on both halves of the measurement window. The values of the dimensionless numbers for the first and second halves can be found in the appendix with the subscript I and II, respectively. These values will serve as error bars in the figures of the next section.

3.3 Results

The experimental protocol provides one main diagnostic, the Nusselt number and three control parameters: $\mathrm{Ra_P}$, E and Pr (the latter ranging from 4 to 6 over the entire data set). For constant H, $\mathrm{Ra_P}$ is approximately a constant and the study consists in measuring Nu for different values of E. The most natural way of showing our results is to plot Nu as a function of E for different $\mathrm{Ra_P}$. Then, with the goal of determining whether the flow is turbulent enough to yield a diffusivity-free scaling regime, we build composite dimensionless numbers independent of the diffusivity coefficients. This way, we will show that our experiment achieves the geostrophic turbulence scaling regime of rapidly rotating convection, defined in the introductory chapter as:

$$\mathrm{Nu} = \mathcal{C}_{\mathrm{Ra}} \times \mathrm{Ra}^{3/2}\mathrm{E}^{2}\mathrm{Pr}^{-1/2}, \tag{3.2}$$

Or, in terms of the control parameter of our experiment:

$$\mathrm{Nu} = \mathcal{C} \times \mathrm{Ra_P}^{3/5}\mathrm{E}^{4/5}\mathrm{Pr}^{-1/5}, \tag{3.3}$$

with $\mathcal{C}$ and $\mathcal{C}_{\mathrm{Ra}}$ two dimensionless prefactors.

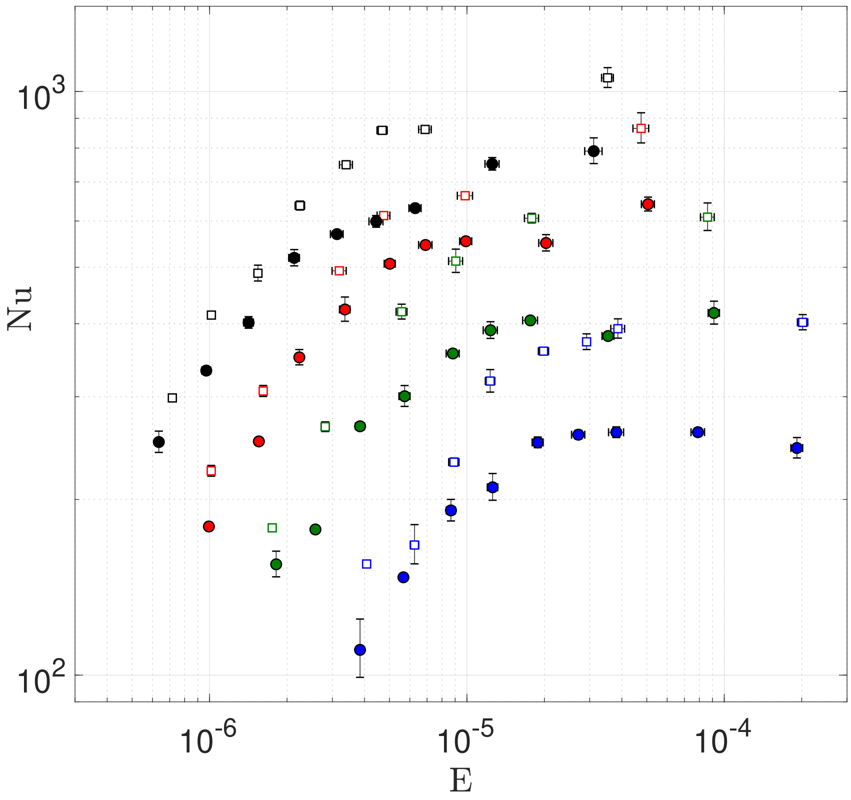

Figure 3.7: Nusselt as a function of Ekman for $l/H = 0.048$, empty squares, and $l/H = 0.024$, filled circles for multiple fluid heights: blue, $H = 10\,\mathrm{cm}$, $\mathrm{Ra_P} \simeq 2.5 \times 10^{10}$; green, $H = 15\,\mathrm{cm}$, $\mathrm{Ra_P} \simeq 1.3 \times 10^{11}$; red, $H = 20\,\mathrm{cm}$, $\mathrm{Ra_P} \simeq 3.5 \times 10^{11}$; black, $H = 25\,\mathrm{cm}$, $\mathrm{Ra_P} \simeq 9 \times 10^{11}$.

3.3.1 Nusselt versus Ekman

Figure 3.7 is a direct representation of the raw data. It clearly shows that, as E decreases, so does Nu. We can see that, for the largest value of E, i.e. for the lowest rotation rates, Nu does not vary. It is particularly true for $H = 10\,\mathrm{cm}$ and $l/H = 0.024$ (the blue circles), where Nu starts decreasing with E only for $\mathrm{E} < 2 \times 10^{-5}$ ($\Omega = 20\,\mathrm{rpm}$). For higher values of $\mathrm{Ra_P}$, i.e. other colors, the threshold E for the system to be affected by rotation decreases, meaning that a higher rotation rate is required.

Unfortunately, we cannot easily infer a scaling law from figure 3.7 as it combines slightly different values of Pr and $\mathrm{Ra_P}$. To assess whether or not we observe the geostrophic turbulence regime of rapidly rotating convection, we first need to verify if the flow is indeed turbulent.

3.3.2 A diffusivity-free representation

The dimensionless numbers used in the previous representation, Nu, Ra and E, involve the diffusivity coefficients. With the goal of establishing the turbulent nature of the flow by assessing the independence of its transport properties with respect to the molecular diffusivities, we form ν- and κ-independent reduced dimensionless numbers. We thus combine the dimensionless numbers to build a diffusivity-free Nusselt number and a diffusivity-free Rayleigh number.

The diffusivity-free Nusselt number $\mathcal{N}$. To find $\mathcal{N} = f(\mathrm{Nu}, \mathrm{E}, \mathrm{Pr})$ that cancels ν and κ there is only one possibility:

$$\mathcal{N} = \mathrm{NuEPr}^{-1} \tag{3.4}$$

Hence, we have a ν- and κ-independent Nusselt number that depends on both the flux P and the rotation rate Ω.

The diffusivity-free Rayleigh number Ra_*. As for the Nusselt number, it is possible to find a ν- and κ-independent combination $\mathrm{Ra}_* = f(\mathrm{Ra}, \mathrm{E}, \mathrm{Pr})$:

$$\mathrm{Ra}_* = \mathrm{RaE}^2\mathrm{Pr}^{-1} \tag{3.5}$$

This diffusivity-free Rayleigh number can be connected to the literature by noticing that it is the square of the temperature-based convective Rossby number used by Aurnou *et al.* (2020). Nevertheless, as ΔT is not our control parameter, it will only be used to make comparisons with the literature.

The diffusivity-free flux-based Rayleigh number $\mathcal{R}$. As for the other composite dimensionless parameters, we want to find $\mathcal{R} = f(\mathrm{Ra_P}, \mathrm{E}, \mathrm{Pr})$ to suppress the effect of ν and κ. The solution is the following:

$$\mathcal{R} = \mathrm{Ra_P E^3 Pr^{-2}} \tag{3.6}$$

This combination is the only dimensionless control parameter if the diffusivities are to play no roles (Christensen (2002); Christensen & Aubert (2006); Schmitz & Tilgner (2009)).

With those new dimensionless parameters the data should collapse on a master curve if the flow is fully turbulent and achieves diffusivity-free scaling. In figure 3.8 we plot

$\mathcal{N}$ as a function of $\mathcal{R}$. We see that, by choosing parameters independent of the diffusivities, the data, for $\ell/H = cst$, collapse on a single curve for high E, when rotation is weak compared to other phenomena, as well as for low E, when rotation impacts significantly the dynamics of the flow. This is a proof that our experiment, already able to achieve a diffusivity-free non rotating regime, can reach a diffusivity-free rapidly rotating regime. We can identify three areas: two regions with a very good collapse connected by a transition zone with slightly more scatter.

3.3.3 First experimental observation of the geostrophic turbulence regime of rapidly rotating convection

In the region where E is very low, the strong collapse of the data shows that the first criterion mentioned earlier for the observation of the geostrophic turbulence regime of convection is satisfied: this experimental set-up achieves a turbulent rotating regime where the diffusion coefficients do not intervene in the relation between the heat flux P and the temperature drop ΔT. We now take a close look at the exponent β that can be extracted from the data. We know that, in an $\mathcal{N} \sim \mathcal{R}^{\beta}$ representation, the geostrophic turbulence regime of convection is characterized by the following scaling law:

$$\mathcal{N} \sim \mathcal{R}^{3/5} \tag{3.7}$$

$$\mathrm{NuEPr}^{-1} \sim \left(\mathrm{Ra_P E^3 Pr^{-2}}\right)^{3/5} \tag{3.8}$$

The exponent β characterizing the geostrophic turbulence regime of turbulent convection is thus 3/5.

We used "ezyfit", a free third party addon for MatLab, to fit the rapidly rotating data. We focus on two ranges of $\mathcal{R}$: $\mathcal{R} \lesssim 3 \times 10^{-7}$ and $\mathcal{R} \lesssim 10^{-7}$. The best fit exponents $\mathcal{N} \sim \mathcal{R}^{\beta}$ are reported in Table 3.1. For $\ell/H = 0.048$, we obtain $\beta = 0.57 \pm 0.01$ and $\beta = 0.62 \pm 0.01$ for $\mathcal{R} \lesssim 3 \times 10^{-7}$ and $\mathcal{R} \lesssim 10^{-7}$, respectively. The $\ell/H = 0.024$ case gives $\beta = 0.59 \pm 0.01$ and $\beta = 0.57 \pm 0.03$. For both ℓ/H we obtain exponents within 5% of the theoretical exponent 3/5. The observation of this regime is also visible in Figure 3.9, where we plot the compensated parameter $\mathcal{N}/\mathcal{R}^{3/5}$ as a function of $\mathcal{R}$. The figure shows the existence of a plateau for $\mathcal{R} \lesssim 3 \times 10^{-7}$. The reader may be more accustomed to representations involving the temperature-based Rayleigh number. In terms of the diffusivity-free Rayleigh number, the scaling law of the geostrophic turbulence regime of rapidly rotating convection becomes:

$$\mathcal{N} \sim \mathrm{Ra_*}^{3/2} \tag{3.9}$$

β	$\mathcal{R} \lesssim 3 \times 10^{-7}$	$\mathcal{R} \lesssim \times 10^{-7}$
$\ell/H = 0.024$	0.59 ± 0.01	0.57 ± 0.03
$\ell/H = 0.048$	0.57 ± 0.01	0.62 ± 0.01

Table 3.1: Best fit exponents of the scaling law $\mathcal{N} \sim \mathcal{R}^{\beta}$ for the data in Figure 3.8. The error on the exponent is estimated by propagating the error on $log\mathcal{N}$ into a standard deviation for the exponent.

In figure 3.10 we plot the data using this representation. As in the previous figure, the experimental points collapse on a master curve. For high rotation rates the exponent increases to 3/2, in agreement with the geostrophic turbulence regime of rotating convection. The previous 5% discrepancy in β for the flux-based representation translates in a ΔT-based representation into exponents within 12% of the theoretical value 3/2.

We saw in a previous chapter that the exponent derived in a system dominated by the boundary layers, as in a RB configuration, is $\beta \sim 3$, very different from the exponent measured here. Radiative forcing bypasses the boundary layers and injects the heat flux directly into the bulk. This innovative way of forcing a convective instability has, again, proved to be one of the few to achieve extreme turbulent regimes of convection. As a result, this set-up provides experimental observations in excellent agreement with the geostrophic turbulence scaling regime of rapidly rotating turbulent convection.

When we decrease the rotation rate we recover a familiar regime of turbulent convection already encountered in Lepot *et al.* (2018) and Bouillaut *et al.* (2019), and discussed in the following.

The high E **region** :

This region is characterized by a flow which does not feel the effect of rotation. Hence we expect to recover a regime where Ω plays no role. for non rotating convection, the scaling law of the fully turbulent regime is $\mathrm{Nu} \sim \sqrt{\mathrm{RaPr}}$ for a fixed value of ℓ/H. With our set of parameters it becomes:

$$\mathcal{N} \sim \mathrm{Ra_*}^{1/2} \tag{3.10}$$

or in a flux-based set of parameters,

$$\mathcal{N} \sim \mathcal{R}^{1/3} \tag{3.11}$$

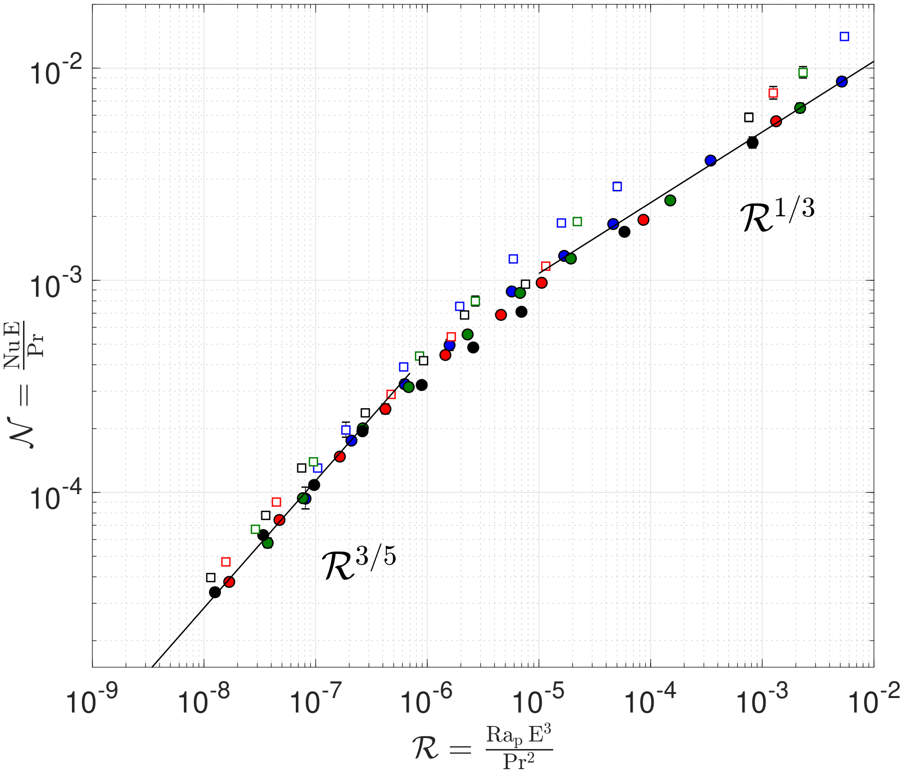

Figure 3.8: Representation of the data in terms of the diffusivity free parameters $\mathcal{N}$ and $\mathcal{R}$. The symbols are the same as Figure 3.7. The solid black lines correspond to the scaling laws expected in the rapidly rotating regime, $\mathcal{N} \sim \mathcal{R}^{3/5}$, and in the non-rotating regime, $\mathcal{N} \sim \mathcal{R}^{1/3}$.

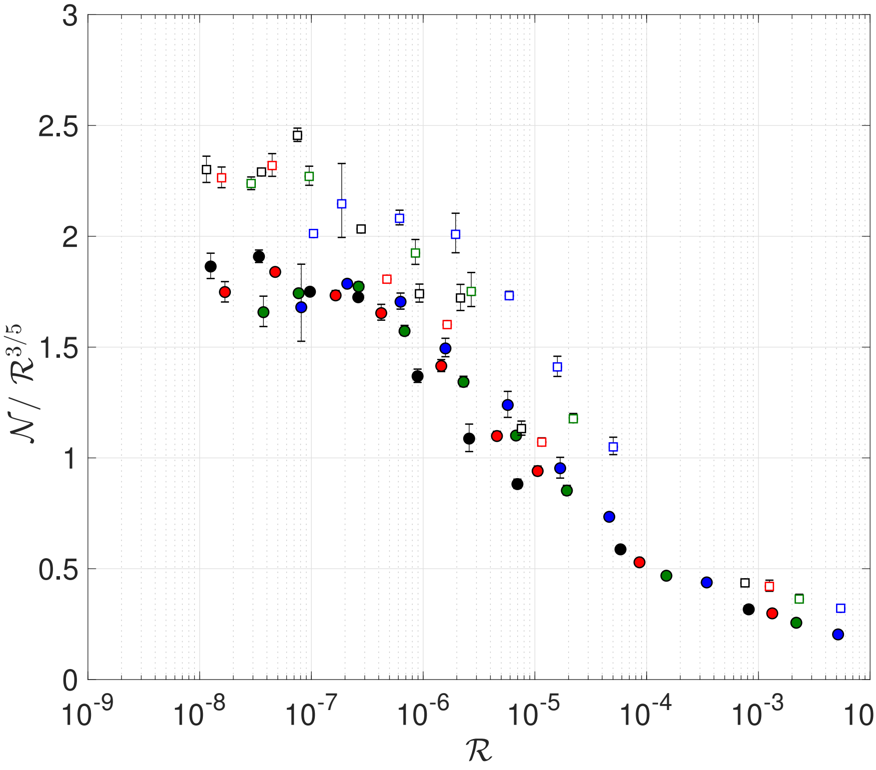

Figure 3.9: Representation of the data compensated by the prediction for the geostrophic turbulence regime $\mathcal{R}^{3/5}$. The symbols are the same as Figure 3.7.

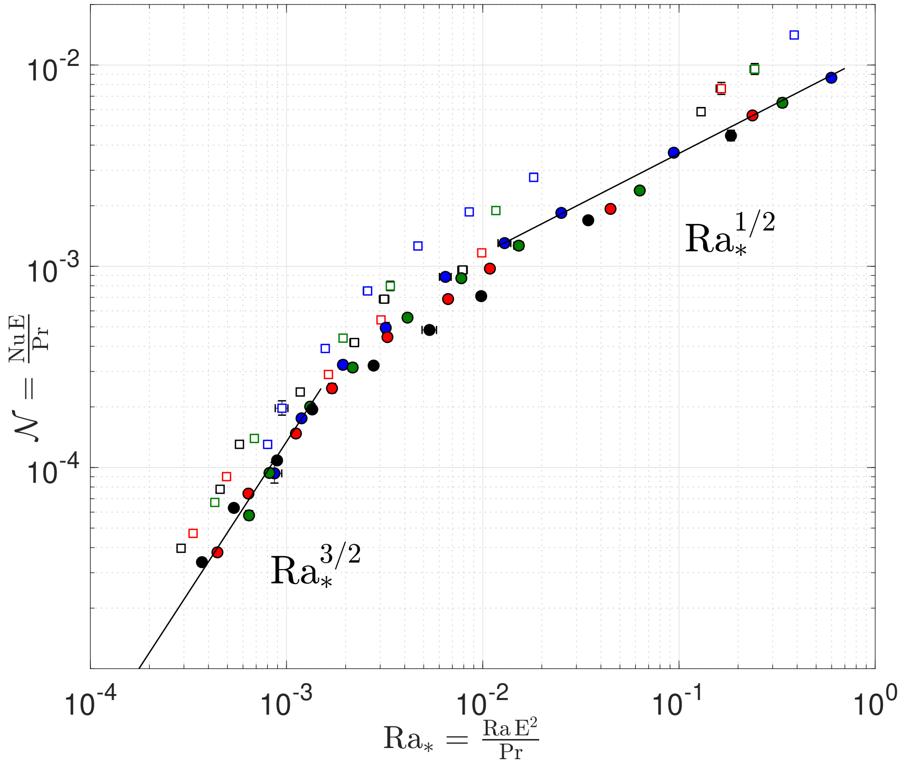

Figure 3.10: Representation of the data in terms of the diffusivity free parameters $\mathcal{N}$ and Ra_*. The symbols are the same as Figure 3.7. The solid black lines correspond to the scaling laws expected in the rapidly rotating regime, $\mathcal{N} \sim {\mathrm{Ra}_*}^{3/2}$, and in the non-rotating regime, $\mathcal{N} \sim {\mathrm{Ra}_*}^{1/2}$.

The scaling law (3.11) is visible on Figure 3.8. For $\ell/H = 0.024$ the data at high E are fully compatible with an exponent $\beta = 1/3$. It shows that we recover the ultimate regime of convection when the rotation rate is low. For $\ell/H = 0.048$ it seems that the data are close to reaching the non-rotating regime but the transition is delayed as compared to $\ell/H = 0.024$.

3.4 Discussion

The heat transport efficiency measured in the present experiment is significantly greater than the one reported in the idealized numerical setups of Barker *et al.* (2014), Stellmach *et al.* (2014) and Julien *et al.* (2012) in Cartesian geometry, and in Gastine *et al.* (2016) in spherical geometry: the experimentally measured value of the prefactor $\mathcal{C}$ is approximately twice as large as the value extracted from Barker *et al.* (2014), it is six times greater than the value reported in Julien *et al.* (2012) and three times larger than the value reported in Gastine *et al.* (2016) (the latter in spherical geometry). In terms of the prefactor appearing in the scaling-law (3.2), this translates respectively into an experimentally measured $\mathcal{C}_{\mathrm{Ra}}$ that is approximately six times greater than the value extracted from Barker *et al.* (2014), sixty times greater than the value reported in Julien *et al.* (2012), and twenty times greater than the value reported in Gastine *et al.* (2016). This points to an unexpected sensitivity of the heat transport efficiency of rapidly rotating turbulent convection to the precise spatial distribution of heat sources and sinks. We confirmed this conclusion experimentally by doubling the value of the absorption length ℓ/H, from $\ell/H = 0.024$ to $\ell/H = 0.048$: this change in the geometry of the heat source leads to an increase in the prefactor $\mathcal{C}$ by approximately 30%, and an approximate doubling of the prefactor $\mathcal{C}_{\mathrm{Ra}}$. Beyond the observation of the geostrophic turbulence heat transport scaling-law (3.3), our laboratory setup thus offers a unique experimental opportunity to determine the dependence of the prefactor on the distribution of heat sources and sinks, which greatly varies from planets to stars.

When dealing with rapidly rotating experiments, centrifugal effects are one of the most important limitation preventing from achieving extreme rotation rates in a laboratory experiment. The strength of the centrifugal term is characterized by a dimensionless number defined in Horn & Aurnou (2018) (see also Horn & Aurnou (2019, 2021)) as $\Omega^2 H/g$. In this article, they evaluate the threshold for centrifugal acceleration to be negligible as $\Omega^2 H/g \lesssim 1$. The exact value of this threshold has been debated in the literature. Indeed, Cheng *et al.* (2020) observed that experimental measurements made for $\Omega^2 H/g \lesssim 2$ remain unaffected by centrifugal acceleration. In the present study this ratio never exceeds two, with only three data points for which this ratio exceeds one (per value of ℓ/H). The non-dominance of centrifugal effects in the present experiment is also shown by the good collapse of the data in various figures presented here-above. The different data points have been made at various centrifugal ratios. The collapse of all those points on a master curve would not have been possible if centrifugal effect were dominant.

To confirm the absence of centrifugal effects we performed 3D Direct Numerical Simulations (DNS). As DNS simulate an idealized system, they are a powerful tool to assess the existence of some experimental biases. In addition to centrifugal effects they also do not take into account non-Boussinesq effects and wall modes. The latter are convective modes that arise near the vertical walls with a lower onset value than the bulk modes (see Buell & Catton (1983); Zhong *et al.* (1991); Ecke *et al.* (1992); Favier & Knobloch (2020)). Even if their impact on the bulk heat transport has been shown to be negligible (de Wit *et al.* (2020)), DNS can be used to assess their sub-dominance. We used the pseudo-spectral code CoRal (Miquel (2021)) to simulate the present radiatively driven set-up, i.e. radiative heating and uniform cooling with a no-slip boundary condition at the bottom and stress-free at the top. The sidewalls are replaced by periodic boundary conditions in the numerical set-up. The various data points have been made for a fixed flux-based Rayleigh number with varying Ekman number for $\ell/H = 0.048$. Figure 3.11 shows that the numerical points are in excellent agreement with the experimental data (Nusselt number slightly larger than its experimental counterpart certainly due to the different geometry). It confirms that this experimental set-up is not affected by centrifugal acceleration nor wall modes, validating the first observation of the geostrophic turbulence regime of rotating convection.

3.5 Conclusion

We have shown that the radiatively forced convection experiment can achieve extreme regimes of rotating convection by bypassing the thermal boundary layers. The absorption of light by the dyed fluid leads to internal heating over a depth tunable through the concentration of dye. This configuration had already proven able to achieve turbulent regimes of non-rotating convection, and the idea behind the present thesis was to gradually add rotation to study the impact of this key feature of geophysical and astrophysical systems.

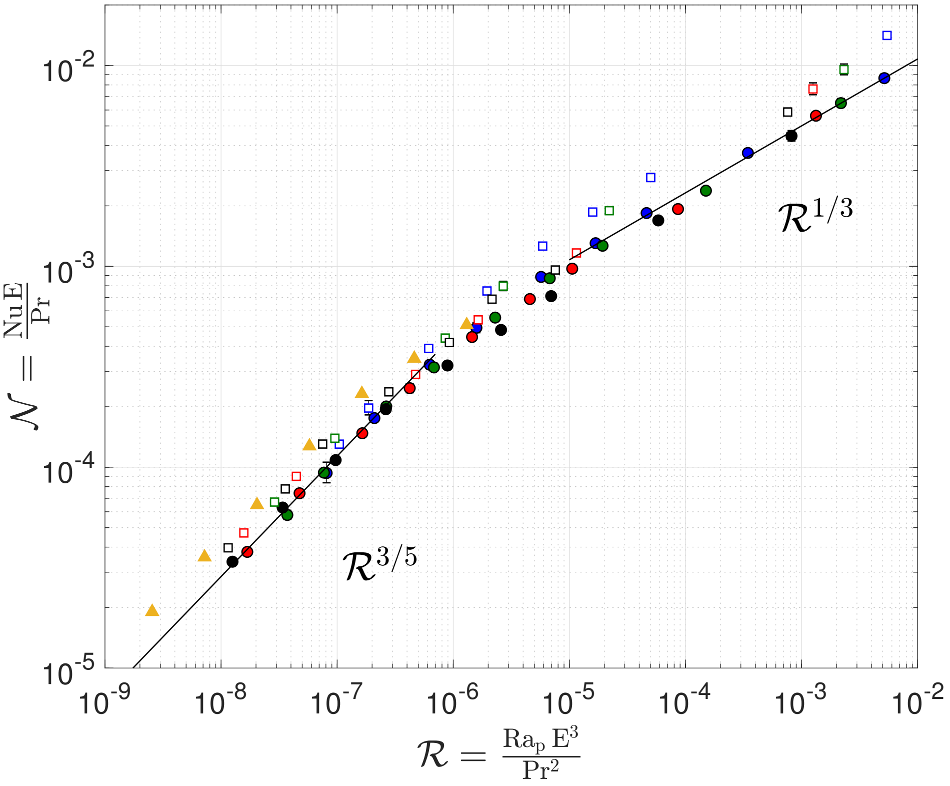

Figure 3.11: Representation of the data in terms of the diffusivity free parameters $\mathcal{N}$ and $\mathcal{R}$. The symbols are the same as Figure 3.7. The filled triangles are 3D DNS data for $\ell/H = 0.048$. The solid black lines correspond to the scaling laws expected in the rapidly rotating regime, $\mathcal{N} \sim \mathcal{R}^{3/5}$, and in the non-rotating regime, $\mathcal{N} \sim \mathcal{R}^{1/3}$.

Modifying and conducting the experiment has represented the main work of the present thesis. This work culminated with the observation of the scaling law $\mathcal{N} \sim (\mathcal{R})^{3/5}$, a signature of the geostrophic turbulence regime of rapidly rotating convection. It is the first experimental realization of this regime, which is extreme in more than one way. It simultaneously demands to rotate rapidly and keep the system in a turbulent state while avoiding the parasitic effects that arise when rotation is too fast. Satisfying both conditions is difficult because rotation tends to lower the velocities of the system, giving the opportunity to the diffusion coefficients to come back into the scaling relation between the flux and the temperature difference.

Bibliography

AURNOU, JONATHAN M., HORN, SUSANNE & JULIEN, KEITH 2020 Connections between nonrotating, slowly rotating, and rapidly rotating turbulent convection transport scalings. *Phys. Rev. Research* **2**, 043115.

BARKER, A. J., DEMPSEY, A. M. & LITHWICK, Y. 2014 Theory and simulations of rotating convection. *Astrophys. J.* **791** (1), 13.

BOUILLAUT, V., LEPOT, S., AUMAÎTRE, S. & GALLET, B. 2019 Transition to the ultimate regime in a radiatively driven convection experiment. *J. Fluid Mech.* **861**, R5.

BUELL, J. C. & CATTON, I. 1983 The Effect of Wall Conduction on the Stability of a Fluid in a Right Circular Cylinder Heated From Below. *Journal of Heat Transfer* **105** (2), 255–260.

CHANDRASEKHAR, S. 1961 *Hydrodynamic and Hydromagnetic Stability*. Dover Publications.

CHENG, JONATHAN S., MADONIA, MATTEO, AGUIRRE GUZMÁN, ANDRÉS J. & KUNNEN, RUDIE P. J. 2020 Laboratory exploration of heat transfer regimes in rapidly rotating turbulent convection. *Phys. Rev. Fluids* **5**, 113501.

CHRISTENSEN, U. R. 2002 Zonal flow driven by strongly supercritical convection in rotating spherical shells. *Journal of Fluid Mechanics* **470**, 115–133.

CHRISTENSEN, U. R. & AUBERT, J. 2006 Scaling properties of convection-driven dynamos in rotating spherical shells and application to planetary magnetic fields. *Geophysical Journal International* **166** (1), 97–114, arXiv: https://academic.oup.com/gji/article-pdf/166/1/97/5891407/166-1-97.pdf.

ECKE, R. E, ZHONG, FANG & KNOBLOCH, E 1992 Hopf bifurcation with broken reflection symmetry in rotating rayleigh-bénard convection. *Europhys. Letters* **19** (3), 177–182.

FAVIER, BENJAMIN & KNOBLOCH, EDGAR 2020 Robust wall states in rapidly rotating rayleigh-bénard convection. *Journal of Fluid Mechanics* **895**, R1.

GASTINE, THOMAS, WICHT, JOHANNES & AUBERT, JULIEN 2016 Scaling regimes in spherical shell rotating convection. *Journal of Fluid Mechanics* **808**, 690–732.

HORN, SUSANNE & AURNOU, JONATHAN M. 2018 Regimes of coriolis-centrifugal convection. *Phys. Rev. Lett.* **120**, 204502.

HORN, SUSANNE & AURNOU, JONATHAN M. 2019 Rotating convection with centrifugal buoyancy: Numerical predictions for laboratory experiments. *Phys. Rev. Fluids* **4**.

HORN, SUSANNE & AURNOU, JONATHAN M. 2021 Tornado-like vortices in the quasi-cyclostrophic regime of coriolis-centrifugal convection. *Journal of Turbulence* **22** (4-5), 297–324.

JULIEN, KEITH, KNOBLOCH, EDGAR, RUBIO, ANTONIO M. & VASIL, GEOFFREY M. 2012 Heat transport in low-rossby-number rayleigh-bénard convection. *Phys. Rev. Lett.* **109**, 254503.

LEPOT, S., AUMAÎTRE, S. & GALLET, B. 2018 Radiative heating achieves the ultimate regime of thermal convection. *Proc. Natl. Acad. Sci.* **115** (36), 8937–8941.

MIQUEL, BENJAMIN 2021 Coral: a parallel spectral solver for fluid dynamics and partial differential equations. *submitted to JOSS* .

SCHMITZ, S. & TILGNER, A. 2009 Heat transport in rotating convection without ekman layers. *Phys. Rev. E* **80**, 015305.

STELLMACH, S., LISCHPER, M., JULIEN, K., VASIL, G., CHENG, J. S., RIBEIRO, A., KING, E. M. & AURNOU, J. M. 2014 Approaching the asymptotic regime of rapidly rotating convection: Boundary layers versus interior dynamics. *Phys. Rev. Lett.* **113**, 254501.

DE WIT, XANDER M., GUZMÁN, ANDRÉS J. AGUIRRE, MADONIA, MATTEO, CHENG, JONATHAN S., CLERCX, HERMAN J. H. & KUNNEN, RUDIE P. J. 2020 Turbulent rotating convection confined in a slender cylinder: The sidewall circulation. *Phys. Rev. Fluids* **5**, 023502.

Zhong, Fang, Ecke, Robert & Steinberg, Victor 1991 Asymmetric modes and the transition to vortex structures in rotating rayleigh-bénard convection. *Phys. Rev. Lett.* **67**, 2473–2476.

Chapter 4

Velocity-informed upper bounds and fully turbulent assumption in non-rotating radiatively driven convection

We focus here on the non-rotating radiatively driven convection setup. It has been presented in the introductory chapter of the present thesis. For more information about the differences between the Rayleigh-Bénard (RB) set-up and the radiatively driven one and the definition of the dimensionless numbers, the reader is referred to the first chapter of this manuscript.

The relation between the heat transport efficiency, i.e., the **Nusselt number** Nu, and the dimensionless temperature difference, i.e., the **Rayleigh number** Ra, takes the form of the general scaling law:

$$\mathrm{Nu} \sim \mathrm{Ra}^{\gamma}. \tag{4.1}$$

At the level of applied mathematics, one may hope to capture the mixing-length exponent $\gamma = 1/2$ of for non-rotating convection driven by internal heat sources and sinks (CISS) through the derivation of rigorous upper bounds on the Nusselt number, an approach pioneered by Howard (1963), Busse (1969), and Doering & Constantin (1996). For the RB setup, this approach leads to upper bounds of the form $\mathrm{Nu} \leq \mathit{const}.\mathrm{Ra}^{1/2}$, i.e., they are characterized by a mixing-length-like scaling exponent $\gamma = 1/2$ greater than the exponent inferred from experiments and DNS.

The natural question then is whether the exponent $\gamma = 1/2$ of CISS corresponds to a maximization of the Nusselt number subject to simple constraints. The PhD work of Simon Lepot answered this question in the negative with upper bounds exhibiting laminar asymptotic flow solutions of CISS characterized by a heat transport efficiency $\mathrm{Nu} \sim \mathrm{Ra}$, exceeding the mixing-length scaling exponent. Although the two are perfectly compatible at the mathematical level, there is a discrepancy between the behavior of upper bounds, which are controlled by unstable (in 3D) laminar solutions with a heat transport exponent $\gamma = 1$, and the seemingly turbulent flows achieved in the laboratory and in 3D DNS, characterized by a mixing-length heat transport exponent $\gamma = 1/2$. In other words, it seems that the turbulent nature of the flow has a profound impact on its transport properties. In the following, we confirm this statement in a precise mathematical sense. We show that restrincting attention to fully turbulent flow solutions further constrains the exponent γ.

Anticipating the precise definitions in section 4.1, we denote the velocity field as $\mathbf{u}(x, y, z, t)$, the kinematic viscosity as ν, the domain height as H, and a spatio-temporal average over the entire fluid domain with angular brackets. The dissipation coefficient $\mathcal{C}$ is then defined as:

$$\mathcal{C} = \frac{H\nu\langle|\nabla\mathbf{u}|^2\rangle}{\langle\mathbf{u}^2\rangle^{3/2}}\,. \tag{4.2}$$

The zeroth-law of turbulence Frisch (1995) states that the dissipation coefficient admits a nonzero finite limit for asymptotically large Reynolds number. In the present context, we thus define a 'fully turbulent branch of solutions' as a continuous family of solutions indexed by $\mathrm{Ra_P}$ that admits a finite nonzero limit of the dissipation coefficient for asymptotically large $\mathrm{Ra_P}$:

$$\text{Fully turbulent branch of solutions} \iff \lim_{\mathrm{Ra_P}\to\infty} \mathcal{C} = \mathcal{C}_\infty > 0. \tag{4.3}$$

While we cannot prove the very existence of such turbulent branches of solutions, one can assume that such a branch of solutions exists – an assumption referred to as the 'fully turbulent' assumption in the following – and address motivational questions at the crossroad of applied mathematics and physics:

- At the mathematical level, can one use information (or assumptions) about the velocity field to improve the upper bound on convective heat transport? Does CISS maximize the heat transport subject to simple constraints, when supplemented with the 'fully turbulent' assumption?
- At the physical level, can we validate this fully turbulent assumption using experimental and numerical data? Does the velocity field obey the free-fall

scaling-law put forward by Spiegel to derive the mixing-length heat transport scaling-law (Spiegel (1963, 1971))?

In section 4.1, we derive rigorous upper bounds on the Nusselt number in terms of the Rayleigh number and the dissipation coefficient. Assuming that a fully turbulent branch of solutions exists, according to the definition above, we show that the Nusselt number cannot increase faster that the square-root of the Rayleigh number over this branch of solutions. In other words, we show that the upper bound $\mathrm{Nu} \lesssim \sqrt{\mathrm{Pr\ Ra}}$ holds for CISS if one restricts attention to fully turbulent solutions. By contrast, laminar flows can realize $\mathrm{Nu} \sim \mathrm{Ra}$, as established in Miquel *et al.* (2019), and we derive an upper bound on the Nusselt number valid for all flow solutions that reproduces this 'laminar' scaling behavior. In section 4.2 we turn to DNS and experimental realizations of CISS to establish the fully turbulent nature of the flow. We report numerical and experimental data pointing to a nonzero limiting value of the dissipation coefficient for increasingly large Ra_P.

4.1 Velocity-informed upper bounds

The computation of the bound was done by Benoît Flesselles during his internship in the group.

4.1.1 Boussinesq system of equations

We consider a fluid layer inside a domain $(x, y, z) \in [0, L_x] \times [0, L_y] \times [0, H]$. Within the Boussinesq approximation, the dimensional equations governing the evolution of the velocity field $\mathbf{u}(x, y, z, t)$ and the temperature field $\theta(x, y, z, t)$ read:

$$\partial_t \mathbf{u} + (\mathbf{u} \cdot \nabla)\mathbf{u} = -\nabla p + \nu \nabla^2 \mathbf{u} + \alpha g \theta \mathbf{e}_z \,, \tag{4.4a}$$

$$\partial_t \theta + \mathbf{u} \cdot \nabla \theta = \kappa \nabla^2 \theta + \frac{P}{\rho C \ell_0} \left[e^{-z/\ell_0} - \frac{\ell_0}{H} \left(1 - e^{-H/\ell_0} \right) \right] \,, \tag{4.4b}$$

where ν denotes the kinematic viscosity, α the thermal expansion coefficient, g is gravity, κ is the thermal diffusivity, ρ is the mean fluid density and C is the specific heat capacity. The last term in equation (4.4b) represents the internal heat sources and sinks. The precise z-dependence of this term is motivated by the experimental realization of CISS, see section 4.2.1. The first term inside the square bracket corresponds to the volumic absorption of light by a dyed fluid, where P denotes the heat flux (in W.m^{-2}) provided by the light source in the form of visible light. This term decreases exponentially with height over an e-folding absorption length ℓ as a result of Beer-Lambert's law. The second term inside the square brackets corresponds to the effective uniform heat sink associated with the secular heating of the body of fluid. We nondimensionalize the variables using H, H^2/κ and $\nu\kappa/(\alpha g H^3)$ as length, time and temperature scales:

$$\mathbf{x} = H\tilde{\mathbf{x}}\,, \quad t = \frac{H^2}{\kappa}\tilde{t}\,, \quad \theta = \frac{\nu\kappa}{\alpha g H^3}\tilde{\theta}\,, \quad \mathbf{u} = \frac{\kappa}{H}\tilde{\mathbf{u}} \quad \ell_0 = H\ell. \tag{4.5}$$

Dropping the tildes to alleviate notations, the dimensionless Boussinesq equations read:

$$\partial_t \mathbf{u} + (\mathbf{u}\cdot\nabla)\mathbf{u} = -\nabla p + \mathrm{Pr}\,\nabla^2\mathbf{u} + \mathrm{Pr}\,\theta\mathbf{e}_z\,, \tag{4.6a}$$

$$\partial_t\theta + \mathbf{u}\cdot\nabla\theta = \nabla^2\theta + \mathrm{Ra_P}\,S(z)\,. \tag{4.6b}$$

The dimensionless control parameters appearing in this set of equations are the Prandtl number and the flux-based Rayleigh number:

$$\mathrm{Pr} = \frac{\nu}{\kappa}\,, \qquad \mathrm{Ra_P} = \frac{\alpha g H^4 P}{\rho C \nu \kappa^2}\,. \tag{4.7}$$

The heat source/sink function $S(z)$ is:

$$S(z) = \frac{e^{-z/\ell}}{\ell} - 1 + e^{-1/\ell}\,, \tag{4.8}$$

The set of equations (4.6a-4.6b) is supplemented with the incompressibility constraint $\nabla\cdot\mathbf{u} = 0$ and impermeable, insulating boundary conditions at $z = 0$ and $z = 1$:

$$w|_{z=0;1} = 0\,, \qquad \partial_z\theta|_{z=0;1} = 0\,. \tag{4.9}$$

We consider a no-slip bottom boundary:

$$u|_{z=0} = v|_{z=0} = 0\,, \tag{4.10}$$

while the top boundary condition is either stress-free or no-slip:

$$u|_{z=1} = v|_{z=1} = 0 \tag{4.11a}$$

$$\text{or} \quad \partial_z u|_{z=1} = \partial_z v|_{z=1} = 0\,. \tag{4.11b}$$

Finally, we consider periodic boundary conditions in the horizontal directions.

We want to characterize the internal temperature fluctuations that emerge in this system. Without loss of generality and to alleviate notations, we assume in the following that θ is mean-zero initially and thus at any subsequent time. We introduce a temperature-based Rayleigh number and an associated Nusselt number using the root-mean-square temperature fluctuations:

$$\mathrm{Ra} = \sqrt{\langle \theta^2 \rangle}\,, \qquad \mathrm{Nu} = \mathrm{Ra_P}/\mathrm{Ra}\,, \tag{4.12}$$

where the angular brackets $\langle \cdot \rangle$ denote a space and time average. These definitions are well-suited for analysis, but experimentalists instead typically measure the vertical temperature drop across a convection cell. To make better contact with that literature, we also introduce an alternate temperature-based Rayleigh number and an associated Nusselt number based on the maximum in the vertical direction of the time and horizontal average of the squared temperature:

$$\mathrm{Ra_{max}} = \max_{z\in[0;1]} \left\{ \sqrt{\overline{\theta^2}} \right\}\,, \qquad \mathrm{Nu_{max}} = \mathrm{Ra_P}/\mathrm{Ra_{max}}\,, \tag{4.13}$$

where the overbar denotes an average with respect to x, y and t. From the equality $\langle \theta^2 \rangle = \int_0^1 \overline{\theta^2} \mathrm{d}z$, we obtain $\langle \theta^2 \rangle \leq \max_{z\in[0;1]}\{\overline{\theta^2}\}$, hence:

$$\mathrm{Ra} \leq \mathrm{Ra_{max}}\,, \qquad \mathrm{Nu_{max}} \leq \mathrm{Nu}\,. \tag{4.14}$$

The upper bounds derived in the following are typically of the form $\mathrm{Nu} \leq c \times \mathrm{Ra}^\gamma$, with γ a positive exponent and c a prefactor. From the inequalities (4.14) one immediately obtains that these bounds carry over in terms of $\mathrm{Ra_{max}}$ and $\mathrm{Nu_{max}}$, i.e., $\mathrm{Nu_{max}} \leq c \times {\mathrm{Ra_{max}}}^\gamma$, the latter form being better-suited for comparison with experimental measurements.

4.1.2 Bounding the heat flux in terms of the root-mean-square velocity

Multiplying the temperature equation (4.6b) by θ before averaging over space and time yields, after a few integration by parts using the boundary conditions:

$$\langle |\nabla \theta|^2 \rangle = \mathrm{Ra_P} \int_0^1 S(z)\overline{\theta}\, \mathrm{d}z\,. \tag{4.15}$$

Similarly, multiplying the temperature equation (4.6b) by z before averaging over space and time yields, after a few integration by parts using the boundary conditions:

$$-\mathrm{Ra}_\mathrm{P}\int_0^1 zS(z)\mathrm{d}z = \langle w\theta\rangle - \int_0^1 \partial_z\overline{\theta}\,\mathrm{d}z\,. \tag{4.16}$$

We bound the second term on the right-hand side using the Cauchy-Schwarz inequality, equation (4.15) and a Jensen's inequality:

$$\begin{aligned}\left|\int_0^1 \partial_z\overline{\theta}\,\mathrm{d}z\right| \le \sqrt{\int_0^1 (\partial_z\overline{\theta})^2\,\mathrm{d}z} \;&\le\; \sqrt{\int_0^1 \overline{(\partial_z\theta)^2}\,\mathrm{d}z} \\ &\le \sqrt{\langle|\nabla\theta^2|\rangle} = \sqrt{\mathrm{Ra}_\mathrm{P}\int_0^1 S(z)\overline{\theta}\,\mathrm{d}z}.\end{aligned} \tag{4.17}$$

Inserting this inequality into (4.16) and applying the Cauchy-Schwarz inequality to both terms on the right-hand side, we obtain:

$$-\mathrm{Ra}_\mathrm{P}\int_0^1 zS(z)\mathrm{d}z \;\le\; \langle w\theta\rangle + \sqrt{\mathrm{Ra}_\mathrm{P}\int_0^1 S(z)\overline{\theta}\,\mathrm{d}z} \tag{4.18}$$

$$\le\; \sqrt{\langle w^2\rangle}\mathrm{Ra} + \sqrt{\mathrm{Ra}_\mathrm{P}\mathrm{Ra}}\left(\int_0^1 S(z)^2\,\mathrm{d}z\right)^{1/4} \tag{4.19}$$

Dividing by the positive quantity $-\mathrm{Ra}\int_0^1 zS(z)\mathrm{d}z$ and using the relation $\mathrm{Ra}_\mathrm{P} = \mathrm{Ra}\,\mathrm{Nu}$ leads to:

$$\mathrm{Nu} - \mathrm{Nu}^{1/2}\frac{c_2}{c_1} - \frac{\sqrt{\langle w^2\rangle}}{c_1} \le 0\,, \tag{4.20}$$

where c_1 and c_2 are the following positive constants (for a given geometry of the setup):

$$c_1 = -\langle zS\rangle = \frac{1}{2} - \ell + e^{-1/\ell}\left(\frac{1}{2}+\ell\right)\,, \tag{4.21}$$

$$c_2 = \langle S^2\rangle^{1/4} = \left[-1 - e^{-2/\ell} + 2e^{-1/\ell} + \frac{1}{2\ell} - \frac{e^{-2/\ell}}{2\ell}\right]^{1/4}\,. \tag{4.22}$$

Seeking the roots of the quadratic function of $\mathrm{Nu}^{1/2}$ on left-hand side of (4.20), one obtains the equivalent inequality:

$$\mathrm{Nu} \leq \frac{1}{4}\left[\frac{c_2}{c_1} + \sqrt{\left(\frac{c_2}{c_1}\right)^2 + 4\frac{\langle w^2\rangle^{1/2}}{c_1}}\right]^2 . \tag{4.23}$$

The right-hand side of the inequality above is an upper bound on the Nusselt number in terms of the root-mean-square vertical velocity.

4.1.3 Bounding the heat flux in terms of the dissipation coefficient and the Rayleigh number

We would like to bound the root-mean-square vertical velocity to turn the upper bound (4.23) into a bound in terms of the Rayleigh number and the dissipation coefficient $\mathcal{C}$. Including the latter into the upper bound allows to readily derive upper bounds that apply to turbulent families of solutions, i.e., to an hypothetical family of solutions characterized by a non-zero limiting value of the dissipation coefficient $\mathcal{C}$ as Ra_P (or Ra) goes to infinity. We first derive the kinetic energy power integral, obtained by taking the dot product of (4.6a) with $\mathbf{u}$ before averaging over space and time. After a few integrations by parts, one obtains:

$$\langle|\nabla\mathbf{u}|^2\rangle = \langle w\theta\rangle . \tag{4.24}$$

In terms of the dimensionless variables, the definition (4.2) of the dissipation coefficient $\mathcal{C}$ becomes:

$$\mathcal{C} = \mathrm{Pr}\,\frac{\langle|\nabla\mathbf{u}|^2\rangle}{\langle\mathbf{u}^2\rangle^{3/2}} \tag{4.25}$$

Using this definition, equation (4.24) and the Cauchy-Schwarz inequality, one obtains successively:

$$\langle w^2\rangle^{3/2} \leq \langle\mathbf{u}^2\rangle^{3/2} = \frac{\mathrm{Pr}}{\mathcal{C}}\langle|\nabla\mathbf{u}|^2\rangle = \frac{\mathrm{Pr}}{\mathcal{C}}\langle w\theta\rangle \leq \frac{\mathrm{Pr\ Ra}}{\mathcal{C}}\langle w^2\rangle^{1/2} . \tag{4.26}$$

Dividing across by $\langle w^2\rangle^{1/2}$ and taking the square-root provides an upper bound on the root-mean-square vertical velocity:

$$\langle w^2\rangle^{1/2} \leq \sqrt{\frac{\mathrm{Pr\ Ra}}{\mathcal{C}}} . \tag{4.27}$$

Substituting this inequality into (4.23) leads to the following upper-bound $\mathcal{B}_1$ on the Nusselt number:

$$\mathrm{Nu} \leq \mathcal{B}_1 = \frac{1}{4}\left[\frac{c_2}{c_1} + \sqrt{\left(\frac{c_2}{c_1}\right)^2 + \frac{4}{c_1}\sqrt{\frac{\mathrm{Pr\ Ra}}{\mathcal{C}}}}\right]^2 . \tag{4.28}$$

We are interested in the behavior of the upper-bound $\mathcal{B}_1$ as the Rayleigh number goes to infinity. For a given geometry (constant coefficients c_1 and c_2), the asymptotic behavior of the upper-bound is then simply:

$$\mathcal{B}_1 \sim \frac{1}{c_1}\sqrt{\frac{\mathrm{Pr\ Ra}}{\mathcal{C}}} . \tag{4.29}$$

Laboratory experiments are typically run in the range of absorption length $\ell \ll 1$: even though the dimensional absorption length ℓ_0 is chosen to be greater than the boundary layer thickness, it remains much smaller than the height of the domain. In that limit, the constant c_1 is approximately given by $c_1 = 1/2 + O(\ell)$. In the asymptotic limit $\mathrm{Ra} \to \infty$ for fixed $\ell \ll 1$, the upper-bound thus takes the compact asymptotic form:

$$\mathcal{B}_1 \sim 2\sqrt{\frac{\mathrm{Pr\ Ra}}{\mathcal{C}}} . \tag{4.30}$$

4.1.4 Restricting attention to fully turbulent solutions

An interesting aspect of the upper bound (4.30) is that it allows to readily characterize the behavior of families of fully turbulent solutions, as defined at the outset. Of course, we have not proven that such families of solutions exist. However, we can assume that such a family of solutions exists and investigate the scaling behavior of the associated Nusselt number. The fully turbulent family of solutions is characterized by a finite nonzero limit of the dissipation coefficient for asymptotically large forcing (asymptotically large Reynolds number, $\mathrm{Ra_P}$ and Ra). In that limit, the upper-bound (4.30) behaves as $\sqrt{\mathrm{Pr\ Ra}}$, i.e., it follows the so-called ultimate regime of thermal convection. Experimental studies report a scaling exponent compatible with this scaling behavior in Ra, while an extensive three-dimensional numerical study has shown that the scaling behavior in both Ra and in Pr agrees well with the ultimate scaling when $\mathrm{Pr} \ll 1$, the behavior in Pr being different for $\mathrm{Pr} \gtrsim 1$. In other words, this upper bound appears to be sharp when compared to the available experimental and 3D numerical data.

However, we have also reported analytical and 2D numerical solutions that exceed the ultimate scaling behavior, with the Nusselt number increasing linearly in Ra. The upper-bound (4.30) immediately indicates that these solutions cannot be fully turbulent, and indeed they appear to be extremely laminar, see Miquel *et al.* (2019). In the following subsection, we derive an upper bound that applies to arbitrary flow solutions (including both laminar and turbulent ones).

4.1.5 Upper bound for arbitrary flow solutions

We now wish to derive an upper bound that holds for any flow solution, i.e., we stop restricting attention to turbulent families of solutions. To wit, we derive an upper bound on the inverse dissipation coefficient $\mathcal{C}^{-1}$. The Poincaré inequality in the vertical direction yields:

$$\langle \mathbf{u}^2 \rangle c_3 \leq \langle (\partial_z \mathbf{u})^2 \rangle \leq \langle |\nabla \mathbf{u}|^2 \rangle = \frac{\mathcal{C}}{\mathrm{Pr}} \langle \mathbf{u}^2 \rangle^{3/2} \,, \tag{4.31}$$

where $c_3 = \pi^2$ for no-slip top and bottom boundaries and $c_3 = \pi^2/4$ for a free-slip top boundary. The inequality above yields:

$$\frac{\mathrm{Pr}}{\mathcal{C}} \leq \frac{\langle \mathbf{u}^2 \rangle^{1/2}}{c_3} \tag{4.32}$$

Using the intermediate steps in (4.26), together with $\langle w^2 \rangle < \langle \mathbf{u}^2 \rangle$, we obtain:

$$\langle \mathbf{u}^2 \rangle \leq \frac{\mathrm{Pr}\ \mathrm{Ra}}{\mathcal{C}} \,, \tag{4.33}$$

which we substitute into (4.32) to get:

$$\frac{\mathrm{Pr}}{\mathcal{C}} \leq \frac{\mathrm{Ra}}{c_3^2} \,. \tag{4.34}$$

Inserting this inequality in the expression of the bound $\mathcal{B}_1$ leads to the following upper bound $\mathcal{B}_2$:

$$\mathrm{Nu} \leq \mathcal{B}_2 = \frac{1}{4} \left[\frac{c_2}{c_1} + \sqrt{\left(\frac{c_2}{c_1} \right)^2 + \frac{4\,\mathrm{Ra}}{c_1 c_3}} \right]^2 \,. \tag{4.35}$$

The upper bound $\mathcal{B}_2$ does not involve the dissipation coefficient anymore. We are interested in the large-Ra low-ℓ asymptotic behavior of the bound, given by:

$$\mathcal{B}_2 \sim \frac{2}{c_3}\,\mathrm{Ra} = \begin{cases} \frac{2}{\pi^2}\,\mathrm{Ra} & \text{for a no-slip top boundary} \ , \\ \frac{8}{\pi^2}\,\mathrm{Ra} & \text{for a free-slip top boundary} \, . \end{cases} \tag{4.36}$$

This upper bound is similar to the one derived in Miquel *et al.* (2019). It scales linearly in Ra, which is precisely the scaling behavior of an exact analytic laminar solution derived in Miquel *et al.* (2019) for free-slip top and bottom boundaries. We thus believe that the upper bound is sharp and governed by the behavior of a laminar large-scale flow solution, but that remains to be proven by including a no-slip bottom boundary condition when deriving an analytic flow solution similar to the one in Miquel *et al.* (2019).

To summarize this section, the Nusselt number of any flow solution cannot increase faster than Ra, while the Nusselt number associated with a turbulent family of solutions cannot increase faster than $\sqrt{\mathrm{Ra}}$. In other words, any scaling exponent γ larger than 1/2 is necessarily associated with non-turbulent solutions, according to the definition given at the outset. In the following, we characterize the dissipation coefficient in experimental and numerical realizations of CISS to assess the fully turbulent nature of the flow.

4.2 Extracting the dissipation coefficient from numerical and experimental data

We now turn to numerical and experimental realizations of CISS. The goal is to extract the dissipation coefficient $\mathcal{C}$ and assess whether the flow is fully turbulent according to the zeroth law of turbulence.

4.2.1 Laboratory experiments

The experimental setup is sketched in Figure 4.1. The apparatus is described extensively in the introductory chapter of the present thesis, and we briefly recall its main characteristics. A cylindrical cell of radius $R = 10$ cm is filled with a homogeneous mixture of water and carbon black dye, up to a height H varying from 4 to 18 cm. A powerful spotlight shines at the tank from below, the latter having a transparent

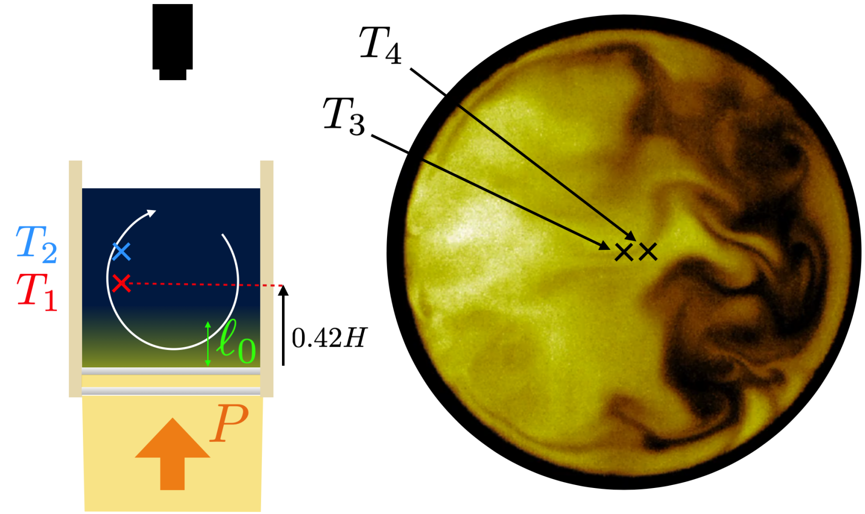

Figure 4.1: On the left: simplified schematics of the experimental apparatus with the thermal camera above, P the heat flux from the lamp and T_1 and T_2 the location of the temperature probes. On the right: picture from the thermal camera recording the upper free surface of the tank, with T_3 and T_4 the location of the two virtual probes.

bottom boundary. Absorption of light by the fluid leads to an internal source of heat, the magnitude of which decreases exponentially with height over an e-folding scale ℓ_0 (Beer-Lambert law). The absorption length ℓ_0 can be tuned through the concentration of dye: for large dye concentrations, ℓ_0 is much smaller than the thermal boundary layer thickness and we recover a standard RB-like boundary-heated configuration. By contrast, for low dye concentrations, ℓ_0 is larger than the boundary layer thickness. The internal heating then bypasses the boundary layers and leads to the mixing-length or "ultimate" scaling regime of turbulent heat transport(Lepot *et al.* (2018); Bouillaut *et al.* (2019)). As one cannot cool down the fluid using a cold plate without inducing a heat-transport-restricting upper boundary layer, we resort to "secular heating" instead: in the absence of cooling and with insulating boundaries, the volume-averaged temperature grows linearly in time. However, the temperature difference between any two points inside the tank is governed by the equations of Boussinesq convection driven by the radiative heat source and effectively cooled at an equal and opposite rate by a uniform internal heat sink (see Lepot *et al.* (2018) for details). This combination of radiative heating decreasing exponentially with height together with uniform effective cooling at an equal and opposite rate is the rationale behind the source/sink term in (4.4b). After a transient, a statistically steady vertical temperature gradient arises.

The fluid being opaque, we cannot resort to standard optical velocimetry techniques to access the Reynolds number Xin *et al.* (1996); Qiu & Tong (2001); Xia *et al.* (2003); Xi *et al.* (2004); Sun *et al.* (2005); Liot *et al.* (2017). Instead we used two different methods to compute the velocity.

Correlation between two thermal probes

The first method consists in using two thermocouples, T_1 and T_2 in figure 4.1, 0.5 cm away from each other, except for the highest $\mathrm{Ra_P} \simeq 2\times10^{11}$ where this distance is 1 cm, located in the rising region of the convection roll, at a height $0.42H$. The idea is to infer the local vertical velocity by computing the correlation function between two temperature probes (Chavanne *et al.* (2001); Castaing *et al.* (1989); Wu *et al.* (1990); Wu & Libchaber (1992)). The timeseries of temperature from both probes can be seen in figure 4.2. From those timeseries we compute the cross correlation function. In all the correlation functions we note the appearance of a peak at a finite time lag τ. The distance Δl between the two thermocouples needs to be sufficiently small for it to be narrow. By dividing the spacing between the probes by the time ag τ associated with the maximum of the cross correlation function, one can build a characteristic velocity of a fluid parcel travelling from one probe to the other:

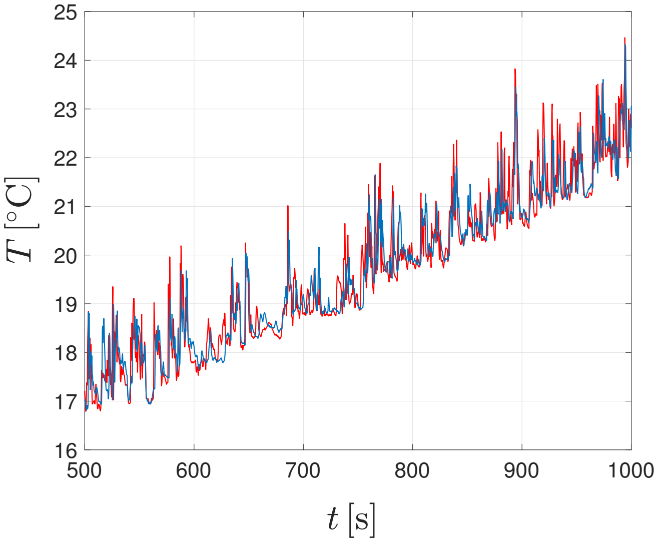

Figure 4.2: Example of timeseries of $T_1(t)$ (red), and $T_2(t)$ (blue). Both temperature signals increase linearly in time. T_2 lags behind T_1 in the rising region of the convection roll. Parameter values are $\ell = 0.048$, $\mathrm{Ra_P} \simeq 2 \times 10^{11}$. The probes are located 1 cm away from each other.

$$U = \frac{\Delta l}{\tau} \tag{4.37}$$

This technique is limited by the acquisition frequency f of the measurement device. Here, $f \simeq 3\,\mathrm{Hz}$ which would lead to an error of approximately 33% on the determination of the peak time lag. To reduce this error, we fit the correlation functions with a spline to obtain a more accurate peak location. This fit decreases the finite-sampling error. We will see in the result section that, although the remaining error induces some scatter of the data points, the determination of scaling-laws is still possible.

Correlation between two virtual probes

The second velocimetry method is based on IR images of the upper free surface of the tank. As for the internal thermal signals, we use the cross-correlation function between two virtual probes, T_3 and T_4 (two square regions of four pixels) in figure 4.1, 1 cm away from each other, to extract a characteristic correlation time and compute the horizontal velocity at the free surface. The virtual probes are located near the center of the free surface. If we take the circular snapshot in figure 4.1 as a reference, we see that the hot plumes impact on the left hand side of the image. Then, movies of the experiment show that the fluid moves to the right. It is the classical motion of the upper part of the well-known convective roll. One issue when using cross-correlation functions between two probes is that it can only measure one direction of the velocity vector. Hence, we need to choose a location for the probes where the velocity vector is mainly unidirectional. This condition is satisfied at the center of the surface. The steps are then the same as the previous technique and allow us to extract a local velocity from the thermal images. The acquisition frequency of the thermal camera is $f = 4\,\mathrm{Hz}$. This method suffers from the same limitation as the correlation between two vertically aligned probes inside the fluid.

Results

We build two Reynolds numbers $\mathrm{Re} = \frac{UH}{\nu}$, with U the characteristic local velocity: one associated with the horizontal local velocity at the upper free surface, Re_h, and one related to the vertical plumes inside the cylindrical cell, Re_v. In Figure 4.3, we plot $\mathrm{Re}_\mathrm{h,v}$ as a function of $\mathrm{Ra}_\mathrm{P}\mathrm{Pr}^{-2}$.They are compatible with a power-law behavior $\mathrm{Re}_\mathrm{h,v} \sim \left(\mathrm{Ra}_\mathrm{P}\,\mathrm{Pr}^{-2}\right)^{\beta}$, with $\beta = 0.32$ and $\beta = 0.35$ for Re_h and Re_v, respectively. These values of β should be compared to the laminar vs. turbulent values of this exponent: a fully turbulent flow that satisfies (4.3) is associated with $\beta = 1/3$. By contrast, a laminar flow dissipating energy at the large scale H would be characterized by a dissipation coefficient that is inversely proportional to the Reynolds number, hence $\beta = 1/2$. The data in figure 4.3 thus clearly discard the laminar scaling while being compatible with the fully turbulent one within measurement accuracy. To characterize more precisely the dissipation coefficient's scaling behavior, we now turn to numerical data.

4.2.2 Direct Numerical Simulations

Numerical solutions to the governing equations (4.6) are computed using Coral, a pseudo-spectral, scalable, time-stepping solver for differential equations Miquel (2021). The computational domain is a unit cube $(x, y, z) \in [0, 1) \times [0, 1) \times [0, 1]$

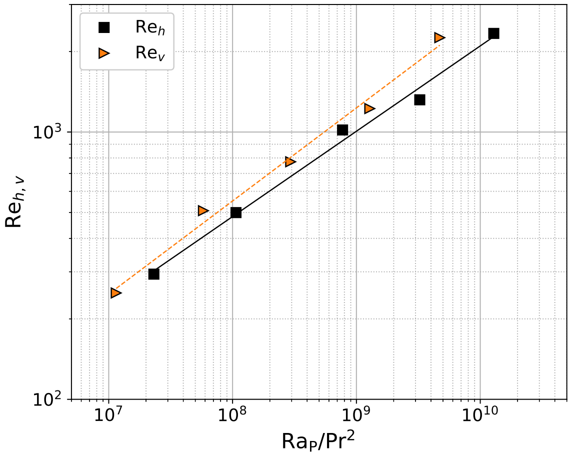

Figure 4.3: Experimental Reynolds number as a function of $\mathrm{Ra_P Pr^{-2}}$ for $l/H = 0.05$ and various measurement methods: correlation applied to IR images (black squares) and correlation applied to temperature probes (green triangles), associated with $\mathrm{Re_h}$ and $\mathrm{Re_v}$, respectively. The dashed line is $\mathrm{Re} = 0.9\left(\mathrm{Ra_P Pr^{-2}}\right)^{0.35}$. The straight line is $\mathrm{Re} = 1.35\left(\mathrm{Ra_P Pr^{-2}}\right)^{0.32}$.

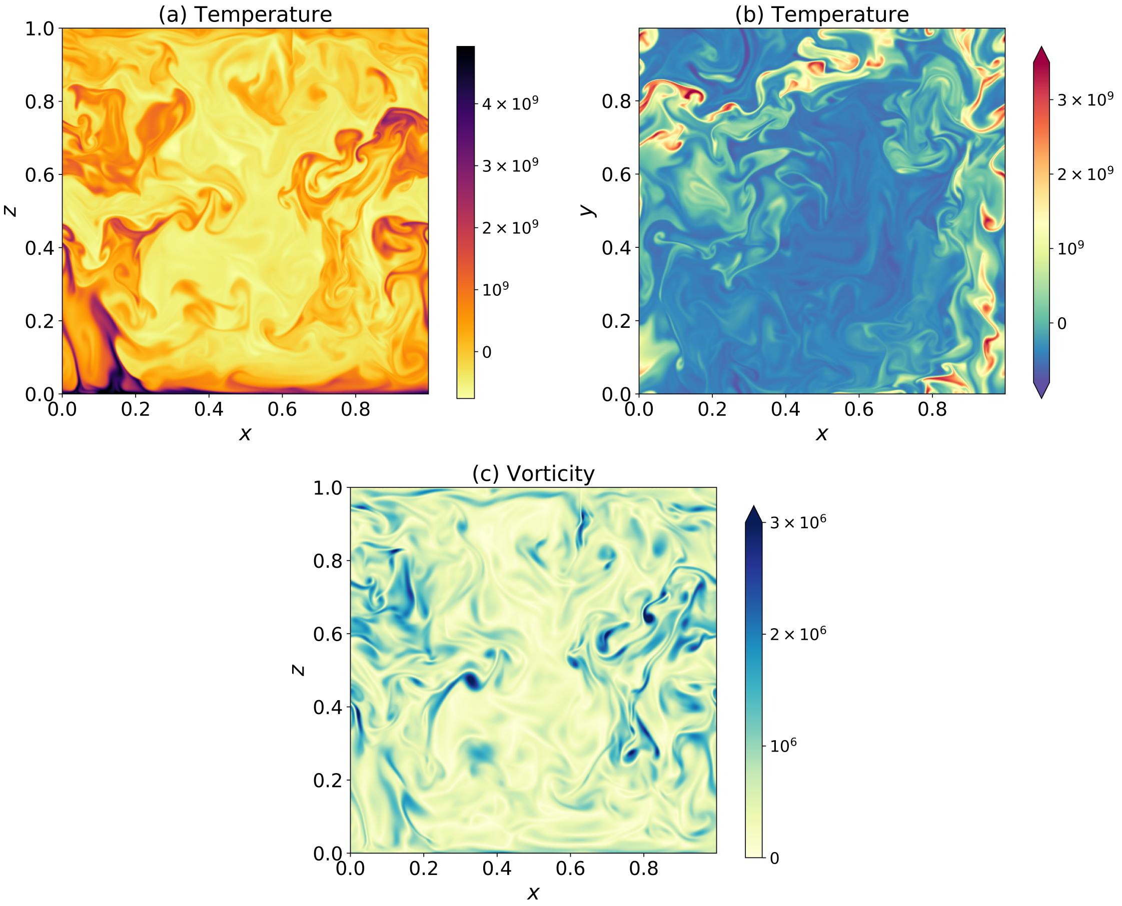

Figure 4.4: Snapshots of a turbulent flow computed numerically for $\mathrm{Ra_P} = 10^{12}$, $\ell = 0.048$ and $\mathrm{Pr} = 7$. (a) Vertical slice of temperature. (b) Horizontal slice of temperature taken at $z = 0.25$. (c) Vertical slice of vorticity $\sqrt{|\boldsymbol{\nabla} \times \mathbf{u}|^2}$.

with periodic boundary conditions along the horizontal directions (x, y). We impose impermeable and thermally insulating boundary conditions along surfaces $z = 0$ and $z = 1$ (equations [4.9]). We model the solid bottom and the free surface of the experiment by imposing no-slip boundary conditions at $z = 0$ (4.10) and stress-free boundary conditions at $z = 1$ (4.11b). In Coral, all these boundary conditions are imposed by using basis recombination, i.e. by expanding the variables ψ, ϕ, θ, *etc.*, on bases of functions obtained as tensor products of Fourier modes along the horizontal and suitable linear combinations of Chebyshev polynomials, each of which obeys the boundary conditions along z (see, e.g., Boyd (2013)). Simulations reported in the present manuscript use the second order semi-implicit scheme of Ascher *et al.* (1997). Finally, the solenoidal field $\mathbf{u}$ is expressed using velocity potentials ϕ and ψ, and horizontally-invariant mean flows U and V:

$$\mathbf{u} = \boldsymbol{\nabla} \times \psi(x, y, z, t)\, \mathbf{e}_z + \boldsymbol{\nabla} \times \boldsymbol{\nabla} \times \phi(x, y, z, t)\, \mathbf{e}_z + U(z, t)\, \mathbf{e}_x + V(z, t)\, \mathbf{e}_y \tag{4.38}$$

Our data is organised in two data sets which correspond to two distinct values for the Prandtl number. We consider both the canonical case $\mathrm{Pr} = 1$, as well as the case $\mathrm{Pr} = 7$ which is relevant for laboratory experiments using water as a working fluid. We fix the dimensionless absorption length to $\ell = 0.024$ and $\ell = 0.048$, two values employed by experiments reported in the literature (Lepot *et al.* (2018); Bouillaut *et al.* (2019, 2021)). Turbulent flows (illustrated on figure 4.4) are obtained by increasing the flux-based Rayleigh number, i.e. the control parameter associated with the vigor of thermal forcing (equation [4.7]), within the range $1.95 \times 10^6 \leq \mathrm{Ra_P} \leq 2.7 \times 10^{10}$ for $\mathrm{Pr} = 1$, and $3 \times 10^9 \leq \mathrm{Ra_P} \leq 10^{12}$ for $\mathrm{Pr} = 7$.

For every control parameter pair $(\mathrm{Pr}, \mathrm{Ra_P})$, the flow is computed from an initial condition taken as either some random small-amplitude noise, or the final state of a run with neighboring control parameters. In both cases, we let the flow equilibrate and reach a statistically stationary regime during which some velocity and temperature diagnostics are computed. More specifically, we output time series of the following quantities. The root-mean square velocity $\sqrt{\langle |\mathbf{u}|^2 \rangle}$ provides a definition of an rms-based Reynolds number:

$$\mathrm{Re_{rms}} = \frac{\sqrt{\langle |\mathbf{u}|^2 \rangle}}{\mathrm{Pr}} . \tag{4.39}$$

The top and bottom temperature, averaged over the $z = 1$ and $z = 0$ surfaces, or alternatively the volume-average of the convective heat flux $\langle w\theta \rangle$, both enter the expression of the friction coefficient $\mathcal{C}$ (eq. [4.25]), via the thermal energy budget.

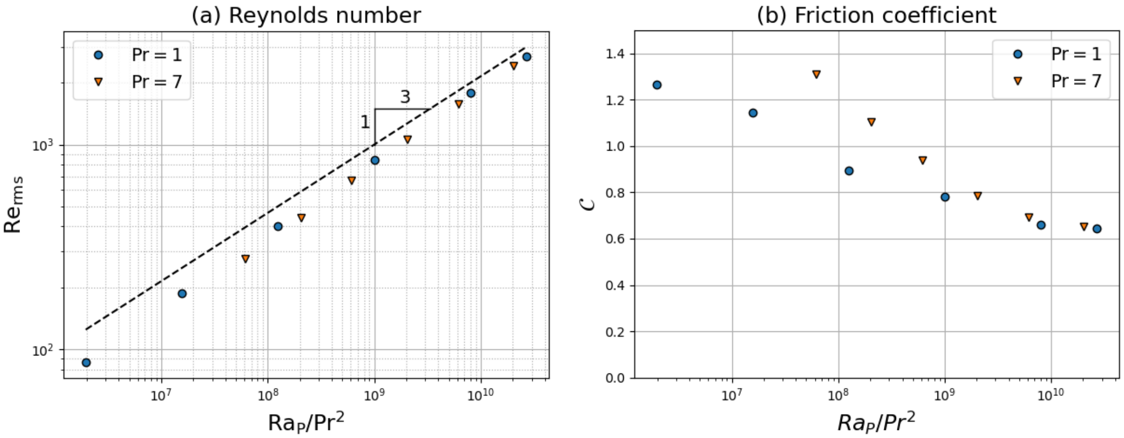

Figure 4.5: (a) Reynolds number, defined in equation (4.39) and (b) Friction coefficient, as defined in equation (4.25). Both quantities are obtained by numerical integration of (4.6) equations and plotted as function of the control parameter $\mathrm{Ra}_{\mathrm{P}}/\mathrm{Pr}^2$.

However, notice that exporting both is redundant, as $\langle w\theta\rangle$ can be deduced from the knowledge of $\overline{\theta}$ at the top and bottom, in virtue of equation (4.16).

We represent on figure 4.5 both the Reynolds number $\mathrm{Re}_{\mathrm{rms}}$ and the friction coefficient, plotted as functions of $\mathrm{Ra}_{\mathrm{P}}/\mathrm{Pr}^2$. Both the $\mathrm{Pr} = 1$ and $\mathrm{Pr} = 7$ datasets behave similarly and indicate a tendency towards turbulent dissipation for our most turbulent flows corresponding to $\mathrm{Re}_{\mathrm{rms}} \gtrsim 2000$. Indeed, these data points seem to asymptote the scaling law $\mathrm{Re}_{\mathrm{rms}} \sim \left(\mathrm{Ra}_{\mathrm{P}}/\mathrm{Pr}^2\right)^{1/3}$, and the friction coefficient $\mathcal{C}$ for both $\mathrm{Pr} = 1$ and $\mathrm{Pr} = 7$ seems to saturate to a constant value slightly above 0.6. Reaching even higher Reynolds number would be necessary for reaching a definitive conclusion and could be the scope of future work. However, the data presented here suggests that radiative convection enters a turbulent regime, as characterized by the zeroth-law of turbulence, for $\mathrm{Re}_{\mathrm{rms}} \gtrsim 2000$. This justifies the applicability of the bounds derived in section 4.1 to this flow.

4.3 Conclusion

The upper bound (4.30) scales as the square-root of the Rayleigh number over turbulent branches of solutions, according to the precise definition given at the outset and assuming that such branches of solutions exist. By contrast, the best upper bound (4.36) over all flow solutions scales linearly in Rayleigh number, a behavior associated with laminar analytic flow solutions such as the one derived in Miquel *et al.* (2019).

We thus turned to numerical and experimental data to validate the existence of turbulent branches of solutions. The numerical data indeed point to a finite limiting value of the dissipation coefficient as the flux-based Rayleigh number — and thus the Reynolds number — increases. Experimental measurements are more local in the present opaque fluid. The experimental data are fully compatible with the DNS data, even though the former would benefit from higher temperature sampling rates to reduce the error on the determination of the time lag. We stress the fact that the validation of the fully turbulent assumption, when combined with the 'ultimate' scaling-law for heat transport $Nu \sim \sqrt{\mathrm{RaPr}}$, leads to Spiegel's free-fall scaling-law for the velocity field $\mathrm{Re}_{\mathrm{rms}} \sim \sqrt{\mathrm{Ra}/\mathrm{Pr}}$. In other words, using CISS we can validate both Spiegel's prediction of a diffusivity-free regime for the heat transport, $Nu \sim \sqrt{\mathrm{RaPr}}$, and the free-fall scaling assumption that underpins it.

The upper bounds derived in the present study provide a useful point of view to discuss the proposed scaling theories for CISS. For instance, Lepot *et al.* (2018) report a scaling exponent $\gamma \simeq 0.55$ for the scaling-law $Nu \sim \mathrm{Ra}^{\gamma}$ at $\mathrm{Pr} = 7$. Assuming that the flow becomes fully turbulent at large driving amplitude, the slight departure of the measured exponent from $1/2$ must be attributed to finite-Reynolds-number effects. As a matter of fact, we showed in Lepot et al. using DNS that the scaling exponent γ is indeed much closer to $1/2$ for $\mathrm{Pr} = 1$ than for $\mathrm{Pr} = 7$, the former corresponding to reduced finite-Reynolds-number effects. The upper bounds (4.30) and (4.36) are also fully compatible with the scaling predictions put forward in Bouillaut *et al.* (2019) and Miquel *et al.* (2020) with regard to the dependence of the Nusselt number on Ra, Pr and the dimensionless absorption length ℓ.

Bibliography

Ascher, U. M., Ruuth, S. J. & Spiteri, R. J. 1997 Implicit-explicit runge-kutta methods for time-dependent partial differential equations. *Applied Numerical Mathematics* **25** (2), 151 – 167, special Issue on Time Integration.

Bouillaut, V., Lepot, S., Aumaître, S. & Gallet, B. 2019 Transition to the ultimate regime in a radiatively driven convection experiment. *J. Fluid Mech.* **861**, R5.

Bouillaut, Vincent, Miquel, Benjamin, Julien, Keith, Aumaître, Sébastien & Gallet, Basile 2021 Experimental observation of the geostrophic turbulence regime of rapidly rotating convection. *Proceedings of the National Academy of Sciences* **118** (44).

Boyd, J.P. 2013 Chebyshev and fourier spectral methods: Second revised edition .

Busse, F. 1969 On howard's upper bound for heat transport by turbulent convection. *J. Fluid Mech.* **37**, 457–477.

Castaing, B., Gunaratne, G., Heslot, F., Kadanoff, L., Libchaber, A., Thomae, S., Wu, X.-Z., Zaleski, S. & Zanetti, G. 1989 Scaling of hard thermal turbulence in Rayleigh–Bénard convection. *J. Fluid Mech.* **204**, 1–30.

Chavanne, X., Chillà, F., Chabaud, B., Castaing, B. & Hébral, B. 2001 Turbulent rayleigh–bénard convection in gaseous and liquid he. *Physics of Fluids* **13** (5), 1300–1320.

Doering, Charles R. & Constantin, Peter 1996 Variational bounds on energy dissipation in incompressible flows. iii. convection. *Phys. Rev. E* **53**, 5957–5981.

Frisch, Uriel 1995 *Turbulence: The Legacy of A. N. Kolmogorov*. Cambridge University Press.

Howard, Louis N. 1963 Heat transport by turbulent convection. *J. Fluid Mech.* **17** (3), 405–432.

Lepot, S., Aumaître, S. & Gallet, B. 2018 Radiative heating achieves the ultimate regime of thermal convection. *Proc. Natl. Acad. Sci.* **115** (36), 8937–8941.

Liot, Olivier, Ehlinger, Quentin, Rusaouën, Éléonore, Coudarchet, Thibaut, Salort, Julien & Chillà, Francesca 2017 Velocity fluctuations and boundary layer structure in a rough rayleigh-bénard cell filled with water. *Phys. Rev. Fluids* **2**, 044605.

Miquel, B. 2021 Coral: a parallel spectral solver for fluid dynamics and partial differential equations. *J. Open Source Soft.* .

Miquel, Benjamin, Bouillaut, Vincent, Aumaître, Sébastien & Gallet, Basile 2020 On the role of the prandtl number in convection driven by heat sources and sinks. *J. Fluid Mech.* **900**, R1.

Miquel, B., Lepot, S., Bouillaut, V. & Gallet, B. 2019 Convection driven by internal heat sources and sinks: Heat transport beyond the mixing-length or “ultimate” scaling regime. *Phys. Rev. Fluids* **4**, 121501.

Qiu, X.-L. & Tong, P. 2001 Large-scale velocity structures in turbulent thermal convection. *Phys. Rev. E* **64**, 036304.

Spiegel, Edward A. 1963 A Generalization of the Mixing-Length Theory of Turbulent Convection. *Ap. J.* **138**, 216.

Spiegel, Edward A 1971 Convection in stars i. basic boussinesq convection. *Annu. Rev. Astro. Astrophys.* **9** (1), 323–352.

Sun, Chao, Xia, Ke-Qing & Tong, P. 2005 Three-dimensional flow structures and dynamics of turbulent thermal convection in a cylindrical cell. *Phys. Rev. E* **72**, 026302.

Wu, Xiao-Zhong, Kadanoff, Leo, Libchaber, Albert & Sano, Masaki 1990 Frequency power spectrum of temperature fluctuations in free convection. *Physical review letters* **64** (18), 2140.

Wu, Xiao-Zhong & Libchaber, Albert 1992 Scaling relations in thermal turbulence: The aspect-ratio dependence. *Physical Review A* **45** (2), 842.

XI, HENG-DONG, LAM, SIU & XIA, KE-QING 2004 From laminar plumes to organized flows: the onset of large-scale circulation in turbulent thermal convection. *J. Fluid Mech.* **503**, 47?56.

XIA, KE-QING, SUN, CHAO & ZHOU, SHENG-QI 2003 Particle image velocimetry measurement of the velocity field in turbulent thermal convection. *Phys. Rev. E* **68**, 066303.

XIN, Y.-B., XIA, K.-Q. & TONG, P. 1996 Measured velocity boundary layers in turbulent convection. *Phys. Rev. Lett.* **77**, 1266–1269.

Chapter 5

Conclusion

The present thesis aimed to study the geostrophic turbulence regime of rapidly rotating convection. The impact of rotation on the turbulent transport of heat and tracers is of primary interest for geophysical and astrophysical flows. These flows are characterized by strong rotation rates and extreme forcings. It has been predicted in the literature that, in those extreme conditions, the heat transport would follow the scaling law of the geostrophic turbulence regime of convection. This regime is based on two assumptions: the relation between the turbulent heat flux and the internal temperature gradient should not involve the molecular diffusivity coefficients, and the heat transport efficiency of the flow depends only on the supercriticality of the system. This prediction dates back to 1979, but its experimental observation remained elusive in the literature despite a worldwide effort to design ever-taller convection cells. Those state-of-the-art laboratory experiments are all based on a Rayleigh-Bénard (RB) geometry, where a layer of fluid is confined between two rigid plates: a hot bottom one and a cold top one. In this configuration, overcoming the throttling effect of the boundary layers is a real challenge.

Recently, Basile Gallet, Sébastien Aumaître, and Simon Lepot (Ph.D. student at the time) developed an innovative experiment able to inject heat directly into the turbulent bulk flow. They ingenuously used light absorbed in an opaque fluid to create an internal heat source able to bypass the limiting boundary layers. Experimentally, it consists in using a cylindrical tank filled with a homogeneous mixture of water and carbon black dye. A powerful spotlight shines at the tank from below. Light is absorbed by the fluid, creating an internal heat source that decreases exponentially. This radiative heating proved able to achieve the "ultimate" regime of non-rotating convection. In the present thesis, we thus used the same heating method to study the "ultimate" regime of rotating convection. We modified the experimental setup to apply uniform rotation to the cylindrical tank. We also changed the measurement system to measure the internal temperature gradient remotely. This new apparatus allowed to study the impact of the rotation rate on the heat transport efficiency.

5.1 The observation of the geostrophic turbulence regime

The scaling law of the geostrophic turbulence regime is based on two assumptions that need to be verified. The first step of the study consisted in assessing if radiative heating modifies the threshold of rotating convection. This question is important as one of the assumptions involves the supercriticality of the system. I performed a linear stability analysis and developed a finite difference code to compute the threshold as a function of the rotation rate. We found that the radiatively driven rotating convection threshold follows the same scaling law (except for the prefactor) as the RB geometry. It implies that radiative heating does not modify the scaling law of the geostrophic turbulence regime.

The second assumption is the turbulent nature of the flow. For a "fully" turbulent flow, the molecular diffusivity coefficients are not involved in the relation between the heat transport and the internal temperature gradient. Building new dimensionless numbers independent of the diffusivity coefficients allowed me to verify whether the flow was indeed in a turbulent regime. In that representation, the experimental data points made at multiple rotation rates for multiple heights of fluid collapsed on a single master curve, thus proving the turbulent nature of the flow. In addition, this master curve followed the scaling law predicted for the geostrophic turbulent regime, which constitutes the first experimental observation of this extreme regime of rotating convection.

5.2 Perspectives for futur work

This study of a radiatively driven rotating convection experiment clearly showed that the system transitions from the non-rotating "ultimate" regime to the rotating one opening an avenue to investigate the latter regime. Additional work could focus on characterizing the transition between the two regimes as a function of the control parameters of the system. More generally, one seeks to determine the boundaries between the various regimes in parameter space, to extrapolate these boundaries to the extreme parameter values of astrophysical objects. One would also like to characterize the flow field more precisely.

I have thus adapted the current experimental setup to record movies of the top free surface with a thermal camera. Figure 5.5a presents an image from the thermal camera recorded during a non-rotating experimental run. We see that the rising hot plumes are concentrated on the left hand side of the image. The corresponding movie shows that the mean circulation consists of a roll that pushes the hot fluid from the left side to the right. The existence of the convective roll is a characteristic feature of non-rotating convection. We recorded similar movies during rotating experimental runs at different fluid heights and rotation rates. A characteristic image from one of these movies is presented in figure 5.5b. We notice that the structures are very different. In the rotating case, we do not see any large-scale convective roll. The rising plumes take the form of swirling vortices whose number and sizes are linked to the rotation rate and fluid height inside the tank. Several scaling laws can be found in the literature that describe the size and the distance between plumes in the geostrophic turbulence regime. Additional work could consist in assessing the validity of those laws in radiatively driven rotating convection.

During this thesis, I have also begun to develop methods to measure the velocity in the non-rotating radiatively driven experiment accurate enough to assess the turbulent nature of the flow. Improving those methods could open the way to a more detailed study of the velocity field, an essential aspect of turbulent convection.

The various results reported in the present thesis have led to the publication of two articles (Bouillaut *et al.* (2019, 2021)), so far the last chapter being currently in press at *Philosophical Transaction of the Royal Society A*. The three articles are included in the appendix. In addition, this thesis also provided me with the opportunity to participate in two numerical studies that led to publications (Miquel *et al.* (2019, 2020)).

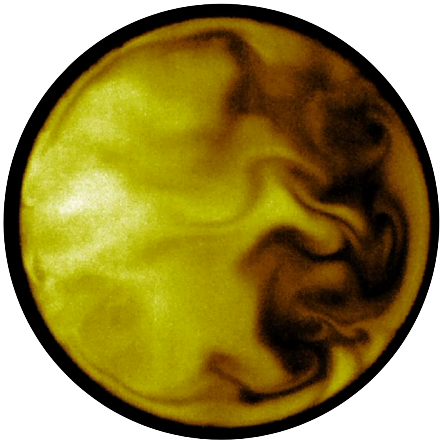

(a) Snapshot of the temperature field at the top free-surface (lighter color for warmer temperature) in the non-rotating case.

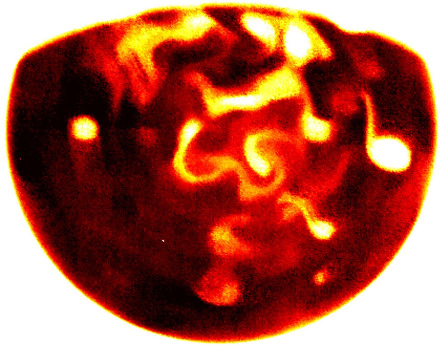

(b) Snapshot of the temperature field showing a fraction of the top free surface in the rotating case. Lighter color corresponds to warmer temperature.

List of Publications

Bouillaut, V., Lepot, S., Aumaître, S. & Gallet, B. 2019 Transition to the ultimate regime in a radiatively driven convection experiment. *J. Fluid Mech.* **861**, R5.

Bouillaut, Vincent, Miquel, Benjamin, Julien, Keith, Aumaître, Sébastien & Gallet, Basile 2021 Experimental observation of the geostrophic turbulence regime of rapidly rotating convection. *Proceedings of the National Academy of Sciences* **118** (44), arXiv: https://www.pnas.org/content/118/44/e2105015118.full.pdf.

Miquel, Benjamin, Bouillaut, Vincent, Aumaître, Sébastien & Gallet, Basile 2020 On the role of the prandtl number in convection driven by heat sources and sinks. *Journal of Fluid Mechanics* **900**, R1.

Miquel, B., Lepot, S., Bouillaut, V. & Gallet, B. 2019 Convection driven by internal heat sources and sinks: Heat transport beyond the mixing-length or "ultimate" scaling regime. *Phys. Rev. Fluids* **4**, 121501.

Résumé en français

La présente thèse a pour but d'étudier le régime de convection géostrophique turbulente en rotation rapide. L'impact de la rotation sur le transport turbulent de la chaleur et de divers traceurs est d'un grand intérêt dans le cas des écoulements géophysiques et astrophysiques. Ces écoulements sont caractérisés par un taux de rotation élevé et par des régimes extrêmes de turbulence. Il a été prédit dans la littérature scientifique que, dans ces conditions extrêmes, le transport de la chaleur suivrait la loi d'échelle de la convection géostophique turbulente. Ce régime se base sur deux hypothèses : la relation entre le flux de chaleur turbulent et le gradient de température interne n'implique plus les coefficients de diffusion moléculaires, et une efficacité dans le transport de la chaleur qui dépend seulement de la supercriticalité du système. Cette prédiction remonte à 1979, mais son observation expérimentale demeure absente dans la littérature scientifique malgré des initiatives internationales tendant à développer des cellules de convection toujours plus grandes. Ces expériences de laboratoire à la pointe de l'état de l'art sont toutes basées sur une géométrie de Rayleigh-Bénard (RB), où une couche de fluide est comprise entre deux plaques : celle du haut est maintenue à une température plus froide que celle du bas. Dans cette configuration, surpasser la barrière des couches limites est un vrai défi.

Récemment, Basile Gallet, Sébastien Aumaître et Simon Lepot (doctorant à l'époque) ont développé une expérience innovante capable d'injecter la chaleur directement dans le corps turbulent de l'écoulement. Ils ont ingénieusement utilisé la lumière absorbée dans un écoulement opaque pour créer une source de chaleur interne capable de court-circuiter ces couches limites contraignantes. Expérimentalement, cela se traduit par l'utilisation d'une cuve cylindrique remplie d'un mélange homogène d'eau et de noir de carbone (de l'encre de Chine). Un puissant projecteur illumine la cuve par dessous. La lumière est absorbée par le fluide, créant ainsi une source interne de chaleur décroissant exponentiellement dans le fluide. Ce chauffage radiatif a prouvé sa capacité à atteindre le régime "ultime" de la convection sans rotation.

Dans la présente thèse, nous avons ainsi utilisé la même méthode de chauffage pour étudier le régime "ultime" de la convection en rotation (voir figure 5.2).

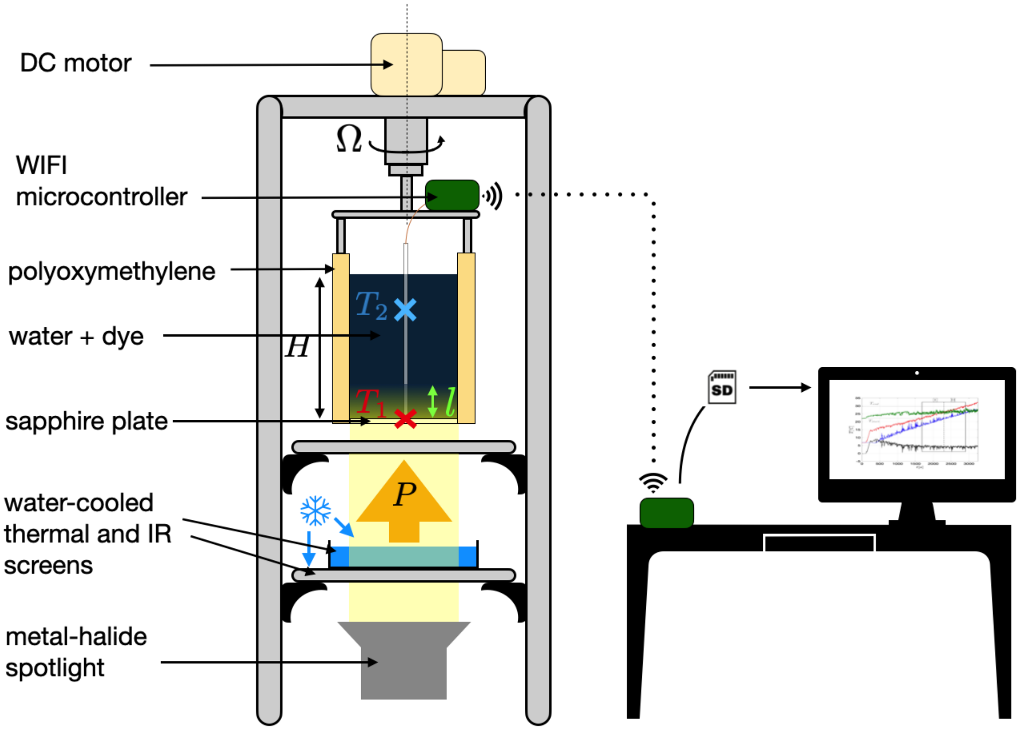

Figure 5.2: Schéma de l'expérience de convection forcée radiativement.

L'observation du régime de turbulence géostrophique

La loi d'échelle du régime de turbulence géostrophique repose sur deux hypothèses qu'il convient de vérifier. La première étape de l'étude a consisté à évaluer si le chauffage radiatif modifie le seuil de convection en rotation. Cette question est importante car l'une des hypothèses implique la supercriticalité du système. J'ai donc effectué une analyse de stabilité linéaire et développé un code aux différences finies pour calculer le seuil en fonction du taux de rotation. Nous avons constaté que le seuil de la convection en rotation entraînée par chauffage radiatif suit la même loi d'échelle (à l'exception du préfacteur) que la géométrie RB. Cela implique

que le chauffage radiatif ne modifie pas la loi d'échelle du régime de turbulence géostrophique comme le montre la courbe de stabilité présentée en figure 5.3.

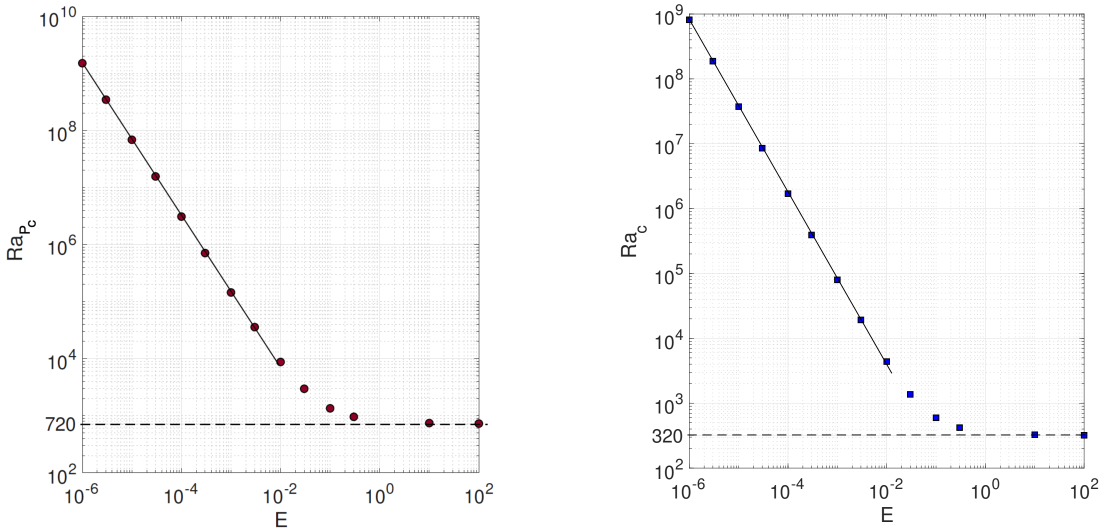

Figure 5.3: Gauche : Stabilité de la convection radiative en rotation pour les conditions aux limites NS-SF et $\ell/H = 0.05$. La ligne pointillée correspond au $\mathrm{Ra}_{\mathrm{P}c}$ calculé par Goluskin sans rotation. La ligne continue correspond à $\mathrm{Ra}_{\mathrm{P}c} = 14.775\mathrm{E}^{-4/3}$. A droite : stabilité de la convection RB pour les conditions aux limites NS-SF. La ligne continue est la loi d'échelle pour la rotation en géométrie de RB. La ligne pointillée correspond au $\mathrm{Ra}_{\mathrm{P}c}$ calculé par Goluskin sans rotation.

La deuxième hypothèse est la nature turbulente de l'écoulement. Pour un écoulement "pleinement" turbulent, les coefficients de diffusivité moléculaire n'interviennent pas dans la relation entre le transport de chaleur et le gradient de température interne. La construction de nouveaux nombres sans dimension indépendants des coefficients de diffusivité m'a permis de vérifier si l'écoulement était bien en régime turbulent. Dans cette représentation, les points de données expérimentaux réalisés à plusieurs vitesses de rotation pour plusieurs hauteurs de fluide (présentés dans la figure 5.4) se sont répartis sur une seule courbe maîtresse, prouvant ainsi la nature turbulente de l'écoulement. De plus, cette courbe maîtresse a suivi la loi d'échelle prédite pour le régime de la convection géostrophique turbulente, ce qui constitue la première observation expérimentale de ce régime extrême de convection en rotation.

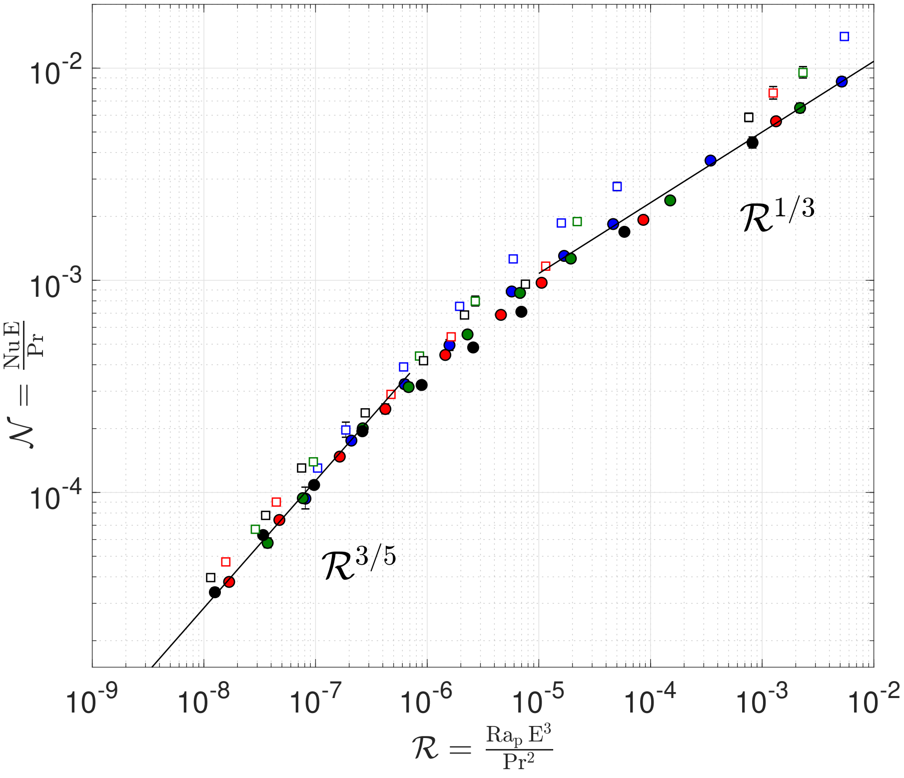

Figure 5.4: Représentation des données en fonction des paramètres indépendants des diffusivités $\mathcal{N}$ et $\mathcal{R}$. Les lignes noires pleines correspondent aux lois d'échelle attendues dans le régime à rotation rapide, $\mathcal{N} \sim \mathcal{R}^{3/5}$, et dans le régime sans rotation, $\mathcal{N} \sim \mathcal{R}^{1/3}$.

Futures pistes de recherche

Cette étude d'une expérience de convection en rotation forcée radiativement a montré que le système passe du régime "ultime" sans rotation à celui en rotation, ouvrant la voie à l'étude de ce dernier régime. Des travaux complémentaires pourraient porter sur la caractérisation de la transition entre les deux régimes en fonction des paramètres de contrôle du système. Plus généralement, on cherche à déterminer les frontières entre les différents régimes dans l'espace des paramètres, pour extrapoler ces frontières aux valeurs extrêmes des paramètres des objets astrophysiques. On aimerait aussi caractériser plus précisément les différents champs de l'écoulement.

J'ai donc adapté la configuration expérimentale actuelle pour enregistrer des films de la surface libre supérieure avec une caméra thermique. La figure 5.5a présente une image issue de la caméra thermique enregistrée lors d'un essai sans rotation. Nous voyons que les panaches chauds ascendants sont concentrés sur le côté gauche de l'image. Le film correspondant montre que la circulation moyenne consiste en un rouleau qui pousse le fluide chaud du côté gauche vers la droite. L'existence du rouleau de convection est une caractéristique de la convection sans rotation. Nous avons enregistré des films similaires lors d'essais expérimentaux en rotation à différentes hauteurs de fluide et taux de rotation. Une image caractéristique d'un de ces films est présentée dans la figure 5.5b. On remarque que les structures sont très différentes. Dans le cas tournant, nous ne voyons aucun rouleau de convection à grande échelle. Les panaches ascendants prennent la forme de tourbillons dont le nombre et la taille sont liés à la vitesse de rotation et à la hauteur du fluide à l'intérieur de la cuve. Plusieurs lois d'échelle peuvent être trouvées dans la littérature scientifique décrivant la taille et la distance entre les panaches dans le régime de turbulence géostrophique. Un travail complémentaire pourrait consister à évaluer la validité de ces lois en convection en rotation forcée radiativement.

Au cours de cette thèse, j'ai également commencé à développer des méthodes pour mesurer la vitesse dans l'expérience sans rotation suffisamment précises pour évaluer la nature turbulente de l'écoulement. L'amélioration de ces méthodes pourrait ouvrir la voie à une étude plus fine du champ de vitesse, aspect essentiel de la convection turbulente.

Les différents résultats rapportés dans la présente thèse ont conduit à la publication de deux articles (Bouillaut *et al.* (2019, 2021)), à ce jour le dernier étant actuellement en attente de publication chez *Philosophical Transaction of the Royal Society A*. Les trois articles sont inclus dans l'annexe. De plus, cette thèse m'a également

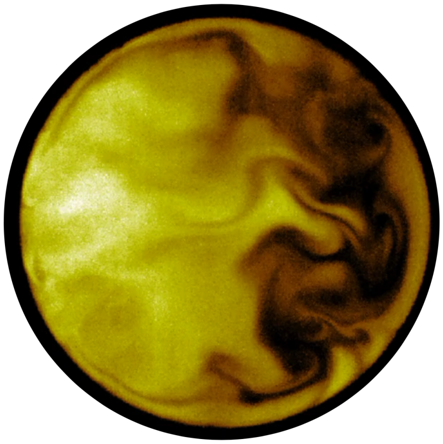

(a) Instantané du champ de température sur la surface libre supérieure (couleur plus claire pour une température plus chaude) dans le cas sans rotation.

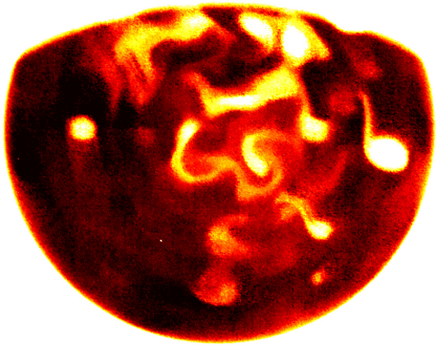

(b) Instantané du champ de température montrant une partie de la surface libre supérieure (couleur plus claire pour une température plus chaude) dans le cas en rotation.

donné l'opportunité de participer à deux études numériques qui ont donné lieu à des publications (Miquel *et al.* (2019, 2020)).

List of Publications

BOUILLAUT, V., LEPOT, S., AUMAÎTRE, S. & GALLET, B. 2019 Transition to the ultimate regime in a radiatively driven convection experiment. *J. Fluid Mech.* **861**, R5.

BOUILLAUT, VINCENT, MIQUEL, BENJAMIN, JULIEN, KEITH, AUMAÎTRE, SÉBASTIEN & GALLET, BASILE 2021 Experimental observation of the geostrophic turbulence regime of rapidly rotating convection. *Proceedings of the National Academy of Sciences* **118** (44), arXiv: https://www.pnas.org/content/118/44/e2105015118.full.pdf.

MIQUEL, BENJAMIN, BOUILLAUT, VINCENT, AUMAÎTRE, SÉBASTIEN & GALLET, BASILE 2020 On the role of the prandtl number in convection driven by heat sources and sinks. *Journal of Fluid Mechanics* **900**, R1.

MIQUEL, B., LEPOT, S., BOUILLAUT, V. & GALLET, B. 2019 Convection driven by internal heat sources and sinks: Heat transport beyond the mixing-length or "ultimate" scaling regime. *Phys. Rev. Fluids* **4**, 121501.

APPENDIX

H	Ω	$\Omega^2 H/\mathrm{g}$	Fr	T_{start}	T_{end}	ΔT_{I}	ΔT_{II}	Ra	Nu_{I}	$\mathrm{Nu}_{\mathrm{II}}$	E_{I}	E_{II}	$\widetilde{\mathrm{Ra}}$	$\widetilde{\mathrm{Ra}_{\mathrm{P}}}$	$\mathcal{N}_{\mathrm{I}}$	$\mathcal{N}_{\mathrm{II}}$	$\mathcal{R}_{\mathrm{I}}$	$\mathcal{R}_{\mathrm{II}}$	Pr_{I}	$\mathrm{Pr}_{\mathrm{II}}$
10	8.901	0.8	0.8	34.2	39.7	8.8	6.9	2.6×10^{8}	99	124	3.93×10^{-6}	3.74×10^{-6}	16	1.77×10^{3}	8.36×10^{-5}	1.05×10^{-4}	7.90×10^{-8}	8.32×10^{-8}	4.6	4.4
10	6.283	0.4	0.4	33.4	37.7	5.6	5.6	1.7×10^{8}	146	147	5.79×10^{-6}	5.53×10^{-6}	17	2.62×10^{3}	1.74×10^{-4}	1.76×10^{-4}	2.04×10^{-7}	2.14×10^{-7}	4.8	4.6
10	4.398	0.2	0.2	28.6	36.3	5.0	4.6	1.3×10^{8}	183	200	9.02×10^{-6}	8.31×10^{-6}	23	4.51×10^{3}	3.09×10^{-4}	3.39×10^{-4}	6.00×10^{-7}	6.55×10^{-7}	5.3	4.8
10	3.142	0.1	0.1	26.5	35.1	4.4	3.9	1.0×10^{8}	199	221	1.31×10^{-5}	1.20×10^{-5}	31	6.63×10^{3}	4.67×10^{-4}	5.24×10^{-4}	1.50×10^{-6}	1.66×10^{-6}	5.6	5.0
10	2.094	0.04	0.04	26.5	35.4	3.7	3.8	9.6×10^{7}	255	245	1.97×10^{-5}	1.79×10^{-5}	48	1.21×10^{4}	8.99×10^{-4}	8.72×10^{-4}	5.40×10^{-6}	6.01×10^{-6}	5.6	5.0
10	1.466	0.02	0.02	25.2	35.8	3.6	3.7	9.4×10^{7}	262	253	2.87×10^{-5}	2.55×10^{-5}	76	1.98×10^{4}	1.31×10^{-3}	1.29×10^{-3}	1.57×10^{-5}	1.79×10^{-5}	5.7	5.0
10	1.047	0.01	0.01	24.7	36.3	3.8	3.6	9.3×10^{7}	255	266	4.06×10^{-5}	3.55×10^{-5}	119	3.12×10^{4}	1.78×10^{-3}	1.89×10^{-3}	4.28×10^{-5}	4.96×10^{-5}	5.7	4.9
10	0.524	0.003	0.003	23.5	34.0	3.6	3.5	8.4×10^{7}	256	265	8.37×10^{-5}	7.42×10^{-5}	287	7.48×10^{4}	3.58×10^{-3}	3.75×10^{-3}	3.21×10^{-4}	3.68×10^{-4}	6.0	5.2
10	0.209	0.0004	0.0004	25.3	34.8	3.7	3.3	8.8×10^{7}	235	255	2.01×10^{-4}	1.81×10^{-4}	976	2.39×10^{5}	8.25×10^{-3}	9.06×10^{-3}	4.86×10^{-3}	5.46×10^{-3}	5.7	5.1
15	8.901	1.2	0.8	32.8	36.8	9.8	8.8	9.5×10^{8}	147	163	1.84×10^{-6}	1.78×10^{-6}	21	3.25×10^{3}	5.49×10^{-5}	6.10×10^{-5}	3.65×10^{-8}	3.79×10^{-8}	4.9	4.7
15	6.283	0.6	0.4	30.9	37.9	6.0	5.8	6.0×10^{8}	176	179	2.66×10^{-6}	2.49×10^{-6}	21	3.77×10^{3}	9.27×10^{-5}	9.52×10^{-5}	7.42×10^{-8}	7.96×10^{-8}	5.0	4.6
15	4.398	0.3	0.2	28.7	36.0	4.9	4.8	4.5×10^{8}	264	269	3.99×10^{-6}	3.68×10^{-6}	27	7.34×10^{3}	1.97×10^{-4}	2.03×10^{-4}	2.53×10^{-7}	2.75×10^{-7}	5.3	4.8
15	3.142	0.2	0.1	25.3	34.2	4.6	4.2	3.6×10^{8}	288	313	6.00×10^{-6}	5.44×10^{-6}	37	1.11×10^{4}	2.99×10^{-4}	3.29×10^{-4}	6.44×10^{-7}	7.19×10^{-7}	5.7	5.1
15	2.094	0.07	0.04	23.5	33.6	3.9	3.7	3.0×10^{8}	350	361	9.33×10^{-6}	8.30×10^{-6}	54	1.94×10^{4}	5.43×10^{-4}	5.67×10^{-4}	2.14×10^{-6}	2.44×10^{-6}	6.0	5.2
15	1.466	0.03	0.02	23.8	35.1	3.5	3.3	2.8×10^{8}	377	403	1.31×10^{-5}	1.15×10^{-5}	80	3.13×10^{4}	8.37×10^{-4}	9.08×10^{-4}	6.30×10^{-6}	7.25×10^{-6}	5.9	5.1
15	1.047	0.02	0.01	22.8	34.4	3.6	3.4	2.7×10^{8}	400	409	1.88×10^{-5}	1.64×10^{-5}	127	5.15×10^{4}	1.24×10^{-3}	1.29×10^{-3}	1.78×10^{-5}	2.07×10^{-5}	6.0	5.2
15	0.524	0.004	0.003	23.8	33.1	3.7	3.5	2.8×10^{8}	375	387	3.72×10^{-5}	3.34×10^{-5}	331	1.26×10^{5}	2.32×10^{-3}	2.43×10^{-3}	1.41×10^{-4}	1.59×10^{-4}	6.0	5.3
15	0.209	0.0007	0.0004	22.6	31.7	3.4	3.0	2.3×10^{8}	399	437	9.57×10^{-5}	8.65×10^{-5}	973	4.06×10^{5}	6.17×10^{-3}	6.84×10^{-3}	2.05×10^{-3}	2.31×10^{-3}	6.1	5.5
20	8.901	1.6	0.8	33.5	37.8	8.2	8.5	2.1×10^{9}	182	177	1.01×10^{-6}	9.72×10^{-7}	21	3.78×10^{3}	3.83×10^{-5}	3.73×10^{-5}	1.64×10^{-8}	1.72×10^{-8}	4.8	4.6
20	6.283	0.8	0.4	29.2	32.9	6.7	6.5	1.3×10^{9}	247	255	1.58×10^{-6}	1.52×10^{-6}	25	6.31×10^{3}	7.28×10^{-5}	7.55×10^{-5}	4.64×10^{-8}	4.83×10^{-8}	5.3	5.1
20	4.398	0.4	0.2	27.8	34.3	5.9	5.5	1.1×10^{9}	340	361	2.31×10^{-6}	2.15×10^{-6}	34	1.21×10^{4}	1.42×10^{-4}	1.52×10^{-4}	1.58×10^{-7}	1.70×10^{-7}	5.5	5.0
20	3.142	0.2	0.1	23.4	32.0	5.0	4.5	8.6×10^{8}	404	444	3.51×10^{-6}	3.19×10^{-6}	43	1.84×10^{4}	2.34×10^{-4}	2.61×10^{-4}	3.99×10^{-7}	4.44×10^{-7}	6.0	5.4
20	2.094	0.09	0.04	23.6	32.5	4.1	4.0	7.4×10^{8}	502	511	5.26×10^{-6}	4.77×10^{-6}	63	3.23×10^{4}	4.38×10^{-4}	4.51×10^{-4}	1.37×10^{-6}	1.53×10^{-6}	6.0	5.4
20	1.466	0.04	0.02	24.5	35.0	4.0	3.8	7.6×10^{8}	538	553	7.31×10^{-6}	6.49×10^{-6}	100	5.49×10^{4}	6.72×10^{-4}	7.02×10^{-4}	4.27×10^{-6}	4.87×10^{-6}	5.8	5.1
20	1.047	0.02	0.01	23.9	33.2	3.4	3.3	6.2×10^{8}	549	558	1.04×10^{-5}	9.36×10^{-6}	132	7.36×10^{4}	9.59×10^{-4}	9.87×10^{-4}	9.94×10^{-6}	1.12×10^{-5}	5.9	5.2
20	0.524	0.006	0.003	22.0	33.0	3.6	3.4	6.2×10^{8}	533	568	2.15×10^{-5}	1.90×10^{-5}	348	1.91×10^{5}	1.85×10^{-3}	2.00×10^{-3}	8.01×10^{-5}	9.25×10^{-5}	6.2	5.3
20	0.209	0.0009	0.0004	22.8	32.9	3.0	2.8	5.3×10^{8}	624	659	5.35×10^{-5}	4.76×10^{-5}	999	6.40×10^{5}	5.43×10^{-3}	5.81×10^{-3}	1.24×10^{-3}	1.41×10^{-3}	6.1	5.3
25	8.901	2.0	0.8	32.9	39.0	9.1	8.3	4.3×10^{9}	240	261	6.49×10^{-7}	6.20×10^{-7}	23	5.92×10^{3}	3.23×10^{-5}	3.54×10^{-5}	1.22×10^{-8}	1.28×10^{-8}	4.8	4.5
25	6.283	1.0	0.4	28.5	36.2	6.9	6.7	2.9×10^{9}	330	334	1.00×10^{-6}	9.32×10^{-7}	28	9.37×10^{3}	6.22×10^{-5}	6.36×10^{-5}	3.24×10^{-8}	3.53×10^{-8}	5.3	4.9
25	4.398	0.5	0.2	27.1	35.3	5.8	5.5	2.3×10^{9}	393	411	1.47×10^{-6}	1.35×10^{-6}	37	1.49×10^{4}	1.05×10^{-4}	1.11×10^{-4}	9.24×10^{-8}	1.01×10^{-7}	5.5	4.9
25	3.142	0.3	0.1	23.8	32.7	4.9	4.5	1.6×10^{9}	502	536	2.23×10^{-6}	2.02×10^{-6}	46	2.41×10^{4}	1.87×10^{-4}	2.01×10^{-4}	2.48×10^{-7}	2.76×10^{-7}	6.0	5.3
25	2.094	0.1	0.04	24.3	34.4	4.2	4.1	1.5×10^{9}	564	575	3.30×10^{-6}	2.94×10^{-6}	72	4.10×10^{4}	3.15×10^{-4}	3.26×10^{-4}	8.35×10^{-7}	9.47×10^{-7}	5.9	5.1
25	1.466	0.05	0.02	24.1	34.9	3.8	4.0	1.4×10^{9}	613	585	4.71×10^{-6}	4.16×10^{-6}	109	6.54×10^{4}	4.89×10^{-4}	4.75×10^{-4}	2.40×10^{-6}	2.75×10^{-6}	5.9	5.1
25	1.047	0.03	0.01	24.1	33.8	3.8	3.7	1.3×10^{9}	627	635	6.63×10^{-6}	5.95×10^{-6}	161	1.01×10^{5}	7.01×10^{-4}	7.19×10^{-4}	6.55×10^{-6}	7.39×10^{-6}	5.9	5.2
25	0.524	0.007	0.003	23.6	34.7	3.3	3.1	1.2×10^{9}	733	770	1.33×10^{-5}	1.17×10^{-5}	355	2.67×10^{5}	1.63×10^{-3}	1.74×10^{-3}	5.42×10^{-5}	6.24×10^{-5}	5.9	5.1
25	0.209	0.001	0.0004	22.6	36.6	2.9	2.6	1.0×10^{9}	752	832	3.35×10^{-5}	2.86×10^{-5}	1026	8.11×10^{5}	4.20×10^{-3}	4.73×10^{-3}	7.49×10^{-4}	8.89×10^{-4}	6.0	5.0

Table 1: Experimental dataset for $l/H = 0.024$. Heights H are in cm, rotation rate Ω in rad.s^{-1} and temperatures are in degree celsius.

H	Ω	$\Omega^2 H/\mathrm{g}$	Fr	T_{start}	T_{end}	ΔT_{I}	ΔT_{II}	Ra	Nu_{I}	$\mathrm{Nu}_{\mathrm{II}}$	E_{I}	E_{II}	$\widetilde{\mathrm{Ra}}$	$\widetilde{\mathrm{Ra}_{\mathrm{P}}}$	$\mathcal{N}_{\mathrm{I}}$	$\mathcal{N}_{\mathrm{II}}$	$\mathcal{R}_{\mathrm{I}}$	$\mathcal{R}_{\mathrm{II}}$	Pr_{I}	$\mathrm{Pr}_{\mathrm{II}}$
10	8.901	0.8	0.8	33.4	35.6	7.7	7.8	2.3×10^{8}	156	153	4.12×10^{-6}	4.02×10^{-6}	15	2.36×10^{3}	1.30×10^{-4}	1.29×10^{-4}	1.04×10^{-7}	1.04×10^{-7}	4.9	4.7
10	6.283	0.4	0.4	27.6	34.3	5.3	4.5	1.2×10^{8}	155	181	6.49×10^{-6}	6.02×10^{-6}	15	2.47×10^{3}	1.82×10^{-4}	2.14×10^{-4}	1.85×10^{-7}	1.87×10^{-7}	5.5	5.0
10	4.398	0.2	0.2	27.2	35.2	4.1	3.9	1.0×10^{8}	228	235	9.31×10^{-6}	8.49×10^{-6}	19	4.48×10^{3}	3.82×10^{-4}	3.99×10^{-4}	6.07×10^{-7}	6.19×10^{-7}	5.5	5.0
10	3.142	0.1	0.1	28.1	35.7	3.2	3.4	8.9×10^{7}	333	305	1.28×10^{-5}	1.17×10^{-5}	25	8.07×10^{3}	7.84×10^{-4}	7.25×10^{-4}	1.93×10^{-6}	1.96×10^{-6}	5.4	4.9
10	2.094	0.04	0.04	24.6	32.4	2.8	2.9	6.7×10^{7}	362	355	2.07×10^{-5}	1.89×10^{-5}	36	1.29×10^{4}	1.26×10^{-3}	1.25×10^{-3}	5.81×10^{-6}	5.94×10^{-6}	5.9	5.3
10	1.466	0.02	0.02	24.5	30.2	2.6	2.7	5.8×10^{7}	384	361	3.01×10^{-5}	2.81×10^{-5}	53	1.95×10^{4}	1.91×10^{-3}	1.81×10^{-3}	1.57×10^{-5}	1.60×10^{-5}	6.0	5.6
10	1.047	0.01	0.01	24.4	35.3	2.8	2.6	6.6×10^{7}	377	407	4.09×10^{-5}	3.62×10^{-5}	87	3.41×10^{4}	2.64×10^{-3}	2.89×10^{-3}	4.93×10^{-5}	5.07×10^{-5}	5.8	5.0
10	0.209	0.0004	0.0004	23.8	31.8	2.5	2.3	5.4×10^{7}	390	414	2.11×10^{-4}	1.92×10^{-4}	647	2.60×10^{5}	1.36×10^{-2}	1.46×10^{-2}	5.37×10^{-3}	5.50×10^{-3}	6.0	5.4
15	8.901	1.2	0.8	34.0	38.3	6.1	5.9	6.5×10^{8}	176	180	1.78×10^{-6}	1.71×10^{-6}	14	2.47×10^{3}	6.60×10^{-5}	6.80×10^{-5}	2.87×10^{-8}	2.89×10^{-8}	4.7	4.5
15	6.283	0.6	0.4	26.9	33.6	5.5	5.3	4.6×10^{8}	261	271	2.91×10^{-6}	2.71×10^{-6}	18	4.92×10^{3}	1.36×10^{-4}	1.42×10^{-4}	9.47×10^{-8}	9.61×10^{-8}	5.6	5.1
15	3.142	0.2	0.1	26.2	35.3	3.9	3.6	3.3×10^{8}	407	432	5.84×10^{-6}	5.30×10^{-6}	33	1.37×10^{4}	4.24×10^{-4}	4.55×10^{-4}	8.42×10^{-7}	8.59×10^{-7}	5.6	5.0
15	2.094	0.07	0.04	22.1	33.0	3.3	3.0	2.3×10^{8}	489	536	9.61×10^{-6}	8.48×10^{-6}	45	2.31×10^{4}	7.56×10^{-4}	8.42×10^{-4}	2.63×10^{-6}	2.72×10^{-6}	6.2	5.4
15	1.047	0.02	0.01	22.4	33.6	2.8	2.6	2.0×10^{8}	595	618	1.89×10^{-5}	1.67×10^{-5}	98	5.92×10^{4}	1.84×10^{-3}	1.94×10^{-3}	2.16×10^{-5}	2.23×10^{-5}	6.1	5.3
15	0.209	0.0007	0.0004	24.2	35.0	2.3	2.0	1.8×10^{8}	578	644	9.14×10^{-5}	8.08×10^{-5}	686	4.17×10^{5}	8.98×10^{-3}	1.01×10^{-2}	2.27×10^{-3}	2.34×10^{-3}	5.8	5.1
20	8.901	1.6	0.8	32.4	37.2	6.3	6.5	1.5×10^{9}	228	219	1.04×10^{-6}	9.86×10^{-7}	16	3.57×10^{3}	4.79×10^{-5}	4.62×10^{-5}	1.56×10^{-8}	1.57×10^{-8}	4.9	4.6
20	6.283	0.8	0.4	26.9	32.1	5.2	5.4	1.0×10^{9}	313	300	1.66×10^{-6}	1.56×10^{-6}	20	6.06×10^{3}	9.17×10^{-5}	8.84×10^{-5}	4.41×10^{-8}	4.47×10^{-8}	5.6	5.3
20	3.142	0.2	0.1	24.8	35.9	4.4	4.3	8.7×10^{8}	493	492	3.39×10^{-6}	2.99×10^{-6}	41	2.01×10^{4}	2.87×10^{-4}	2.92×10^{-4}	4.65×10^{-7}	4.78×10^{-7}	5.8	5.0
20	2.094	0.09	0.04	25.5	35.6	3.5	3.5	7.2×10^{8}	618	607	5.01×10^{-6}	4.47×10^{-6}	58	3.53×10^{4}	5.42×10^{-4}	5.40×10^{-4}	1.61×10^{-6}	1.65×10^{-6}	5.7	5.0
20	1.047	0.02	0.01	23.0	35.0	3.0	3.0	5.7×10^{8}	672	653	1.05×10^{-5}	9.17×10^{-6}	120	7.98×10^{4}	1.17×10^{-3}	1.15×10^{-3}	1.12×10^{-5}	1.16×10^{-5}	6.0	5.1
20	0.209	0.0009	0.0004	24.2	36.8	2.0	1.8	3.9×10^{8}	816	919	5.08×10^{-5}	4.41×10^{-5}	674	5.82×10^{5}	7.14×10^{-3}	8.19×10^{-3}	1.22×10^{-3}	1.26×10^{-3}	5.8	4.9
25	8.901	2.0	0.8	28.3	32.5	7.6	7.8	3.0×10^{9}	302	294	7.33×10^{-7}	6.99×10^{-7}	20	5.83×10^{3}	4.00×10^{-5}	3.92×10^{-5}	1.12×10^{-8}	1.18×10^{-8}	5.5	5.2
25	6.283	1.0	0.4	28.0	33.0	6.2	6.0	2.3×10^{9}	409	418	1.04×10^{-6}	9.89×10^{-7}	24	1.01×10^{4}	7.69×10^{-5}	7.89×10^{-5}	3.47×10^{-8}	3.67×10^{-8}	5.5	5.2
25	4.398	0.5	0.2	24.5	30.8	4.1	3.8	1.3×10^{9}	473	504	1.59×10^{-6}	1.48×10^{-6}	25	1.21×10^{4}	1.25×10^{-4}	1.35×10^{-4}	7.21×10^{-8}	7.79×10^{-8}	5.9	5.5
25	3.142	0.3	0.1	22.2	29.7	4.4	4.2	1.4×10^{9}	626	649	2.33×10^{-6}	2.14×10^{-6}	41	2.63×10^{4}	2.31×10^{-4}	2.42×10^{-4}	2.64×10^{-7}	2.92×10^{-7}	6.3	5.7
25	2.094	0.1	0.04	20.8	30.9	3.7	3.6	1.1×10^{9}	741	757	3.58×10^{-6}	3.19×10^{-6}	60	4.47×10^{4}	4.10×10^{-4}	4.25×10^{-4}	8.63×10^{-7}	9.89×10^{-7}	6.4	5.6
25	1.466	0.05	0.02	23.1	31.1	2.4	2.4	8.3×10^{8}	865	850	4.89×10^{-6}	4.47×10^{-6}	66	5.64×10^{4}	6.88×10^{-4}	6.84×10^{-4}	2.04×10^{-6}	2.27×10^{-6}	6.1	5.5
25	1.047	0.03	0.01	20.3	30.0	3.3	3.3	1.0×10^{9}	856	865	7.26×10^{-6}	6.49×10^{-6}	135	1.16×10^{5}	9.47×10^{-4}	9.70×10^{-4}	7.06×10^{-6}	8.08×10^{-6}	6.5	5.7
25	0.209	0.001	0.0004	21.7	29.8	2.3	2.1	6.6×10^{8}	1016	1098	3.70×10^{-5}	3.33×10^{-5}	765	8.07×10^{5}	5.60×10^{-3}	6.13×10^{-3}	7.10×10^{-4}	8.07×10^{-4}	6.7	5.9

Table 2: Experimental dataset for $l/H = 0.048$. Heights H are in cm, rotation rate Ω in rad.s^{-1} and temperatures are in degree celsius.

Experimental observation of the geostrophic turbulence regime of rapidly rotating convection

Vincent Bouillaut[a], **Benjamin Miquel**[a], **Keith Julien**[b], **Sébastien Aumaître**[a], **and Basile Gallet**[a,1]

[a]Service de Physique de l'Etat Condensé, Université Paris-Saclay, CNRS, Commissariat à l'énergie atomique et aux énergies alternatives, 91191 Gif-sur-Yvette, France; and [b]Department of Applied Mathematics, University of Colorado, Boulder, CO 80309

Edited by Jonathan M. Aurnou, University of California, Los Angeles, CA, and accepted by Editorial Board Member Michael Manga September 14, 2021 (received for review March 15, 2021)

The competition between turbulent convection and global rotation in planetary and stellar interiors governs the transport of heat and tracers, as well as magnetic field generation. These objects operate in dynamical regimes ranging from weakly rotating convection to the "geostrophic turbulence" regime of rapidly rotating convection. However, the latter regime has remained elusive in the laboratory, despite a worldwide effort to design ever-taller rotating convection cells over the last decade. Building on a recent experimental approach where convection is driven radiatively, we report heat transport measurements in quantitative agreement with this scaling regime, the experimental scaling law being validated against direct numerical simulations (DNS) of the idealized setup. The scaling exponent from both experiments and DNS agrees well with the geostrophic turbulence prediction. The prefactor of the scaling law is greater than the one diagnosed in previous idealized numerical studies, pointing to an unexpected sensitivity of the heat transport efficiency to the precise distribution of heat sources and sinks, which greatly varies from planets to stars.

turbulent convection | geophysical and astrophysical fluid dynamics | rotating flows

The strong buoyancy gradients inside planets and stars drive turbulent convective flows that are responsible for the efficient transport of heat and tracers, as well as for the generation of the magnetic fields of these objects through the dynamo effect. This thermal and/or compositional driving competes with the global rotation of the astrophysical object: While moderate global rotation only affects the largest flow structures (1–3), rapid global rotation greatly impedes radial motion through the action of the Coriolis force, thereby restricting the convective heat transfer (4, 5). Because astrophysical and geophysical flows operate at extreme parameter values, beyond what will ever be achieved in laboratory experiments and numerical simulations, the characterization of these highly complex flows proceeds through the experimental or numerical determination of the constitutive equation, or scaling law, that relates the turbulent heat flux to the internal temperature gradients. Extrapolating this scaling law to the extreme parameter values of astrophysical objects sets the effective transport coefficients, the turbulent energy dissipation rate, the mixing efficiency, and the power available to induce magnetic field (4, 6–11).

Within the Boussinesq approximation (12) and adopting a local Cartesian geometry, the scaling laws are cast in terms of the dimensionless parameters that govern the system: the flux-based Rayleigh number $\mathrm{Ra_P} = \alpha g P H^4/\rho C \kappa^2 \nu$ quantifies the strength of the heat flux P, where H denotes the height of the fluid domain, α is the coefficient of thermal expansion, g is the acceleration of gravity, κ is the thermal diffusivity, ν is the kinematic viscosity, ρ is the mean density, and C is the specific heat capacity. The Nusselt number $\mathrm{Nu} = PH/\rho C \kappa \Delta T$ measures the heat transport efficiency of the turbulent flow, as compared to that of a steady motionless fluid, in terms of the typical vertical temperature drop ΔT. Finally, the magnitude of the Coriolis force can be quantified through the Ekman number $\mathrm{E} = \nu/2\Omega H^2$, a low value of E corresponding to a rapid global rotation rate Ω.

At the theoretical level, several arguments have been put forward to predict the scaling law for the heat transport efficiency of rotationally constrained turbulent convection, as measured by the Nusselt number Nu. Central to these theories is the assumption that the scaling relation between the turbulent heat flux and the internal temperature gradient should not involve the tiny molecular diffusivities κ and ν. In the physics community, this assumption is sometimes referred to as the existence of an "ultimate regime" (13), while, in the astrophysical community, it is often referred to as the "mixing-length" regime, because the latter theory neglects molecular diffusivities at the outset (6, 14).

The second assumption is that the heat transport efficiency of the flow depends only on the supercriticality of the system, that is, on the ratio of the Rayleigh number to the threshold Rayleigh number for the emergence of thermal convection. This idea is put on firm analytical footing through careful asymptotic expansions of the equations of thermal convection in the rapidly rotating limit (5, 15–17). When combined, these two assumptions lead to the following scaling law for turbulent heat transport by rapidly rotating thermal convection (see ref. 4 for the initial derivation):

$$\mathrm{Nu} = \mathcal{C} \times \mathrm{Ra_P}^{3/5}\, \mathrm{E}^{4/5}\, \mathrm{Pr}^{-1/5}, \qquad \textbf{[1]}$$

where $\mathrm{Pr} = \nu/\kappa$ is the Prandtl number and $\mathcal{C}$ is a dimensionless prefactor. Eq. **1** is referred to as the "geostrophic

Significance

Turbulent convection is the main process through which nature moves fluids around, be it in deep planetary and stellar interiors or in the external fluid layers of planets and their satellites. Laboratory studies aim at reproducing the resulting fully turbulent flows, with the goal of determining the effective transport coefficients to be input into coarse geophysical or astrophysical models. Crucial to these applications is planetary or stellar rotation, which competes with convective processes to set the emergent transport properties. Building on a recent experimental approach that bypasses the limitations of boundary-forced convective flows, we report laboratory measurements in quantitative agreement with the fully turbulent regime of rotating convection.

Author contributions: V.B., B.M., S.A., and B.G. designed research; V.B., B.M., S.A., and B.G. performed research; V.B., B.M., K.J., S.A., and B.G. analyzed data; and V.B., B.M., K.J., S.A., and B.G. wrote the paper.

The authors declare no competing interest.

This article is a PNAS Direct Submission. J.M.A. is a guest editor invited by the Editorial Board.

[1]To whom correspondence may be addressed. Email: basile.gallet@cea.fr.

This article contains supporting information online at https://www.pnas.org/lookup/suppl/doi:10.1073/pnas.2105015118/-/DCSupplemental.

Published October 25, 2021.

turbulence" scaling law of rapidly rotating convection.* In terms of the temperature-based Rayleigh number $\mathrm{Ra} = \mathrm{Ra_P}/\mathrm{Nu}$, this scaling law becomes

$$\mathrm{Nu} = \mathcal{C}_{\mathrm{Ra}} \times \mathrm{Ra}^{3/2}\,\mathrm{E}^{2}\,\mathrm{Pr}^{-1/2}\,, \qquad [2]$$

where the dimensionless prefactor is $\mathcal{C}_{\mathrm{Ra}} = \mathcal{C}^{5/2}$. Over the last decade, several state-of-the-art laboratory experiments have been developed to observe this extreme scaling regime and validate the geostrophic turbulence scaling law [**1**]: the Turbulent Rotating Convection to the Extreme (TROCONVEX) experiment in Eindhoven (18), the rotating U-boot experiment in Göttingen (19, 20), the Trieste experiment at International Centre for Theoretical Physics (21, 22), and the Romag and Nomag experiments at University of California, Los Angeles (23, 24). The goal is to produce a strongly turbulent convective flow in which rotational effects remain predominant (hence the ever-taller convective cells), while avoiding parasitic centrifugal effects (25). These experiments are all based on the Rayleigh–Bénard (RB) geometry, where a layer of fluid is contained between a hot bottom plate and a cold top one. A particularly challenging task then is to overcome the throttling effect of the boundary layers near these two plates: Fluid hardly moves there, and heat needs be diffused away from those regions (26). Even though asymptotic analysis indicates that heat transport should be controlled by the bulk turbulent flow in rapidly rotating RB convection, laboratory realizations indicate that the boundary processes keep limiting the heat transfer throughout the entire cell (27), bringing the molecular diffusivities back into play and preventing the observation of the scaling law [**1**] associated with the bulk rotating turbulent flow. Forty years after its initial derivation (4) and despite a worldwide effort to design ever-taller convection cells, the geostrophic regime of rapidly rotating convection still awaits experimental validation (28).

Recently, we introduced an innovative laboratory setup to overcome the above-mentioned limitations of RB convection as a model for bulk natural flows (29). Specifically, we used a combination of radiative internal heating and effective internal cooling to bypass the throttling boundary layers of traditional RB convection and achieve the fully turbulent–or "ultimate"–regime of nonrotating convection (29–31). These recent experimental developments suggest an alternative route to observe the geostrophic regime of rapidly rotating turbulent convection in the laboratory: Instead of trying to overcome the throttling effect of the RB boundary layers through intense thermal forcing, one can take advantage of the radiatively driven setup, where these boundary layers are readily bypassed, and subject the radiatively driven turbulent convective flow to rapid global rotation.

The resulting experimental setup, sketched in Fig. 1, is an evolution over the nonrotating setup described in a previous publication (29). The apparatus consists of a cylindrical tank of radius 10 cm with a transparent sapphire bottom boundary, filled with a light-absorbing mixture of water and carbon-black dye. A powerful spotlight located under a water-cooled infrared (IR) screening stage shines at the tank from below. Absorption of light by the dye results in an internal heat source that decreases exponentially with height z measured upward from the bottom of the tank, transferring to the fluid a total heat flux P over an e-folding absorption length ℓ. This source term causes the temperature at every location inside the tank to increase linearly with time. Superposed to this linear drift are internal temperature gradients that develop inside the tank and rapidly reach a statistically steady state. As recalled in *Materials and Methods*, the internal temperature difference between any two points inside the tank is then governed by a combination of the exponential radiative heat source together with an effective uniform heat sink.

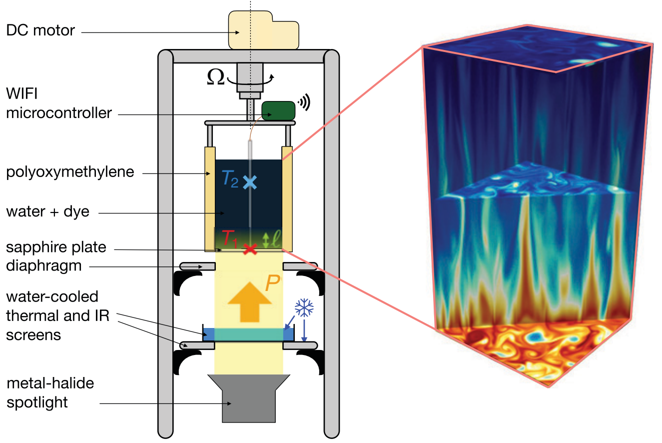

Fig. 1. Radiatively driven rotating convection. A powerful spotlight shines from below at a mixture of water and dye. The resulting internal heat source decreases exponentially with height over the absorption length ℓ, delivering a total heat flux P. The cylindrical tank is attached from above to a DC motor that imposes global rotation at a rate Ω (slight curvature of the top free surface not represented). Two thermocouples T_1 and T_2 measure the vertical temperature drop in the rotating frame, the data being communicated through WIFI to a remote Arduino microcontroller. On the right-hand side is a DNS snapshot of the temperature field in horizontally periodic geometry devoid of centrifugal and sidewall effects, highlighting the vertically elongated structures of rotating convection ($\mathrm{Ra_P} = 10^{12}$, $\mathrm{E} = 2 \times 10^{-6}$, $\mathrm{Pr} = 7$, $\ell/H = 0.048$, arbitrary color scale ranging from blue for cool fluid to red for warm fluid).

The experimental tank is attached from above to a DC motor that drives global rotation at a constant rate $\Omega \in [0; 85]$ rpm around the vertical axis of the cylinder. Rotation results in a slight curvature of the free surface: The relative variations in fluid height between center and periphery reach $\pm 20\%$ and $\pm 13\%$ for the two most rapidly rotating and shallowest data points, but are below $\pm 10\%$ (and often much below) for the remaining $\sim$60 data points. Onboard temperature measurements are performed using two thermocouples, one in contact with the bottom sapphire plate and one at $z = 3H/4$, where H denotes the height of the free surface on the axis of the cylindrical cell, where the probes are located. The temperature signals are transmitted through WIFI to a remote Arduino microcontroller to ensure live monitoring of the experimental runs.

We show, in Fig. 2, the Nusselt number based on the time-averaged temperature difference ΔT between the two probes, for experimental runs spanning 1.5 decades in $\mathrm{Ra_P}$ and 2.5 decades in E, and two values of the dimensionless absorption length ℓ/H. The dataset is provided in *SI Appendix*, Tables 1–2, together with estimates of the error bars. In a similar fashion to the more standard RB system, for an approximately constant $\mathrm{Ra_P}$, an increase in the global rotation rate leads to a dramatic drop in the heat transport efficiency as measured by the Nusselt number Nu. †

With the goal of establishing the turbulent nature of the flow and assessing the independence of its transport properties with respect to the molecular diffusivities, we form the ν- and κ-independent reduced Nusselt number $\mathcal{N} = \mathrm{Nu}\,\mathrm{E}/\mathrm{Pr}$, together with the composite control parameter $\mathcal{R} = \mathrm{Ra_P}\,\mathrm{E}^3/\mathrm{Pr}^2$. The latter combination is the only dimensionless control parameter if

---

*Geostrophy refers to the large-scale balance between the Coriolis and pressure forces.

†As shown in *SI Appendix*, Tables 1–2, the temperature range varies between different data points, the consequence being that $\mathrm{Ra_P}$ and Pr vary between different points of a constant-H curve in Fig. 2. The entire range of Pr spanned by the experimental data is $4.4 \leq \mathrm{Pr} \leq 6.7$.

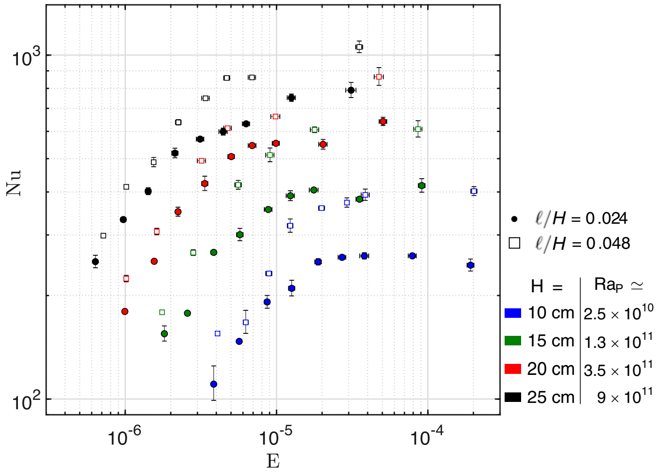

Fig. 2. Suppression of heat transport by global rotation. Heat transport efficiency Nu as a function of the Ekman number E, for various fluid heights: blue, $H = 10$ cm, $\mathrm{Ra_P} \simeq 2.5 \times 10^{10}$; green, $H = 15$ cm, $\mathrm{Ra_P} \simeq 1.3 \times 10^{11}$; red, $H = 20$ cm, $\mathrm{Ra_P} \simeq 3.5 \times 10^{11}$; black, $H = 25$ cm, $\mathrm{Ra_P} \simeq 9 \times 10^{11}$. The dimensionless absorption length is $\ell/H = 0.024$ (filled circles) or $\ell/H = 0.048$ (open squares). For fixed H and ℓ, the mixing efficiency dramatically decreases with increasing rotation rate (decreasing E). Error bars are estimated from the values obtained for the first and second halves of the measurement interval; see *Materials and Methods* and *SI Appendix*.

the diffusivities are to play no roles (9, 10, 32). $\mathcal{R}$ is also the cube of the so-called flux-based convective Rossby number, identified as the main control parameter of open ocean convection (17, 33). We plot $\mathcal{N}$ as a function of $\mathcal{R}$ in Fig. 3 (data points and estimates of the error are provided in *SI Appendix*). In this representation, the dataset for a given value of ℓ/H collapses onto a single master curve, which validates the fact that the molecular diffusivities are irrelevant: We conclude that the present experimental setup achieves a "fully turbulent" scaling regime, according to the definition given at the outset. The collapse is particularly good for rapid global rotation and slow global rotation–low and large $\mathcal{R}$, respectively–with a bit more scatter for intermediate values. For slow global rotation (large $\mathcal{R}$), the master curve gradually approaches the scaling law of radiatively driven nonrotating convection, reported in previous publications (29–31). This regime is associated with a large-$\mathcal{R}$ asymptote of the form $\mathcal{N} \approx \mathcal{R}^{1/3}$, represented in Fig. 3: After crossing out E from both sides of the scaling relation $\mathcal{N} \approx \mathcal{R}^{1/3}$, one recovers the ultimate scaling law of nonrotating convection, where Nu is proportional to the square root of Ra (29–31). The approach to that asymptotic behavior is clearly visible for $\ell/H = 0.024$ at large $\mathcal{R}$, with a bit more scatter for $\ell/H = 0.048$.[‡] More interestingly, the focus of the present study is on the rapidly rotating regime that arises for $\mathcal{R} \lesssim 3 \times 10^{-7}$. In this parameter range, the master curve follows a power-law behavior $\mathcal{N} \approx \mathcal{R}^{\beta}$ over one and a half decades. The best-fit exponents β are given in Table 1. Over the last decade in $\mathcal{R}$, we measure $\beta = 0.57 \pm 0.03$ and $\beta = 0.62 \pm 0.01$, respectively, for $\ell/H = 0.024$ and $\ell/H = 0.048$. These values are within 5% of the theoretical exponent $\beta = 3/5$ associated with the geostrophic turbulence scaling-law [**1**].

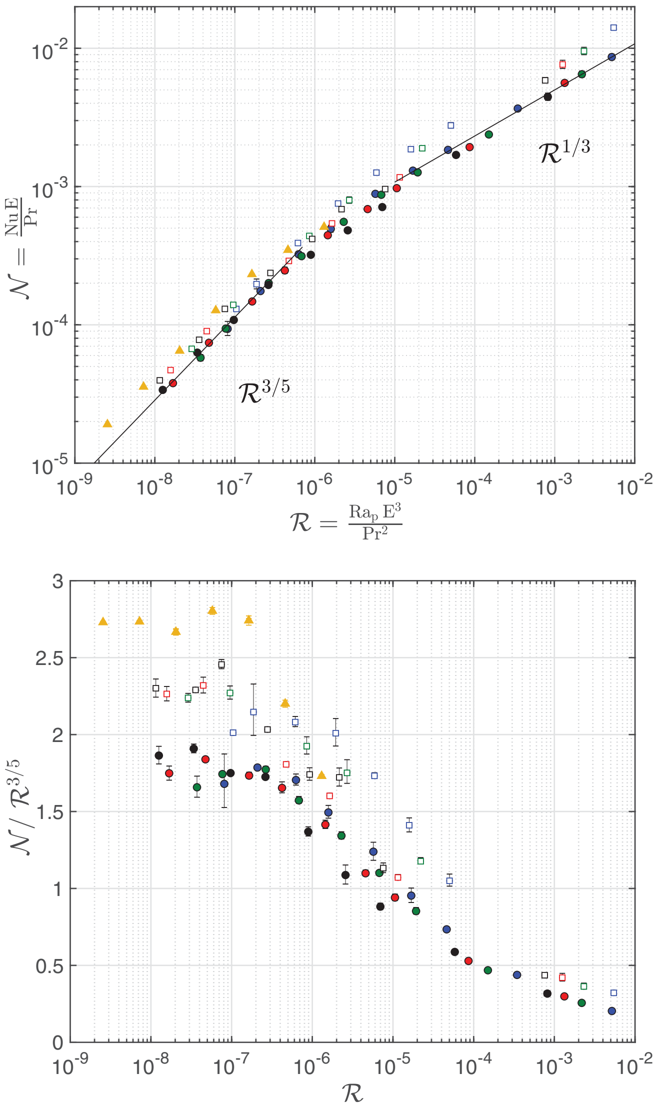

Fig. 3. Observation of the geostrophic turbulence regime. (*Top*) In terms of the diffusivity-independent parameters $\mathcal{N}$ and $\mathcal{R}$, the data gathered for a given value of ℓ/H collapse onto a master curve, which validates the "fully turbulent" assumption. In the rapidly rotating regime $\mathcal{R} \lesssim 3 \times 10^{-7}$, the master curve displays a power-law behavior over one and a half decades in $\mathcal{R}$, in excellent agreement with the prediction $\mathcal{N} \approx \mathcal{R}^{3/5}$ associated with the geostrophic turbulence scaling regime of rapidly rotating convection (shown as an eye guide; see Table 1 for best-fit exponents). Same symbols as in Fig. 2 for the experimental data. The triangles are DNS data for $\mathrm{Ra_P} = 10^{12}$, $\mathrm{Pr} = 7$, and $\ell/H = 0.048$. Experimental and numerical error bars are visible when larger than the symbol size. (*Bottom*) Same data compensated by the geostrophic turbulence scaling prediction. An approximate plateau is observed for $\mathcal{R} \lesssim 3 \times 10^{-7}$.

While the flux-based parameter $\mathcal{R}$ is the natural control parameter of the present experiment, the reader accustomed to the standard RB setup may be interested in characterizing the data in terms of the Rayleigh number Ra based on the emergent temperature gradient. In *SI Appendix*, we thus plot $\mathcal{N}$ as a function of the diffusivity-free Rayleigh number $\mathrm{Ra}_* = \mathrm{Ra\,E^2/Pr}$ [also known as the square of the temperature-based convective Rossby number (17)]. This representation is equivalent to the one in Fig. 3, with an equally satisfactory collapse of the dataset. The power-law fits reported in Table 1 translate into power laws $\mathcal{N} \approx \mathrm{Ra}_*^{\gamma}$, where the exponent γ is within 12% of the theoretical prediction 3/2 ($\gamma = 1.33 \pm 0.14$ and $\gamma = 1.63 \pm 0.07$, respectively, for $\ell/H = 0.024$ and $\ell/H = 0.048$).

These values contrast with the scaling exponent γ in the constant-E scaling law $\mathrm{Nu} \approx \mathrm{Ra}^{\gamma}$ reported in laboratory studies of rotating RB convection (see ref. 34 for a recent review). According to the literature, the RB exponent measured experimentally achieves a value close to 1/3 in the slowly rotating

---

[‡] One would probably need to reach larger $\mathcal{R}$ to avoid any signature of the intermediate-$\mathcal{R}$ scatter.

Table 1. Best-fit exponent β for laboratory and DNS data, to be compared to the theoretical prediction 3/5 associated with the geostrophic turbulence scaling regime

β	$\mathcal{R} \le 3 \times 10^{-7}$	$\mathcal{R} \le 10^{-7}$
Experiments $\ell/H = 0.024$	0.59 ± 0.01	0.57 ± 0.03
Experiments $\ell/H = 0.048$	0.57 ± 0.01	0.62 ± 0.01
DNS $\ell/H = 0.048$	0.601 ± 0.002	0.601 ± 0.002

The error $\pm\sigma_\beta$ is estimated by propagating the error on $\log \mathcal{N}$ into an SD σ_β for the exponent.

regime, in line with the "classical theory" of nonrotating RB convection (26). For fast rotation and moderate supercriticality, laboratory experiments typically enter a transitional regime where the exponent γ increases sharply. An extension of the experimental data using direct numerical simulations (DNS) indicates that γ eventually reaches a value ranging between three and four (23), the lower value, three, being again associated with a "classical" regime controlled by marginally stable boundary layers (35), while the larger value, four, has been attributed to Ekman pumping (36) (see also ref. 37 for a theoretical demonstration of increasing heat transport exponents as a result of boundary layer pumping). By contrast, in the present experiment, radiative heating bypasses the boundary layers of standard rotating RB convection, thus circumventing the limitations of this traditional setup and providing experimental observations in excellent agreement with the geostrophic scaling regime of rapidly rotating turbulent convection.

As a side note, we stress the fact that the system operates far above the instability threshold. In the rapidly rotating limit, convection arises above a threshold value of the order of 15 for the reduced flux-based Rayleigh number $\mathrm{Ra_P}\,\mathrm{E}^{4/3}$. We report the values of $\mathrm{Ra_P}\,\mathrm{E}^{4/3}$ in *SI Appendix*: In the rapidly rotating regime, this parameter ranges between 1.5×10^3 and 2.5×10^4, orders of magnitude above its threshold value. This large distance from threshold is confirmed by the large values of the Nusselt number in Fig. 2, which range between 10^2 and 10^3. The collapse in Fig. 3 is thus not a mere consequence of near-onset behavior, a phenomenon reported in Cheng and Aurnou (38) for synthetic near-onset data. We illustrate this point further in Fig. 3, *Bottom*, where we plot $\mathcal{N}$ compensated by the geostrophic turbulence scaling law $\mathcal{R}^{3/5}$, in semilogarithmic coordinates. This rather stringent representation confirms 1) the good collapse of the data and 2) the existence of a plateau at low $\mathcal{R}$, in agreement with the geostrophic turbulence scaling law. By contrast, the near-onset data discussed by Cheng and Aurnou would not display such a collapse onto a plateau in compensated form, as illustrated in *SI Appendix*, Fig. S2. We further emphasize this point in *SI Appendix* by plotting the Nusselt number multiplied by $\sqrt{\mathrm{Pr}}$–to collapse the various Pr data points, according to the geostrophic turbulence scaling–as a function of the reduced temperature-based Rayleigh number $\mathrm{Ra}\,\mathrm{E}^{4/3}$. The resulting *SI Appendix*, Fig. S3 makes it clear that the present data do not correspond to the near-onset behavior discussed by Cheng and Aurnou in the RB context: They are associated with greater supercriticality–the latter being better estimated by the even greater reduced flux-based Rayleigh number $\mathrm{Ra_P}\,\mathrm{E}^{4/3}$ in the present context–and a scaling exponent compatible with the $\gamma = 3/2$ geostrophic turbulence value (see *SI Appendix* for details).

It proves insightful to compare the present experimental results to existing numerical studies. DNS have been used as an extremely valuable tool both to address rotating convection inside full or partial spheres (39) and also to develop thought experiments in which one can alter the exact equations and/or boundary conditions to identify the mechanisms at play. This leads to idealized situations in which the geostrophic scaling regime emerges. Some studies have considered stress-free boundary conditions instead of the no-slip boundaries of experimental tanks (40, 41), some have used tailored internal heat sources and sinks that conveniently vanish at the boundaries of the domain (42, 43), and some have focused on reduced sets of equations obtained through an asymptotic expansion of the rapidly rotating Boussinesq equations (15, 16, 44). DNS also offer an opportunity to eliminate the potential biases of laboratory experiments. One source of experimental bias is the centrifugal acceleration, which increases with global rotation rate and distance from the rotation axis. Horn and Aurnou (25) proposed the criterion $\Omega^2 H/g \lesssim 1$ for centrifugal effects to be negligible in standard rotating RB convection (see also refs. 45 and 46). The precise threshold value on the right-hand side of this inequality can probably be debated and requires further investigation; specifically, Cheng et al. (18) report experimental measurements unaffected by centrifugal effects even when $\Omega^2 H/g$ is as large as two. In *SI Appendix*, we provide the value of $\Omega^2 H/g$ for all the experimental data points: This ratio never exceeds two, with only three data points for which this ratio exceeds one (per value of ℓ/H). A second distinction between the idealized horizontally unbounded convective layer and the finite-size experimental tanks is the possible emergence of localized convective modes near the vertical walls of the latter (47–50). Wall modes have a lower onset than bulk modes and can dominate the dynamics near the instability threshold of the latter. However, they have also been shown to have a negligible impact on bulk heat transport in the turbulent regime (51). The collapse of the various data points in Fig. 3–which differ in terms of both centrifugal ratio $\Omega^2 H/g$ and aspect ratio–is a first indication that the present measurements are not impacted by the centrifugal acceleration nor the sidewalls.

With the goal of further validating the experimental results and the subdominance of centrifugal, sidewall, and non-Boussinesq effects, we have performed DNS of the present radiatively driven setup in the idealized horizontally periodic plane layer geometry. The combination of radiative heating and uniform internal cooling is implemented in a pseudospectral code that solves the rotating Boussinesq equations of thermal convection with a no-slip insulating bottom boundary and a stress-free insulating top one (see *Materials and Methods* for details). We provide a snapshot of the temperature field in statistically steady state in Fig. 1, for $\mathrm{Ra_P} = 10^{12}$, $\mathrm{E} = 2 \times 10^{-6}$, $\mathrm{Pr} = 7$, and $\ell/H = 0.048$. This temperature field displays the typical vertically elongated structures that characterize rapidly rotating convection (28), with a predominance of thin warm plumes emanating from the heating region. The full numerical dataset consists in a sweep of the Ekman number E for $\mathrm{Ra_P} = 10^{12}$, $\mathrm{Pr} = 7$, and $\ell/H = 0.048$, the resulting data points being plotted in Fig. 3. The error bars on these data points, provided in *SI Appendix*, Table 3, are much smaller than the size of the symbols. The low-$\mathcal{R}$ numerical data again display a power-law behavior, with a best-fit exponent β within 0.5% of the theoretical exponent 3/5 associated with the geostrophic turbulence scaling regime; see Table 1. The numerical data points lie very close to the experimental ones for the same value of ℓ/H, the reduced Nusselt number being slightly larger for the DNS data (by ∼20%), possibly as a consequence of the somewhat different geometries of the numerical and experimental setups. Overall, the quantitative agreement between experiments and DNS, together with the good collapse in Fig. 3 of data points obtained for various aspect ratios and centrifugal ratios, indicates that the aforementioned potential biases are subdominant in the present experiment. As far as the present heat transport measurements are concerned, the central region of the tank seems hardly affected by the centrifugal effects, by the sidewalls, by the slight curvature of the free surface, or by non-Boussinesq effects.

In some sense, our experiment follows a strategy similar to Barker et al. (42) while proposing a situation that can be realized in the laboratory. It thus comes as a surprise that the heat transport efficiency measured in the present experiment is significantly greater than the one reported in the idealized numerical setups of Barker et al. (42), Stellmach et al. (40), and Julien et al. (16) in Cartesian geometry, and in Gastine et al. (39) in spherical geometry: The experimentally measured value of the prefactor $\mathcal{C}$ is approximately twice as large as the value extracted from Barker et al. (42), it is 6 times greater than the value reported in Julien et al. (16), and it is 3 times larger than the value reported in Gastine et al. (39) (the latter in spherical geometry). In terms of the prefactor appearing in the scaling law [**2**], this translates into an experimentally measured $\mathcal{C}_{\mathrm{Ra}}$ that is approximately 6 times greater than the value extracted from Barker et al. (42), 60 times greater than the value reported in Julien et al. (16), and 20 times greater than the value reported in Gastine et al. (39). This points to an unexpected sensitivity of the heat transport efficiency of rapidly rotating turbulent convection to the precise spatial distribution of heat sources and sinks. We confirmed this conclusion experimentally by doubling the value of the absorption length ℓ/H, from $\ell/H = 0.024$ to $\ell/H = 0.048$: this change in the geometry of the heat source leads to an increase in the prefactor $\mathcal{C}$ by approximately 30%, and an approximate doubling of the prefactor $\mathcal{C}_{\mathrm{Ra}}$. Beyond the observation of the geostrophic turbulence heat transport scaling law [**1**], our laboratory setup thus offers a unique experimental opportunity to determine the dependence of the prefactor on the distribution of heat sources and sinks, which greatly varies from planets to stars.

Materials and Methods

Radiative Heating and Effective Uniform Cooling. Within the framework of the Boussinesq approximation, and denoting the temperature and velocity fields as T and $\mathbf{u}$, respectively, the temperature equation for the radiatively heated fluid reads

$$\partial_t(\rho C T) + \mathbf{u}\cdot\boldsymbol{\nabla}(\rho C T) = \rho C \kappa \boldsymbol{\nabla}^2 T + \frac{P}{\ell} e^{-z/\ell}, \qquad [3]$$

where the radiative heating term–the last term on the right-hand side–results from Beer–Lambert's law. In this expression, z denotes the vertical coordinate measured upward from the bottom of the tank, and P is the total heat flux. The boundaries are thermally insulating: $\boldsymbol{\nabla} T\cdot\mathbf{n} = 0$ at all boundaries, with $\mathbf{n}$ the unit vector normal to the boundary. Denoting as $\overline{T}(t)$ the spatial average of the temperature field inside the fluid domain, the spatial average of Eq. **3** yields

$$\frac{\mathrm{d}\overline{T}(t)}{\mathrm{d}t} = \frac{P}{\rho C H}\left(1 - e^{-H/\ell}\right). \qquad [4]$$

The spatially averaged temperature increases linearly with time. Once the system reaches a quasi-stationary drifting state, the temperature everywhere inside the tank drifts at a mean rate given by the right-hand side of [**4**]. We can thus extract the power P from the drift of the time series.

Consider now the deviation from the spatial mean, $\theta(\mathbf{x}, t) = T(\mathbf{x}, t) - \overline{T}(t)$. We form the equation for θ by subtracting Eq. **4** from Eq. **3**/ρC,

$$\partial_t\theta + \mathbf{u}\cdot\boldsymbol{\nabla}\theta = \kappa\boldsymbol{\nabla}^2\theta + S(z), \qquad [5]$$

where the source/sink term $S(z)$ is

$$S(z) = \frac{P}{\rho C}\left(\frac{1}{\ell}e^{-z/\ell} - \frac{1 - e^{-H/\ell}}{H}\right). \qquad [6]$$

The second term inside the parentheses is an effective cooling term associated with the secular heating of the body of fluid. It balances the heating term, on average over the domain, but has a different spatial structure. Eq. **5** is coupled to the rotating Navier–Stokes equation,

$$\partial_t\mathbf{u} + (\mathbf{u}\cdot\boldsymbol{\nabla})\mathbf{u} + 2\Omega\mathbf{e}_z \times \mathbf{u} = -\boldsymbol{\nabla}p + \alpha g\theta\,\mathbf{e}_z + \nu\boldsymbol{\nabla}^2\mathbf{u}, \qquad [7]$$

where the generalized pressure term absorbs the contribution from the mean temperature $\overline{T}(t)$ and the centrifugal acceleration has been neglected.

The set of Eqs. **5**–**7** corresponds to the standard equations of rotating Boussinesq convection, with internal heating decreasing exponentially with height and uniform cooling at an equal and opposite rate. The solutions to this set of equations reach a statistically steady state, and the temperature difference $\Delta\theta$ realized by [**5**–**7**] is equal to the temperature difference ΔT of the initial setup.

Detailed Experimental Protocol. An experimental run consists of the following steps: The tank is filled with 7 °C water mixed with carbon-black dye to obtain a target value of ℓ. The tank is set into uniform rotation at a rate Ω. After an initial waiting period, for the fluid to achieve solid body rotation, the 2,500-W metal-halide spotlight is turned on. Two thermocouples horizontally centered inside the tank give access to the temperature at heights $z = 0$ and $z = 3H/4$. The corresponding temperature signals are measured by an Arduino microcontroller and transmitted through WIFI to a second Arduino microcontroller, which allows for live monitoring of the signals. An example of time series is provided in Fig. 4. After an initial transient phase, the system settles into a quasi-stationary state characterized by a linear drift of the two time series at an equal rate (visible for $t \gtrsim 1{,}500$ s in Fig. 4), together with a statistically steady temperature difference between the two probes. The fact that the two time series drift at a constant and equal rate is a first indication that thermal losses are negligible. We determine the input heat flux P from the drift rate of the two signals using relation [**4**]. The time average of the temperature difference between $z = 0$ and $z = 3H/4$ yields the temperature drop ΔT. This average is performed over the boxed time interval in Fig. 4. The dimensionless parameters are computed using the fluid properties evaluated for the mean bottom temperature over that interval. To quantify the error associated with the slow temporal drift of the various fluid properties (diffusivities, thermal expansion, etc.), we also compute the various quantities and dimensionless parameters using the first and second halves of the boxed region, denoted, respectively, as subregion I and subregion II in Fig. 4. For each of the two subregions, we average the temperature difference over the subinterval, and we compute the dimensionless parameters using the mean bottom temperature inside the subinterval. The corresponding values are reported in *SI Appendix* with a subscript I or II depending on the subinterval. Also reported are the initial and final bottom temperatures of the boxed measurement interval, denoted as T_{start} and T_{end}, respectively. The error bars in Figs. 2 and 3 correspond to the values obtained by restricting attention to a single subinterval. When estimating the best-fit exponent β, we first compute the rms error on $\log\mathcal{N}$ over the range of $\mathcal{R}$ of interest (of the order of 5%), before propagating this error into an SD σ_β for the best-fit exponent β.

DNS. We solve Eqs. **5**–**7** inside a horizontally periodic domain with the pseudospectral solver Coral (52), previously used for nonrotating convective flows (31) and validated against both analytical results (53) and solutions computed with the Dedalus software (54). The bottom boundary is insulating and no slip, while the top boundary is insulating and stress-free. Depending on the Ekman number, the horizontal extent $L_\perp$ of the domain is set to $0.4H$ or $0.5H$, to account for the variation in the characteristic horizontal scale of the rotating flow. The equations are discretized on a grid containing $(N_x, N_y, N_z) = (441, 441, 576)$ points, which corresponds to 296 alias-free Fourier modes in the horizontal directions and 384 Chebyshev

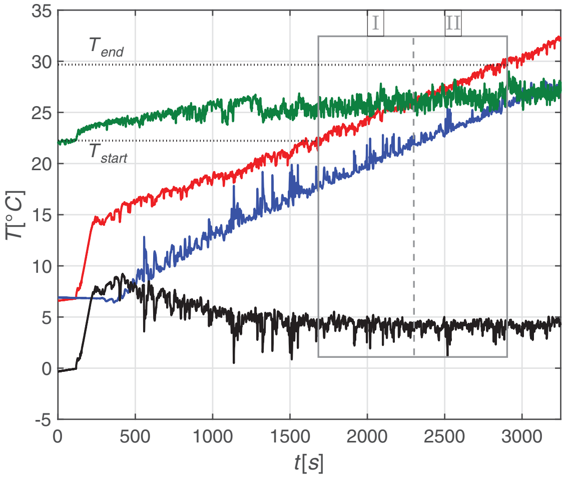

Fig. 4. Raw signals from thermocouples T_1 (red, $z = 0$) and T_2 (blue, $z = 3H/4$) as a function of time t for $H = 25$ cm, $\Omega = 30$ rpm, and $\ell/H = 0.048$. Also shown are the instantaneous temperature drop between the two probes (black), and room temperature (green). The solid box indicates the total measurement interval, separated by a dashed line into two subintervals, I and II.

polynomials along the vertical. The initial condition is chosen as either small-amplitude noise or a checkpoint from a previous simulation with smaller supercriticality. We restrict attention to the statistically steady state that arises after the initial transient. We denote as $\tau_{\rm meas}$ the duration of integration in this statistically steady state, and we focus on the difference between the horizontally averaged temperatures at $z=0$ (bottom boundary) and $z=3H/4$: The time average of the resulting signal yields the temperature drop from which $\mathcal{N}$ is inferred. The SD σ of the signal and its correlation time $\tau_{\rm corr}$ (time lag of the first zero of the autocovariance function) allow us to estimate the statistical error on $\mathcal{N}$. Following, for example, ref. 18, we compute the number of "effectively independent realizations" $N_{\rm eff}=\tau_{\rm meas}/\tau_{\rm corr}$ before estimating the statistical error $\sigma_{\mathcal{N}}$ on the mean temperature drop as $\sigma/\sqrt{N_{\rm eff}}$. The resulting error bars are provided in *SI Appendix*, together with the values of $\mathcal{N}$ obtained by averaging over only the first or second half of the signal, denoted as $\mathcal{N}_{\rm I}$ and $\mathcal{N}_{\rm II}$, respectively.

Data Availability. All study data are included in the article and *SI Appendix*.

ACKNOWLEDGMENTS. This research is supported by the European Research Council under Grant Agreement FLAVE 757239. The numerical study was performed using HPC resources from Centre Informatique National de l'Enseignement Supérieur and Très Grand Centre de Calcul (Grants 2020-A0082A10803 and 2021-A0102A10803). K.J. acknowledges support from NSF Grant DMS-2009319.

1. S. M. Hanasoge, T. L. Duvall Jr., K. R. Sreenivasan, Anomalously weak solar convection. *Proc. Natl. Acad. Sci. U.S.A.* **109**, 11928–11932 (2012).
2. S. M. Hanasoge, H. Hotta, K. R. Sreenivasan, Turbulence in the sun is suppressed on large scales and confined to equatorial regions. *Sci. Adv.* **6**, eaba9639 (2020).
3. J. Schumacher, K. R. Sreenivasan, Colloquium: Unusual dynamics of convection in the sun. *Rev. Mod. Phys.* **92**, 041001 (2020).
4. D. J. Stevenson, Turbulent thermal convection in the presence of rotation and a magnetic field: A heuristic theory. *Geophys. Astrophys. Fluid Dyn.* **12**, 139–169 (1979).
5. K. Julien, E. Knobloch, A new class of equations for rotationally constrained flows. *Theor. Comput. Fluid Dyn.* **11**, 251–261 (1998).
6. E. A. Spiegel, Convection in stars I. Basic Boussinesq convection. *Annu. Rev. Astron. Astrophys.* **9**, 323–352 (1971).
7. R. H. Kraichnan, Turbulent thermal convection at arbitrary Prandtl number. *Phys. Fluids* **5** 1374–1389 (1962).
8. G. Ahlers, S. Grossmann, D. Lohse, Heat transfer and large scale dynamics in turbulent Rayleigh–Bénard convection. *Rev. Mod. Phys.* **81**, 503–537 (2009).
9. U. R. Christensen, Zonal flow driven by strongly supercritical convection in rotating spherical shells. *J. Fluid Mech.* **470**, 115–133 (2002).
10. U. R. Christensen, J. Aubert, Scaling properties of convection-driven dynamos in rotating spherical shells and application to planetary magnetic fields. *Geophys. J. Int.* **166**, 97–114 (2006).
11. J. M. Aurnou *et al.*, Rotating convective turbulence in earth and planetary cores. *Phys. Earth Planet. Inter.* **246**, 52–71 (2015).
12. E. A. Spiegel, G. Veronis, On the Boussinesq approximation for a compressible fluid. *Astrophys. J.* **131**, 442 (1960).
13. X. Chavanne *et al.*, Observation of the ultimate regime in Rayleigh–Bénard convection. *Phys. Rev. Lett.* **79**, 3648–3651 (1997).
14. E. Vitense, Die wasserstoffkonvecktionszone der sonne [in German]. *Z. Astrophys.* **32**, 135–164 (1953).
15. M. Sprague, K. Julien, E. Knobloch, J. Werne, Numerical simulation of an asymptotically reduced system for rotationally constrained convection. *J. Fluid Mech.* **551**, 141–174 (2006).
16. K. Julien, E. Knobloch, A. M. Rubio, G. M. Vasil, Heat transport in low-Rossby-number Rayleigh-Bénard convection. *Phys. Rev. Lett.* **109**, 254503 (2012).
17. J. M. Aurnou, S. Horn, K. Julien, Connections between nonrotating, slowly rotating, and rapidly rotating turbulent convection transport scalings. *Phys. Rev. Res.* **2**, 043115 (2020).
18. J. S. Cheng, M. Madonia, A. J. Aguirre Guzmán, R. P. J. Kunnen, Laboratory exploration of heat transfer regimes in rapidly rotating turbulent convection. *Phys. Rev. Fluids* **5**, 113501 (2020).
19. X. Zhang *et al.*, Boundary zonal flow in rotating turbulent Rayleigh-Bénard convection. *Phys. Rev. Lett.* **124**, 084505 (2020).
20. M. Wedi, D. P. M. van Gils, E. Bodenschatz, S. Weiss, Rotating turbulent thermal convection at very large Rayleigh numbers. *J. Fluid Mech.* **912**, A30 (2021).
21. J. J. Niemela, L. Skrbek, K. R. Sreenivasan, R. J. Donnelly, Turbulent convection at very high Rayleigh numbers. *Nature* **404**, 837–840 (2000).
22. R. E. Ecke, J. J. Niemela, Heat transport in the geostrophic regime of rotating Rayleigh-Bénard convection. *Phys. Rev. Lett.* **113**, 114301 (2014).
23. J. S. Cheng *et al.*, Laboratory-numerical models of rapidly rotating convection in planetary cores. *Geophys. J. Int.* **201**, 1–17 (2015).
24. E. M. King, J. M. Aurnou, Turbulent convection in liquid metal with and without rotation. *Proc. Natl. Acad. Sci. U.S.A.* **110**, 6688–6693 (2013).
25. S. Horn, J. M. Aurnou, Regimes of Coriolis-centrifugal convection. *Phys. Rev. Lett.* **120**, 204502 (2018).
26. W. V. R. Malkus, The heat transport and spectrum of thermal turbulence. *Proc. R. Soc. Lond. A Math. Phys. Sci.* **225**, 196–212 (1954).
27. E. M. King, S. Stellmach, J. Noir, U. Hansen, J. M. Aurnou, Boundary layer control of rotating convection systems. *Nature* **457**, 301–304 (2009).
28. J. S. Cheng, J. M. Aurnou, K. Julien, R. P. J. Kunnen, A heuristic framework for next-generation models of geostrophic convective turbulence. *Geophys. Astrophys. Fluid Dyn.* **112**, 277–300 (2018).
29. S. Lepot, S. Aumaître, B. Gallet, Radiative heating achieves the ultimate regime of thermal convection. *Proc. Natl. Acad. Sci. U.S.A.* **115**, 8937–8941 (2018).
30. V. Bouillaut, S. Lepot, S. Aumaître, B. Gallet, Transition to the ultimate regime in a radiatively driven convection experiment. *J. Fluid Mech.* **861**, R5 (2019).
31. B. Miquel, V. Bouillaut, S. Aumaître, B. Gallet, On the role of the Prandtl number in convection driven by heat sources and sinks. *J. Fluid Mech.* **900**, R1 (2020).
32. S. Schmitz, A. Tilgner, Heat transport in rotating convection without Ekman layers. *Phys. Rev. E Stat. Nonlin. Soft Matter Phys.* **80**, 015305 (2009).
33. J. Marshall, F. Schott, Open-ocean convection: Observations, theory, and models. *Rev. Geophys.* **37**, 1–64 (1999).
34. P. J. R. Kunnen, The geostrophic regime of rapidly rotating turbulent convection. *J. Turbul.* **22**, 267–296 (2021).
35. E. M. King, S. Stellmach, J. M. Aurnou, Heat transfer by rapidly rotating Rayleigh-Bénard convection. *J. Fluid Mech.* **691**, 568–582 (2012).
36. M. Plumley, K. Julien, P. Marti, S. Stellmach, The effects of ekman pumping on quasi-geostrophic Rayleigh-Bénard convection. *J. Fluid Mech.* **803**, 51–71 (2016).
37. K. Julien *et al.*, A nonlinear model for rotationally constrained convection with Ekman pumping. *J. Fluid Mech.* **798**, 50–87 (2016).
38. J. S. Cheng, J. M. Aurnou, Tests of diffusion-free scaling behaviors in numerical dynamo datasets. *Earth Planet. Sci. Lett.* **436**, 121–129 (2016).
39. T. Gastine, J. Wicht, J. Aubert, Scaling regimes in spherical shell rotating convection. *J. Fluid Mech.* **808**, 690–732 (2016).
40. S. Stellmach *et al.*, Approaching the asymptotic regime of rapidly rotating convection: Boundary layers versus interior dynamics. *Phys. Rev. Lett.* **113**, 254501 (2014).
41. P. J. R. Kunnen *et al.*, Transition to geostrophic convection: The role of the boundary conditions. *J. Fluid Mech.* **799**, 413–432 (2016).
42. A. J. Barker, A. M. Dempsey, Y. Lithwick, Theory and simulations of rotating convection. *Astrophys. J.* **791**, 13 (2014).
43. L. K. Currie, A. J. Barker, Y. Lithwick, M. K. Browning, Convection with misaligned gravity and rotation: Simulations and rotating mixing length theory. *Mon. Not. R. Astron. Soc.* **493**, 5233–5256 (2020).
44. C. Guervilly, P. Cardin, N. Schaeffer, Turbulent convective length scale in planetary cores. *Nature* **570**, 368–371 (2019).
45. S. Horn, J. M. Aurnou, Rotating convection with centrifugal buoyancy: Numerical predictions for laboratory experiments. *Phys. Rev. Fluids* **4**, 073501 (2019).
46. S. Horn, J. M. Aurnou, Tornado-like vortices in the quasi-cyclostrophic regime of Coriolis-centrifugal convection. *J. Turbul.* **22**, 297–324 (2021).
47. J. C. Buell, I. Catton, The effect of wall conduction on the stability of a fluid in a right circular cylinder heated from below. *J. Heat Transfer* **105**, 255–260 (1983).
48. F. Zhong, R. Ecke, V. Steinberg, Asymmetric modes and the transition to vortex structures in rotating Rayleigh-Bénard convection. *Phys. Rev. Lett.* **67**, 2473–2476 (1991).
49. R. E. Ecke, F. Zhong, E. Knobloch, Hopf bifurcation with broken reflection symmetry in rotating Rayleigh-Bénard convection. *Europhys. Lett.* **19**, 177–182 (1992).
50. B. Favier, E. Knobloch, Robust wall states in rapidly rotating Rayleigh-Bénard convection. *J. Fluid Mech.* **895**, R1 (2020).
51. X. M. de Wit *et al.*, Turbulent rotating convection confined in a slender cylinder: The sidewall circulation. *Phys. Rev. Fluids* **5**, 023502 (2020).
52. B. Miquel, Coral: A parallel spectral solver for fluid dynamics and partial differential equations. *J. Open Source Software* **6**, 2978 (2021).
53. B. Miquel, S. Lepot, V. Bouillaut, B. Gallet, Convection driven by internal heat sources and sinks: Heat transport beyond the mixing-length or "ultimate" scaling regime. *Phys. Rev. Fluids* **4**, 121501 (2019).
54. K. J. Burns, G. M. Vasil, J. S. Oishi, D. Lecoanet, B. P. Brown, Dedalus: A flexible framework for numerical simulations with spectral methods. *Phys. Rev. Res.* **2**, 023068 (2020).

J. Fluid Mech. (2019), *vol.* 861, R5, doi:10.1017/jfm.2018.972

JFM RAPIDS
journals.cambridge.org/rapids

Transition to the ultimate regime in a radiatively driven convection experiment

Vincent Bouillaut[1], **Simon Lepot**[1], **Sébastien Aumaître**[1]
and Basile Gallet[1,†]

[1]Service de Physique de l'État Condensé, CEA, CNRS UMR 3680, Université Paris-Saclay,
CEA Saclay, 91191 Gif-sur-Yvette, France

(Received 2 October 2018; revised 8 November 2018; accepted 29 November 2018)

We report on the transition between two regimes of heat transport in a radiatively driven convection experiment, where a fluid gets heated up within a tunable heating length ℓ in the vicinity of the bottom of the tank. The first regime is similar to that observed in standard Rayleigh–Bénard experiments, the Nusselt number Nu being related to the Rayleigh number Ra through the power law $Nu \sim Ra^{1/3}$. The second regime corresponds to the 'ultimate' or mixing-length scaling regime of thermal convection, where Nu varies as the square root of Ra. Evidence for these two scaling regimes has been reported in Lepot *et al.* (*Proc. Natl Acad. Sci. USA*, vol. 115, 2018, pp. 8937–8941), and we now study in detail how the system transitions from one to the other. We propose a simple model describing radiatively driven convection in the mixing-length regime. It leads to the scaling relation $Nu \sim (\ell/H)Pr^{1/2}Ra^{1/2}$, where H is the height of the cell and Pr is the Prandtl number, thereby allowing us to deduce the values of Ra and Nu at which the system transitions from one regime to the other. These predictions are confirmed by the experimental data gathered at various Ra and ℓ. We conclude by showing that boundary layer corrections can persistently modify the Prandtl number dependence of Nu at large Ra, for $Pr \gtrsim 1$.

Key words: turbulent convection

1. Introduction

In many geophysical and astrophysical flows, turbulent convection is driven by local internal heating. For instance, the absorption of sunlight within the first few metres of water inside frozen lakes induces convective mixing and penetrative convection (Farmer 1975; Bengtsson 1996; Mironov *et al.* 2002; Jonas *et al.* 2003; Lecoanet *et al.* 2015; Toppaladoddi & Wettlaufer 2018; Ulloa, Wüest & Bouffard 2018). A second example is the interior of stars, where, depending on the stellar

---

† Email address for correspondence: basile.gallet@cea.fr

mass, internal heating due to thermonuclear reactions can directly overlap with the convective region (Kippenhahn & Weigert 1990; Barker, Dempsey & Lithwick 2014). Inside Earth's mantle, radioactive decay induces internal heating as well (Davaille, Girard & Le Bars 2002; Limare *et al.* 2015). Finally, convection driven by a flux of neutrinos within collapsing stellar cores is believed to affect the shape of supernovae explosions (Herant, Benz & Colgate 1992; Janka & Müller 1996; Radice *et al.* 2016; Kazeroni *et al.* 2018). To reproduce such convection in the laboratory, in a previous study we introduced an experimental set-up in which a turbulent flow is driven by the absorption of a flux of light (Lepot, Aumaître & Gallet 2018). A powerful spotlight shines from below at an experimental cell with a transparent bottom plate. The cell contains a mixture of water and dye, which absorbs the light flux and converts it into heat. The heating is therefore localized near the bottom of the tank, on a typical height ℓ that can be tuned through the concentration of the dye. We showed that when ℓ is much smaller than the boundary layers near the bottom of the tank, radiative heating is similar to that of a standard Rayleigh–Bénard (RB) experiment, i.e., of a plate heated at constant power (through a Boussinesq symmetry, the system is equivalent to convection driven by uniform internal heating together with a fixed-flux cooling upper boundary, as introduced by Goluskin (2015)). In terms of Nusselt and Rayleigh numbers Nu and Ra (see (2.4) for definitions), we measured a power law close to $Nu \sim Ra^{1/3}$, which corresponds to the regime of standard RB experiments (Malkus 1954; Chavanne *et al.* 1997; Niemela *et al.* 2000; Chavanne *et al.* 2001; Alhers, Grossmann & Lhose 2009; Roche *et al.* 2010): the heat transport efficiency is restricted by the diffusion of heat across the marginally stable boundary layer located near the bottom plate. The thickness of this marginally stable boundary layer is independent of the height of the fluid layer, and so is the relation between the heat flux and the temperature drop across the cell, hence the scaling law $Nu \sim Ra^{1/3}$. More interestingly, when ℓ is large enough for heat to be input directly into the bulk turbulent flow, we observed that radiative heating leads to the mixing-length or 'ultimate' scaling regime, $Nu \sim Ra^{1/2}$, which corresponds to a fully turbulent regime where the molecular diffusion coefficients are irrelevant (Kraichnan 1962; Spiegel 1963, 1971).

The goal of the present study is to understand the transition between these two regimes: what happens for intermediate values of the heating length ℓ? Indeed, as compared to RB studies, our set-up has an additional dimensionless parameter: the dimensionless absorption length ℓ/H, where H denotes the height of the fluid layer. What is the dependence of the Nusselt number on this new parameter? Dimensional analysis leads to:

$$Nu = \mathcal{F}(\ell/H, Ra, Pr), \tag{1.1}$$

where Pr is the Prandtl number. Because ℓ/H governs the transition between two different scaling regimes, the relation (1.1) does not in general take the form of a power law. However, once we are in a given scaling regime we can write (1.1) as a power law:

$$Nu = \text{const.} \left(\frac{\ell}{H}\right)^{\beta} Ra^{\gamma} Pr^{\chi}. \tag{1.2}$$

In the following we propose simple models leading to predictions for the values of the exponents β, γ and χ, before confronting these predictions with the experimental data.

We introduce the experimental set-up in § 2. In § 3, we present the experimental data for the Nusselt number, before introducing a simple model that predicts the scaling

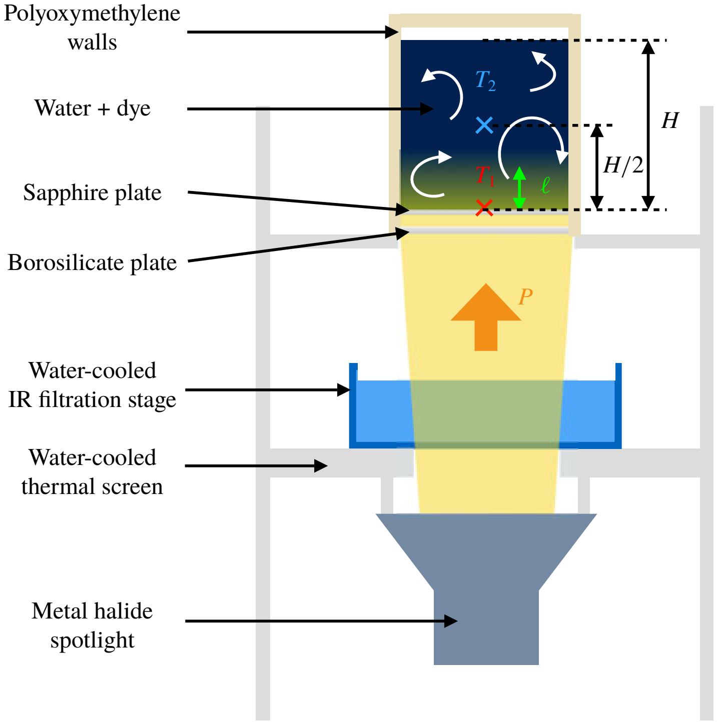

FIGURE 1. Radiatively driven convection in the laboratory: a powerful spotlight shines from below at a cell containing a mixture of water and dye. This triggers volumic heating near the bottom plate, over a typical length ℓ that can be tuned through the concentration of the dye.

behaviour (1.2) in the ultimate regime, with the exponents $\beta = 1$, $\gamma = 1/2$ and $\chi = 1/2$. We show that the experimental data are compatible with these values of β and γ. The discussion § 4 focuses on the dependence in Pr, which cannot be probed within the present experimental set-up. While the value $\chi = 1/2$ should be achieved at low Pr, a refinement of the model indicates that, for finite or large Pr, the injection of even a tiny fraction of the radiative heat flux into the boundary layers could result in a persistent modification of the exponent χ, while maintaining $\beta = 1$ and $\gamma = 1/2$.

2. Experimental set-up

2.1. *Radiative heating in the laboratory*

The experimental set-up is sketched in figure 1. It has been described in a previous publication (Lepot *et al.* 2018) and we only mention its key characteristics here. A 2500 W metal-halide spotlight shines at a cylindrical experimental cell of radius $R = 10$ cm containing a homogeneous mixture of water and carbon black dye. The sidewalls of the tank are made of polyoxymethylene, while the bottom boundary is a transparent sapphire plate. The light flux penetrates into the tank, where it is absorbed by the dye and turned into heat. Beer–Lambert law states that the light flux inside the tank then decreases exponentially with the height z measured upwards from the bottom plate, and so does the heating rate. The bulk heating rate $Q(z)$ inside the tank therefore reads:

$$Q(z) = \frac{P}{\ell} \exp(-z/\ell), \tag{2.1}$$

where P is the heat flux radiated by the spotlight in the form of visible light (in units of W m^{-2}). The absorption length ℓ is inversely proportional to the dye concentration.

By changing the latter, we can achieve either standard RB heating, when ℓ is much smaller than the boundary layer thickness, or significant heating of the bulk turbulent flow, when ℓ is much greater than the boundary layer thickness.

2.2. *‘Secular’ cooling*

A key aspect of the experiment is to avoid boundary layers at the cooling side as well. Indeed, a fixed temperature cooling plate would produce standard boundary layers restricting the heat flux. Because of this cold boundary layer, traditional studies of internally heated convection have led to scaling laws similar to that of standard RB convection (Kulacki & Goldstein 1972; Goluskin 2016). We follow a different approach, inspired by the ‘secular heating’ invoked in many studies of convection in Earth’s interior (Gubbins *et al.* 2003; Aubert, Labrosse & Poitou 2009; Landeau & Aubert 2011): if we do not cool down the system, the temperature at any point within the fluid drifts with time at a constant rate. On top of this linear drift, the flow develops some stationary internal temperature gradients. If $T(\boldsymbol{x}, t)$ denotes the temperature field inside the tank and $\overline{T}(t)$ its spatial average, one can show easily that $\overline{T}(t)$ increases linearly in time at a rate proportional to the radiative flux of the spotlight:

$$\frac{\mathrm{d}\overline{T}}{\mathrm{d}t} = \frac{P}{\rho C H}(1-\mathrm{e}^{-H/\ell}), \tag{2.2}$$

where ρ is the average density of the fluid and C its specific heat capacity. The local deviation from the mean temperature is $\theta(\boldsymbol{x}, t) = T(\boldsymbol{x}, t) - \overline{T}(t)$. One can easily show that the field $\theta(\boldsymbol{x}, t)$ obeys the equations of Boussinesq convection for a fluid that is radiatively heated and cooled uniformly in space. In particular, the heat equation becomes:

$$\partial_t \theta + \boldsymbol{u}\boldsymbol{\cdot}\nabla\theta = \kappa\nabla^2\theta + \frac{1}{\rho C}\left[Q(z) - \frac{P}{H}(1-\mathrm{e}^{-H/\ell})\right], \tag{2.3}$$

where κ denotes the thermal diffusivity. On average over space, the uniform cooling term – the second term in the square bracket – balances the radiative heating rate, so that, after a transient, $\theta(\boldsymbol{x}, t)$ reaches a statistically steady state.

2.3. *Measurements and control parameters*

We measure the internal temperature gradients using two thermocouples. The first one touches the bottom sapphire plate and gives access to its temperature T_1, while the second one measures the temperature T_2 at mid-depth inside the tank. Both probes are centred horizontally. As discussed in the previous subsection, the measured temperature difference $\Delta T = T_1 - T_2 = \theta_1 - \theta_2$ is governed by the Boussinesq equations subject to both radiative heating and uniform ‘secular’ cooling.

Metal-halide spotlights cannot be operated over a large range of power. To scan a broad range of Rayleigh numbers, we therefore vary the depth H of the fluid layer from 4 cm to 19 cm. The second control parameter of the experiment is the dye concentration, which allows us to vary the dimensionless absorption length ℓ/H over several orders of magnitude.

A typical experimental run consists in starting with the mixture of water and dye around 8 °C before turning the spotlight on. Both temperatures increase with time, and a stationary temperature difference between the two probes is achieved after a few turnover times (roughly 200 s). We keep the part of the temperature signals

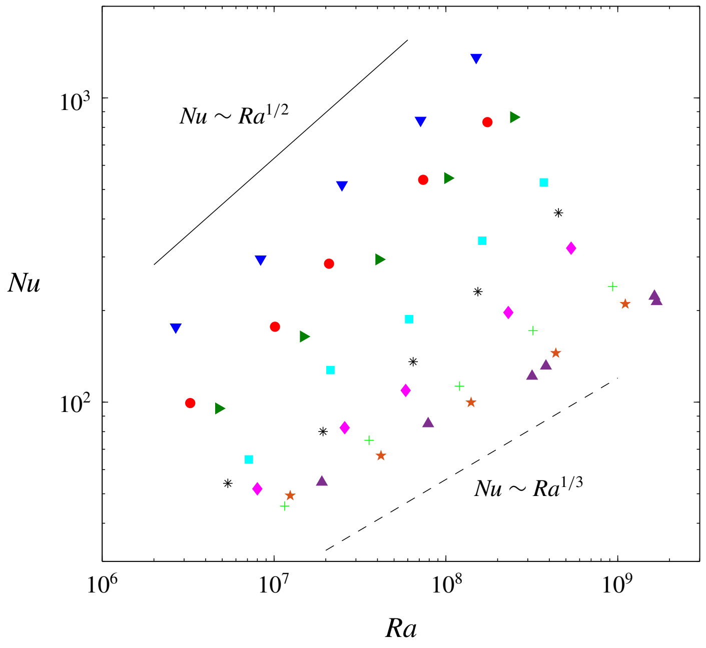

FIGURE 2. Nusselt number as a function of the Rayleigh number for various values of the absorption length ℓ. At fixed Ra, the Nusselt number increases with ℓ/H. Symbols are $\triangle$: $\ell = 5\times10^{-6}$ m; $\star$: $\ell/H = 0.0015$; $+$: $\ell/H = 0.0030$; $\diamond$: $\ell/H = 0.0060$; $*$: $\ell/H = 0.012$; $\square$: $\ell/H = 0.024$; $\triangleright$: $\ell/H = 0.048$; $\bigcirc$: $\ell/H = 0.05$; $\triangledown$: $\ell/H = 0.096$. The solid and dashed lines are eyeguides.

corresponding to a bottom temperature between ±2 °C of room temperature. We average ΔT over this time interval, and we extract the heat flux P from the slope of the common temporal drift of the two signals (see (2.2)). We finally compute the Rayleigh and Nusselt numbers as:

$$Ra = \frac{\alpha g \langle \Delta T\rangle H^3}{\kappa \nu}, \quad Nu = \frac{PH}{\lambda \langle \Delta T\rangle}, \tag{2.4}$$

where α denotes the thermal expansion coefficient, g is gravity, ν is the kinematic viscosity, λ is the thermal conductivity, and $\langle\cdot\rangle$ denotes time average.

3. From the Rayleigh–Bénard regime to the mixing-length regime

We have performed several sets of experimental runs for various quantities of dye, i.e., for various dimensionless absorption lengths ℓ/H. We show in figure 2 the corresponding Nu versus Ra curves. We also reproduce the data from Lepot *et al.* (2018), where the absorption length is either $\ell/H < 10^{-4}$, or $\ell/H = 0.05$. The former case corresponds to a RB situation and displays a power law behaviour $Nu \sim Ra^{0.31}$, while for the latter case heat is input inside the bulk turbulent flow, which leads to a power law $Nu \sim Ra^{0.54}$ close to the prediction of Spiegel and Kraichnan. The new data points span the transition region between these two limiting regimes. While the curves for the lowest values of ℓ/H are superimposed onto the RB case, for larger ℓ/H and fixed Ra the Nusselt number increases with ℓ/H. The various Nu versus Ra curves of figure 2 are roughly compatible with power laws. However, while the corresponding power law fits are very good for extreme values of ℓ/H, the residuals

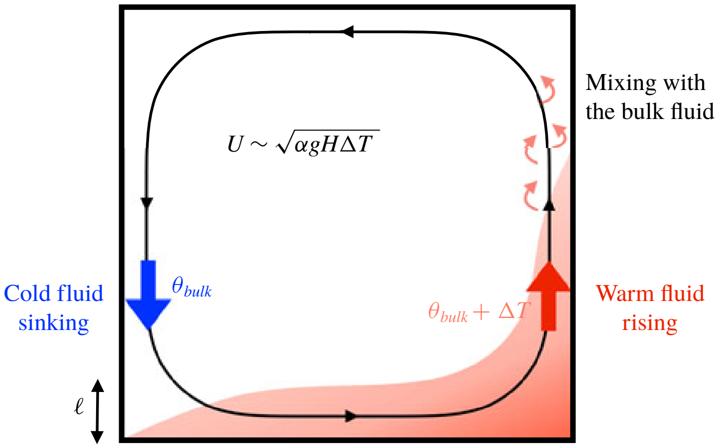

FIGURE 3. Model of radiatively heated convection roll: the black line is a streamline of the mean flow. Near the bottom-left corner, a cold fluid element at the bulk temperature enters the heating region. It gets heated as it travels along the bottom boundary, gaining an overall temperature increment of the order of ΔT during a time of flight H/U. The fluid element has maximum temperature as it passes near the bottom-right corner. It then starts rising and follows the mean cellular motion while mixing with the bulk fluid.

are larger for intermediate values of ℓ/H: for instance, the Nu versus Ra curve for $\ell/H = 0.012$ exhibits a slight positive convexity in log scales, which we will argue is a signature of the crossover region between the RB and the ultimate scaling regimes. Roughly speaking, the transition to the ultimate regime takes place when radiative heating bypasses the boundary layers and injects the heat directly into the bulk flow, i.e., when ℓ is much larger than the boundary layer thickness. This can be achieved either by increasing ℓ/H for fixed Ra, or by increasing Ra with fixed ℓ/H to decrease the boundary layer thickness. In the following we propose a simple model to further investigate this transition.

3.1. *A roll model*

In figure 3 we sketch a simple model to estimate the temperature difference ΔT within the experimental cell. At large scale, turbulent convective flows typically consist of cellular motion, as sketched in figure 3. The typical temperature difference ΔT inside the cell can be estimated by considering a fluid element evolving on a streamline near the periphery of the convective roll. Near the left-hand boundary of the domain in figure 3, the fluid particle is close to the bulk temperature. It gets advected downwards by the convective roll and enters the heating region. This Lagrangian fluid element then travels close to the bottom boundary, within the heating region. During this phase it gets heated up, its temperature increasing from the bulk temperature θ_{bulk} to approximately $\theta_{bulk} + \Delta T$ as it reaches the bottom-right corner. As long as the particle remains close to the bottom boundary, we have $z \ll \ell \ll H$, and the dominant balance in (2.3) written for the fluid particle reads:

$$\frac{\mathrm{D}\theta}{\mathrm{D}t} \simeq \frac{1}{\rho C}\left[Q(z) - \frac{P}{H}(1 - \mathrm{e}^{-H/\ell})\right] \simeq \frac{P}{\rho C \ell}, \tag{3.1}$$

where $\mathrm{D}\cdot/\mathrm{D}t$ denotes the total derivative. For a convective roll of unit aspect ratio, the travel time of the fluid element from the bottom-left to the bottom-right corner is

$\Delta t \sim H/U$, where U is the typical velocity of the convective roll. Assuming that U follows the free-fall scaling law:

$$U \sim \sqrt{\alpha g \Delta T H}, \tag{3.2}$$

the temperature increase during the heating phase is estimated as:

$$\Delta T \sim \frac{P}{\rho C \ell} \Delta t \sim \frac{PH}{\rho C \ell U} \sim \frac{PH}{\rho C \ell \sqrt{\alpha g \Delta T H}}, \tag{3.3}$$

which, in terms of dimensionless quantities, yields:

$$Nu \sim \frac{\ell}{H} Pr^{1/2} Ra^{1/2}. \tag{3.4}$$

The warm fluid element then starts rising. It exits the heating region and gradually mixes with the bulk fluid as it moves around the cell. It has relaxed to the bulk fluid temperature when it reaches the bottom-left corner of the convection roll again, and a new cycle starts.

3.2. *Transition point and rescaling of the data*

To test the compatibility between the prediction (3.4) and the experimental data, one can focus on the transition between the two asymptotic regimes. For small absorption length or small Rayleigh number, we expect to recover the scaling regime of Rayleigh–Bénard convection. A marginally stable boundary layer argument then yields the power law $Nu \sim Ra^{1/3}$, i.e., $\gamma = 1/3$ and $\beta = \chi = 0$ in the general scaling relation (1.2). For higher Rayleigh numbers, ℓ is much larger than the boundary layer thickness. Heat is input predominantly inside the bulk turbulent flow and the regime (3.4) eventually sets in, with $\beta = 1$ and $\gamma = \chi = 1/2$. As Ra increases from low values, the RB regime should hold until the thickness δ of the marginally stable thermal boundary layer becomes comparable to ℓ. Indeed, a similar argument for convection over rough plates successfully predicts a departure from the standard RB regime when δ is comparable to the typical roughness height (Shen, Tong & Xia 1996; Toppaladoddi, Succi & Wettlaufer 2017; Xie & Xia 2018; Rusaouën *et al.* 2018). However, in the present set-up the transition is slightly more subtle, and $\ell \sim \delta$ is not the threshold where the scaling law (3.4) sets in. To see this, one can perform an energy budget inside the heating region $z \lesssim \ell$ in figure 3: fluid enters this region near the bottom-left corner at temperature θ_{bulk} and exits the domain near the bottom-right corner, with a temperature $\theta_{bulk} + \Delta T$. The power (heat per unit time, in Joules per second) evacuated from this region by the large-scale roll is therefore $\phi_U \sim H \ell U \rho C \Delta T$, while the power input by the radiative heating is PH^2. If we substitute the optimistic free-fall estimate (3.2) for U, the ratio of the former over the latter becomes:

$$\frac{\phi_U}{PH^2} \sim \frac{\ell}{H} \frac{Pr^{1/2} Ra^{1/2}}{Nu}. \tag{3.5}$$

At the point where $\ell \sim \delta$, the RB scaling still holds: substituting $Nu \sim Ra^{1/3}$ and $\ell \sim \delta \sim Ra^{-1/3}$ into (3.5) yields $\phi_U / PH^2 \sim Pr^{1/2} Ra^{-1/6} \ll 1$. We conclude that the roll is too slow to efficiently extract the heat input radiatively inside the heating region when $\delta = \ell$. The roll mechanism described above therefore sets in at higher Rayleigh numbers. The ratio (3.5) is then of the order of unity, which again yields the scaling law (3.4).

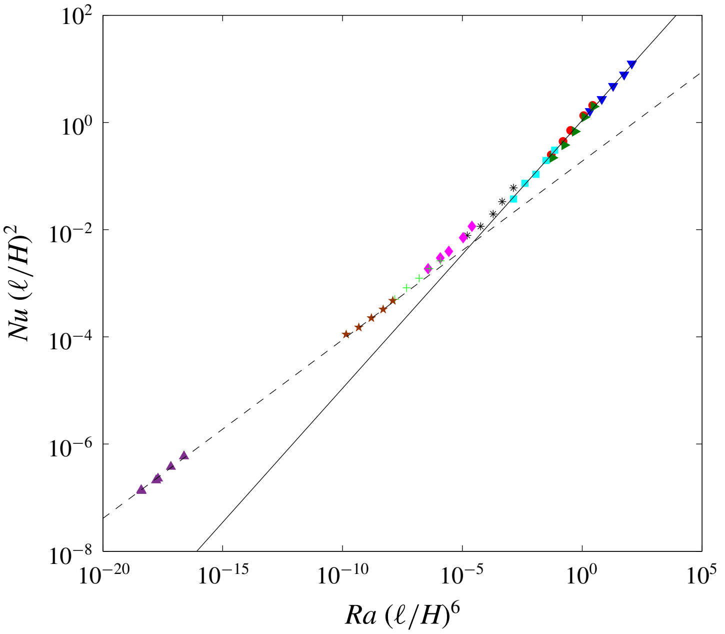

FIGURE 4. Rescaled Nusselt number as a function of the rescaled Rayleigh number, for various values of the absorption length ℓ (same symbols as figure 2). The data indicate a clear transition from an exponent $\gamma = 1/3$ (dashed line) to an exponent $\gamma = 1/2$ (solid line).

Because of the limited power of the spotlight, these two transitions – the end of the RB scaling regime and the beginning of the ultimate regime – cannot be distinguished in our experiment. Instead, we will show that the data is well described by a single overall transition point (Ra_{tr}, Nu_{tr}) lying at the intersection between the two extreme scaling laws $Nu \sim Ra^{1/3}$ and (3.4):

$$Nu_{tr} \sim Ra_{tr}^{1/3} \sim \frac{\ell}{H} Pr^{1/2} Ra_{tr}^{1/2}, \tag{3.6}$$

from which we deduce:

$$Ra_{tr} \sim Pr^{-3} \left(\frac{\ell}{H}\right)^{-6}, \quad Nu_{tr} \sim Pr^{-1} \left(\frac{\ell}{H}\right)^{-2}. \tag{3.7}$$

One way to test the predictions of this model is to plot the Rayleigh and Nusselt numbers rescaled by their values at the transition, i.e., Nu/Nu_{tr} as a function of Ra/Ra_{tr}. In figure 4, we thus plot $Nu\,(\ell/H)^2$ as a function of $Ra\,(\ell/H)^6$. In this representation the data obtained for various values of the absorption length ℓ collapse onto a single master curve. The latter starts off with an exponent $1/3$, before transiting to a second power law with an exponent compatible with the $1/2$ prediction of the model above. This representation confirms the dependence of Nu with ℓ/H and Ra in the two regimes.

4. Discussion: dependence in Pr and persistent boundary layers

While the roll model described above successfully predicts the dependence of the Nusselt number with ℓ/H and Ra in the ultimate regime, the predicted dependence

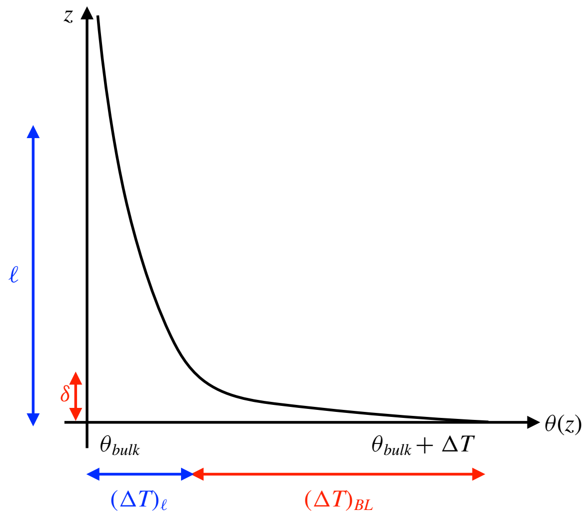

FIGURE 5. Schematic vertical temperature profile showing the temperature drop $(\Delta T)_\ell$ within the absorption region, together with an additional temperature drop $(\Delta T)_{BL}$ within a boundary layer of thickness $\delta \ll \ell$.

with Pr cannot be tested with the present experimental set-up. As a word of caution, we therefore wish to discuss how the boundary layers can affect the Pr-dependence of the Nusselt number. Coming back to the general scaling relation (1.2), we will show that these boundary layers can induce a persistent modification of the exponent χ at high Rayleigh numbers, while leaving the values $\beta = 1$ and $\gamma = 1/2$ unchanged.

Near the bottom wall is a boundary layer, for the velocity field to satisfy the no-slip boundary condition. The velocity is reduced within this boundary layer; coming back to the simple picture of figure 3, the heating phase is longer if the fluid element travels on a streamline that is contained inside the boundary layer. It accumulates more heat than fluid particles travelling outside the boundary layer, and reaches higher temperatures. There is therefore also a boundary layer for the temperature field. A schematic of the resulting horizontally averaged and time averaged temperature profile is provided in figure 5. We expect a temperature drop $(\Delta T)_\ell$ on a vertical scale ℓ, associated with the roll model described above, together with an additional temperature difference $(\Delta T)_{BL}$ associated with the boundary layer region, within which diffusion plays a central role. Inside a boundary layer of thickness $\delta \ll \ell$, the heat input by the radiative forcing is approximately $Q(z=0) \times \delta = P \times \delta/\ell$. This heat flux is diffused outside of the boundary layer, which leads to:

$$P\frac{\delta}{\ell} \sim \frac{\lambda(\Delta T)_{BL}}{\delta}. \tag{4.1}$$

From this equality we deduce $(\Delta T)_{BL}$ in terms of thickness δ of the temperature boundary layer. The total temperature drop ΔT is then the sum of $(\Delta T)_{BL}$ and of the temperature drop $(\Delta T)_\ell$ outside of the boundary layer, which we estimate using expression (3.3). We obtain:

$$\Delta T = (\Delta T)_\ell + (\Delta T)_{BL} = c_0 \frac{PH^2}{\lambda\ell} Pr^{-1/2} Ra^{-1/2} + c_1 \frac{PH^2}{\lambda\ell} \times \frac{\delta^2}{H^2}, \tag{4.2}$$

where the $(c_i)_{i\in\mathbb{N}}$ are dimensionless constants. The next step is to insert scaling laws for the boundary layer thickness δ, to examine their consequences on the scaling relation (1.2). We distinguish between low- and large-Prandtl-number fluids.

4.1. *Low-Prandtl-number fluids*

Let us denote as δ_ν the thickness of the velocity boundary layer. The standard estimate for δ_ν is:

$$\delta_\nu \sim \frac{H}{\sqrt{Re}}, \tag{4.3}$$

where the Reynolds number is defined as $Re = UH/\nu$. Substituting the free-fall velocity estimate (3.2) for U yields:

$$\delta_\nu \sim H\,Pr^{1/4}Ra^{-1/4}. \tag{4.4}$$

In a low-Prandtl-number fluid, the temperature field shares this boundary layer thickness, as it gets mixed very efficiently by the turbulent flow outside of it. Inserting $\delta = \delta_\nu$ into expression (4.2) leads to:

$$\Delta T = c_0\frac{PH^2}{\lambda\ell}Pr^{-1/2}Ra^{-1/2} + c_2\frac{PH^2}{\lambda\ell}Pr^{1/2}Ra^{-1/2}. \tag{4.5}$$

The boundary layer correction to the temperature drop – the second term in (4.5) – is smaller than the main contribution of the roll model by a factor Pr. Although it may be possible to detect it for moderately low Pr, it is negligible for $Pr \ll 1$.

4.2. *Large-Prandtl-number fluids*

If the Prandtl number is much greater than unity, the boundary layer of the temperature field is much thinner than δ_ν: the temperature drop associated with the thermal boundary layer takes place within the velocity boundary layer. The velocity field in this region can be approximated by a uniform shear flow, the shear being $S \sim U/\delta_\nu$. Following Shraiman & Siggia (1990), the thermal boundary layer thickness δ is then:

$$\delta \sim \left(\frac{\kappa H}{S}\right)^{1/3} \sim \left(\frac{\kappa H\delta_\nu}{U}\right)^{1/3} \sim HPr^{-1/12}Ra^{-1/4}, \tag{4.6}$$

where we have substituted the estimates (3.2) and (4.4) for U and δ_ν. Inserting this expression for the thermal boundary layer thickness into (4.2) yields:

$$\Delta T = c_0\frac{PH^2}{\lambda\ell}Pr^{-1/2}Ra^{-1/2} + c_3\frac{PH^2}{\lambda\ell}Pr^{-1/6}Ra^{-1/2}, \tag{4.7}$$

The boundary layer correction to ΔT is important in this large-Pr regime, as it becomes the main contribution to ΔT in the limit $Pr \gg 1$. In this limit, the scaling law for the Nusselt number (2.4) becomes:

$$Nu \sim \frac{\ell}{H}Pr^{1/6}Ra^{1/2}. \tag{4.8}$$

The boundary layer correction leads to $\chi = 1/6$ instead of $\chi = 1/2$, with still $\beta = 1$ and $\gamma = 1/2$. This is a persistent modification of χ, in the sense that the scaling law is modified up to arbitrarily large Rayleigh number. While this discussion section is only here to highlight possible modifications of the exponent χ by boundary layer dynamics, the precise determination of χ remains an experimental challenge. A dedicated numerical study may be a simpler approach to address the dependence of Nu over several decades of Pr. In the meantime, we shall compare the results of this study to convective flows inside frozen great lakes, the Prandtl number of which is only twice our experimental value. To wit, it is desirable to re-express the transition point between the RB and ultimate regimes in terms of control parameters only, independent of the measured temperature drop ΔT. We thus introduce the flux-based Rayleigh number $Ra_P = Nu \times Ra = \alpha g P H^4/\lambda\kappa\nu$. On the one hand, equation (3.7) together with the data of figure 4 indicate that the ultimate scaling regime sets in for $Ra_P(\ell/H)^8 \gtrsim 3\times 10^{-7}$, for the Prandtl number of water at 28 °C. We can compare this criterion to the typical value of Ra_P for frozen great lakes in the spring (Mironov *et al.* 2002; Ulloa *et al.* 2018): with a light flux $P \simeq 100$ W m^{-2}, an absorption length $\ell \simeq 1$ m and a mixed-layer depth H ranging from 4 m to 40 m, we obtain $Ra_P(\ell/H)^8$ in the range 10^5–10^9, well inside the region of parameter space where the mixing-length scaling regime holds. This confirms that radiative heating – as opposed to fixed-flux heating at the boundary – is a key ingredient of any laboratory of numerical set-up aimed at describing the thermal structure of such lakes.

Acknowledgement

We thank V. Padilla for his help during the development of the experimental set-up. This research is supported by the European Research Council under grant agreement FLAVE 757239, and by Labex PALM ANR-10-LABX-0039.

References

Alhers, G., Grossmann, S. & Lhose, D. 2009 Heat transfer and large-scale dynamics in turbulent Rayleigh–Bénard convection. *Rev. Mod. Phys.* **81**, 503.

Aubert, J., Labrosse, S. & Poitou, C. 2009 Modelling the Palaeo-evolution of the geodynamo. *Geophys. J. Intl* **179**, 1414–1428.

Barker, A. J., Dempsey, A. M. & Lithwick, Y. 2014 Theory and simulations of rotating convection. *Astrophys. J.* **791**, 13.

Bengtsson, L. 1996 Mixing in ice-covered lakes. *Hydrobiologia* **322**, 91–97.

Chavanne, X., Chillá, F., Castaing, B., Hébral, B., Chabaud, B. & Chaussy, J. 1997 Observation of the ultimate regime in Rayleigh–Bénard convection. *Phys. Rev. Lett.* **79**, 3648.

Chavanne, X., Chillá, F., Chabaud, B., Castaing, B. & Hébral, B. 2001 Turbulent Rayleigh–Bénard convection in gaseous and liquid He. *Phys. Fluids* **13**, 1300.

Davaille, A., Girard, F. & Le Bars, M. 2002 How to anchor hotspots in a convecting mantle? *Earth Planet. Sci. Lett.* **203**, 621–634.

Farmer, D. 1975 Penetrative convection in the absence of mean shear. *Q. J. R. Meteorol. Soc.* **101**, 869–891.

Goluskin, D. 2015 Internally heated convection beneath a poor conductor. *J. Fluid Mech.* **771**, 36–56.

Goluskin, D. 2016 *Internally Heated Convection and Rayleigh–Bénard Convection*. Springer.

Gubbins, D., Alfé, D., Masters, G., David Price, G. & Gillan, M. J. 2003 Can the Earth's dynamo run on heat alone? *Geophys. J. Intl.* **155**, 609–622.

Herant, M., Benz, W. & Colgate, S. 1992 Postcollapse hydrodynamics of SN 1987A: two-dimensional simulations of the early evolution. *Astrophys. J.* **395**, 642–653.

Janka, H.-T. & Müller, E. 1996 Neutrino heating, convection, and the mechanism of type-II supernova explosion. *Astron. Astrophys.* **306**, 167.

Jonas, T., Terzhevik, A. Y., Mironov, D. V. & Wüest, A. 2003 Radiatively driven convection in an ice-covered lake investigated using temperature microstructure technique. *J. Geophys. Res.* **108**, 3183.

KAZERONI, R., KRUEGER, B. K., GUILET, J., FOGLIZZO, T. & POMARÉDE, D. 2016 The non-linear onset of neutrino-driven convection in two- and three-dimensional core-collapse supernovae. *Mon. Not. R. Astron. Soc.* **480**, 261–280.

KIPPENHAHN, R. & WEIGERT, A. 1990 *Stellar Structure and Evolution*. Springer.

KRAICHNAN, R. H. 1962 Turbulent thermal convection at arbitrary Prandtl number. *Phys. Fluids* **5**, 1374.

KULACKI, F. A. & GOLDSTEIN, R. J. 1972 Thermal convection in a horizontal fluid layer with uniform volumetric energy sources. *J. Fluid Mech.* **55**, 271–287.

LANDEAU, M. & AUBERT, J. 2011 Equatorially asymmetric convection inducing a hemispherical magnetic field in rotating spheres and implications for the past Martian dynamo. *Phys. Earth Planet. Inter.* **185**, 61–74.

LECOANET, D., LE BARS, M., BURNS, K. J., VASIL, G. M., BROWN, B. P., QUATAERT, E. & OISHI, J. S. 2015 Numerical simulations of internal wave generation by convection in water. *Phys. Rev.* E **91**, 063016.

LEPOT, S., AUMAÎTRE, S. & GALLET, B. 2018 Radiative heating achieves the ultimate regime of thermal convection. *Proc. Natl Acad. Sci. USA* **115**, 8937–8941.

LIMARE, A., VILELLA, K., DI GIUSEPPE, E., FARNETANI, C. G., KAMINSKI, E., SURDUCAN, E., SURDUCAN, V., NEAMTU, C., FOUREL, L. & JAUPART, C. 2015 Microwave-heating laboratory experiments for planetary mantle convection. *J. Fluid Mech.* **777**, 50–67.

MALKUS, W. V. R. 1954 The heat transport and spectrum of thermal turbulence. *Proc. R. Soc. Lond.* A **225**, 196–212.

MIRONOV, D., TERZHEVIK, A., KIRILLIN, G., JONAS, T., MALM, J. & FARMER, D. 2002 Radiatively driven convection in ice-covered lakes: observations, scaling, and a mixed-layer model. *J. Geophys. Res.* **107**, 2001JC000892.

NIEMELA, J. J., SKRBEK, L., SREENIVASAN, K. R. & DONNELLY, R. J. 2000 Turbulent convection at very high Rayleigh numbers. *Nature* **404**, 837–840.

RADICE, D., OTT, C. D., ABDIKAMALOV, E., COUCH, S. M., HAAS, R. & SCHNETTER, E. 2016 Neutrino-driven convection in core-collapse supernovae: high-resolution simulations. *Astrophys. J.* **820**, 76.

ROCHE, P.-E., GAUTHIER, F., KAISER, R. & SALORT, J. 2010 On the triggering of the ultimate regime of convection. *New. J. Phys.* **12**, 085014.

RUSAOUËN, E., LIOT, O., CASTAING, B., SALORT, J. & CHILLÁ, F. 2018 Thermal transfer in Rayleigh–Bénard cell with smooth or rough boundaries. *J. Fluid Mech.* **837**, 443–460.

SHEN, Y., TONG, P. & XIA, K.-Q. 1996 Turbulent convection over rough surfaces. *Phys. Rev. Lett.* **76**, 908.

SHRAIMAN, B. I. & SIGGIA, E. D. 1990 Heat transport in high-Rayleigh-number convection. *Phys. Rev.* A **42**, 3650(R).

SPIEGEL, E. A. 1963 A generalization of the mixing-length theory of thermal convection. *Astrophys. J.* **138**, 216–225.

SPIEGEL, E. A. 1971 Convection in stars I. Basic Boussinesq convection. *Annu. Rev. Astron. Astrophys.* **9**, 323–352.

TOPPALADODDI, S., SUCCI, S. & WETTLAUFER, J. S. 2017 Roughness as a route to the ultimate regime of thermal convection. *Phys. Rev. Lett.* **118**, 074503.

TOPPALADODDI, S. & WETTLAUFER, J. S. 2018 Penetrative convection at high Rayleigh numbers. *Phys. Rev. Fluids* **3**, 043501.

ULLOA, H. N., WÜEST, A. & BOUFFARD, D. 2018 Mechanical energy budget and mixing efficiency for a radiatively heated ice-covered waterbody. *J. Fluid Mech.* **852**, R1.

XIE, Y.-C. & XIA, K.-Q. 2017 Turbulent thermal convection over rough plates with varying roughness geometry. *J. Fluid Mech.* **825**, 573–599.

PHILOSOPHICAL
TRANSACTIONS A

rsta.royalsocietypublishing.org

Research

Check for updates

Article submitted to journal

Keywords:

Thermal convection, Turbulence

Author for correspondence:

Basile Gallet

e-mail: basile.gallet@cea.fr

Velocity-informed upper bounds on the convective heat transport induced by internal heat sources and sinks

Vincent Bouillaut, Benoît Flesselles,
Benjamin Miquel, Sébastien Aumaître, and
Basile Gallet

[1] SPEC, CEA, CNRS, Université Paris Saclay, F-91191
Gif-sur-Yvette, France

Three-dimensional convection driven by internal heat sources and sinks (CISS) leads to experimental and numerical scaling-laws compatible with a mixing-length – or 'ultimate' – scaling regime $\mathrm{Nu} \sim \sqrt{\mathrm{Ra}}$. However, asymptotic analytic solutions and idealized 2D simulations have shown that laminar flow solutions can transport heat even more efficiently, with $\mathrm{Nu} \sim \mathrm{Ra}$. The turbulent nature of the flow thus has a profound impact on its transport properties. In the present contribution we give this statement a precise mathematical sense. We show that the Nusselt number maximized over all solutions is bounded from above by const. $\times$ Ra, before restricting attention to 'fully turbulent branches of solutions', defined as families of solutions characterized by a finite nonzero limit of the dissipation coefficient at large driving amplitude. Maximization of Nu over such branches of solutions yields the better upper-bound $\mathrm{Nu} \lesssim \sqrt{\mathrm{Ra}}$. We then provide 3D numerical and experimental data of CISS compatible with a finite limiting value of the dissipation coefficient at large driving amplitude. It thus seems that CISS achieves the maximal heat transport scaling over fully turbulent solutions.

THE ROYAL SOCIETY
PUBLISHING

1. Introduction

Thermal convection refers to the fluid motion induced by the combined effect of vertical temperature gradients and gravity. The resulting motion enhances the heat transport from the warm to the cool fluid regions, as compared to the purely diffusive motionless state. A central question in both physics and applied mathematics of the Navier-Stokes equations is to determine this enhanced heat flux as a function of the strength of the driving mechanism. The most common setup is the Rayleigh-Bénard (RB) geometry, where a layer of fluid lies between a hot bottom plate and a cool top one, the two plates being maintained at constant temperature. In dimensionless form, the temperature difference between the two plates is quantified by the Rayleigh number Ra. One then measures the heat flux across the cell, which after dividing by the purely diffusive heat flux of a motionless fluid layer yields the Nusselt number Nu. The central question above then reduces to the determination of the asymptotic behavior of Nu as a function of Ra, typically sought under the form $\mathrm{Nu} \sim \mathrm{Ra}^{\gamma}$ (leaving aside the Prandtl number Pr, defined as the ratio of the kinematic viscosity over the thermal diffusivity).

As initially proposed by Priestley and Malkus [1,2], the emergent heat flux in the RB geometry is strongly restricted by the boundary layers adjacent to the top and bottom plates. This leads to the classical theory, characterized by a scaling exponent $\gamma = 1/3$. This prediction departs from the mixing-length prediction of Spiegel [3]: in the context of astrophysical fluids, where solid boundaries are irrelevant, Spiegel assumes that the heat flux is related to the temperature drop in a way that does not involve the tiny molecular diffusivities. This 'diffusivity-free' argument leads to $\mathrm{Nu} \sim \sqrt{\mathrm{Ra\,Pr}}$, that is, $\gamma = 1/2$. While the RB studies do not agree on when and whether RB convection can achieve a heat transport exponent γ greater than $1/3$ [4–11], they agree on the fact that the effective heat transport exponent is always significantly less than $1/2$, with experimental values in the range $\gamma \in [0.28 - 0.38]$. This makes it clear that the relationship between the heat flux and the temperature difference in experimental RB convection always involves the molecular diffusivities, either in a power-law or in a logarithmic fashion.

With the goal of circumventing the limitations of the RB setup, we recently introduced an alternate setup where convection is driven by internal heat sources and sinks (CISS). A combination of volumic sources and sinks deposits and removes heat directly inside the bulk turbulent flow, thus bypassing the throttling boundary layers of RB convection. In CISS, the heat flux is imposed and the vertical temperature drop is the emergent quantity that one measures or extracts from a numerical simulation. In dimensionless terms, the flux-based Rayleigh number $\mathrm{Ra_P} = \mathrm{Nu} \times \mathrm{Ra}$ is the control parameter, and the goal is to determine the Rayleigh number Ra for a given $\mathrm{Ra_P}$ (or, equivalently, to determine the Nusselt number $\mathrm{Nu} = \mathrm{Ra_P}/\mathrm{Ra}$). In the laboratory, the internal heat source corresponds to volumic absorption of light by a dyed fluid, while effective uniform cooling is realized by letting the body of fluid heat up – the so-called 'secular heating' – and focusing on the departure of the local temperature from the uniform drift (see [12,13] for details). We showed that this setup leads to the mixing-length regime of thermal convection, $\gamma = 1/2$, provided the internal heating and cooling regions extend significantly beyond the thin boundary layers [14]. The dependence in Prandtl number was further investigated through a suite of 3D direct numerical simulations (DNS), see [15]. For a free-slip bottom boundary the Nusselt number satisfies Spiegel's mixing-length prediction in both Ra and Pr, i.e., $\mathrm{Nu} \sim \sqrt{\mathrm{Ra\,Pr}}$. The same holds for a no-slip bottom boundary condition at low Pr, while persistent boundary layer corrections modify the behavior in Pr for large Pr, with $\mathrm{Nu} \sim \mathrm{Pr}^{1/6}\,\sqrt{\mathrm{Ra}}$.

At the level of applied mathematics, one may hope to capture the mixing-length exponent $\gamma = 1/2$ of CISS through the derivation of rigorous upper bounds on the Nusselt number, an approach pioneered by Howard, Busse and Doering & Constantin [16–18]. For the RB setup, this approach leads to upper bounds of the form $\mathrm{Nu} \leq \text{const.} \times \mathrm{Ra}^{1/2}$, i.e., they are characterized by a diffusivity-free scaling exponent $\gamma = 1/2$ greater than the exponent inferred from experiments and DNS. The natural question then is whether the exponent $\gamma = 1/2$ of CISS corresponds to a maximization of the Nusselt number subject to simple constraints. We recently answered this question in the negative, computing upper bounds and exhibiting laminar asymptotic flow solutions of CISS characterized by a heat transport efficiency $\mathrm{Nu} \sim \mathrm{Ra}$, exceeding the mixing-length scaling exponent. Although the two are perfectly compatible at the mathematical level, there is a discrepancy between the behavior of upper bounds, which are saturated by unstable (in 3D) laminar solutions with a heat transport exponent $\gamma = 1$, and the seemingly turbulent flows achieved in the laboratory and in 3D DNS, characterized by a mixing-length heat transport exponent $\gamma = 1/2$. In other words, it seems that the turbulent nature of the flow has a profound impact on its transport properties. In the following, we confirm this statement in a precise mathematical sense. We show that restricting attention to fully turbulent flow solutions further constrains the scaling exponent γ. The overall approach, where rigorous bounding methods are augmented with physically sound and mathematically precise assumptions, resonates with other contributions to the present themed issue [19].

Anticipating the precise definitions in section 2, we denote the velocity field as $\mathbf{u}(x, y, z, t)$, the kinematic viscosity as ν, the domain height as H, and a spatio-temporal average over the entire fluid domain with angular brackets. The dissipation coefficient $\mathcal{C}$ of the flow is then defined as:

$$\mathcal{C} = \frac{H\nu \left\langle |\boldsymbol{\nabla}\mathbf{u}|^2 \right\rangle}{\langle \mathbf{u}^2 \rangle^{3/2}} . \tag{1.1}$$

'Turbulent dissipation' or 'anomalous dissipation' refers to the singular limit of (1.1) as viscosity is lowered for constant large-scale forcing: even though viscosity appears at the numerator, turbulent flows develop stronger and stronger velocity gradients as viscosity is lowered, in such a way that (1.1) reaches a finite (strictly) positive limit as the Reynolds number goes to infinity [20]. Such anomalous dissipation is used as the definition of a fully turbulent flow in the present study. More precisely, we define a 'fully turbulent branch of solutions' as a continuous family of solutions indexed by $\mathrm{Ra_P}$ that admits a finite nonzero limit of the dissipation coefficient for asymptotically large $\mathrm{Ra_P}$:

$$\text{Fully turbulent branch of solutions} \iff \lim_{\mathrm{Ra_P} \to \infty} \mathcal{C} = \mathcal{C}_\infty > 0. \tag{1.2}$$

While we cannot prove the very existence of such turbulent branches of solutions, one can assume that such a branch of solutions exists – an assumption referred to as the 'fully turbulent' assumption in the following – and address motivational questions at the crossroad of applied mathematics and physics:

- At the mathematical level, can one use information (or assumptions) about the velocity field to improve the upper bound on convective heat transport? Does CISS maximize the heat transport subject to simple constraints, when supplemented with the 'fully turbulent' assumption?
- At the physical level, can we validate this fully turbulent assumption using experimental and numerical data? Does the velocity field obey the free-fall scaling-law put forward by Spiegel to derive the mixing-length heat transport scaling-law [3,21]?

In section 2, we derive rigorous upper bounds on the Nusselt number in terms of the Rayleigh number and the dissipation coefficient. Assuming that a fully turbulent branch of solutions exists according to the definition (1.2) above, we show that the Nusselt number cannot increase faster that the square-root of the Rayleigh number over this branch of solutions. In other words, we show that the upper bound $\mathrm{Nu} \lesssim \sqrt{\mathrm{Pr}\ \mathrm{Ra}}$ holds for CISS if one restricts attention to fully turbulent solutions. By contrast, laminar flows can realize $\mathrm{Nu} \sim \mathrm{Ra}$, as established in [22], and we derive an upper bound on the Nusselt number valid for all flow solutions that reproduces this 'laminar' scaling behavior: $\mathrm{Nu} \lesssim \mathrm{Ra}$. In section 3 we turn to DNS and experimental realizations of CISS to establish the fully turbulent nature of the flow. We report experimental data pointing to fully turbulent dissipation and clearly discarding laminar-like dissipation. DNS allow for a careful study of the behavior of $\mathcal{C}$ with $\mathrm{Ra_P}$. The data point to a nonzero limiting value of the dissipation coefficient for increasingly large $\mathrm{Ra_P}$, in line with (1.2). We conclude in section 4, the different results and data points being summarized in the schematic Figure 5, before making contact with the existing literature on CISS.

2. Velocity-informed upper bounds

(a) Boussinesq system of equations

We consider a fluid layer inside a domain $(x, y, z) \in [0, L_x] \times [0, L_y] \times [0, H]$. Within the Boussinesq approximation, the dimensional equations governing the evolution of the velocity field $\mathbf{u}(x, y, z, t)$ and the temperature field $\theta(x, y, z, t)$ read:

$$\partial_t \mathbf{u} + (\mathbf{u} \cdot \boldsymbol{\nabla})\mathbf{u} = -\boldsymbol{\nabla} p + \nu \boldsymbol{\nabla}^2 \mathbf{u} + \alpha g \theta \mathbf{e}_z \,, \tag{2.1a}$$

$$\partial_t \theta + \mathbf{u} \cdot \boldsymbol{\nabla}\theta = \kappa \boldsymbol{\nabla}^2 \theta + \frac{P}{\rho C \ell_0} \left[e^{-z/\ell_0} - \frac{\ell_0}{H}\left(1 - e^{-H/\ell_0}\right) \right] \,, \tag{2.1b}$$

where ν denotes the kinematic viscosity, α the thermal expansion coefficient, g is gravity, κ is the thermal diffusivity, ρ is the mean fluid density and C is the specific heat capacity. The last term in equation (2.1*b*) represents the internal heat sources and sinks. The precise z-dependence of this term is motivated by the experimental realization of CISS, see section (a). The first term inside the square bracket corresponds to the volumic absorption of light by a dyed fluid, where P denotes the heat flux (in W.m^{-2}) provided by the light source in the form of visible light. This term decreases exponentially with height over an absorption length ℓ_0 as a result of Beer-Lambert's law. The second term inside the square brackets corresponds to the effective uniform heat sink associated with the secular heating of the body of fluid. This uniform cooling term balances the radiative heat source on space average, i.e., the integral of the bracketed term over the domain height vanishes. We nondimensionalize the variables using H, H^2/κ and $\nu\kappa/(\alpha g H^3)$ as length, time and temperature scales:

$$\mathbf{x} = H\tilde{\mathbf{x}} \,, \quad t = \frac{H^2}{\kappa}\tilde{t} \,, \quad \theta = \frac{\nu\kappa}{\alpha g H^3}\tilde{\theta} \,, \quad \mathbf{u} = \frac{\kappa}{H}\tilde{\mathbf{u}} \,. \tag{2.2}$$

Dropping the tildes to alleviate notations, the dimensionless Boussinesq equations read:

$$\partial_t \mathbf{u} + (\mathbf{u} \cdot \boldsymbol{\nabla})\mathbf{u} = -\boldsymbol{\nabla} p + \mathrm{Pr}\, \boldsymbol{\nabla}^2 \mathbf{u} + \mathrm{Pr}\, \theta \mathbf{e}_z \,, \tag{2.3a}$$

$$\partial_t \theta + \mathbf{u} \cdot \boldsymbol{\nabla}\theta = \boldsymbol{\nabla}^2 \theta + \mathrm{Ra_P}\, S(z) \,. \tag{2.3b}$$

The dimensionless control parameters appearing in this set of equations are the Prandtl number and the flux-based Rayleigh number:

$$\mathrm{Pr} = \frac{\nu}{\kappa} \,, \qquad \mathrm{Ra_P} = \frac{\alpha g H^4 P}{\rho C \nu \kappa^2} \,. \tag{2.4}$$

The heat source/sink function $S(z)$ is:

$$S(z) = \frac{e^{-z/\ell}}{\ell} - 1 + e^{-1/\ell} \,, \tag{2.5}$$

where $\ell = \ell_0/H$ denotes the dimensionless absorption length. The integral of $S(z)$ from $z = 0$ to $z = 1$ vanishes, because the uniform heat sink removes precisely the amount of heat input by the radiative heat source (over space average and per unit time).

The set of equations (2.3*a*-2.3*b*) is supplemented with the incompressibility constraint $\boldsymbol{\nabla} \cdot \mathbf{u} = 0$ and impermeable insulating boundary conditions at $z = 0$ and $z = 1$:

$$w|_{z=0;1} = 0 \,, \qquad \partial_z \theta|_{z=0;1} = 0 \,. \tag{2.6}$$

We consider a no-slip bottom boundary:

$$u|_{z=0} = v|_{z=0} = 0 \,, \tag{2.7}$$

while the top boundary condition is either free-slip or no-slip:

$$u|_{z=1} = v|_{z=1} = 0 \tag{2.8a}$$

$$\text{or} \quad \partial_z u|_{z=1} = \partial_z v|_{z=1} = 0\,. \tag{2.8b}$$

Finally, we consider periodic boundary conditions in the horizontal directions.

We want to characterize the internal temperature fluctuations that emerge in this system. Integrating equation (2.3*b*) over the entire fluid domain indicates that the space average of θ is independent of time, because the vertical average of $S(z)$ vanishes: if heat is input and removed at the same rate inside an insulated container, the space-averaged fluid temperature remains constant. Without loss of generality and to alleviate notations, we thus assume in the following that θ is mean-zero initially and therefore at any subsequent time. As the first moment of the temperature field vanishes, the simplest nonzero measure of the emergent temperature fluctuations is arguably the second moment of the temperature field. One can thus quantify the emergent temperature fluctuations through a Rayleigh number Ra based on the root-mean-square temperature. In terms of the dimensionless variables, this leads to the simple definition $\mathrm{Ra} = \sqrt{\langle \theta^2 \rangle}$, where the angular brackets $\langle \cdot \rangle$ denote a space and time average. To define a Nusselt number, one can estimate the typical diffusive flux associated with the emergent temperature scale $\sqrt{\langle \theta^2 \rangle}$, had it been imposed at the large scale H (that is, the diffusive flux that would arise if an equivalent temperature drop were imposed at large scale to a solid with the same thermal properties than the fluid). This equivalent diffusive flux is estimated simply as $\sqrt{\langle \theta^2 \rangle}$ in dimensionless form. We finally build the Nusselt number Nu by dividing the total input heat flux – $\mathrm{Ra_P}$ in dimensionless form – by this equivalent diffusive flux $\sqrt{\langle \theta^2 \rangle}$, which yields:

$$\mathrm{Nu} = \mathrm{Ra_P}/\mathrm{Ra}\,, \qquad \mathrm{Ra} = \sqrt{\langle \theta^2 \rangle}\,. \tag{2.9}$$

These definitions are well-suited for analysis and will be used extensively throughout this study. The reader might object that the Nusselt number defined above is not necessarily equal to unity in the diffusive state, a complication that would only modify the prefactors but not the scaling exponents of the bounds derived below.

An alternate definition for the Nusselt could be based on the partitioning of the input potential energy into a diffusive and a convective contribution, see equation (2.14) below. The complication here is that one could imagine a situation where the emergent temperature fluctuations are large, albeit with a negligible diffusive vertical flux. This situation arises precisely for the analytical solution computed in Ref. [22]: the dominant temperature field in the expansion has a vanishing horizontal average at any height, and thus a vanishing (horizontally averaged) diffusive flux in the vertical direction at any height. A compromise between these two possible definitions for the Nusselt number is to base the estimate of the emergent temperature drop on the horizontally averaged squared temperature (instead of the horizontally averaged temperature). We thus consider an alternate temperature-based Rayleigh number built with the maximum in the vertical direction of the time and horizontal average of the squared temperature:

$$\mathrm{Ra_{max}} = \max_{z\in[0;1]} \left\{ \sqrt{\overline{\theta^2}} \right\}\,, \tag{2.10}$$

where the overbar denotes an average with respect to x, y and t. A Nusselt number is then defined as the ratio of the input flux over the diffusive flux associated with the temperature estimate (2.10) established over the entire height of the cell, leading to:

$$\mathrm{Nu_{max}} = \mathrm{Ra_P}/\mathrm{Ra_{max}}\,. \tag{2.11}$$

The definitions of $\mathrm{Ra_{max}}$ and $\mathrm{Nu_{max}}$ allow us to make better contact with the literature, as experimentalists typically measure the vertical temperature drop across a convection cell. In both laboratory experiments and DNS of radiatively driven convection, the maximum temperature is achieved at the bottom of the fluid domain and fluctuates moderately in the horizontal directions. $\mathrm{Ra_{max}}$ is then a good proxy for the Rayleigh number based on the temperature drop between the bottom boundary and the bulk of the fluid (the latter definition for the Rayleigh number being the one used in previous experimental and numerical studies of this system, see Refs. [12,14,15]). Another desirable feature of $\mathrm{Ra}_{\mathrm{max}}$ and $\mathrm{Nu}_{\mathrm{max}}$ is that, up to factors of two, they reduce to the standard definitions of the Rayleigh and Nusselt numbers when applied to the canonical fixed-temperature Rayleigh-Bénard setup.

In the following, we derive upper bounds on Nu in terms of Ra, but we stress the fact that all these bounds carry over to $\mathrm{Nu}_{\mathrm{max}}$ and $\mathrm{Ra}_{\mathrm{max}}$. Indeed, from the definition $\left\langle \theta^2 \right\rangle = \int_0^1 \overline{\theta^2} \mathrm{d}z$, we obtain $\left\langle \theta^2 \right\rangle \le \max_{z\in[0;1]}\{\overline{\theta^2}\}$, hence:

$$\mathrm{Ra} \le \mathrm{Ra}_{\mathrm{max}} \,, \qquad \mathrm{Nu}_{\mathrm{max}} \le \mathrm{Nu} \,. \tag{2.12}$$

The upper bounds derived in the following are typically of the form $\mathrm{Nu} \le c \times \mathrm{Ra}^{\gamma}$, with γ a positive exponent and c a prefactor. From the inequalities (2.12) one immediately obtains that these bounds carry over in terms of $\mathrm{Ra}_{\mathrm{max}}$ and $\mathrm{Nu}_{\mathrm{max}}$, i.e., $\mathrm{Nu}_{\mathrm{max}} \le c \times {\mathrm{Ra}_{\mathrm{max}}}^{\gamma}$, the latter form being better-suited for comparison with experimental measurements.

(b) Bounding the heat flux in terms of the root-mean-square velocity

Multiplying the temperature equation (2.3*b*) by θ before averaging over space and time yields, after a few integration by parts using the boundary conditions:

$$\left\langle |\boldsymbol{\nabla}\theta|^2 \right\rangle = \mathrm{Ra}_{\mathrm{P}} \int_0^1 S(z)\overline{\theta}\, \mathrm{d}z \,. \tag{2.13}$$

Similarly, multiplying the temperature equation (2.3*b*) by z before averaging over space and time yields, after a few integration by parts using the boundary conditions:

$$-\mathrm{Ra}_{\mathrm{P}} \int_0^1 z S(z) \mathrm{d}z = \langle w\theta \rangle - \int_0^1 \partial_z \overline{\theta}\, \mathrm{d}z \,. \tag{2.14}$$

We bound the second term on the right-hand side using the Cauchy-Schwarz inequality, equation (2.13) and Jensen's inequality:

$$\begin{aligned} \left| \int_0^1 \partial_z \overline{\theta}\, \mathrm{d}z \right| \le \sqrt{\int_0^1 (\partial_z \overline{\theta})^2\, \mathrm{d}z} \quad &\le \quad \sqrt{\int_0^1 \overline{(\partial_z \theta)^2}\, \mathrm{d}z} \\ &\le \sqrt{\langle |\boldsymbol{\nabla}\theta^2| \rangle} = \sqrt{\mathrm{Ra}_{\mathrm{P}} \int_0^1 S(z)\overline{\theta}\, \mathrm{d}z}. \end{aligned} \tag{2.15}$$

Inserting this inequality into (2.14) and applying the Cauchy-Schwarz inequality to both terms on the right-hand side, we obtain:

$$-\mathrm{Ra}_{\mathrm{P}} \int_0^1 z S(z) \mathrm{d}z \quad \le \quad \langle w\theta \rangle + \sqrt{\mathrm{Ra}_{\mathrm{P}} \int_0^1 S(z)\overline{\theta}\, \mathrm{d}z} \tag{2.16}$$

$$\le \quad \sqrt{\langle w^2 \rangle} \mathrm{Ra} + \sqrt{\mathrm{Ra}_{\mathrm{P}} \mathrm{Ra}} \left(\int_0^1 S(z)^2\, \mathrm{d}z \right)^{1/4} \tag{2.17}$$

Dividing by the positive quantity $-\mathrm{Ra} \int_0^1 z S(z) \mathrm{d}z$ and using the relation $\mathrm{Ra}_{\mathrm{P}} = \mathrm{Ra}\, \mathrm{Nu}$ leads to:

$$\mathrm{Nu} - \mathrm{Nu}^{1/2} \frac{c_2}{c_1} - \frac{\sqrt{\langle w^2 \rangle}}{c_1} \le 0 \,, \tag{2.18}$$

where c_1 and c_2 are the following positive constants (for a given geometry of the setup):

$$c_1 = -\langle zS \rangle = \frac{1}{2} - \ell + e^{-1/\ell}\left(\frac{1}{2} + \ell\right), \tag{2.19}$$

$$c_2 = \left\langle S^2 \right\rangle^{1/4} = \left[-1 - e^{-2/\ell} + 2e^{-1/\ell} + \frac{1}{2\ell} - \frac{e^{-2/\ell}}{2\ell}\right]^{1/4}. \tag{2.20}$$

Seeking the roots of the quadratic function of $\mathrm{Nu}^{1/2}$ on left-hand side of (2.18), one obtains the equivalent inequality:

$$\mathrm{Nu} \leq \frac{1}{4}\left[\frac{c_2}{c_1} + \sqrt{\left(\frac{c_2}{c_1}\right)^2 + 4\frac{\langle w^2\rangle^{1/2}}{c_1}}\right]^2. \tag{2.21}$$

The right-hand side of the inequality above is an upper bound on the Nusselt number in terms of the root-mean-square vertical velocity.

(c) Bounding the heat flux in terms of the dissipation coefficient and the Rayleigh number

We would like to bound the root-mean-square vertical velocity to turn the upper bound (2.21) into a bound in terms of the Rayleigh number and the dissipation coefficient $\mathcal{C}$. Including the latter into the upper bound allows to readily derive upper bounds that apply to turbulent families of solutions, that is, to an hypothetical family of solutions characterized by a non-zero limiting value of the dissipation coefficient $\mathcal{C}$ as $\mathrm{Ra_P}$ (or Ra) goes to infinity, see (1.2). We first derive the kinetic energy power integral, obtained by taking the dot product of (2.3*a*) with $\mathbf{u}$ before averaging over space and time. After a few integrations by parts, one obtains:

$$\left\langle |\boldsymbol{\nabla}\mathbf{u}|^2 \right\rangle = \langle w\theta \rangle. \tag{2.22}$$

In terms of the dimensionless variables, the definition (1.1) of the dissipation coefficient $\mathcal{C}$ becomes:

$$\mathcal{C} = \mathrm{Pr}\frac{\left\langle |\boldsymbol{\nabla}\mathbf{u}|^2 \right\rangle}{\langle \mathbf{u}^2\rangle^{3/2}} \tag{2.23}$$

Using this definition, equation (2.22) and the Cauchy-Schwarz inequality, one obtains successively:

$$\left\langle w^2 \right\rangle^{3/2} \leq \left\langle \mathbf{u}^2 \right\rangle^{3/2} = \frac{\mathrm{Pr}}{\mathcal{C}}\left\langle |\boldsymbol{\nabla}\mathbf{u}|^2 \right\rangle = \frac{\mathrm{Pr}}{\mathcal{C}}\langle w\theta \rangle \leq \frac{\mathrm{Pr\ Ra}}{\mathcal{C}}\left\langle w^2 \right\rangle^{1/2}. \tag{2.24}$$

Dividing across by $\left\langle w^2 \right\rangle^{1/2}$ and taking the square-root provides an upper bound on the root-mean-square vertical velocity:

$$\left\langle w^2 \right\rangle^{1/2} \leq \sqrt{\frac{\mathrm{Pr\ Ra}}{\mathcal{C}}}. \tag{2.25}$$

Substituting this inequality into (2.21) leads to the following upper-bound $\mathcal{B}_1$ on the Nusselt number:

$$\mathrm{Nu} \leq \mathcal{B}_1 = \frac{1}{4}\left[\frac{c_2}{c_1} + \sqrt{\left(\frac{c_2}{c_1}\right)^2 + \frac{4}{c_1}\sqrt{\frac{\mathrm{Pr\ Ra}}{\mathcal{C}}}}\right]^2. \tag{2.26}$$

We are interested in the behavior of the upper-bound $\mathcal{B}_1$ as the Rayleigh number goes to infinity. For a given geometry (constant coefficients c_1 and c_2), the asymptotic behavior of the upper-bound is then simply:

$$\mathcal{B}_1 \sim \frac{1}{c_1}\sqrt{\frac{\mathrm{Pr}\ \mathrm{Ra}}{\mathcal{C}}}\,. \tag{2.27}$$

Laboratory experiments are typically run in the range of absorption length $\ell \ll 1$: even though the dimensional absorption length ℓ_0 is chosen to be greater than the boundary layer thickness, it remains much smaller than the height of the domain. In that limit, the constant c_1 is approximately given by $c_1 = 1/2 + O(\ell)$. In the asymptotic limit $\mathrm{Ra} \to \infty$ for fixed $\ell \ll 1$, the upper-bound thus takes the compact asymptotic form:

$$\mathcal{B}_1 \sim 2\sqrt{\frac{\mathrm{Pr}\ \mathrm{Ra}}{\mathcal{C}}}\,. \tag{2.28}$$

(d) Restricting attention to fully turbulent solutions

An interesting aspect of the upper bound (2.28) is that it allows to readily characterize the behavior of families of fully turbulent solutions, as defined at the outset. Of course, we have not proven that such families of solutions exist. However, one can assume that such a family of solutions exists and investigate the scaling behavior of the associated Nusselt number. The fully turbulent family of solutions is characterized by a finite nonzero limit of the dissipation coefficient for asymptotically large forcing (asymptotically large Reynolds number, $\mathrm{Ra_P}$ and Ra), see (1.2). In that limit, the upper-bound (2.28) behaves as $\sqrt{\mathrm{Pr}\ \mathrm{Ra}}$, i.e., it follows the so-called ultimate regime of thermal convection. Experimental studies report a scaling exponent compatible with this scaling behavior in Ra, while an extensive three-dimensional numerical study has shown that the scaling behavior in both Ra and in Pr agrees well with the ultimate scaling when $\mathrm{Pr} \ll 1$, the behavior in Pr being different for $\mathrm{Pr} \gtrsim 1$. In other words, this upper bound appears to be sharp in Rayleigh number when compared to the available experimental and 3D numerical data.

However, we have also reported analytical and 2D numerical solutions of CISS that exceed the ultimate scaling behavior, with the Nusselt number increasing linearly in Ra. The upper-bound (2.28) immediately indicates that these solutions cannot be fully turbulent, and indeed they appear to be extremely laminar, see [22]. In the following subsection, we derive an upper bound that applies to arbitrary flow solutions (including both laminar and turbulent ones).

(e) Upper bound for arbitrary flow solutions

We now wish to derive an upper bound that holds for any flow solution, i.e., we stop restricting attention to fully turbulent branches of solutions. To wit, we derive an upper bound on the inverse dissipation coefficient $\mathcal{C}^{-1}$. The Poincaré inequality in the vertical direction yields:

$$\left\langle \mathbf{u}^2 \right\rangle c_3 \leq \left\langle (\partial_z \mathbf{u})^2 \right\rangle \leq \left\langle |\boldsymbol{\nabla} \mathbf{u}|^2 \right\rangle = \frac{\mathcal{C}}{\mathrm{Pr}} \left\langle \mathbf{u}^2 \right\rangle^{3/2}\,, \tag{2.29}$$

where $c_3 = \pi^2$ for no-slip top and bottom boundaries and $c_3 = \pi^2/4$ for a free-slip top boundary. The inequality above yields:

$$\frac{\mathrm{Pr}}{\mathcal{C}} \leq \frac{\left\langle \mathbf{u}^2 \right\rangle^{1/2}}{c_3} \tag{2.30}$$

Using the intermediate steps in (2.24), together with $\left\langle w^2 \right\rangle < \left\langle \mathbf{u}^2 \right\rangle$, we obtain:

$$\left\langle \mathbf{u}^2 \right\rangle \leq \frac{\mathrm{Pr}\ \mathrm{Ra}}{\mathcal{C}}\,, \tag{2.31}$$

which we substitute into (2.30) to get:

$$\frac{\mathrm{Pr}}{\mathcal{C}} \leq \frac{\mathrm{Ra}}{c_3^2} \,. \tag{2.32}$$

Inserting this inequality in the expression of the bound $\mathcal{B}_1$ leads to the following upper bound $\mathcal{B}_2$:

$$\mathrm{Nu} \leq \mathcal{B}_2 = \frac{1}{4}\left[\frac{c_2}{c_1} + \sqrt{\left(\frac{c_2}{c_1}\right)^2 + \frac{4\,\mathrm{Ra}}{c_1 c_3}}\right]^2 . \tag{2.33}$$

The upper bound $\mathcal{B}_2$ does not involve the dissipation coefficient anymore. We are interested in the large-Ra low-ℓ asymptotic behavior of the bound, given by:

$$\mathcal{B}_2 \sim \frac{2}{c_3}\,\mathrm{Ra} = \begin{cases} \frac{2}{\pi^2}\,\mathrm{Ra} & \text{for a no-slip top boundary} \,, \\ \frac{8}{\pi^2}\,\mathrm{Ra} & \text{for a free-slip top boundary} \,. \end{cases} \tag{2.34}$$

This upper bound is similar to the one derived in Ref. [22] , with the same scaling in Ra, but a prefactor much better-suited to the source/sink function (2.5): the prefactor of the upper bound in Ref. [22] diverges as $\ell \to 0$, whereas the prefactor of $\mathcal{B}_2$ reaches a finite limit as $\ell \to 0$, see (2.34). The upper bound scales linearly in Ra, which is precisely the scaling behavior of an exact analytic laminar solution derived in Ref. [22] for free-slip top and bottom boundaries. The scaling behaviour of the upper bound is thus sharp for free-slip top and bottom boundaries. We believe it is probably also sharp for no-slip boundary conditions, but that remains to be proven. One way to prove this would be to adapt the analytic flow solution in Ref. [22] to no-slip boundaries instead of stress-free boundaries (see Refs. [23–26] for the computation of steady convective flows with various boundary conditions).

To summarize this section, the Nusselt number of any flow solution cannot increase faster than Ra, while the Nusselt number associated with a turbulent family of solutions cannot increase faster than $\sqrt{\mathrm{Ra}}$. In other words, any scaling exponent γ larger than $1/2$ is necessarily associated with non-turbulent solutions, according to the definition given at the outset. In the following, we characterize the dissipation coefficient in experimental and numerical realizations of CISS to assess the fully turbulent nature of the flow.

3. Assessing the fully turbulent nature of the flow from experimental and DNS data

We now turn to numerical and experimental realizations of CISS. The goal is to extract the dissipation coefficient $\mathcal{C}$ and assess whether the flow is fully turbulent according to (1.2).

(a) Laboratory experiments

The experimental setup, sketched in Figure 1, is described extensively in Ref. [12]. We briefly recall its main characteristics. A cylindrical cell of radius $R = 10$ cm is filled with a homogeneous mixture of water and carbon black dye, up to a height H ranging from 4 to 18 cm. A powerful spotlight shines at the tank from below, the latter having a transparent bottom boundary. Absorption of light by the fluid leads to an internal source of heat, the magnitude of which decreases exponentially with height over a scale ℓ_0 (Beer-Lambert's law). The absorption length ℓ_0 can be tuned through the concentration of dye: for high dye concentration ℓ_0 is much smaller than the thermal boundary layer thickness and we recover a standard RB-like boundary-heated configuration. By contrast, for low dye concentration ℓ_0 is larger than the boundary layer thickness. The internal heating then bypasses the boundary layers and leads to the diffusivity-free mixing-length scaling regime of turbulent heat transport [12,14]. As one cannot cool down the fluid using a cold plate without inducing a heat-transport-restricting upper boundary layer, we resort to 'secular heating' instead: in the absence of cooling and with insulating boundaries,

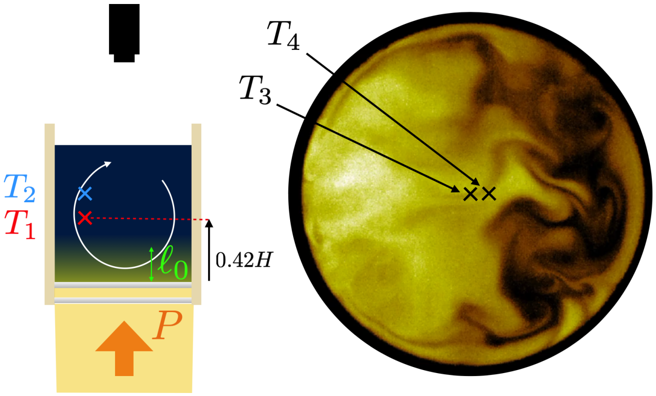

Figure 1. **Left:** Schematic of the experimental setup with the thermal camera imaging the top free surface. P denotes the total heat flux radiated from the spotlight in the form of visible light. T_1 and T_2 are the two vertically aligned temperature probes. **Right:** snapshot of the temperature field on the top free-surface (lighter color for warmer temperature). From such snapshots we extract two local temperature signals at locations indicated by T_3 and T_4.

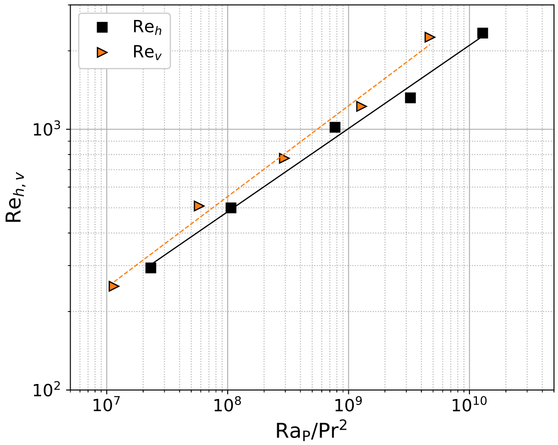

Figure 2. Experimental estimates of the Reynolds number as functions of $\mathrm{Ra_P\,Pr^{-2}}$ for $\ell = \ell_0/H = 0.048$. The dashed line is $\mathrm{Re} = 0.90\left(\mathrm{Ra_P\,Pr^{-2}}\right)^{0.35}$, while the straight line is $\mathrm{Re} = 1.35\left(\mathrm{Ra_P\,Pr^{-2}}\right)^{0.32}$. $\mathrm{Re_h}$ (resp. $\mathrm{Re_v}$) refers to the Reynolds number inferred from the horizontal (resp. vertical) velocity estimate.

the volume-averaged temperature grows linearly in time. However, the temperature difference between any two points inside the tank is governed by the equations of Boussinesq convection driven by the radiative heat source and effectively cooled at an equal and opposite rate by a uniform internal heat sink (see Ref. [12] for details). This combination of radiative heating decreasing exponentially with height together with uniform effective cooling at an equal and opposite rate is the rationale behind the source/sink term in (2.1*b*). After a transient, a statistically steady vertical temperature drop arises.

The fluid being opaque, we cannot resort to standard optical velocimetry techniques to access the Reynolds number [27–32]. We thus infer the local velocity from the temporal correlation between two neighboring temperature probes [6,33–35]. A vertical velocity estimate U_v si inferred

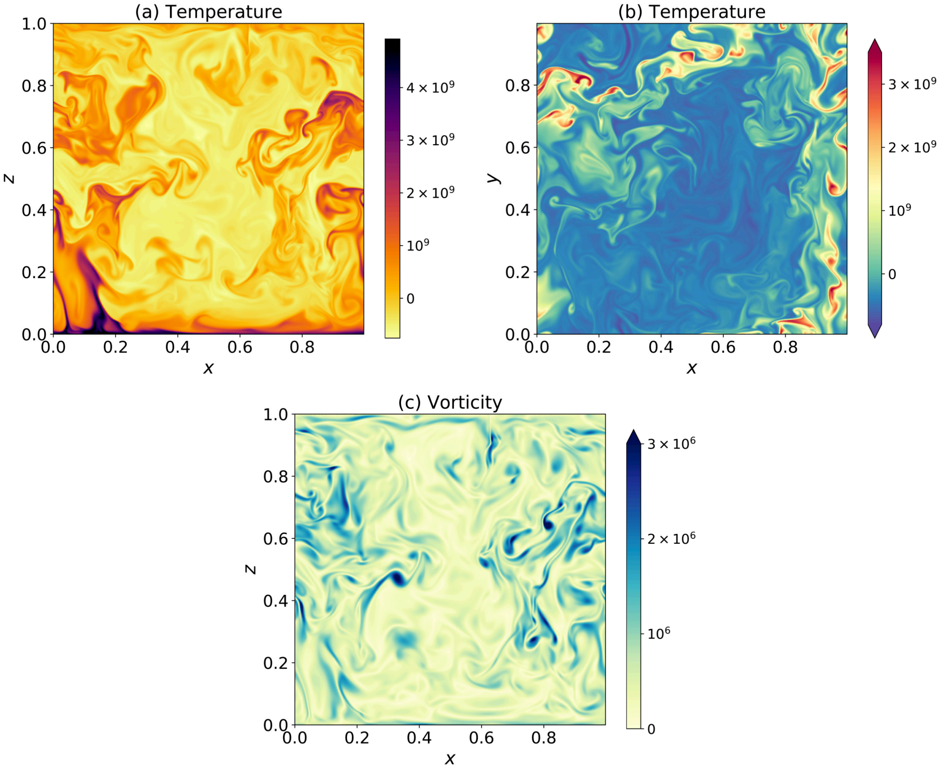

Figure 3. Snapshots of a turbulent flow computed numerically for $\mathrm{Ra_P} = 10^{12}$, $\mathrm{Pr} = 7$ and $\ell = 0.048$. (a) Vertical slice of temperature. (b) Horizontal slice of temperature at $z = 0.25$. (c) Vertical slice of vorticity $\sqrt{|\boldsymbol{\nabla} \times \mathbf{u}|^2}$.

from the vertically aligned probes T_1 and T_2 in Figure 1 (located at mid-radius, $0.42H$ above the bottom boundary and 0.5 cm apart, except for the highest $\mathrm{Ra_P}$ where they are 1 cm apart). We compute the correlation function between the two probes, before dividing the spacing between the probes by the time-lag associated with the maximum of the cross-correlation function. This gives access to the characteristic velocity of a fluid parcel travelling from one probe to the other. In a similar fashion, we estimate the characteristic horizontal velocity U_h through the cross-correlation between two virtual probes T_3 and T_4 (consisting of squares of four pixels each, 1 cm apart) extracted from the thermal images, see Figure 1.

We build the inferred Reynolds number $\mathrm{Re_{h,v}} = U_{h,v} H/\nu$ and plot them in Figure 2 as functions of $\mathrm{Ra_P Pr^{-2}}$. They are compatible with a power-law behavior $\mathrm{Re_{h,v}} \sim \left(\mathrm{Ra_P Pr^{-2}}\right)^{\beta}$, with $\beta = 0.32$ and $\beta = 0.35$ for $\mathrm{Re_h}$ and $\mathrm{Re_v}$, respectively. These values of β should be compared to the laminar vs. turbulent values of this exponent: a fully turbulent flow that satisfies (1.2) is associated with $\beta = 1/3$. By contrast, a laminar flow dissipating energy at the large scale H would be characterized by a dissipation coefficient that is inversely proportional to the Reynolds number, hence $\beta = 1/2$. The data in Figure 2 thus clearly discard the laminar scaling, while being compatible with the fully turbulent one within measurement accuracy. The measurement accuracy is insufficient to characterise the scaling behavior of the dissipation coefficient more precisely, and we turn to numerical data instead.

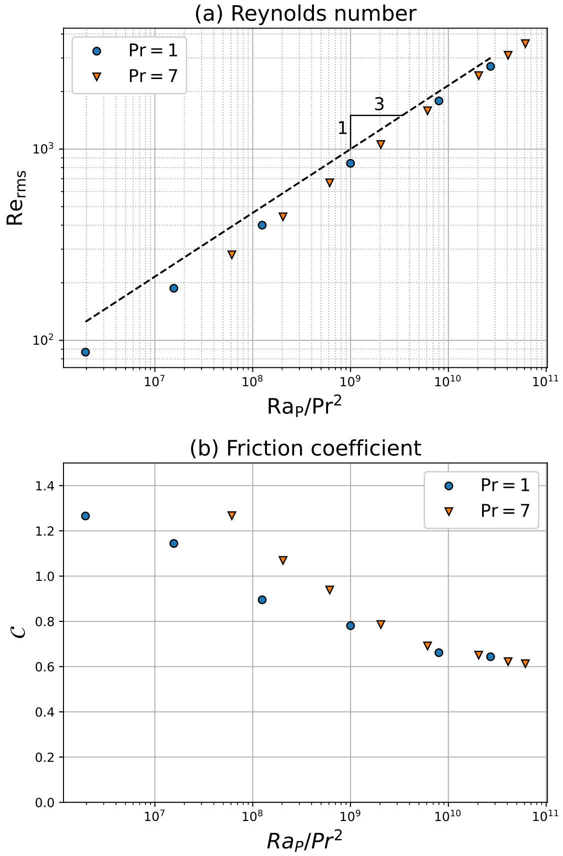

Figure 4. (a) Reynolds number, defined in equation (3.2) and (b) Dissipation coefficient, defined in equation (2.23), obtained by DNS and plotted as functions of the control parameter $\mathrm{Ra_P}/\mathrm{Pr}^2$. ●: $\mathrm{Pr} = 1$ and $\ell = 0.024$; $\triangledown$: $\mathrm{Pr} = 7$ and $\ell = 0.048$.

(b) Direct Numerical Simulations

We compute numerical solutions to the governing equations (2.3) using Coral, a pseudo-spectral, scalable, time-stepping solver for differential equations [36]. The computational domain is a unit cube $(x, y, z) \in [0, 1) \times [0, 1) \times [0, 1]$ with periodic boundary conditions along the horizontal directions (x, y). We impose impermeable and thermally insulating boundary conditions along surfaces $z = 0$ and $z = 1$, see equations (2.6). We model the solid bottom and the free surface of the experiment by imposing no-slip boundary conditions at $z = 0$ (2.7) and free-slip boundary conditions at $z = 1$ (2.8*b*). In Coral, these boundary conditions are imposed through basis recombination, i.e., by expanding the variables on bases of functions obtained as tensor products of Fourier modes along the horizontal and suitable linear combinations of Chebyshev polynomials, each of which obeys the boundary conditions along z (see, e.g., Ref. [37]). Simulations reported in the present manuscript use the second order semi-implicit time-stepping scheme of [38]. Finally, the divergence-free constraint is readily imposed by expressing the solenoidal velocity field $\mathbf{u}$ in terms of velocity potentials ϕ and ψ, and horizontally-invariant mean flows U and V:

$$\mathbf{u} = \boldsymbol{\nabla} \times \psi(x, y, z, t)\, \mathbf{e}_z + \boldsymbol{\nabla} \times \boldsymbol{\nabla} \times \phi(x, y, z, t)\, \mathbf{e}_z + U(z, t)\, \mathbf{e}_x + V(z, t)\, \mathbf{e}_y\,. \tag{3.1}$$

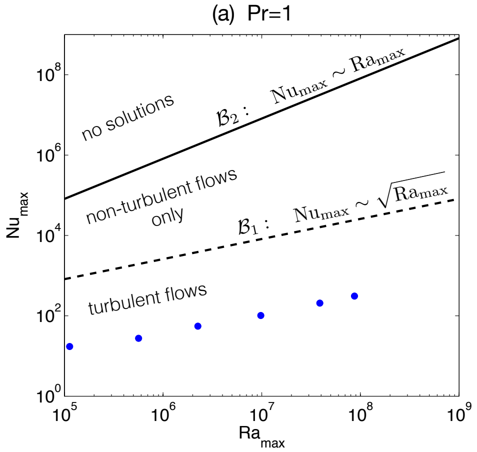

Figure 5. Numerical data (blue symbols) together with upper bounds $\mathcal{B}_1$ and $\mathcal{B}_2$ in the plane $(\mathrm{Ra}_{\text{max}}, \mathrm{Nu}_{\text{max}})$ for (a) $\mathrm{Pr} = 1$ and (b) $\mathrm{Pr} = 7$. The upper bound $\mathcal{B}_1$ over turbulent branches of solutions is represented using the numerically determined asymptotic value of the dissipation coefficient $\mathcal{C}_\infty \simeq 0.6$. The absorption length used in the DNS is $\ell = 0.024$ for panel (a) and $\ell = 0.048$ for panel (b).

The data consist in sweeps of the flux-based Rayleigh number Ra_P for two values of the Prandtl number: the canonical case $\mathrm{Pr} = 1$ with $\ell = 0.024$, and the value $\mathrm{Pr} = 7$ of laboratory experiments using water as the working fluid, together with a dimensionless absoprtion length $\ell = 0.048$. We illustrate in Figure 3 the turbulent flow obtained for $\mathrm{Ra}_\mathrm{P} = 10^{12}$, $\mathrm{Pr} = 7$ and $\ell = 0.048$.

For each set of parameters, the flow is computed from an initial condition taken as either random small-amplitude noise, or the final state of a run with neighboring control parameters. We let the flow equilibrate and reach a statistically stationary regime during which some velocity and temperature diagnostics are computed. In the following, we focus specifically on the dissipation coefficient $\mathcal{C}$, the Rayleigh and Nusselt numbers – using the definitions (2.10-2.11) for ease of comparison with experiments – and the Reynolds number Re based on the height of the domain and the root-mean-square velocity. In terms of the dimensionless variables, Re is defined as:

$$\mathrm{Re} = \frac{\sqrt{\left\langle |\mathbf{u}|^2 \right\rangle}}{\mathrm{Pr}} . \tag{3.2}$$

We plot in figure 4 both the Reynolds number Re and the dissipation coefficient $\mathcal{C}$, as functions of $\mathrm{Ra}_\mathrm{P}/\mathrm{Pr}^2$. Both the $\mathrm{Pr} = 1$ and $\mathrm{Pr} = 7$ datasets behave similarly and indicate a tendency towards turbulent dissipation for our most turbulent flows, corresponding to $\mathrm{Re} \gtrsim 2000$. Indeed, these data points seem to asymptote the scaling law $\mathrm{Re} \sim \left(\mathrm{Ra}_\mathrm{P}/\mathrm{Pr}^2\right)^{1/3}$, and the dissipation coefficient $\mathcal{C}$ for both $\mathrm{Pr} = 1$ and $\mathrm{Pr} = 7$ seems to saturate to a limiting value $\mathcal{C}_\infty \simeq 0.6$. Data at even higher Reynolds number may be necessary to reach a definitive conclusion. However, the present data strongly suggest that CISS enters a fully turbulent regime characterized by anomalous dissipation for $\mathrm{Re} \gtrsim 2000$, in line with (1.2), which justifies the applicability of both bounds $\mathcal{B}_1$ and $\mathcal{B}_2$ in section 2 to this flow.

4. Discussion

Focusing on convection induced by heat sources and sinks, we have derived lower bounds on the emergent root-mean-square temperature in terms of the flux-based Rayleigh number. To make better contact with the vast literature on thermal convection, we have expressed these bounds in terms of the emergent temperature-based Rayleigh and Nusselt numbers. As argued at the outset, the definitions (2.10-2.11) are probably best-suited for comparison with experimental results, and we provide in Figure 5 a summary of the bounds in the plane $(\mathrm{Ra}_{\max}, \mathrm{Nu}_{\max})$. The upper bound (2.28) on the Nusselt number scales as the square-root of the Rayleigh number. It applies only to turbulent branches of solutions, according to the definition (1.2) given at the outset and assuming that such branches of solutions exist. By contrast, the best upper bound (2.34) over all flow solutions scales linearly in Rayleigh number, a behavior associated with laminar analytic flow solutions such as the one derived in Ref. [22].

We then turned to numerical and experimental data to validate the existence of turbulent branches of solutions. The numerical data indeed point to a finite limiting value of the dissipation coefficient as the flux-based Rayleigh number – and thus the Reynolds number – increases. We stress the fact that the validation of the fully turbulent assumption (1.2), when combined with the 'ultimate' scaling-law for heat transport $\mathrm{Nu} \sim \sqrt{\mathrm{RaPr}}$, leads to Spiegel's free-fall scaling-law for the velocity field $\mathrm{Re} \sim \sqrt{\mathrm{Ra}/\mathrm{Pr}}$, where the Reynolds number Re is based on the height of the domain and the root-mean-square velocity. In other words, using CISS we can validate both Spiegel's prediction of a diffusivity-free regime for the heat transport, $\mathrm{Nu} \sim \sqrt{\mathrm{RaPr}}$, and the free-fall scaling assumption that underpins it [21].

The upper bounds derived in the present study provide a useful point of view to discuss the proposed scaling theories for CISS. For instance, in Lepot et al. [12] we report a scaling exponent $\gamma \simeq 0.55$ for the scaling-law $\mathrm{Nu} \sim \mathrm{Ra}^{\gamma}$ at $\mathrm{Pr} = 7$. Assuming that the flow becomes fully turbulent at large driving amplitude, the slight departure of the measured exponent from $1/2$ must be attributed to finite-Reynolds-number effects. As a matter of fact, we showed in Lepot et al. using DNS that the scaling exponent γ is indeed much closer to $1/2$ for $\mathrm{Pr} = 1$ than for $\mathrm{Pr} = 7$, the former corresponding to reduced viscous effects. The upper bounds (2.28) and (2.34) are also fully compatible with the scaling predictions that we put forward in Refs. [14] and [15] with regard to the dependence of the Nusselt number on Ra, Pr and the dimensionless absorption length ℓ. By contrast, the upper bounds challenge some scaling predictions recently put forward in Ref. [39] for CISS: out of the five scaling regimes proposed in Ref. [39], three correspond to a scaling exponent $\gamma > 1$ and are thus discarded by the general upper bound (2.34). The remaining two scaling regimes have a scaling exponent $\gamma > 1/2$: they appear to violate the upper-bound (2.28) on fully turbulent branches of solutions and thus require a dissipation coefficient that vanishes asymptotically at large driving amplitude. It thus appears that care must be taken when applying the intuition gathered from the Rayleigh-Bénard setup to CISS. The present data indicate that, to some extent, CISS behaves in a much simpler fashion than RB convection: as in most instances of fully turbulent flows, the speed, the dissipated power and the transport properties seem to become independent of molecular diffusivities for large-enough driving amplitude. In other words, in line with Spiegel's intuition [21] the convective flow achieves fully turbulent dissipation, the free-fall velocity scaling-law and the ultimate heat transport scaling-law.

Funding. This research is supported by the European Research Council under grant agreement FLAVE 757239. The numerical study was performed using HPC resources from GENCI-CINES and TGCC (grant 2020-A0082A10803 and grant 2021-A0102A10803).

Data availability statement. The experimental and numerical data are available online (https://doi.org/10.6084/m9.figshare.16811299.v1). The numerical code is publicly available, as described in Ref. [36].

Authors' contributions. VB, SA and BG designed the experiment and performed the experimental measurements. VB, BM, SA and BG analysed the experimental data. BM wrote the numerical code. VB and BM performed the DNS. BF and BG computed the theoretical bounds. VB, BF, BM, SA and BG wrote the paper.

References

1. Priestley CHB. 1954 Convection from a Large Horizontal Surface. *Australian Journal of Physics* **7**, 176.
2. Malkus WVR. 1954 The heat transport and spectrum of thermal turbulence. *Proceedings of the Royal Society of London. Series A. Mathematical and Physical Sciences* **225**, 196–212.
3. Spiegel EA. 1963 A Generalization of the Mixing-Length Theory of Turbulent Convection. *Ap. J.* **138**, 216.
4. Chavanne X, Chillà F, Castaing B, Hébral B, Chabaud B, Chaussy J. 1997 Observation of the ultimate regime in Rayleigh–Bénard convection. *Phys. Rev. Lett.* **79**, 3648–3651.
5. Niemela J, Skrbek L, Sreenivasan K, Donnelly R. 2000 Turbulent convection at very high Rayleigh numbers. *Nature* **404**, 837.
6. Chavanne X, Chillà F, Chabaud B, Castaing B, Hébral B. 2001 Turbulent Rayleigh-Bénard convection in gaseous and liquid he. *Physics of Fluids* **13**, 1300–1320.
7. Roche PE, Gauthier F, Kaiser R, Salort J. 2010 On the triggering of the ultimate regime of convection. *New J. Phys.* **12**, 085014.
8. He X, Funfschilling D, Nobach H, Bodenschatz E, Ahlers G. 2012 Transition to the ultimate state of turbulent Rayleigh-Bénard convection. *Phys. Rev. Lett.* **108**, 024502.
9. Iyer KP, Scheel JD, Schumacher J, Sreenivasan KR. 2020 Classical 1/3 scaling of convection holds up to $\mathrm{Ra} = 10^{15}$. *Proceedings of the National Academy of Sciences* **117**, 7594–7598.
10. Doering CR, Toppaladoddi S, Wettlaufer JS. 2019 Absence of evidence for the ultimate regime in two-dimensional Rayleigh-Bénard convection. *Phys. Rev. Lett.* **123**, 259401.
11. Doering CR. 2020 Absence of evidence for the ultimate state of turbulent Rayleigh-Bénard convection. *Phys. Rev. Lett.* **124**, 229401.
12. Lepot S, Aumaître S, Gallet B. 2018 Radiative heating achieves the ultimate regime of thermal convection. *Proc. Natl. Acad. Sci.* **115**, 8937–8941.
13. Bouillaut V, Miquel B, Julien K, Aumaître S, Gallet B. 2021 Experimental observation of the geostrophic turbulence regime of rapidly rotating convection. *Proc. Natl. Acad. Sci.* .
14. Bouillaut V, Lepot S, Aumaître S, Gallet B. 2019 Transition to the ultimate regime in a radiatively driven convection experiment. *J. Fluid Mech.* **861**, R5.
15. Miquel B, Bouillaut V, Aumaître S, Gallet B. 2020 On the role of the prandtl number in convection driven by heat sources and sinks. *J. Fluid Mech.* **900**, R1.
16. Howard LN. 1963 Heat transport by turbulent convection. *J. Fluid Mech.* **17**, 405–432.
17. Busse F. 1969 On howard's upper bound for heat transport by turbulent convection. *J. Fluid Mech.* **37**, 457–477.
18. Doering CR, Constantin P. 1996 Variational bounds on energy dissipation in incompressible flows. iii. convection. *Phys. Rev. E* **53**, 5957–5981.
19. Wen B, Ding Z, Chini G, Kerswell R Heat transport in Rayleigh-Bénard convection with linear marginality. *Phil. Trans. A* **in press**.
20. Frisch U. 1995 *Turbulence: The Legacy of A. N. Kolmogorov*. Cambridge University Press.
21. Spiegel EA. 1971 Convection in stars i. basic boussinesq convection. *Annual Review of Astronomy and Astrophysics* **9**, 323–352.

22. Miquel B, Lepot S, Bouillaut V, Gallet B. 2019 Convection driven by internal heat sources and sinks: Heat transport beyond the mixing-length or "ultimate" scaling regime.
Phys. Rev. Fluids **4**, 121501.
23. Jimenez J, Zufiria JA. 1987 A boundary-layer analysis of Rayleigh-Bénard convection at large Rayleigh number.
Journal of Fluid Mechanics **178**, 53–71.
24. Chini G, Cox S. 2009 Large Rayleigh number thermal convection: heat flux predictions and strongly nonlinear solutions.
Physics of Fluids **21**.
25. Waleffe F, Boonkasame A, Smith L. 2015 Heat transport by coherent Rayleigh-Bénard convection.
Physics of Fluids **27**.
26. Wen B, Goluskin D, LeDuc M, Chini GP, Doering CR. 2020 Steady Rayleigh-Bénard convection between stress-free boundaries.
Journal of Fluid Mechanics **905**, R4.
27. Xin YB, Xia KQ, Tong P. 1996 Measured velocity boundary layers in turbulent convection.
Phys. Rev. Lett. **77**, 1266–1269.
28. Qiu XL, Tong P. 2001 Large-scale velocity structures in turbulent thermal convection.
Phys. Rev. E **64**, 036304.
29. Xia KQ, Sun C, Zhou SQ. 2003 Particle image velocimetry measurement of the velocity field in turbulent thermal convection.
Phys. Rev. E **68**, 066303.
30. Xi HD, Lam S, Xia KQ. 2004 From laminar plumes to organized flows: the onset of large-scale circulation in turbulent thermal convection.
J. Fluid Mech. **503**, 47–56.
31. Sun C, Xia KQ, Tong P. 2005 Three-dimensional flow structures and dynamics of turbulent thermal convection in a cylindrical cell.
Phys. Rev. E **72**, 026302.
32. Liot O, Ehlinger Q, Rusaouën E, Coudarchet T, Salort J, Chillà F. 2017 Velocity fluctuations and boundary layer structure in a rough Rayleigh-Bénard cell filled with water.
Phys. Rev. Fluids **2**, 044605.
33. Castaing B, Gunaratne G, Heslot F, Kadanoff L, Libchaber A, Thomae S, Wu XZ, Zaleski S, Zanetti G. 1989 Scaling of hard thermal turbulence in Rayleigh–Bénard convection.
J. Fluid Mech. **204**, 1–30.
34. Wu XZ, Kadanoff L, Libchaber A, Sano M. 1990 Frequency power spectrum of temperature fluctuations in free convection.
Phys. Rev. Lett. **64**, 2140–2143.
35. Wu XZ, Libchaber A. 1992 Scaling relations in thermal turbulence: The aspect-ratio dependence.
Phys. Rev. A **45**, 842–845.
36. Miquel B. 2021 Coral: a parallel spectral solver for fluid dynamics and partial differential equations.
J. Open Source Soft. .
37. Boyd J. 2013 *Chebyshev and Fourier Spectral Methods: Second Revised Edition*.
Dover Books on Mathematics. Dover Publications.
38. Ascher UM, Ruuth SJ, Spiteri RJ. 1997 Implicit-explicit runge-kutta methods for time-dependent partial differential equations.
Applied Numerical Mathematics **25**, 151 – 167.
Special Issue on Time Integration
39. Creyssels M. 2020 Model for classical and ultimate regimes of radiatively driven turbulent convection.
Journal of Fluid Mechanics **900**, A39.